

DIE WELTRAUMQUALIFIZIERTE DATENAKQUISITION  
DES ÜBERGANGSSTRAHLUNGSDETEKTORS  
IM AMS-02 EXPERIMENT  
AUF DER INTERNATIONALEN RAUMSTATION

Andreas Sabellek

Zur Erlangung des akademischen Grades eines  
DOKTORS DER NATURWISSENSCHAFTEN  
von der Fakultät für Physik der  
Universität Karlsruhe (TH)

genehmigte

DISSERTATION

von

**Dipl.-Phys. Andreas Sabellek**  
aus Mannheim

Tag der mündlichen Prüfung: 05.12.2008

Referent: Prof. Dr. Willem de Boer, Institut für Experimentelle Kernphysik  
Korreferent: Prof. Dr. Thomas Müller, Institut für Experimentelle Kernphysik



## Deutsche Inhaltsübersicht

Die vorliegende Arbeit wurde im Rahmen der Mitarbeit am AMS-02 Experiment angefertigt. AMS-02 ist ein Spektrometer für geladene Teilchen und Gammastrahlung der kosmischen Strahlung, welches für den wartungsfreien Betrieb auf der Internationalen Raumstation für mindestens drei Jahre konzipiert ist. Die hohe Präzision basiert auf der redundanten Messung durch die zahlreichen Subdetektoren des Experiments. Das Institut für Experimentelle Kernphysik (IEKP) der Universität Karlsruhe hat hierbei die Verantwortung für Entwicklung, Bau und Betrieb der Datenauslese für den Übergangsstrahlungsdetektor (TRD) des Experiments übernommen.

Im Folgenden wird die Fertigstellung der weltraumqualifizierten Ausleseelektronik mit den dafür durchgeführten Tests während und nach der Produktion in Taiwan beschrieben. Die finale Integration in den AMS-02 Detektorverbund wurde im Jahr 2007 vorgenommen.

Zur Überprüfung der Funktionalität und der Entwicklung von sowohl Steuerungs- als auch Kontrollsoftware für den TRD wurde bereits früh ein Teststand am IEKP aufgebaut, welcher den Betrieb eines Prototypen zur Messung von kosmischer Strahlung erlaubt. Desweiteren wurde ein Betriebstest des finalen Übergangsstrahlungsdetektors an der RWTH Aachen durchgeführt, bei dem der Detektor erstmals im vollen Umfang kosmische Strahlung vermessen konnte. Probleme mit dem Detektor oder der Datenauslese wurden hierbei erkannt und behoben.

Während der ersten Datennahme im Jahr 2008 des gesamten AMS-02 Detektors am CERN in Genf wurden große Mengen an Daten kosmischer Strahlung aufgezeichnet und analysiert. Der Übergangsstrahlungsdetektor wurde dabei vor Ort oder über Fernzugriff aus Karlsruhe kontrolliert. Hiermit konnten die hervorragenden Eigenschaften des Übergangsstrahlungsdetektors und der digitalen Datenprozessierung bestätigt werden, welche für die Ausleseelektronik entwickelt wurde, um die großen Datenmengen bereits vor dem Verlassen des Experiments auf die wesentlichen physikalischen Informationen zu reduzieren.

Zusammenfassend hat der Betrieb des Übergangsstrahlungsdetektors unter Aufsicht des IEKP, als auch des gesamten AMS-02 Spektrometers bewiesen, dass der geplanten Fertigstellung und dem Transport mit dem Space Shuttle der NASA ins All im Jahr 2010 nichts entgegen steht.



The Space Qualified Data Acquisition  
for the Transition Radiation Detector of the  
AMS-02 Experiment on the International Space Station

**Andreas Sabellek**

March 8, 2009



# Contents

<b>1</b>	<b>Introduction</b>	<b>1</b>
<b>2</b>	<b>Physics with AMS-02</b>	<b>5</b>
2.1	Origin and Composition of Cosmic Ray Particles . . . . .	5
2.2	Gamma Ray Astronomy . . . . .	7
2.3	Measurement of Parameters of the Galactic Propagation Model . . . . .	7
2.4	Search for Heavy Antimatter . . . . .	8
2.5	Dark Matter Physics . . . . .	9
<b>3</b>	<b>The Alpha Magnetic Spectrometer AMS-02</b>	<b>17</b>
3.1	The AMS Project . . . . .	17
3.2	AMS-02 System Overview . . . . .	18
3.3	The Transition Radiation Subdetector (TRD) . . . . .	29
3.3.1	Detector Design . . . . .	29
3.3.2	Physics Principle of the TRD . . . . .	31
3.3.3	Theory of the Transition Radiation . . . . .	35
3.3.4	Gas Gain Factors of the TRD . . . . .	37
3.3.5	Contribution of the TRD to the AMS-02 Performance . . . . .	40
3.4	The AMS-02 Electronics . . . . .	42
3.5	Detector Environment on the ISS . . . . .	43
<b>4</b>	<b>The TRD Readout Electronics</b>	<b>47</b>
4.1	Overview of the System . . . . .	47
4.2	The Front End Electronics . . . . .	50
4.3	U-Crate Readout Electronics . . . . .	52
4.3.1	The J Interface Board JINF . . . . .	53
4.3.2	The Data Processing and Reduction Board UDR2 . . . . .	54
4.3.3	The Linear Regulator Board for Power Supply of the Front End UPSFE . . . . .	56
4.3.4	The High Voltage Generator Board UHVG . . . . .	58
4.4	Power Distribution Electronics . . . . .	60
4.4.1	DC/DC Converter Boards . . . . .	62
4.4.2	The UPD Controller S9011AU . . . . .	63
4.4.3	Boxes Interconnection Scheme and Cabling . . . . .	64
4.5	Space Qualification Phase . . . . .	66
4.5.1	Board Level Test . . . . .	66
4.5.2	Environmental Stress Screening - Thermal and Vibration Stress . . . . .	67

4.5.3	Electromagnetic Compatibility Test . . . . .	69
4.5.4	Thermal-Vacuum Test . . . . .	73
4.5.5	Summary of the Qualification Test Results . . . . .	77
4.6	The Prototype Cosmics Test in Karlsruhe . . . . .	77
<b>5</b>	<b>Electronics Flight Assembly and Acceptance Test</b>	<b>85</b>
5.1	The Board Level Acceptance Test . . . . .	85
5.1.1	Test Setup and Procedures . . . . .	85
5.1.2	Test Result Summary of the Board Level Tests . . . . .	88
5.2	Assembly of the Power Distribution Boxes . . . . .	90
5.3	Assembly of the U-Crates and the Power Cabling . . . . .	92
5.4	The Flight Hardware Acceptance Test at Crate Level . . . . .	94
5.4.1	Acceptance Test Parameters . . . . .	94
5.4.2	Test Result Summary . . . . .	98
5.5	UHVG Board High Voltage Calibration . . . . .	101
5.6	The AMS-02 Pre-integration Phase . . . . .	103
<b>6</b>	<b>TRD Data Processing in AMS-02</b>	<b>105</b>
6.1	The AMS-02 Data Acquisition System . . . . .	105
6.1.1	Physics Event Building . . . . .	106
6.1.2	Electronics Slow Control . . . . .	107
6.1.3	Data links . . . . .	108
6.2	Digital Signal Processing of the TRD . . . . .	112
6.2.1	DSP Programming . . . . .	112
6.2.2	AMS-02 Flight Software Framework . . . . .	115
6.3	The Data Processing in the UDR2 . . . . .	116
6.3.1	The UDR2 Sequencer . . . . .	116
6.3.2	The Data Calibration Routine . . . . .	117
6.3.3	The Data Processing and Reduction Routine . . . . .	122
6.3.4	The DAC Calibration Routine . . . . .	126
6.4	Subsystem Status Monitoring by the QList . . . . .	129
6.5	Data of the TRD in the AMS-02 Data Format . . . . .	131
<b>7</b>	<b>Cosmic Ray Test and Data Analysis with the TRD</b>	<b>135</b>
7.1	The TRD Cosmic Ray Test at RWTH Aachen . . . . .	135
7.1.1	TRD Standalone Test Setup . . . . .	135
7.1.2	Data Analysis and Results . . . . .	137
7.2	The AMS-02 Cosmic Ray Test at CERN . . . . .	148
7.2.1	AMS-02 Pre-Integration Phase . . . . .	148
7.2.2	Run Control Development for the Ground Support Computer . . . . .	151
7.2.3	Results from Cosmic Ray Data for the TRD . . . . .	154
<b>8</b>	<b>Summary</b>	<b>163</b>
8.1	AMS-02 Flight Status and Outlook . . . . .	166
	<b>Bibliography</b>	<b>169</b>

# Chapter 1

## Introduction

High energy physics, which is a synonym for particle physics, is facing an extremely interesting and promising decade. A number of discoveries are expected from current big experiments, which are built and operated by huge worldwide collaborations. The question of an unacquainted person might be, how do you discover new things in particle physics? The simple answer is you look to a giant number of tracks of particles in known conditions. What you then have to find out is, which tracks or energy spectra you can explain and which you cannot. In latter case you are close to a new discovery, maybe already predicted by an existing theory. Yet a lot of theories are developed, which actually extend the current standard model of particle physics.

To be able to look for tracks, you first need the tools to get the tracks. This is the same in experiments on Earth such as at the LHC<sup>1</sup> and in space. A deep understanding of the tools you are using is essential, otherwise the results simply have no meaning. Development and operation of such a tool heading to new discoveries is the AMS-02 experiment on board the International Space Station. The project is lead by Samuel Ting, professor at MIT, in a relatively small international collaboration. The logo of the experiment is shown in figure 1.1. Billions of tracks caused by charged cosmic ray particles and gamma rays will be recorded with this precision instrument within its three years scheduled operation. It is the first time, that the same device will measure all spectra with such a precision and statistics. The key principle of AMS-02 is the independent and redundant measurement of the properties of each crossing particle in different subdetectors. In fact AMS-02 has more subdetectors than any other particle detector built so far.

This thesis deals with the development and commisioning of the transition radiation subdetector (TRD) sitting on top of the experiment. It is the first one, which is hit by a particle in AMS-02. Due to its low density as a gaseous detector, particle properties are almost not influenced, but valuable information is acquired to determine the type of the particle. The TRD is able to distinguish between electrons and protons by taking advantage of the transition radiation effect of relativistic particles. The TRD detector is designed and built by RWTH Aachen University<sup>2</sup> and the TRD gas supply unit by MIT<sup>3</sup>. The data acquisition system of the TRD is developed and built under responsibility of the IEKP at University of Karlsruhe.

---

<sup>1</sup>Large Hadron Collider operated at CERN

<sup>2</sup>Rheinisch-Westfälische Technische Hochschule Aachen

<sup>3</sup>Massachusetts Institute of Technology

The challenge of design and production of an electronics system for a space experiment is to ensure the capability to reliably operate in space. The system like the entire detector has to be maintenance free. Therefore all parts are built with redundancy on different levels. Restrictions apply for parameters such as weight, power consumption and part procurement. A prototype of the system has been built to pass through a space qualification procedure, which covers thermal stress, operation in vacuum and mechanical stress simulating the shuttle launch during transport to space. Furthermore strict limits are set by NASA<sup>1</sup> for electromagnetic radiation emitted by equipment to be operated on board the ISS, which needs to be tested in electromagnetic compatibility tests. In the case any of the tests is not passed actions have to be taken to allow conformance with the requirements.

Once the qualification model passed the test procedure, the flight hardware, consisting of two identical units of the system, is produced. Acceptance tests are carried out in order to identify production defects and to guarantee full functionality on delivery to CERN<sup>2</sup> AMS-02 integration area.

At the same time the fully functional qualification model of the readout system can be deployed to test the assembled detector. A test stand at University of Karlsruhe consisting of a single TRD chamber provides a possibility to develop software tools for the operation of the complete detector. In order to accomplish the first readout of the entire TRD the qualification model electronics and developed software is used to take data of cosmic rays at the assembly area at the RWTH Aachen. Recorded data allowed to understand the detector characteristics and to identify difficulties of the detector readout.

The final integration of all subdetectors to AMS-02 takes place at CERN in a dedicated clean room area. During a pre-integration phase, early available subsystems are mechanically fitted. Although this phase is focused on the identification of mechanical problems, installed subsystems can already be integrated into the main DAQ system allowing first data of cosmic rays to be recorded with AMS-02 as a whole. Control of the TRD readout system is accomplished by AMS-02 run control software and the AMS-02 main DAQ computer. Since this is the first time all components are operated together, bottlenecks in the DAQ system can be identified and eliminated. A close cooperation with various groups and a knowledge of operation of all subsystems is essential.

During all runs the raw data digitized by the TRD front end electronics is processed by detector specific software running on a digital signal processor on board of the data reduction electronics of the U-Crate. Once in orbit a link of two megabit bandwidth for transmission to ground is reserved for AMS-02, which includes all subdetector physics data. The data reduction software has to preserve physics data during processing, since any discarded information is lost forever. In the same time it has to suppress non-physics data and noise to reduce the amount of data to a minimum taking into account detector characteristics. The development has to ensure an error free operation and high efficiency of the code with a minimum influence on the dead time of the system. In the end this basic software will process and deliver any data to AMS-02, which contains tracks and presumably will lead to discoveries in astroparticle physics.

Introductory drafted the main physics goals of the AMS-02 experiment and recent results on indirect dark matter searches are presented in chapter 2. The AMS-02 instrument and the

---

<sup>1</sup>National Aeronautics and Space Administration, agency of the United States government

<sup>2</sup>European Organization for Nuclear Research, Geneva

transition radiation subdetector in detail is described in chapter 3. The development and space qualification tests of the TRD readout system are presented in chapter 4. Furthermore an overview of the system is given. The production of the flight model and results of the production acceptance test are summarized in chapter 5. In chapter 6 the data processing code running on digital signal processors of the readout system is described in detail. Finally results of the data acquisition phases of the TRD with cosmic rays at RWTH Aachen and in the frame of the AMS-02 pre-integration test at CERN are presented in chapter 7. Identified and solved problems as well as the performance of the TRD are discussed. In chapter 8 a summary and concluding remarks are given and the flight status of the AMS-02 experiment is outlined.



Figure 1.1: *Experiment logo of AMS-02.*



## Chapter 2

# Rare Components in Cosmic Rays - Physics with AMS-02

*The Alpha Magnetic Spectrometer (AMS-02) will be the largest particle detector for direct measurement of cosmic rays in space so far. In contrast to ground experiments the delivery of AMS-02 to Earth orbit has the advantage, that interaction with the Earth's atmosphere does not affect the spectrum of cosmic rays before entering into a detector. In balloon experiments this difficulty for a precise measurement is avoided, but time of flight is significantly shorter than projected time of operation of AMS-02. With its high precision as well as statistics AMS-02 is capable to enhance our knowledge in various fields of particle- and astrophysics. In the following a overview of cosmic rays, AMS-02 is exposed to, will be given. Mission goals of major relevance will be described, focusing on indirect dark matter search, which is a matter of particular interest in modern astrophysics.*

### 2.1 Origin and Composition of Cosmic Ray Particles

Cosmic rays denote all particles as well as gamma rays, which hit the Earth from outer space. About 97% of the particles are nuclei and the remaining 3% leptons. The nuclei can be divided into 87% protons, 12% helium and about 1% heavy nuclei. All elements of the periodic table from hydrogen to the actinide metals are found. The energies of cosmic ray particles cover a wide range up to a few hundred EeV<sup>1</sup>.

Cosmic rays were already discovered in 1912 by Victor Hess<sup>2</sup>, who was able to prove with a balloon flight up to 5,000 meters altitude, that the intensity of radioactive radiation increases with distance from the ground, which also excluded prior assumptions of a terrestrial source. Besides the already mentioned matter, a certain fraction of antimatter like antiprotons and positrons can be found in the cosmic rays. Figure 2.1 shows the complete spectrum of cosmic rays. The flux  $I(E)$  of the particles as a function of the energy is described by an exponential law. Above energies of the so-called knee of the spectrum, the exponential decrease to higher energies becomes steeper. At about  $5 \cdot 10^{19} eV$  the GZK cutoff<sup>3</sup> is expected to be visible, because interaction of particles with the background radiation becomes possible. However

---

<sup>1</sup> $10^{18} eV$

<sup>2</sup>Victor Franz Hess (born 1883; died 1964) was an Austrian physicist, who was awarded the Nobel Prize in 1936 for the discovery of cosmic radiation

<sup>3</sup>Limit named after Greisen, Zatsepin and Kuzmin, from which the process  $\gamma + p \rightarrow \Delta^+$  becomes possible.

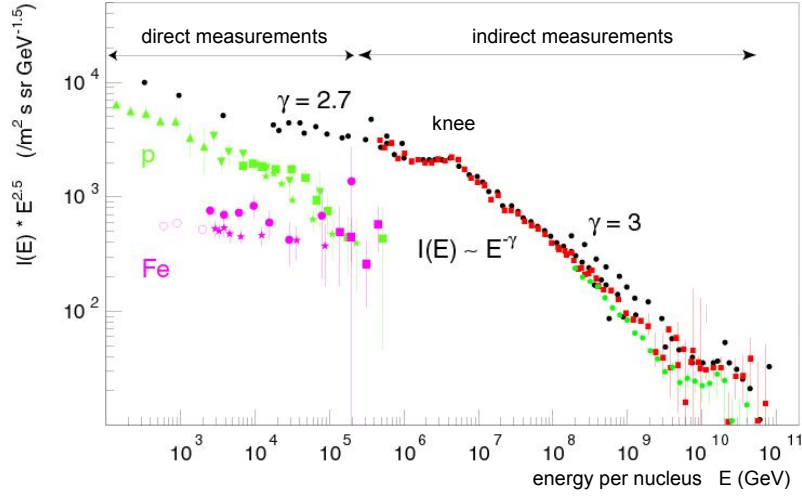


Figure 2.1: *Measured spectrum of cosmic ray particles. Easy to identify is the knee of the spectrum, where the energy dependence becomes steeper. Particles at energies below the knee originate mainly from inside the Milky Way. At energies above  $10^{14}$  eV only indirect measurements in large area detector arrays by observation of particle showers triggered by the primary particle are possible due to the extremely low particle fluxes. Direct measurements are carried out by particle spectrometers placed on balloons or satellites outside the Earth's atmosphere. From [51]*

the region of ultra high energetic particles is main subject to current experiments, since trajectories of these particles are not bend in the magnetic field of the galaxy and allow to point to their sources.

Part of the low energetic cosmic rays up to a few GeV is produced by the sun. Particles of medium energy up to  $10^{18}$  eV have their source inside the Milky Way mainly from supernova explosions. The process of acceleration is a statistical effect first described by Fermi [22]. Shock waves are traversed several times due to a diffusion process gaining energy in each transition. For higher energies also galaxies or quasars are considered as accelerators. However the origin of the highest energetic particles still is unknown.

The knee in the spectrum is caused by the strong decrease of heavy elements in the primary cosmic rays, since trapping in the galaxy's magnetic field depends on the rigidity<sup>1</sup> of a particle and thus charge and mass dependent cut-offs for the primary spectra of the different nuclei are expected. Only a handful of cosmic ray particles were directly observed so far for energies below the knee by balloon or satellite experiments. The isotopic composition for these energies in the spectrum still is widely unexplored in the linking range between detection by air shower experiments and the direct measurements. Current big experiments are the southern Pierre Auger observatory in Argentina, which will be operated on an area of  $3,000 \text{ km}^2$  to detect extensive air showers [46], and the PAMELA satellite launched in 2006 as a detector for primary cosmic rays in an altitude between 350 and 610 km [48].

---

<sup>1</sup> $R = \frac{p}{Ze \cdot B}$

## 2.2 Gamma Ray Astronomy

In contrast to particles of cosmic rays (apart from the ultra high energetic particles) gamma rays allow to identify their sources in the sky, because there is no influence by the magnetic field of our galaxy. There are a lot of processes in the universe, which create high energetic photons, including interaction of particles with interstellar gas, production of Bremsstrahlung in electromagnetic fields or supernova explosions.

First of all solar flares are origin of gamma rays in the MeV range in our direct vicinity. The diffuse gamma ray background in the GeV range mainly describes intra-galactic processes. Well known are the gamma ray bursts of extra galactic origin, which were for the first time detected by a military satellite looking for nuclear weapons, and can be observed from time to time as flashes of a seconds to a few minutes duration.

The most energetic gamma rays up to several TeV are detected by ground experiments with modern Cherenkov telescopes. In 2008 NASA launched the Fermi Gamma Ray Telescope<sup>1</sup> in order to precisely measure the diffuse gamma ray background and to continue search for new point sources in the sky [47]. A previous sky survey, shown in figure 2.2, by EGRET showed an unexplained excess of gamma rays in the GeV region, which does not comply with current models of our galaxy [32].

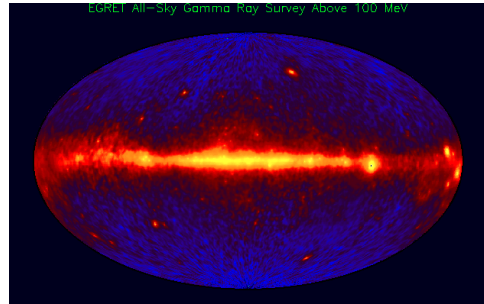


Figure 2.2: *EGRET gamma ray sky survey.*

## 2.3 Measurement of Parameters of the Galactic Propagation Model

Particles of cosmic rays primarily consist of protons and Helium nuclei. Only a small fraction of nuclei can be found with charge  $Z > 2$  with an abundance similar to the abundance of elements in our solar system. The ratio of the radioactive isotope of Beryllium  $^{10}\text{Be}$  to its stable neighbor isotope  $^9\text{Be}$  can be directly measured, which is a scale for the age of cosmic rays.  $^{10}\text{Be}$  has a half-life of  $1.6 \times 10^6$  years. A high rate implies a high fraction of young matter particles in the cosmic rays, and if in contrast only a few  $^{10}\text{Be}$  isotopes can be found, enough time passed by after production to decay to a large extend. With the RICH detector AMS-02 has the means to reliably distinguish isotopes with charges up to  $Z = 26$ . Figure 2.3 shows results of previous experiments and the expected precision of AMS-02 data after one year.

Further information parametrized by propagation models, which a measurement of the spectrum of heavy nuclei provides, is based on the abundance of elements like Lithium or Boron. These nuclei are produced in spallation interaction of heavy nuclei of primary cosmic rays during propagation through our galaxy's gas. Studying the ratio of primary to its secondary nuclei like Boron, the mean traversed mass of cosmic rays during propagation can be deduced. Figure 2.4 shows projected precision of the AMS-02 measurement of the ratio of Carbon to its secondary Boron.

---

<sup>1</sup>formally GLAST

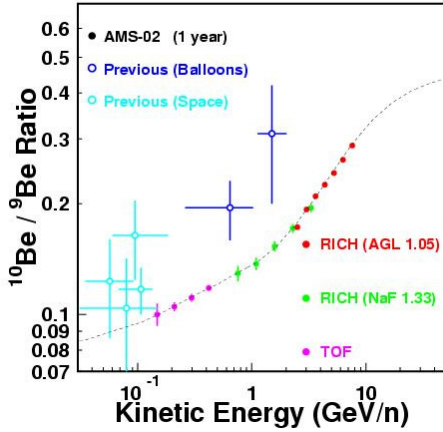


Figure 2.3: *Ratio of Beryllium isotopes in cosmic rays. The ratio implies information about parameters like confinement time and galactic halo size.*

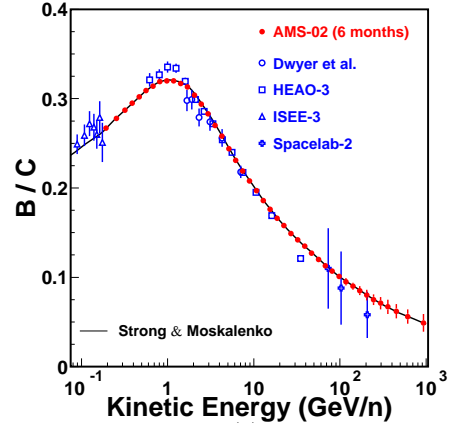


Figure 2.4: *Ratio of Carbon to its spallation secondary Boron up to 1TeV/n. The ratio gives information about amount of matter traversed and diffusion processes, which helps to understand propagation and to fix free parameters of current models.*

## 2.4 Search for Heavy Antimatter

Besides matter also a less abundant fraction of antimatter can be found in cosmic rays. The major part of positrons and anti-protons is most likely produced in the interaction of charged particles with interstellar gas, even though deviations from current model prediction can be found and might be hints for new physics (see also section 2.5).

Cosmic antimatter with  $Z > 1$  such as anti-helium has never been observed by any experiment up to now. This fact confirms one of the profound problems in particle physics. In the Big Bang an equilibrium of matter and antimatter should have pervaded the universe. This is based on one of the basic principles of physics, the symmetry of nature. But in fact, the primordial antimatter content of the universe is still unknown. In contrast to antiprotons the appearance of antihelium in interaction with cosmic gas is suppressed by more than 50 magnitudes. If only a single antihelium nucleus is found, the existence of regions in the universe dominated by antimatter is possible. Large-scale structures like stars and galaxies made of antimatter would presumably not be distinguishable by their emitted light from objects known to us. Certainly they can send their antimatter in explosive processes up to us. Figure 2.5 shows limits AMS-02 is capable to set for antihelium flux in there years of operation, if no heavy anti-nucleus is found.

If in spite of the long time of operation no antimatter is found besides antiprotons, regions dominated and formed by antimatter can be located more far apart than supposed. An admissible explanation for this observation could also be given by theories, which predict a small asymmetry between matter and antimatter during the Big Bang.

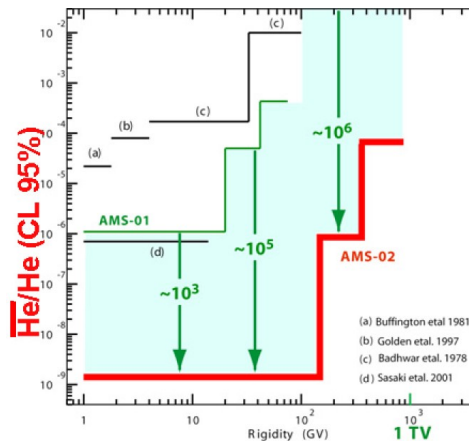


Figure 2.5: *Antimatter limits of past experiments and expected limit set by AMS-02 after three years of operation. If no antihelium is found, this means there is no heavy antimatter in the universe.*

## 2.5 Dark Matter Physics

Exploring the nature of dark matter certainly is one of the most challenging goals of modern astrophysics. It requires new theoretical models in particle physics to present candidates for it, which surely have to go beyond the standard model. But it also requires measurements by precision instruments and newest technology to extend our knowledge about its existence as well as to find out more about its nature. In the end it leads to development of tools and experimental technologies which might also change our lives. Such a high technology and precision instrument exploring dark matter is the AMS-02 detector, which is able to measure at the same time possible dark matter signals in charged particle as well as  $\gamma$ -ray fluxes.

### The WIMP

Astronomical observations show clear evidence for the existence of dark matter. A central observation and the major hint for the existence of dark matter is the rotation speed of our own galaxy, which is too fast for the gravitational force from the visible matter in it. The rotation speed of a star around the galactic center can easily be obtained by equating the gravitational force from the galactic center and the centrifugal force

$$\frac{mv^2}{r} = G \frac{mM_{R<r}}{r^2} \quad . \quad (2.1)$$

Assuming a constant mass distribution of the galaxy this would result in a velocity distribution of  $v \sim 1/\sqrt{r}$ , which disagrees with the observation showing to a large extend a flat rotation curve at large radii. An explanation is given by the assumption, that up to 90% of the galactic mass exists in form of an invisible matter halo around the galactic disc.

Actually in 1930s the astrophysicist Fritz Zwicky already assumed there must be a dark fraction of matter in the universe to explain the observed movement of galaxies in the Coma cluster [52]. A more recent estimation of the *dark matter* content of the universe is concluded from the anisotropy of the cosmic microwave background measured by WMAP [31]. The

gravitational lensing effects observed by the Hubble Telescope even can be considered as direct detection of the dark matter, although the nature on small scale stays unclear. On a large scale it is settled, that only weakly interacting particles explain the wide distribution around a galactic center. Furthermore it must be cold, at least for a large amount, in order to explain galaxy formation after the Big Bang.

This assumption means there must be another kind of fundamental heavy particle, which have not observed on Earth yet, although it is all around us. These particles interact by gravitational and weak force with extremely small cross sections and are known as WIMPs, derived from Weakly Interacting Massive Particles. They could amount up to 25% of the total energy density in the universe. In contrast the energy density of the universe consists of only 5% of the matter we are familiar with and the remaining 70% is the so called dark energy, which is characterized by an anti-gravitational force.

The leading idea of a WIMP is some kind of not-yet-seen heavy particle like a lightest SUSY partner particle in an R-conserving model. The SUSY candidate will be introduced at the end of the section, for the following discussion the actual type of particle is not relevant.

### Methods of Direct Searches

Direct search experiments looking for extremely low event rates suffer from background events caused for example by neutrons. Experiments are based on the detection of the nuclear elastic scattering of WIMPs in the detector mass. The released energy of nuclear recoils can be either detected by ionization, scintillation or released heat in form of phonons or a combination of these. Current experiments amongst others are DAMA [8], CRESST<sup>1</sup> and XENON10 at Gran Sasso laboratory, CDMS<sup>2</sup> in the Soudan mine and Edelweiss<sup>3</sup>, but no direct observation of a WIMP has been redundantly made so far.

A much higher detector mass will be main attribute of future setups like the EURECA<sup>4</sup> experiment by the CRESST and Edelweiss collaboration. It will be a one ton cryogenic detector with a much higher sensitivity. All direct searches have to assume, that the Earth is not located inside a void of dark matter, which most likely forms to clumps in the galaxy.

### Methods of Indirect Searches

The key idea to dark matter exploration in astrophysics is the annihilation of its elementary particles. The annihilation of WIMPs in the halo of our galaxy contributes to the particle fluxes of normal matter in cosmic rays, which can be detected. Figure 2.6 illustrates the annihilation of cold dark matter particles in between normal cosmic ray collisions, which form the background for the annihilation signal. Although the initial particles are not known, the annihilation process by the weak force and resulting particles are well studied. In the initial state one simply has to replace the electron and positron from for example LEP experiments with the WIMP annihilation vertex. According to observations in accelerator experiments, predominantly quark-antiquark pairs are produced, which create stable particles by hadronization.

---

<sup>1</sup>Cryogenic Rare Event Search with Superconducting Thermometers

<sup>2</sup>Cryogenic Dark Matter Search

<sup>3</sup>Expérience pour DEtecter Les Wimps En Site Souterrain, installed to the Frejus-tunnel

<sup>4</sup>European Underground Rare Event Calorimeter Array

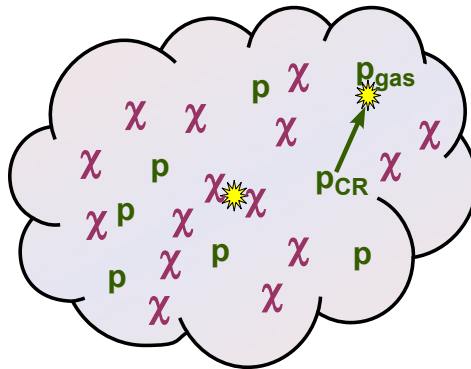


Figure 2.6: *The production of gamma rays in the GeV range is dominated by pion decay, which are produced in cosmic ray collisions with the interstellar gas. Interaction between cold dark matter particles and normal matter can be neglected because of the extremely small cross section. On the contrary a significant fraction of energetic photons is produced in dark matter annihilation and leads to a deviation of the gamma ray flux calculated from cosmic ray collisions of visible matter.*

Of special interest in the process are energetic photons and components, which are rare in the cosmic rays such as antiparticles exemplary listed:

$$\chi\bar{\chi} \rightarrow q\bar{q}, WW, ZZ, \gamma\gamma, l\bar{l} \rightarrow X + \bar{p}, e^+, \gamma, \bar{D} \quad . \quad (2.2)$$

Protons and electrons are clearly dominated by the contribution from standard sources in our galaxy. Figures 2.7 and 2.8 exemplary show two measurements of rare components, which will be performed with AMS-02 with unprecedented precision. The trajectories of charged particles are affected by the magnetic fields in the galaxy, but photons allow to point to their sources. This could be the key to illuminate the dark matter in the universe by recording their gamma ray flashes of the annihilation.

Independent of the kind of the particle, the cross section for the annihilation of two WIMPs can be derived from the evolution of the universe to

$$\langle \sigma v \rangle = 2 \times 10^{-26} \text{cm}^2 \cdot \text{cm/s} \quad . \quad (2.3)$$

A freeze-out occurred when the expansion rate of the universe described by the Hubble constant became bigger than the annihilation rate.

As already suggested, the excess to propagation model predictions should not only be seen in the gamma ray flux, but also in a significantly higher flux of antiprotons and positrons. Even though it is a challenging task to separate positrons from the huge background of protons, past experiments have hinted an excess at energies in the GeV range. The High Energy Antimatter Telescope (HEAT) flown on a balloon several times in the 1990s is one of the most important of them [7]. In standard physics antideuterons in cosmic rays are produced with high energies, whereas antideuterons from WIMP annihilation can be found below 1 GeV. Since this excess would be orders of magnitude, the extraction of a WIMP signal could be of much higher significance than from antiprotons. A large acceptance spectrometer is required to measure these still extremely low fluxes.

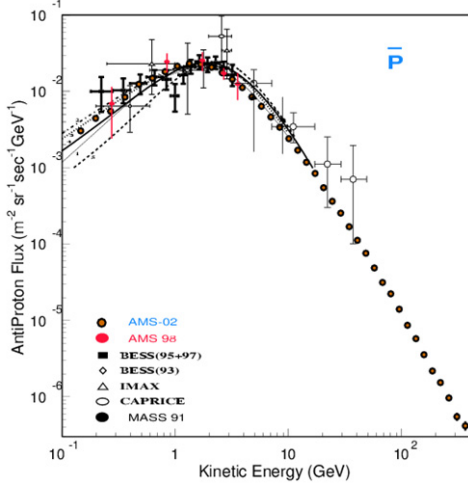


Figure 2.7: *Antiprotons in cosmic rays and expected precision of AMS-02 measurement.*

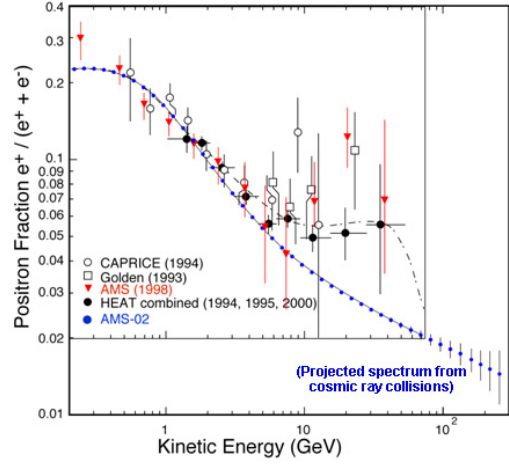


Figure 2.8: *Positrons in cosmic rays and expected precision of AMS-02 measurement.*

Nevertheless so far the experimental data is not sufficient to make current propagation models of cosmic rays in our galaxy more precise in order to be able to identify an excess, and at the same time identify the excess itself of certain rare components in cosmic rays with high statistics over a wide range of energy. The strength of AMS-02 is, that it will simultaneously measure antiparticle and gamma ray spectra.

### Recent Results on Indirect Dark Matter Search

First of all the gamma ray spectrum should be discussed, since the propagation of photons is less dependent on models than the propagation of charged particles in our galaxy. The results summarized in the following are presented in detail in [18].

Gamma rays can be regarded as an indirect evidence of the dark matter. The EGRET<sup>1</sup> satellite has measured diffuse gamma rays up to energies of a few GeV. The data shows a significantly higher flux of diffuse gamma rays at high energies than current models describing processes in our galaxy predict [32].

One can understand the excess assuming that gamma rays are produced in the annihilation process of dark matter particles, which creates amongst other particles neutral  $\pi^0$  mesons decaying predominantly into photons. The flux expected to be measured in a detector then is a function of the cross section 2.3 of the annihilation and the integral of the line of sight along the density of the dark matter. Looking into the space the contributions from different sources of gamma rays in this direction just add up to the measured flux. A boost factor takes into account the clumping of the dark matter similar to the visible matter, which amplifies the probability for collisions of dark matter particles and with it the probability for the annihilation in this region.

Figure 2.9 shows the measured gamma ray flux after fitting simultaneously the shapes of the

<sup>1</sup>The Energetic Gamma Ray Telescope has acquired a full map of gamma rays between 1991 and 2000 on board of NASA's Compton Gamma Ray Observatory

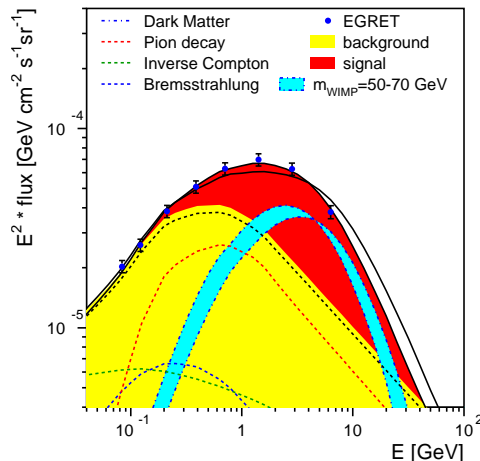


Figure 2.9: *Fit of a dark matter annihilation signal to EGRET data at high energies. For different line of sight of the telescope a three dimensional model of the distribution of dark matter in our galaxy can be obtained.*

background and WIMP annihilation contribution for a WIMP mass of 60 GeV. The shape of the background is known from accelerator experiments, mainly from so-called fixed target experiments, in which a proton beam is scattered on a hydrogen target. An independent fitting of the shapes in 180 sky directions reveals, our galaxy has an extended halo of dark matter in addition to the visible matter. There is also strong evidence, that also a ring like structure of dark matter exists in our galaxy. The outer ring at about 13kpc can be explained taking into account the rotation curve by remains of a dwarf galaxy, which has fallen into the Milky Way. The inner ring at about 4kpc coincidences with a ring of molecular hydrogen dust and might also remain from the disruption of a dwarf galaxy. Furthermore the shape of the rotation curve can be described in agreement with the data taking these rings into account. From the very same fit limits to the WIMP mass can be set between 50 and 70 GeV.

By far more complex to describe is the propagation of charged particles in our galaxy and with it the positron and antiproton spectra, which are as well created by hadronization in the annihilation processes. These particles should constitute an excess over the cosmic ray background in the antiproton and positron spectra. Based on current propagation models implemented in GALPROP, a well-known program used to simulate cosmic ray propagation in our galaxy, a dark matter distribution as extracted from the fit of a signal to the gamma ray excess clearly leads to an antiproton flux in an order of magnitude above the measured flux.

Recent data of experiments such as the ROSAT<sup>1</sup> satellite revealed there must be strong convective winds in the halo of our galaxy blowing away particles from the center. This observation drastically changes the situation assumed by the current GALPROP model. An anisotropic diffusion in this way obviously reduces the contribution by the annihilation of dark matter in the large halo around the galactic disc. Cosmic rays in the halo simply drift to outer space instead of isotropically propagate through our galaxy.

<sup>1</sup>from German: ROentgenSATtelite, an X-ray telescope, which was operational from 1990 to 1999. See also [21], which explains the evidence for Galactic winds obtained by ROSAT.

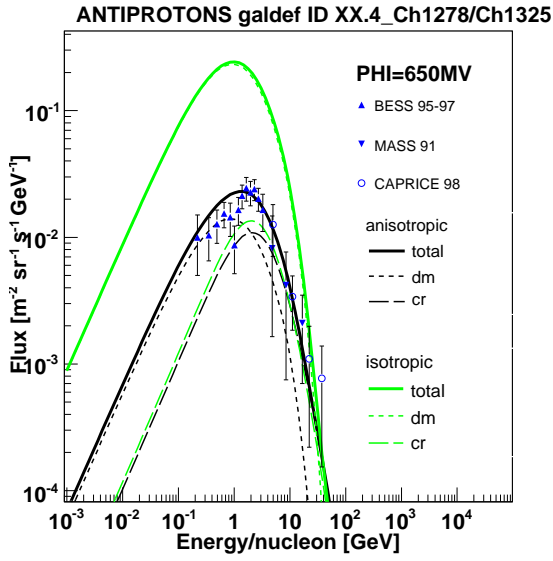


Figure 2.10: *Antiproton flux in isotropic and anisotropic propagation models. In isotropic models the signal from dark matter annihilation extracted from gamma ray observation clearly dominates the cosmic ray flux and is inconsistent with the data. In anisotropic models the flux is much reduced by blowing away dark matter signal originating in the halo of the galaxy.*

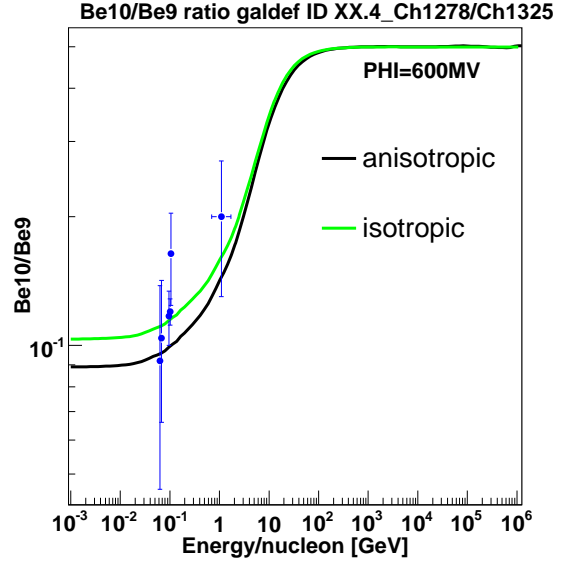


Figure 2.11: *Ratio of Beryllium isotopes in isotropic and anisotropic propagation models. The transport time extracted from the ratio of  $^{10}\text{Be}/^9\text{Be}$  is well described in both models.*

The antiproton spectrum resulting from either conventional isotropic or the anisotropic propagation is shown in figure 2.10. Clearly visible is the suppressed fraction expected by dark matter annihilation in an anisotropic GALPROP model. However without the contribution of a dark matter signal, cosmic ray models would result in a too low antiproton flux. The required antiproton flux from annihilation is consistent with the dark matter distribution obtained from the analysis of gamma ray spectra. An influence of anisotropic propagation as well is expected for other nuclei, which are used to determine for instance the age of cosmic rays as described in section 2.3. The flux is consistent with current data as shown in figure 2.11.

The positron fraction in cosmic rays measured by the HEAT balloons shows a possible excess of positrons at high energies with respect to the GALPROP prediction indicated in figure 2.8 using an isotropic propagation model. The excess often is interpreted as a dark matter annihilation signal, hence it is expected to decline at energies in the order of the WIMP mass. Therefore it is often regarded as the most promising measurement in indirect dark matter searches.

Certainly an anisotropic propagation in the galaxy changes the situation. Of major influence is the source of the particles. Positrons are created in the decay of positively charged pions either from cosmic ray collisions or dark matter annihilation, whereas the production of electrons is

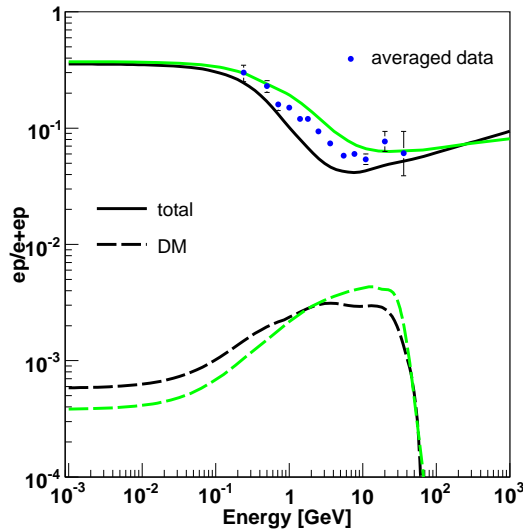


Figure 2.12: *Positron fraction in cosmic rays in anisotropic propagation models. At high energies electrons suffer from energy losses by synchrotron radiation traveling through the galactic disc, thus locally created positrons become more important and lead to an increase in the fraction. The two lines indicate the fraction obtained for different magnetic field models. So the HEAT excess [7] can as well be explained without dark matter annihilation. In fact the contribution by positrons from dark matter annihilation is quite small since the convection blows away positrons produced in the dark matter halo.*

dominated by supernova remnants. Due to the convection in the halo, electrons leaving the galactic disc are blown away, so that they have to travel through the galactic disc suffering an energy loss by synchrotron radiation. The energy loss by synchrotron radiation observed by WMAP<sup>1</sup> [23] peaks at high energies and of course is dependent of the magnetic field model. In contrast positrons are produced everywhere to the same extend and not in discrete sources. Created nearby they suffer less synchrotron losses before the detection. Taking this together, the fraction of positrons at high energies must increase with respect to the electrons in an anisotropic propagation model as shown in figure 2.12. Hence a measurement at higher energies and of the absolute positron flux is of utmost importance in order to be able to decide, if the excess is a dark matter signal or just a feature of the anisotropic particle propagation in our galaxy.

It is worth to mention again, that for all methods of data analysis it is essential to know the parameters of the standard propagation model of our galaxy as precisely as possible in order to be able to identify the extend of a possible excess correctly. These particle fluxes will be measured with AMS-02 in a wide energy range and with highest precision.

In addition to precision measurements of the parameters the propagation model itself is under improvement. In models describing an anisotropic propagation of particles in our galaxy the convective winds dominate the propagation of the particles, which leads to a smaller yield of charged particles produced in dark matter annihilation.

The results are a summary of the recent analysis presented in [17] and [16].

<sup>1</sup>Wilkinson Microwave Anisotropy Probe

### The Neutralino as WIMP Candidate

There is no particle of the standard model, which could explain the dark matter content of the Universe. A possible candidate for the WIMPs is predicted by an extension theory of the standard model. In supersymmetric (SUSY) models there is symmetry between fermions and bosons, which is achieved by duplication of number of particles with respect to the standard model. For SUSY particles an additional quantum number, the R-parity +1 for the known matter of the standard model, and -1 for the SUSY partners is introduced. Assuming conservation of R-parity, which is a multiplicative quantum number, means SUSY particles can only be created in pairs. At the end of the decay chain there is always the lightest supersymmetric particle (LSP), the stable neutralino  $\chi^0$ , which for this reason could form the major part of the dark matter. It can be indirectly detected by its decay products after the annihilation process as previously discussed for a WIMP in common. Neutralino pairs  $\bar{\chi}^0\chi^0$  release visible matter via  $Z_0$ ,  $W^\pm$  or  $q\bar{q}$ , whose decay products such as protons, electrons, antiparticles and photons are well known from accelerator experiments on Earth and can be detected.

The lightest neutralino  $\tilde{\chi}^0$  is the mass eigenstate of the linear combination the supersymmetric partners of the photon  $\tilde{\gamma}$  and the Z boson  $\tilde{Z}^0$  and two neutral higgsinos  $\tilde{H}_1^0$  and  $\tilde{H}_2^0$ , since all four have the same quantum numbers. Produced at accelerator experiments the neutralino should be visible by large missing energy and momentum, since it is stable and escapes from the detector. Detected in cosmic ray spectrometers the neutralino is visible as discussed by particles and gamma rays created by the annihilation. The AMS-02 detector is looking for a dark matter signal in the  $\gamma^-$ ,  $\bar{p}$ ,  $\bar{D}$  and  $e^+$ - decay channels of the neutralino annihilation.

## Chapter 3

# The Alpha Magnetic Spectrometer AMS-02

*The Alpha Magnetic Spectrometer 02 (AMS-02) is a large acceptance spectrometer for energetic charged particles and photons in the cosmic radiation. It is designed for the maintenance-free operation on board of the International Space Station (ISS) for a duration of at least three years. The redundant detection in several subdetectors allows an accurate particle identification and precision measurements offering a unique opportunity of the exploration of cosmic rays. In general the science potential of AMS-02 is broad as discussed in chapter 2. Technologically AMS-02 consists of more different types of subdetectors than any other detector built so far. In the following the AMS-02 instrument and the transition radiation subdetector in detail will be described. The information given in this chapter is taken from [5], otherwise the source is indicated.*

### 3.1 The AMS Project

In 1995 Samuel C.C. Ting proposed the Alpha Magnetic Spectrometer as the head of a new collaboration, which partially consisted of the members of his former collaboration at LEP<sup>1</sup>. AMS should be the most precise detector for cosmic rays operated in space so far. Ting was born in 1936 and became famous for the experimental discovery of the **J** meson at the Brookhaven National Laboratory, which extended the quark model by the additional charm flavor. In 1976 he was awarded the Nobel Prize in Physics. Since 1969 he is professor at the Massachusetts Institute of Technology (MIT). Today the AMS collaboration has members in 16 countries in Europe, Asia and North America. Although the collaboration is relatively small, AMS is considered to be one of the most expensive experiments in physics due to the huge effort that has to be taken to deploy this instrument in space. Three flights to space in the Space Shuttle were planned to be provided by NASA in the first contract with the collaboration.

In June 1998 the prototype version AMS-01 has successfully been flown on board of the Space Shuttle Discovery for ten days in an altitude of 320 to 380 km to the Earth's orbit during the mission STS-91. This engineering flight has provided essential information about the detector operation and performance under space-conditions before AMS-02 should be

---

<sup>1</sup>Large Electron-Positron Collider operated at CERN between 1989 and 2000

designed, assembled and installed on the International Space Station. The picture of AMS-01 shown in figure 3.1 was taken from the space station MIR<sup>1</sup>. AMS-01 generally can be considered as a slim version of AMS-02, with a silicon tracker inside a permanent magnet, a time-of-flight measurement and a small prototype of a Cherenkov counter.



Figure 3.1: *AMS-01 on board of the Space Shuttle.*

Special attention during the precursor flight was paid to the stability of the silicon tracker. Its alignment was continuously monitored by a laser alignment system. Tests in several particle beams on the ground before and after the flight have proven that there was no degrading of the detector performance due to the stress during the shuttle launch or the thermal stress in orbit. With the flight in the payload bay of the space shuttle, as the main objective, the concept of AMS was validated.

Although it was a prototype flight interesting physics data was collected with the about 100 million triggered events, which results are summarized in [4] and help to understand the environment conditions for an operation on the ISS. As the primary aspect of the mission the best limit for antihelium in cosmic rays so far was set. No antihelium particle was found in about  $2.86 \cdot 10^6$  detected helium nuclei.

For the first time the proton flux was measured in an altitude of 380km between the atmosphere and the radiation belt. The observation at energies below the geomagnetic cutoff was different to the extrapolation made from data of balloon flight measurements and satellite measurements in the radiation belt at 680km. Moreover the existence of two spectra in the proton flux was found originating from complex particle trajectories in the Earth's magnetic field. This data is of major importance for the calculation of the flux of atmospheric neutrinos. A similar observation was made for leptons in the near earth orbit. Even more surprising is the result, that for energies below the geomagnetic cutoff positrons are dominating the electron flux. The HEAT excess of positrons at higher energies could not be excluded from measured primary lepton flux. For helium nuclei, the second spectrum at energies of 0.1 to 1.2 GeV/nucleon Helium was identified as almost pure  ${}^3\text{He}$ , which also was completely unexpected.

In 2003 flights of the Space Shuttle were suspended after the Columbia disaster, but were resumed after the upgrade of the remaining shuttles. Although this certainly caused a delay of the assembly of the AMS-02 instrument, today the collaboration together with NASA targets a launch of the experiment in 2010. The about 1000-times higher statistics of AMS-02 data will widely improve our knowledge about the propagation and the sources of cosmic rays. AMS-02 also will allow searches for heavy antimatter nuclei and dark matter signatures, which profits from the improved proton rejection in AMS-02 in the order of  $10^6$  by the transition radiation detector and the electromagnetic calorimeter.

## 3.2 AMS-02 System Overview

The AMS-02 experiment is a complex particle detector designed for the operation on the International Space Station (ISS), which will provide precise information about the spectrum

<sup>1</sup>MIR was a Soviet (and later Russian) orbital station until 2001.

0.3 TeV	e <sup>-</sup>	P	He	C	Fe	γ
TRD						
TOF						
Tracker (magnet on)						
RICH						
Calorimeter						

Figure 3.2: *Signatures of particles of equal energy in the AMS-02 subdetectors.*

and the composition of primary cosmic rays during its operation for at least three years. The collected data will contain more than  $10^{10}$  datasets of impacting particles. In the end the duration of the data acquisition is only restricted by the superconducting magnets, which are dependent on the volatilizing Helium. An extended time of operation nevertheless is possible, although without a momentum measurement of cosmic ray particles in a magnetic field.

With the successful operation of AMS-01 the development and assembly of AMS-02 could be started, which will allow the measurement of spectra of cosmic ray particles up to the energy of TeV and for energetic gamma rays up to few hundred GeV simultaneously with the same instrument. Furthermore a charge separation up to  $Z = 26$ , an isotope separation up to  $A = 25$  and a proton-positron separation up to 300 GeV are features of the detector.

These characteristics cannot be achieved by a single detector. Instead the AMS-02 instrument is based on the combination of measurements in different subdetectors. AMS-02 consists of a silicon tracker, a time-of-flight detector (ToF), a ring imaging Cherenkov counter (RICH), an electromagnetic calorimeter (ECAL), a transition radiation detector (TRD), a star tracker and anti-coincidence counters (ACC), all together controlled and read out by about 650 space qualified processor units.

AMS-02 not only features a wide energy range for the measurements, in addition impacting particles can be separated by charge, mass and direction of impact in a redundant way. Tracker, RICH and ToF subdetectors measure the particles charge, ToF, RICH and TRD the velocity of the particle. In the following only a very brief description of the individual subdetectors will be given, ignoring that each of them is already a challenging project of an international collaboration on its own. As basis of this thesis the TRD will be discussed separately in section 3.3 more in detail.

Figure 3.2 illustrates the expected signal in the different subdetectors for different particles of equal energy. Common for almost all subdetectors, which are based on a particle detection by ionization, is, that the energy loss is proportional to the charge  $Z$  of a particle, which finally allows a particle separation. In addition the TRD takes advantage of detection of transition radiation emitted by light particles, which can be combined with shower profile

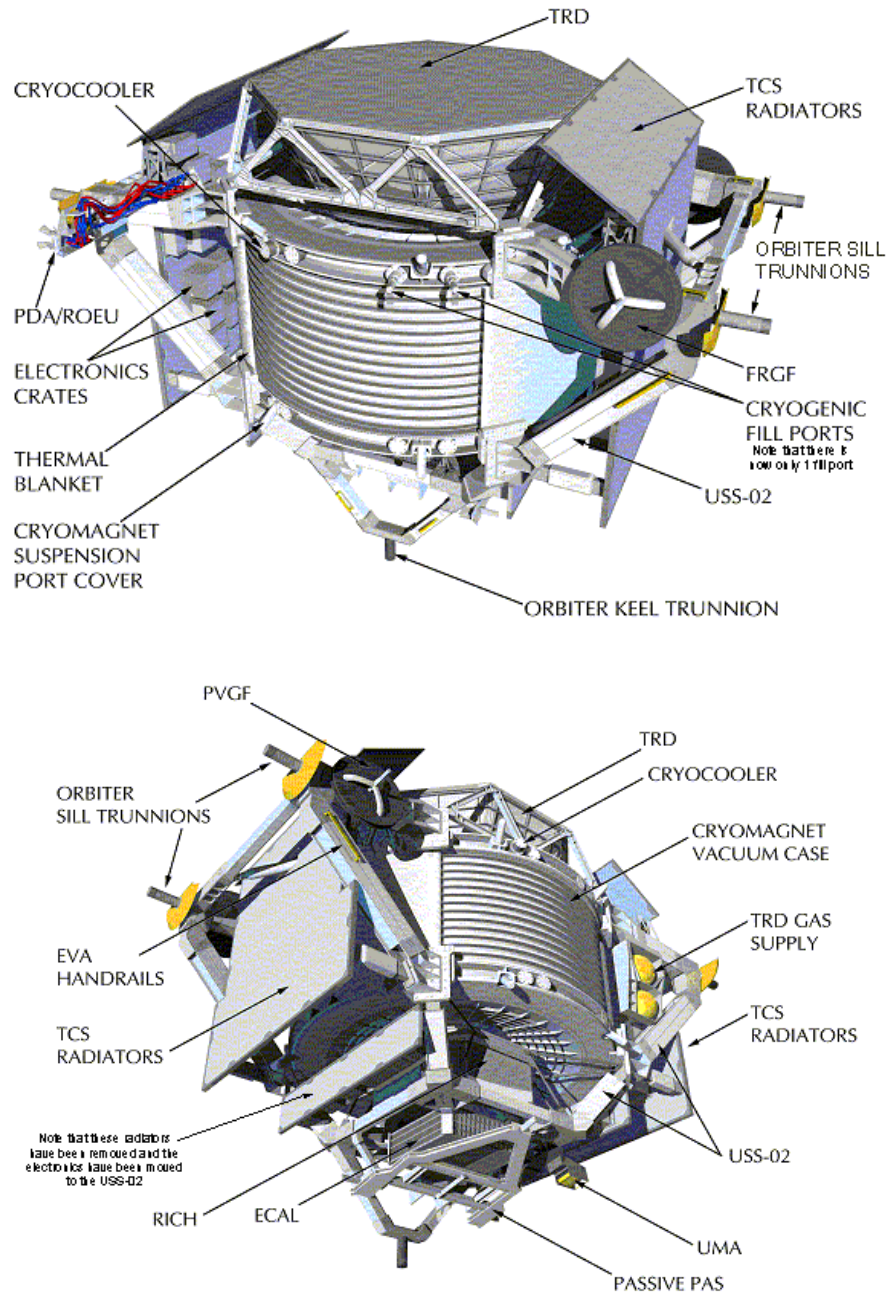


Figure 3.3: Schematic view of the AMS-02 periphery. The subdetectors are mounted inside a unique support structure (USS), which allows the mounting to the Space Shuttle bay by standardized trunnions and to the ISS by an attachment system (PAS) on the bottom. The vacuum case for the cryogenics system is the central part of the structure. The heat dissipated by the electronics systems are radiated into space by four radiator plates.

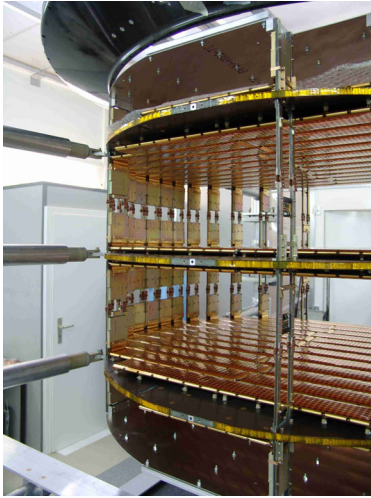


Figure 3.4: *The six layers of the AMS-02 tracker mounted in its transport frame. The top and bottom layer are mounted separately on the top and bottom cover of the tracker.*

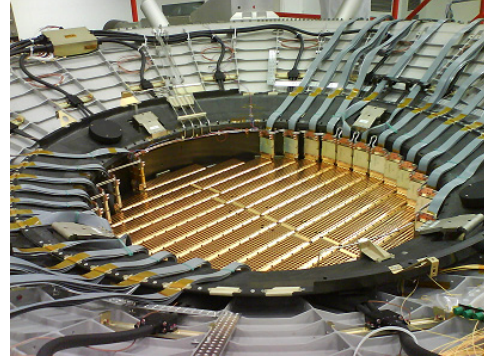


Figure 3.5: *The AMS-02 tracker mounted in the center of the vacuum case. The picture was taken during the pre-assembly of AMS-02.*

measurement of an electromagnetic cascade in the ECAL to identify electron-like particles. The bending of the trajectories of particles in a magnetic field according to the momentum and charge is monitored by the tracker. RICH contributes to the charge measurement by detecting Cherenkov cones. The actual speed of the particle is directly measured between two scintillator layers of the ToF. As an additional feature of AMS-02 gamma rays can be detected either by direct measurement in the ECAL or by the identification of a produced electron-positron pair on top of the experiment.

The main support structure of AMS-02, which all subsystems are mounted to, is provided by NASA. Figure 3.3 depicts the various subsystems attached to the unique support structure (USS). The central element is the vacuum case for the cryogenic coils of the superconducting magnet. For the fixation inside the payload bay of the space shuttle standardized trunnions are present on two sides and on bottom of AMS-02. The passive payload attachment system (PAS) on the bottom of AMS-02 will connect to the ISS truss. The control and readout electronics of the subdetectors are mounted on two main radiators, which dissipate the generated heat to the space. Two smaller ones on top are present for the independently operating thermal control system of the silicon tracker.

### Silicon Tracker

The core of AMS-02 is the silicon particle tracker, which is operated inside a superconducting magnet. The observation of the bending radius allows a measurement of the particle's momentum and charge. The silicon sensors of the tracker cover an overall area of  $6.6 \text{ m}^2$ , which are read out in about 200,000 channels. The 2,500 sensors are arranged in eight layers. Figure 3.4 shows a picture of the middle six silicon layers of the tracker in a transport frame ready to be mounted in the center of the vacuum case of the magnet as shown in figure 3.5.

If a charged particle traverses the detector, its energy deposition in the silicon bulk material is described by the Bethe-Bloch formula. On location of the energy deposition a signal can be read out, which in the end allows to reconstruct the trajectory of the particle through the eight layers of the tracker. The bending of the flight path depends on the charge and the momentum and is described by the Lorentz equation

$$\vec{F}_L = q(\vec{v} \times \vec{B}) \quad . \quad (3.1)$$

The particle follows a circular trajectory perpendicular to its flight path and the magnetic field. The radius of the bending can be obtained by equating the Lorentz- and the centrifugal force. From

$$F_L = qvB = \frac{mv^2}{R} = F_Z \quad (3.2)$$

the dependence of the observed radius and the applied magnetic field can be derived to

$$RBc = \frac{E}{q} \quad , \quad (3.3)$$

with  $E = pc$  for relativistic particles.  $RB$  is also known as the rigidity of the particle. The information about the particle's charge either is provided by the other subdetectors or can be calculated by the energy deposition in the silicon, which is described by the Bethe-Bloch formula. Finally one gets the particle's momentum.

The precision of the momentum measurement is directly related to the spatial resolution of the strip readout. The strips on the silicon sensor are perpendicular on the front and back side, so that the position of a signal can be detected in direction of the magnetic field to  $30\mu m$  and in the bending direction in the magnetic field up to  $10\mu m$  accuracy. A schematic picture of a tracker ladder is shown in figure 3.6. The sensor bulk material is made out of n-doped silicon of  $300\mu m$  thickness.

On the front side the strip implants are p-doped, on the bottom side n-doped silicon. The strips on n-side measure the coordinate perpendicular to the bending direction. Strips on the p-side have a finer structure and provide the coordinates in bending direction. In this way a precise measurement of the particle momentum is possible up to rigidities of  $2TV/c$ . The sensors are operated fully depleted. To avoid currents on the surface, on n-side p-strips are implanted in between.

Several test beam measurements confirmed the resolution in bending and non bending direction. Furthermore the charge measurement by the energy deposition in the silicon bulk could be tested with heavy ions. The results presented in figure 3.7 show, that a good particle identification is possible up to Zinc ( $Z=30$ ).

Due to the thermal stress or vibration during the Space Shuttle launch a displacement of the eight layers relative to each other might be not avoidable. In order to compensate this effect, an infrared laser tracker alignment system (TAS) identifies the relative position of each layer frequently during the operation.

**Superconducting Magnet** A particle's momentum can be determined for higher energies, if also the magnetic field in the tracker is stronger. The superconducting magnet of AMS-02 has a maximum magnetic flux density of  $B = 0.86 T$  in the center. It consists of a pair of main coils which store an energy of  $5.2 MJ$  during the operation. Six smaller ones, which are mounted between them, are designed to also contribute to the inner field, but mainly to

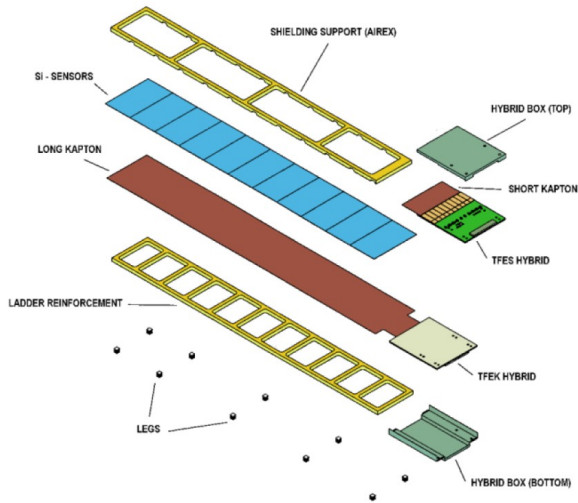


Figure 3.6: *Exploded view of a ladder of the silicon tracker. Wire bonds connect the strips between the sensors such that they are read out at once by the readout hybrid attached to the last sensor. The perpendicular strips on the backside are interconnected from sensor to sensor by a metalized polyimide foil in order to equally allow a simultaneous readout at the last sensor.*

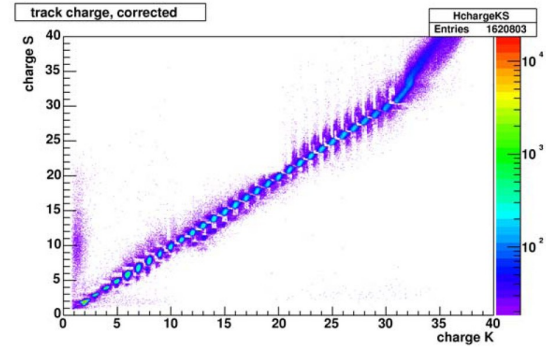


Figure 3.7: *Measurement of the energy deposition with a tracker sensor. The particle identification is possible up to a charge of  $Z=30$ .*

suppress the outer magnetic field. A large outer field would result in a torque on the AMS-02 instrument in the Earth's magnetic field, thus to an unregulated influence on the orientation of the ISS.

Figure 3.8 shows the two main coils and the smaller bucking coils. They are made of coiled Niobium-Titanium wire and reinforced by Aluminum. The current of  $\sim 460 A$  can be maintained as long as the superconducting phase of the Niobium-Titanium (Nb/Ti) wire is kept. Niobium-Titanium is a type-II superconductor, which fades slowly to normal conducting phase at about  $10 K$ . The targeted operating temperature of the Helium is  $1.8 K$  at a pressure of  $16 mbar$ . The superconductivity is maintained by cooling with  $2,500 l$  superfluid Helium-II. This is a phase of liquid Helium, which can be found below the so-called Lambda point of Helium at a temperature of  $2.18 K$ . The biggest advantage of Helium-II over Helium-I is the significantly higher and almost infinite conductivity of heat, which allows also in absence of convection an isothermal temperature distribution all over the system. Furthermore more liquid can be stored in the equal volume due to the higher density. However a phase separating mechanism is needed, which is capable to operate in a zero-gravity environment. In AMS-02 this is a phase separator developed by the Linde company, which takes advantage of the thermo-mechanical fountain-effect<sup>1</sup>.

<sup>1</sup>The fountain effect is a consequence of the zero viscosity, which allows to let superfluid Helium pass a porous plug, but reject the normal Helium.



Figure 3.8: *The coils of the superconducting magnet and the Helium tank. Both will be embedded in the AMS-02 vacuum case.*

### Ring Imaging Cherenkov Counter (RICH)

The RICH subdetector is based on the effect, that a charged particle emits light when traversing matter, if its velocity is larger than the speed of light in this material. If  $v > c_{\text{radiator}}$  is satisfied, photons can be observed known as Cherenkov light. This effect leads to characteristic ring images, which can be detected in forward direction behind a radiator-plane. In the AMS-02 RICH an array of photomultiplier tubes of spatial pixel size  $8.5 \times 8.5 \text{ mm}$  is mounted in a distance of  $45 \text{ cm}$  behind the radiator. In addition a conical mirror surrounds the space in between in order to extend the acceptance. The three parts are shown separated in figure 3.9 and finally assembled in 3.10. The radiator plane is composed of two radiator materials with two different refractive indexes  $n$ . These are aerogel with  $n = 1.035$  and NaF with  $n = 1.336$  in the center. Depending on the refractive index, for half of the opening angle  $\Theta_{Ch}$  of the Cherenkov cone applies

$$\cos\Theta_{Ch} = \frac{1}{n\beta} \quad , \quad (3.4)$$

which allows a determination of the particle's velocity  $\beta = v/c$ . The velocity can be measured in this way with a precision of 0.1% for  $\beta > 0.95$ . An approximation of the particle's charge  $Z$  can also be obtained. The number of emitted Cherenkov photons in the frequency  $d\omega$  behind a radiator of the thickness  $dx$  is given by

$$\frac{d^2N}{d\omega dx} \sim Z^2 \sin^2\Theta \quad , \quad (3.5)$$

which means the more charge the particle carries, the more photons are emitted and detected in the photomultiplier array. Figure 3.11 shows the expected Cherenkov rings from different ions.

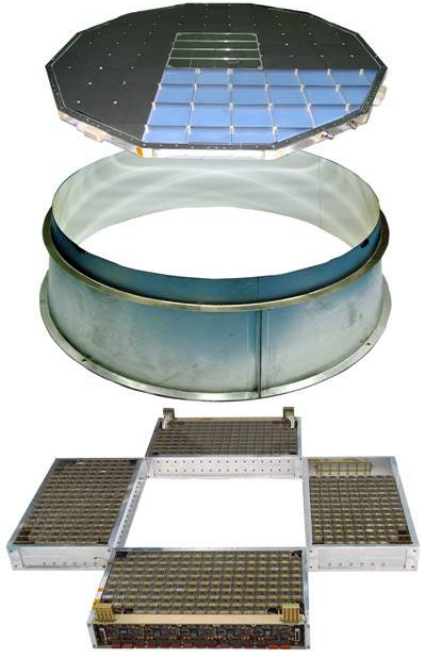


Figure 3.9: *The RICH detector consisting of the radiator with NaF and aerogel, the reflector and the photomultiplier array for the detection of the Cherenkov photons.*

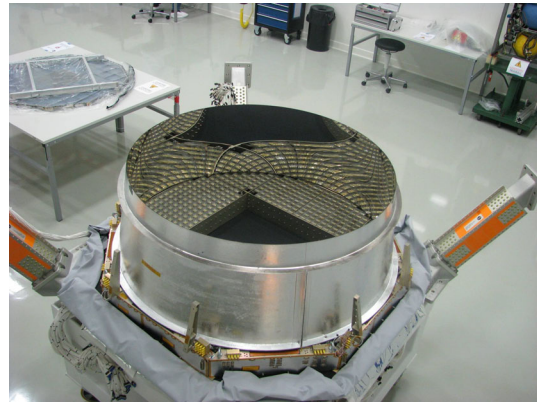


Figure 3.10: *The RICH assembled and mounted on top of the ECAL to the lower unique support structure (USS).*

### Time of Flight (ToF)

The ToF subdetector directly measures the velocity and the direction of a particle crossing the AMS-02 detector. It consists of two components above and below the tracker. These are equipped each with two layers of crossed scintillator panels, which are read out by photomultiplier tubes at the ends. The signal from ToF serves as a primary fast trigger for the entire AMS-02 detector. The time resolution is about  $120\text{ps}$ , which allows a velocity measurement of the crossing particle with a precision of  $d\beta/\beta < 3\%$ . In addition to the RICH detector also the particle's charge can be determined. The energy deposition in first order is proportional to the square of the charge  $Z$ . The energy resolution is good enough to distinguish particles up to a charge of  $Z \approx 20$ . Figures 3.12 and 3.13 show pictures of the ToF planes during the assembly.

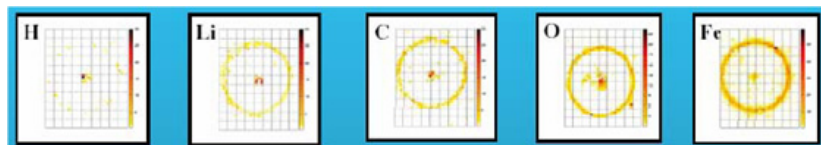


Figure 3.11: *Cherenkov rings as detected by the photomultiplier array. The images show the results from a test beam with heavy ions.*

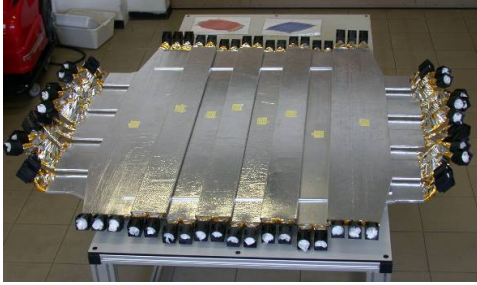


Figure 3.12: *One out of two ToF planes. Each plane consist of two layers of crossed scintillator panels. Photomultiplier tubes are attached to the ends of the panels.*



Figure 3.13: *Picture of the assembled upper and lower ToF.*

### Anti-coincidence Counters (ACC)

The purpose of the anti-coincidence counters is to identify particles, which leave the tracker sideways and do not hit all subdetectors of AMS-02. Therefore the tracker is surrounded by 16 cylindrical shell paddles of plastic scintillators of  $8\text{mm}$  thickness engraved by wavelength shifting fibers, which are read out by photomultiplier tubes. The signal of the ACC gives a veto for the primary trigger from the ToF subdetector, only allowing readout of particles, which leave a signal in all subdetectors. Figure 3.14 shows a picture of the ACC mounted inside the AMS-02 vacuum case for the magnet.

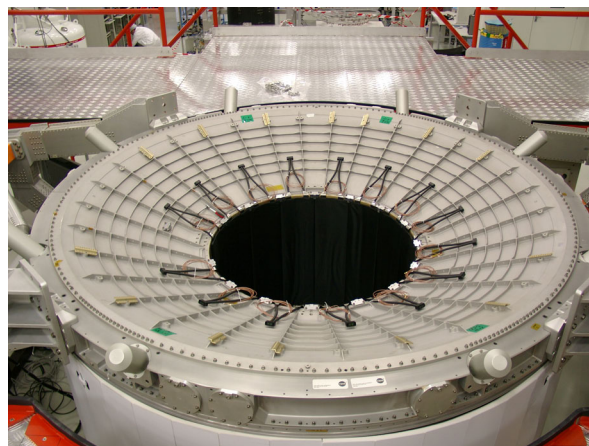


Figure 3.14: *ACC panels mounted inside the vacuum case for the magnet before the installation of the tracker.*

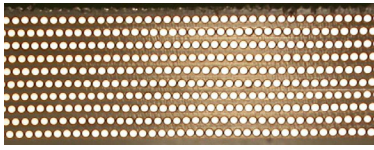


Figure 3.15: *ECAL fibers embedded in 640 kg of lead arranged in 18 layers.*

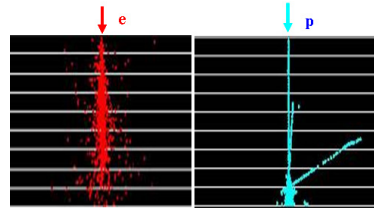


Figure 3.16: *Separation of leptons and hadrons. The radiation length for leptons of the ECAL is about  $X_0 = 16$  and the interaction length of hadrons  $\lambda_h = 0.5$ .*

### Electromagnetic Calorimeter (ECAL)

The electromagnetic calorimeter is mounted on bottom of AMS-02 and by that it is the last subdetector a particle hits. It is built out of 18 layers of lead with scintillator-fiber inserts as shown in figure 3.15. An impacting particle produces secondary particles by electromagnetic interaction. The ECAL allows a precise 3D image of these particle shower by the readout of photomultiplier arrays on the fiber ends. The shower profile allows a easy separation between leptons and hadrons as illustrated in figure 3.16.

The shape of the shower profile and the spectrum of signals in the scintillator material is characteristic for different primary particles. While electrons and photons in the energy range of MeV mainly loose their energy by the photoelectric effect and Compton scattering, in the energy range of GeV electrons are dominated by production of Bremsstrahlung and electron/positron pairs. The produced electrons and positrons again emit Bremsstrahlung, which leads to development of the electromagnetic cascade. The cascade dies out when the energy of secondary particles drops below a critical energy  $E_c$ , when further production of particles is not possible anymore. It is

$$\frac{E_0}{N} < E_c \quad , \quad (3.6)$$

where  $E_0$  is the energy of the primary particle. Figure 3.17 shows typical shower profiles for two particles of different energy  $E_0$ .

Hadrons cannot produce an electromagnetic shower, since the emission of Bremsstrahlung strongly depends on the mass of the particle and decreases with higher mass. For these particles instead the Bethe-Bloch formula applies for the energy deposition in an absorber and a track of the particle can be detected. In this way particles with different mass, but equal charge can be distinguished. Figure 3.18 shows a picture of the assembled ECAL before the mounting to the USS. It has a total mass of 640 kg, which corresponds to a radiation length of  $X_0 = 16$  compared to a minimum amount of material in the other subdetectors above the ECAL with about  $X_0 = 0.4$ . The nuclear interaction length adds up to only  $\lambda_h = 0.5$  for the entire detector. The ECAL achieves a proton suppression for positions with a factor of  $10^3$  to  $10^4$ .

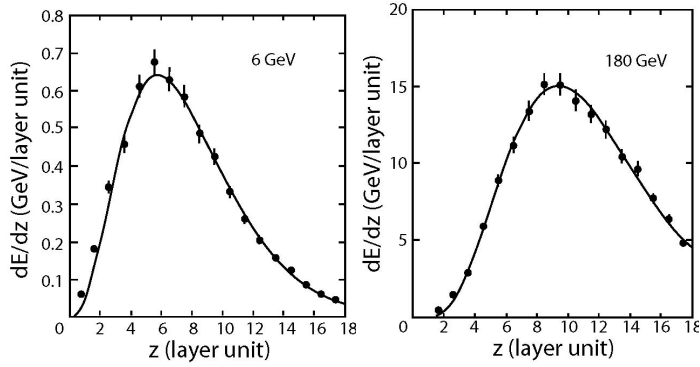


Figure 3.17: Shower profiles in the ECAL. The images show the energy deposition in each of the 18 layers for primary electrons of different energy.



Figure 3.18: The ECAL before the integration into AMS-02.

### AMICA Star Tracker

The AMICA<sup>1</sup> star tracker is not a particle detector. Equipped with two CCD<sup>2</sup> cameras it is able to determine the orientation of AMS-02 in space. The image seen by the camera is compared to star maps, which allows to measure the line-of-sight to a second of an angle precisely. In addition a GPS<sup>3</sup> receiver delivers information about the exact time and the position for the AMS-02 detector.

The information about the direction is especially of interest for the detection of gamma rays. Photons are not influenced by the magnetic fields in the galaxy, which allows to directly look to their sources. Identified sources of gamma rays can then be matched with existing star maps.

### Gamma Ray Detection with AMS-02

The AMS-02 instrument is able to detect gamma rays by two complementary modes. The *single photon mode* is purely based on a measurement in the ECAL. In this case, an interaction in the other subdetectors should not be visible. The readout then is trigger by the ECAL itself. This mode is characterized by the very good energy resolution at high energies. The *conversion mode* on the contrary has an excellent angular resolution. The impacting photon converts into an electron/positron pair on top of AMS-02 inside the TRD or upper ToF. In the magnetic field of the tracker the direction and total momentum of the pair then can easily be measured. In this mode the ECAL contributes to a redundant measurement of the energy of the pair.

Figure 3.19 shows the angular and the energy resolution for both complementary modes. The resolution of EGRET and FERMI<sup>4</sup> satellites are indicated for comparison. A big advantage of AMS-02 over other experiments is the large acceptance allowing to record huge statistics and also short duration events in the Universe with a good time resolution.

<sup>1</sup>Astro Mapper for Instrument Check of Attitude

<sup>2</sup>Charge-Coupled Device

<sup>3</sup>Global Positioning System

<sup>4</sup>formally GLAST

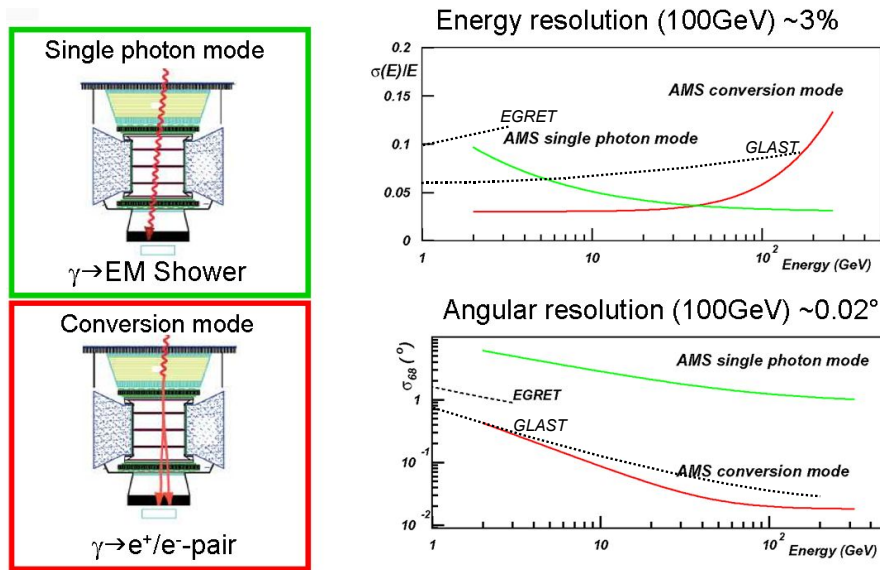


Figure 3.19: *AMS-02* modes for gamma ray detection. In the single photon mode the photon passes the entire detector before triggering a shower in the ECAL with a good energy resolution at higher energies. In the conversion mode the photon converts into an  $e^+/e^-$  pair on top of *AMS-02*, which can be identified in the tracker with a good angular resolution.

### 3.3 The Transition Radiation Subdetector (TRD)

The transition radiation detector (TRD) is placed on top of the *AMS-02* experiment. Its operation is based on an effect observable for charged particles with high Lorentz factors  $\gamma \geq 1000$ . When a charged particle passes over from one medium with the dielectric constant  $\epsilon_1$  to another medium with  $\epsilon_2 \neq \epsilon_1$ , energetic photons are emitted. The production of the transition radiation is a function of the particle's mass and energy. The TRD separates particles of the equal charge and energy, but different mass on the basis of the transition radiation effect. It is possible to distinguish positrons from protons and electrons from antiprotons. Combined with the ECAL, both subdetectors achieve a suppression of the proton background for positrons by a factor of  $10^5$  to  $10^6$ .

The big advantage of transition radiation detectors is, that the information about the particle's properties can be acquired almost without a manipulating effect on the properties of the particle. Similar information is also collected by an electromagnetic calorimeter, but in contrast to the measurement by the TRD the particle most time is stopped or destroyed.

#### 3.3.1 Detector Design

Although transition radiation detectors are widely used in high energy physics, the development for operation in space is a new challenge, which has to respect many different aspects such as mechanical stability during transport, safety considerations during operation on the ISS and a maintenance free design.

The actual detector volume consists of tubes of 3 mm in diameter and a length between 1.5 and 2.2 meters. In total 5248 so-called *straw tubes* are arranged and built in modules of 16

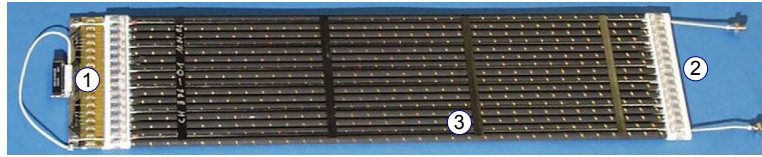


Figure 3.20: A TRD straw tube module. The 16 tubes are connected to the  $Xe/CO_2$  gas circuit by a manifold (2). On the opposite side the tube end board (1) is attached, which connects the high voltage and decouples the signal by 16 capacitors from each straw tube. Additional carbon fiber stiffeners (3) are glued between the tubes.

tubes each as shown in figure 3.20. The walls of these straw tubes are made out of two  $25\mu m$  thick and outgassing free polyimide layers, which are stabilized by a polyurethane layer of  $10\mu m$  thickness in between. A thin Aluminum film on both sides makes the straw tubes electrically conductive. The outer layers are carbon fiber polyimide layers of  $6\mu m$  thickness. The sense wire in the center of the tube is made of  $30\mu m$  gold plated Tungsten. In order to ensure a perfect centering of the wire, built straw tubes were inspected in a computer-tomography scan. On its end the readout electronics board and on the opposite side stainless steel tubes for the gas supply are attached.

The supporting structure of the TRD is formed as a conical octagon of  $1.5m$  width on bottom to  $2.2m$  on top, which houses in total 328 straw tube modules in 20 layers. The mounting precision is better than  $100\mu m$  to avoid a bending of the tubes affecting the detector homogeneity. The walls are made of an aluminum-honeycomb structure covered by carbon fiber on the surface as shown in figure 3.21. The entire octagon is mounted inside an M-shaped aluminum structure, which connects the TRD to the AMS-02 unique support structure. Figure 3.22 shows the TRD and the M-structure during a lifting operation before the integration to AMS-02. The design has taken into account results from an excitation analysis to avoid resonance frequencies, which could be excited during shuttle launch.

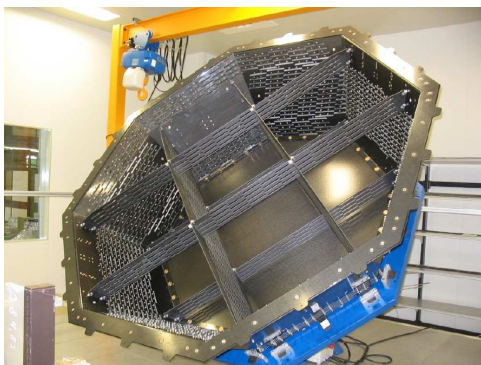


Figure 3.21: The TRD carbon fiber support structure. The twelve layers of straw tube modules in the middle (1) are rotated by  $90^\circ$  with respect to the four layers on top (2) and four layers on bottom.



Figure 3.22: The assembled TRD lifted by a crane. The carbon fiber structure is stabilized by the M-structure machined from solid Aluminum.

Transition radiation is an effect, which can be observed at the boundary layers between two media. The probability, that radiation is emitted, is quite small. For that reason the TRD radiator is not composed of a single layer only. The transition radiation is produced in a 22 mm fleece radiator with irregular fibers of 10  $\mu\text{m}$  in diameter<sup>1</sup> placed in between the straw tube modules. The fiber fleece has a mean density of only 0.06g/cm<sup>3</sup>. The principle of the production of the transition radiation is described later in this chapter.

### The TRD gas system

The gas supply is provided by a separate subsystem. The  $\text{Xe}/\text{CO}_2$  gas mixture will be mixed in space and permanently be circulated through the detector. The gas is stored and supplied by Box-S. The circulation is controlled by Box-C containing redundant pumps mounted together with Box-S to the AMS-02 support structure as shown on the picture in figure 3.23. The gas stored in separate vessels is transferred to a mixing vessel before entering the TRD gas

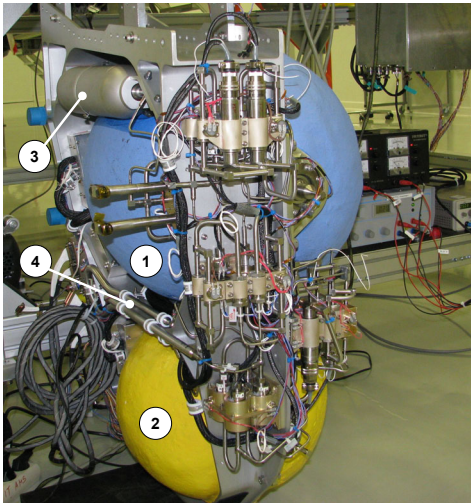


Figure 3.23: *The TRD Gas supply system. The big vessels of Box-S store the Xenon (1) and carbon dioxide (2). The gas mixing vessel of Box-S (3) releases the premixed gas to the circulation Box-C, which controls the circulation of the gas through the detector. A buffer volume (4) is used to extract the gas from the storage vessels in small amounts. The pumps and a  $\text{CO}_2$  sensor are mounted inside a gas tight vessel, which in case of a leak prevents loss of the detector gas.*

circuit. The TRD is divided into independent gas circuits controlled by manifolds mounted to the TRD octagon. The straw tube modules are interconnected by steel tubings such that the outlet of one module is the inlet of the next one on the opposite side. Pressure sensors allow the immediate identification and isolation of leaky segments by the gas electronics. A schematic sketch of the TRD gas system is illustrated in figure 3.24. The gas system has to maintain a stable mixture of Xenon and  $\text{CO}_2$  gases of 4:1 at about 1.2 bar under nominal conditions and therefore has to compensate losses of mainly  $\text{CO}_2$  by diffusion through the tube walls. A contingency of Xenon provides a replacements in the case of losses due to leaks in the system.

### 3.3.2 Physics Principle of the TRD

The TRD belongs to the group of proportional counter gaseous detectors, which are deployed for the measurement at the same time of the localization of a particle and its energy loss in the detector gas. In a simple ionization chamber, a charged particle's energy loss by ionization or the complete energy deposition of photons is determined, as the liberated charge carriers

<sup>1</sup>LRP-375 BK polypropylene/polyethylene manufactured by Freudenberg company, Germany

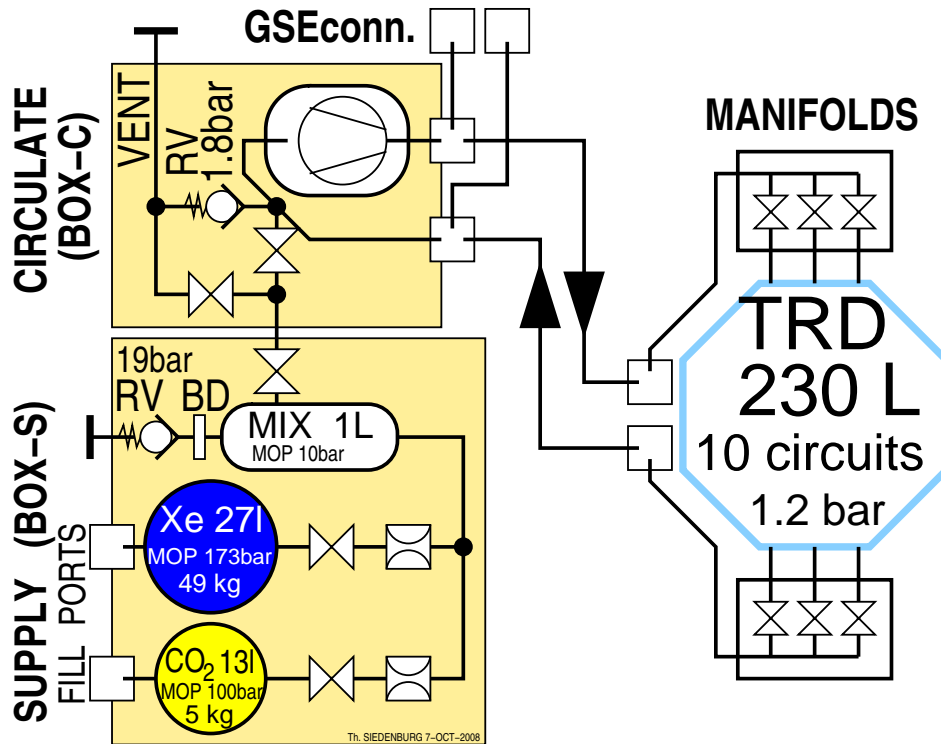


Figure 3.24: General layout of the TRD gas system. The Box-C houses two redundant pumps to circulate the gas through the detector. Premixed gas can be refilled by the Box-S. Independent gas circuits controlled by manifolds at the detector allow to isolate leaky modules. An overpressure in the system is avoided by several release valves.

in the gas are separated in an electric field, which are read out as signal. The proportional counter is based on the same principle, but the number of released charge carriers is amplified. The gain is achieved by the acceleration of the electrons drifting to the anode by high electric fields, so that they are able to ionize other gas atoms on their way resulting in an avalanche of electrons. The high field can be achieved by applying a high voltage or by taking profit of the geometry of the detector. Near the anode wire the field increases to high values in cylindrical chambers due to the  $1/r$  dependence. A proportional chamber is shown in figure 3.25. In section 3.3.4 the derivation of the gas gain factor is given. The Diethorn formula 3.25 describes the dependence between gain and the type of gas, the environmental parameters such as the temperature and pressure, geometry of the chamber and the voltage. For parameters of the AMS-02 TRD it can be shown, that the electron avalanche develops only in immediate vicinity of the anode wire in the center of the tube, while in the rest of the volume the electrons show a drifting behavior only. With this an equal initial energy deposition will result in an amplified signal of equal height. The proportional range of the detector is characterized by the fact, that the gas gain factor  $G$  is equal in a wide range of energies. With this the signal is proportional to the amount of ionization, which allows the energy measurement.

The number of liberated electrons is detector gas dependent. Figure 3.26 shows the cross section of different types of gas. The proportional chamber of the TRD uses Argon gas during the test mode on the ground in order to be cost efficient and Xenon gas during

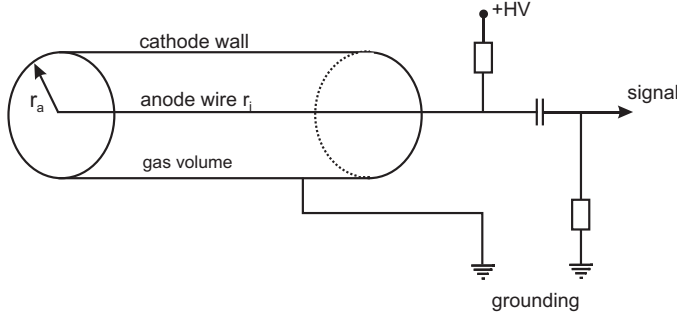


Figure 3.25: Schematic of the proportional chamber of the TRD. In an avalanche near the anode wire the electrons liberated in the gas by ionization are amplified. The signal is read out decoupled from the high voltage by a capacitor.

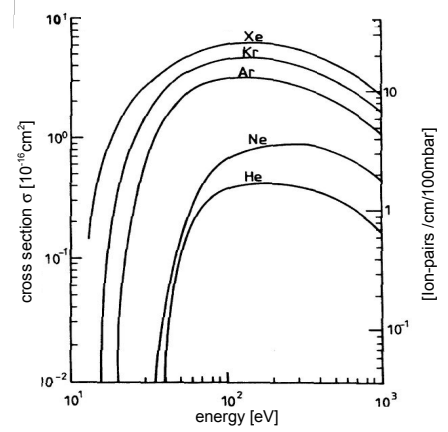


Figure 3.26: Cross section of detector gases for charged particles. In the order of  $10^2$  electrons are liberated by a MIP at 1.2bar in a TRD straw tube.

operation on board the ISS. The small number of liberated electrons stresses the need of an amplification in the avalanche near the anode wire, but also the minimum influence on the energy of the crossing particle. To avoid the proportional chamber to act like a Geiger counter, an admixture of a quench gas is required in order to absorb UV photons, which are produced in the avalanche and could trigger additional avalanches by the absorption in the detector gas. The quench gas  $CO_2$  on the contrary absorbs the photon energy and dissipates the energy in form of elastic scattering without ionization. So the admixture of 20% of  $CO_2$  gas in the detector is made optimizing the signal.

Photons from the transition radiation are detected in the same proportional tubes between the layers of fleece radiator, which also measure the energy loss from the ionization by a particle. A proportional chamber as described is schematically shown in figure 3.25.

The contribution to the energy deposition by the ionization of the gas is described by the Bethe-Bloch formula [28]

$$-\frac{dE}{dx} = 4\pi N_A r_e^2 m_e c^2 \frac{Z z}{A \beta} \left[ \ln \frac{2m_e c^2 \gamma^2 \beta^2}{I} - \beta^2 - \frac{\delta}{2} \right] \quad (3.7)$$

Process	detector gas charge dependence	photon energy dependence
Photoelectric effect	$\sim Z^4$ to $Z^5$	$\hbar\omega^{-3,5}$ to $\hbar\omega^{-3}$
Compton effect	$\sim Z$	$\hbar\omega^{-1}$
Pair production	$\sim Z^2$	$\ln \hbar\omega$

Table 3.1: Processes of photon interaction in matter. [9]

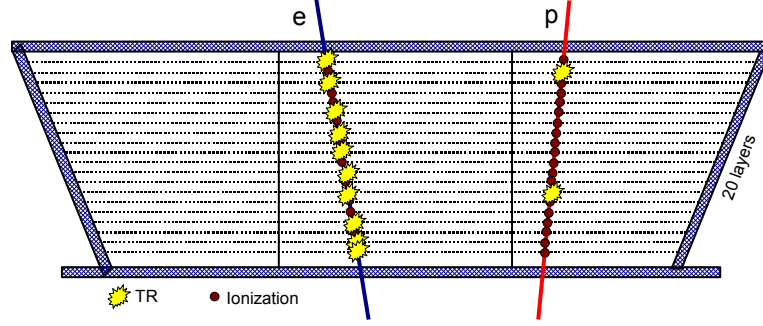


Figure 3.27: The TRD allows to distinguish between electron-like particles, which produce transition radiation, and proton-like particles, which lose energy by ionization only. The probability of creation and detection of a transition radiation photon by an electron in each layer is about 60% according to [39].

The process of the absorption of photons in the proportional chambers is described by the Lambert-Beer law. For the intensity  $I$  after crossing an absorber material of the thickness  $x$  by a primary photon beam of intensity  $I_0$  is

$$I = I_0 e^{-\mu(E)x} \quad (3.8)$$

with the photon energy dependent absorption coefficient  $\mu(E)$ . Depending on the energy of the photon there are three contributing processes, namely the photoelectric effect, Compton scattering and pair production:

$$\mu(E) = \mu_{ph} + \mu_{\text{Compton}} + \mu_{\text{pair}} \quad . \quad (3.9)$$

Table 3.1 lists the main properties of the different processes. Compton scattering can be observed at energies above  $100 \text{ keV}$  and pair production requires a minimum photon energy of twice the electron mass. Hence these two processes can be neglected for photon energies of the transition radiation of a few keV. A photon of the transition radiation is absorbed by the photoelectric effect by the outer electron of a gas atom and produces a free electron. The gap in the electron shell of the atom is located mainly in the K- and the L-shell. With the move up of electrons to higher shells, again photons are emitted, which can ionize other atoms in the gas by the photoelectric effect. So the number of liberated photons depends of the energy of the primary photon.

A decision, if a transition radiation photon is involved can be taken by statistically analyzing the signal amplitudes of all 20 layers of the TRD as illustrated in figure 3.27.

In order to reduce the fraction of direct ionization by the primary particles, the gas inside the proportional chamber has been chosen to be Xenon. The high atomic number of Xenon with  $Z = 54$  causes a high absorption coefficient by the photoelectric effect, which cross section is proportional to  $Z^5$ . With the low thickness of the tubes, an increase of the signal by transition radiation compared to pure energy deposition by ionization, which is proportional to  $Z$  according to equation 3.7, in this way is visible in an optimal way.

Main task of the TRD within AMS-02 is to distinguish particles of same energy and charge, but different mass. Light particles such as electrons and positrons in an energy range from 10

to  $300 \text{ GeV}/c^2$  emit transition radiation with a much higher probability than heavy particles such as protons. A suppression of electrons and protons against antiprotons and positrons can be achieved with a factor of  $10^2$  to  $10^3$  and leads in combination with ECAL to the before mentioned suppression in the AMS-02 experiment. In the following, a more detailed description of the dependencies for emission and the physics principle of transition radiation will give information about potential of this measurement.

### 3.3.3 Theory of the Transition Radiation

Radiation processes of charged particles can always be observed, if the electromagnetic field, which accompanies the moving particle, is exposed to extreme conditions. This is, for example, the case, when the particle's velocity is greater than the speed of light in a medium. As a result, Cherenkov photons are emitted. Amplitudes of the field add up at the surface of a cone, similarly to a sonic boom. Another case is the transition of a fast charged particle through a boundary layer, at which the refraction index and the relative permittivity  $\epsilon$  respectively changes. Here the strength of the electromagnetic field has to adapt the new properties of the medium quickly, which again leads to the emission of photons known as transition radiation. These emission processes have a common theoretical basis, the Bremsstrahlung. All mentioned microscopic signals are produced by moving charge in matter. The effect of transition radiation was first theoretically predicted by Ginsburg and Frank in 1946 [27]. Following considerations will specify the main characteristics of the transition radiation. A first complete description of the effect was given by [25].

The total energy loss of a charged particle by the transition radiation is proportional to the Lorentz factor. Hence relativistic positrons emit transition radiation in the energy range of x-rays, protons of equal energy due to the higher mass do not. The emitted x-rays are strongly forward directed. The radiation angle is in the order of  $1/\gamma$ . A detector such as the proportional counter tubes of the TRD then reads out two additive components of the energy deposition on the track of the particle as the signal. Figure 3.28 shows both components

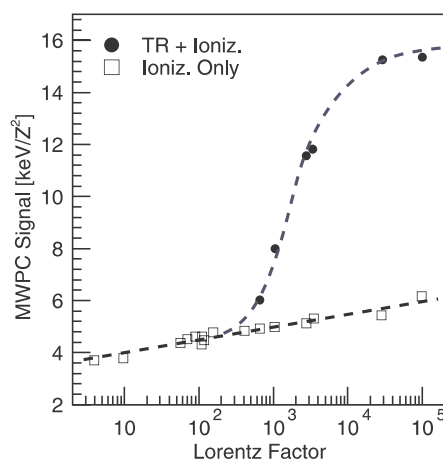


Figure 3.28: *The energy deposition from ionization and transition radiation for high Lorentz factors. At high energies the contribution from the transition radiation saturates. [50]*

against the Lorentz factor  $\gamma$ . One part is the energy loss due to the ionization as described by the Bethe-Bloch formula, the other part originates from the absorbed transition radiation photons, which are produced on the track in the radiator material. A possible way to separate the transition radiation from the ionization on the track more clearly would be to apply a magnetic field, but in AMS-02 the TRD is mounted outside the magnetic field.

### Transition Radiation at a Single Interface

For energetic photons the electrons inside a medium represent an electron gas. In this case, the dielectric constant  $\epsilon$  of the material can be written as a function of the frequency  $\omega$  of the photons. It is

$$\epsilon(\omega) = 1 - \frac{\omega_P^2}{\omega^2} = 1 - \xi^2 \quad , \quad (3.10)$$

where  $\omega_P^2 = 4\pi n_e e^2 / m_e^*$  is the plasma frequency of the electrons,  $m_e^*$  the effective electron mass and  $n_e$  the number of electrons per volume.

If a relativistic particle crosses the boundary to this medium, the radiated photon intensity  $dW$  into the solid angle  $d\Theta$  is described by

$$\frac{d^2W}{d\omega d\Theta} = 2\pi\Theta |a(\omega)|^2 \quad (3.11)$$

with the amplitude

$$a(\omega) = \frac{\sqrt{\alpha}\Theta}{\pi} [(\gamma^{-2} + \Theta^2 - \xi_1^2)^{-1} - (\gamma^{-2} + \Theta^2 - \xi_2^2)^{-1}] \quad . \quad (3.12)$$

Here  $\alpha$  is the fine structure constant<sup>1</sup>,  $\xi_i = \omega_i/\omega$ ,  $\omega$  the energy of the radiated photon and  $\omega_i$  the plasma frequency of medium  $i$ .

This approximation is valid as long as high frequencies  $\omega \gg \omega_i$  and small angles  $\Theta \ll 1$  are concerned. In addition the particles need to be relativistic with  $\gamma \gg 1$ . In this case one can realize, that radiation is emitted with a sharp maximum in the forward direction at an angle  $\Theta \simeq 1/\gamma$ .

By integration over the solid angle  $\Theta$  the differential energy spectrum  $\frac{dW}{d\omega}$  is obtained. It is

$$\frac{dW}{d\omega} = \frac{\alpha\hbar}{\pi} \left[ \left( \frac{\omega_1^2 + \omega_2^2 + 2\omega^2/\gamma^2}{\omega_1^2 - \omega_2^2} \right) \ln \frac{\gamma^{-2} + \omega_1^2/\omega^2}{\gamma^{-2} + \omega_2^2/\omega^2} - 2 \right] \quad (3.13)$$

and a further integral over the frequency  $\omega$  finally provides the photon intensity emitted at a boundary by a relativistic particle:

$$W = \frac{\alpha\hbar}{3} \frac{(\omega_1 - \omega_2)^2}{\omega_1 + \omega_2} \gamma \quad . \quad (3.14)$$

Immediately the linear dependence from the Lorentz factor  $\gamma$  is visible, which in the end allows the separation of the particle masses at an equal energy in the TRD.

In average the number of transition radiation photons is small and in the range of the fine structure constant. By an integration one gets the number of photons

$$N_\gamma = \int \frac{1}{\omega} \frac{dW}{d\omega} \sim \alpha \quad , \quad (3.15)$$

which makes the necessity of a multi-layer radiator obvious in order to get enough detectable photons in a detector.

---

<sup>1</sup> $\alpha = \frac{e^2}{\hbar c}$

### Multi-layer Radiators

An appropriate radiator consists of many boundary layers of the kind just discussed, which leads to a significantly higher yield of production of transition radiation photons. If this radiator has layers perpendicular to the flight path of the particle, the total intensity after  $N$  transitions can be expressed as described in [45] by

$$\left(\frac{d^2W}{d\omega d\Theta}\right)_{N \text{ layers}} = N_{eff} \left(\frac{d^2W}{d\omega d\Theta}\right)_{single \text{ layer}} \quad (3.16)$$

Here

$$N_{eff} = \frac{1 - e^{-N\sigma}}{1 - e^{-\sigma}} \quad (3.17)$$

is the effective number of layers, which contribute to the production of transition radiation. Interference effects at thin layers, as well as the absorption of already produced photons in the radiator material are taken into account.  $\sigma(\omega)$  is the absorption coefficient. With an increasing number  $N$  of layers the radiation intensity finally saturates. For

$$\lim_{N \rightarrow \infty} = (1 - e^{-\sigma})^{-1} \quad (3.18)$$

the creation and absorption of photons balances out. Thus the production of photons in a radiator is limited.

A further feature of the transition radiation is shown in figure 3.28 as well. With an increasing Lorentz factor  $\gamma$  the intensity of transition radiation saturates. Unlike the linear dependence at the single layer transition, this is an effect of a multi-layer radiator. If the thickness of the layers is too small or the Lorentz factor is too big to let the particle and the produced photon separate more than a wave length, the transition radiation will be suppressed by effects of interference.

The thickness and spacing of layers should be chosen such that the intensity of the electromagnetic waves, which are produced at the boundaries, will add up by constructive interference. Manufacturing of radiators of the described characteristics is quite complex. For this reason most detectors use irregular radiators like fleece, foam or fibers. Compared to regular radiators the radiation intensity is reduced by a factor of 10% to 30%. The AMS-02 TRD is equipped with a radiator fleece produced by Freudenberg company. It consists of 85% polypropylene and 15% polyethylene fibers, which are oriented vertical to the flightpath of the particles through AMS-02. [50]

### 3.3.4 Gas Gain Factors of the TRD

The principle of the creation and detection of transition radiation produced by particles of high Lorentz factors is illustrated in figure 3.29. In a proportional chamber tube both contributions from transition radiation and ionization by the charged particle is detected. The amplification or gain of the released charge inside the straw tubes below the radiator at an adjusted high voltage is strongly dependent on the pressure and the temperature of the detector gas. In any environment of operation the TRD certainly is exposed to fluctuations of these parameters. If one wants to make the data over a long period comparable, it is necessary to correct all data sets to standard conditions, which are typically chosen to be

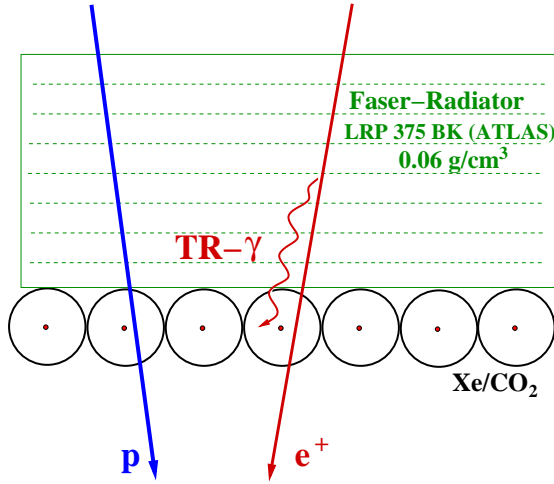


Figure 3.29: The principle of transition radiation. The photon is emitted in direction of flight of the electron.

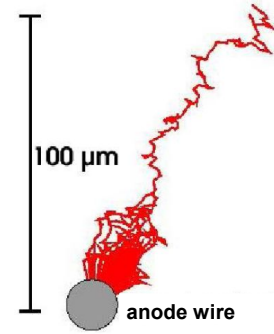


Figure 3.30: The amplifying avalanche developing near the anode wire. The electrons are liberated in the gas either by ionization by the particle or absorption of transition radiation photons. [29]

1013mbar and 20°C. Furthermore the gain can be adjusted by the high voltage applied to the proportional chambers.

For a better understanding of corrections applied during the data analysis it is essential to have a closer look to the gas gain factors of the chambers. A pair of an electron and an ion liberated in the detector gas volume is separated according to their electric charge in the electric field. The positively charged ion is attracted by the cathode, hence drifting to the chamber outer wall. The electron drifts to the central anode wire of the tube. The electric field  $E(r)$  inside the straw tube with a cylindrical geometry is described by

$$R(r) = \frac{U}{\ln(b/a)} \frac{1}{r} \quad (3.19)$$

Here  $U$  is the applied high voltage,  $a$  and  $b$  the radius of the anode wire and the inner radius of the straw tube. An amplification of the number of electrons then can take place in an avalanche process, if the field strength is big enough to accelerate the electrons to energies above the ionization energy of the detector gas. In a radial-symmetric potential this is the case only near the anode wire. The number of electrons in the amplifying avalanche should be generally proportional to initial charge. This allows a direct measurement of the deposited energy in the gas volume. In the case of a photon, it is the total energy, for an ionizing particle it is the released energy according to Bethe-Bloch formula along the flight path through the volume.

In order to ensure the proportional amplification all released primary electrons have to yield the very same amplification process. An electron released in the avalanche volume would clearly not give as many secondary electrons as an electron outside this region does. For the proportional chamber of the TRD the dimension of the critical volume can be estimated by equation 3.19. The diameter  $2 \cdot a$  of the anode wire is  $30 \mu\text{m}$  and the inner diameter  $2 \cdot b$  of the tube is  $6 \text{mm}$ . At an applied voltage of  $1350 \text{V}$  one gets a field strength of  $170 \text{kV/cm}$  at the surface of the anode, which decreases with a factor of  $1/r$  to the outside. For ionization

of an atom of the gas a field is necessary of about  $35\text{ kV/cm}$  for an  $\text{Ar}/\text{CO}_2$  mixture. The field has decreased to this value at a distance from the center  $r_C$  of  $74\mu\text{m}$ , which corresponds to a fraction of 0.06% of the volume of the straw tube. This means for the biggest number of the electrons the same gain factor is valid independently of their location of production. Figure 3.30 shows a schematic avalanche near the anode wire after a long drift path of the electron.

The gas gain factor is deduced from considerations of the avalanche [10]. In the volume of avalanche the number of electrons per distance increases very fast and is described by

$$\frac{dn}{n} = \alpha(E(x))dx \quad . \quad (3.20)$$

$\alpha(E)$  is the Townsend-coefficient, which for a cylindrical geometry of the tube is dependent of the field strength  $E(r)$ .

The gas gain factor  $G$  is described by the ratio of the number of secondary electrons  $N$ , which arrive at the anode wire, and the number of initial primary electrons  $N_0$ . It is  $G = N/N_0$ , where  $N$  can be substituted by the solution of equation 3.20, which is an exponential increase. One gets

$$\ln G = \ln \frac{N}{N_0} = \int_a^{r_c} \alpha(E(r))dr \quad (3.21)$$

and further

$$\ln G = \int_{E(a)}^{E_{min}} \alpha(E)dE \quad (3.22)$$

in dependence of the electric field  $E$ . Here the radial field of the TRD geometry from equation 3.19 has to be substituted. A description of the dependence  $\alpha(E)$  is given by the method of Diethorn. The Townsend-coefficient is set proportional to the electric field, so that

$$\alpha = \beta E \quad (3.23)$$

with  $\beta = \ln 2/\Delta V$ .  $\Delta V$  is the required difference of the potential for ionization. With this equation 3.22 can be integrated.  $E_{min}$  is the minimum field necessary to produce a secondary charge, which carries the dependence from the temperature and pressure or generally the density  $\rho$  of the gas in a closed system. A linear correlation can be found. With the density under normal conditions  $\rho_0$  at a temperature  $T_0 = 20^\circ\text{C}$  and a pressure of  $m = 1013\text{mbar}$ ,  $E_{min}$  can be expressed by

$$E_{min}(\rho) = E_{min}(\rho_0) \frac{\rho}{\rho_0} \quad (3.24)$$

with  $\rho = \frac{p}{T}\rho_0$ . As a result the *Diethorn formula* describing the gas gain  $G$  in dependence of the environmental parameters  $T$  and  $p$ , as well as the applied voltage  $U$  is obtained. It is

$$G = \left( \frac{U}{\ln \frac{b}{a} \cdot a \cdot E_{min}(\rho_0) \cdot \frac{\rho}{\rho_0}} \right)^{\frac{\ln 2 \cdot U}{\ln \frac{b}{a} \cdot \Delta V}} \quad . \quad (3.25)$$

In addition the geometry parameters  $a$  and  $b$  enter to the formula. The Diethorn parameters  $\delta V$  and  $E_{min}(\rho_0)$ , which are characteristic for the gas, have to be determined empirically. The Diethorn parameters for the  $\text{Xe}/\text{CO}_2$  gas mixture used in the TRD in space are

$$E_{min} = (54.0 \pm 0.1)\text{kV/cm} \quad (3.26)$$

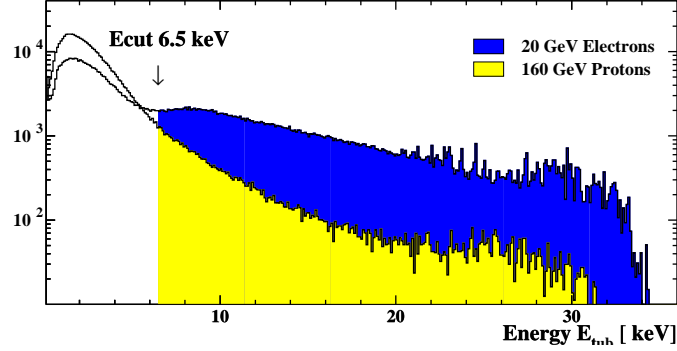


Figure 3.31: *The spectrum of the energy deposition in a tube acquired from an electron and a proton beam. For the likelihood analysis of the data, a probability of a certain energy then can be extracted to decide if the particle is an electron or a proton. For the cluster-counting method only hits above an energy cut value  $E_{cut}$  are counted and according to this number a decision is taken. It was shown, that the latter method is less efficient.*

and

$$\Delta V = (29.3 \pm 1.1)V \quad , \quad (3.27)$$

which allows a gas gain of about 3000 at an anode voltage of 1500V. The parameters for the  $Ar/CO_2$  mixture used during testing on the ground are  $E_{min} = 45.09 \text{ kV/cm}$  and  $\Delta V = 26.88 \text{ V}$ . [24]

### 3.3.5 Contribution of the TRD to the AMS-02 Performance

The major contribution of the AMS-02 TRD for the experiment is the separation between electrons and protons. In addition the TRD contributes to the overall energy loss measurement as well as the tracking of impacting particles. In the following a brief introduction to the methods applied for the particle separation will be given. A more detailed description of the data analysis is presented in [44] and [39].

The most promising method to get the required proton rejection for the detector is the *likelihood analysis*. Starting point is a track identification, which allows to exclude hits off the track from the analysis. In a next step for each hit on the track a probability is assigned, that it originates from a proton-like  $P_p$  or electron-like  $P_e$  particle. This information is extracted from either beam test energy spectra shown in figure 3.31 or Monte Carlo simulations. The latter case requires a deep understanding of the processes inside the detector and is subject to current studies. Uncertainties predominantly effect the proton spectrum, since additional transition radiation starts to be produced in the high energetic range.

The geometric mean of the probabilities for each hit on the track then is calculated by

$$P_{e,p}^{mean} = \sqrt[n]{\prod_{k=1}^n P_{e,p}^k(E_{dep})} \quad . \quad (3.28)$$

The likelihood, that a n entire track is electron-like, then is defined by

$$L_e = \frac{P_e^{mean}}{P_e^{mean} + P_p^{mean}} \quad . \quad (3.29)$$

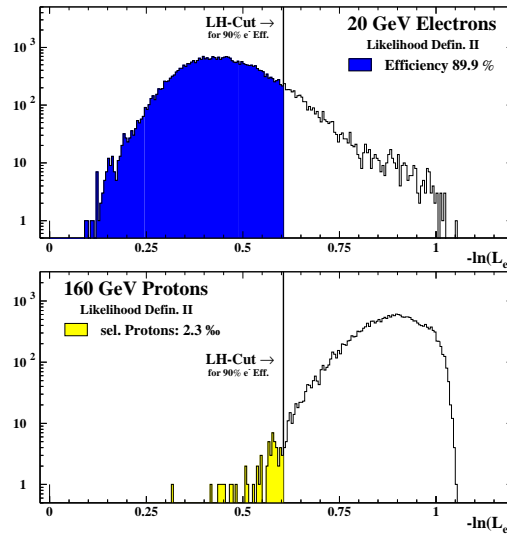


Figure 3.32: *The likelihood-cut definition. The cut is defined such that 90% of electrons are identified correctly. The proton rejection factor is the inverted number of wrongly identified protons and is for all energies well above 100.*

This likelihood can be calculated for each event of the data set. To be determined is the likelihood-cut value, which at least is required to identify a particle as an electron. Therefore the likelihood analysis is performed for a sample of proton data and a sample of electron data, which is shown in figure 3.32. The likelihood-cut is defined such that 90% of the electrons in the sample are correctly identified as electrons. The proton rejection then can be estimated from the number of protons, which are wrongly identified as electrons. The proton rejection

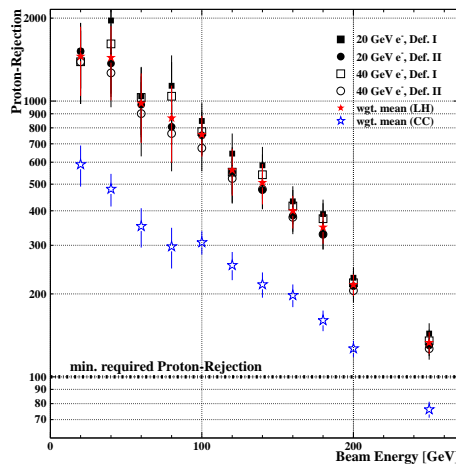


Figure 3.33: *Rejection factors from beam tests for different energies of the proton beam analyzed in [39]. Another analysis method, the cluster counting method, is also plotted, but results in lower rejection factors.*

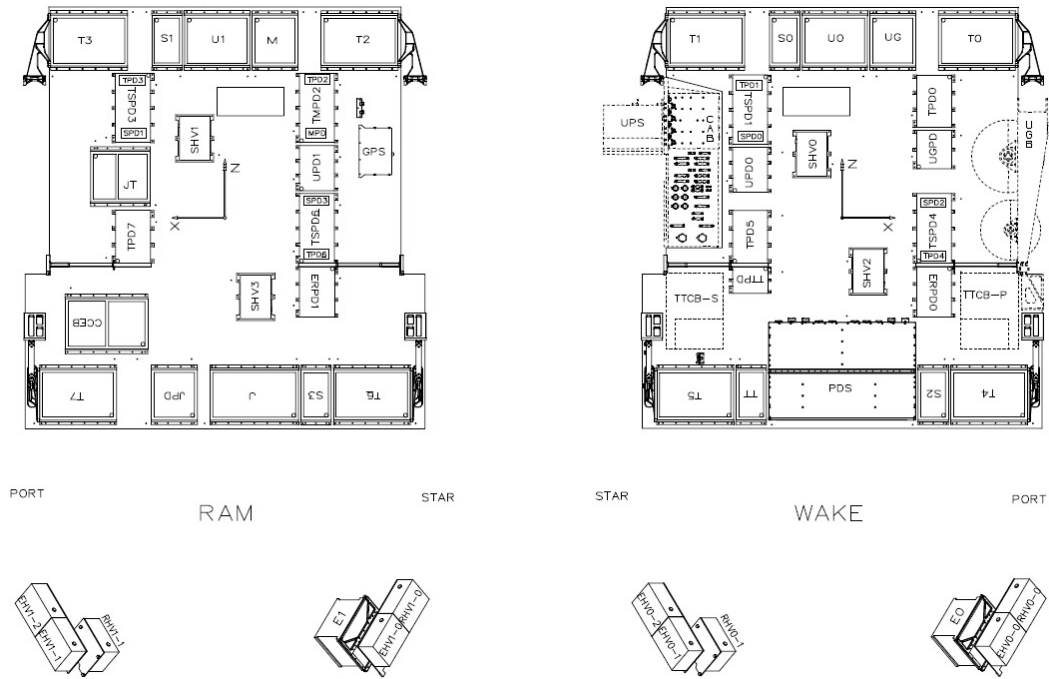


Figure 3.34: Mapping of the electronics crates mounted to the two main heat radiators.

factor is given as the inverted percentage of the wrongly identified protons to the total number of proton events in the sample.

Figure 3.33 shows the results from test beams performed with a 20-layer prototype of the TRD in the years 2002 and 2003. Proton beam energies up to 250 GeV were available at the CERN facilities. As the electron reference a 20 and a 40 GeV beam were analyzed. The proton rejection as a function of the beam energy shows, that all rejection factors are above the requirement for the experiment of 100 up to the highest energies. Nevertheless a deviation from experiment and Monte Carlo extracted rejection factors can be found at high energetic protons giving a hint of not understood additional processes. Result of the investigation of this problem is the topic of [44].

### 3.4 The AMS-02 Electronics

The AMS-02 instrument is controlled and read out by custom made and space qualified electronics. More than 300 computational nodes running permanently in parallel monitor the system status and process the raw data retrieved from the various detector front end electronics. A description of the organization of the data acquisition system will be given in chapter 6.

The electronics components are inserted into solid aluminum crates and boxes, which feature a good heat transfer to the main heat radiators they are mounted to. The radiator plates have an uncovered surface on the outside, which allows to radiate the dissipated power into the space. Each subdetector has its own identifier label in the system. The tracker is identified by a T, the RICH by an R and so on. A complete list of crate identifiers is given in table 3.2 as an



Figure 3.35: *Picture of the partially equipped RAM radiator during the pre-integration phase in 2007.*

overview. The digital electronics is housed by the x-Crates, the analog DC/DC converters by the xPD boxes. All subdetectors are read out to two sides of AMS-02 in order to reduce the cable lengths. Therefore two radiators are installed and identified according to the direction of flight on board of the International Space Station. Figure 3.34 shows a picture of both WAKE and RAM radiator and the mounting position of the various crates. The RICH and ECAL electronics is mounted separately to the lower USS. The entire detector is controlled by a main DAQ computer in the J-Crate installed on RAM radiator. Power supplied by the ISS is converted to 28V and distributed by a central power distribution system (PDS) mounted on the WAKE side radiator. A picture of the electronics of most subsystems mounted on the RAM radiator during the lifting to the AMS-02 supporting structure is shown in figure 3.35. Special focus during design of the electronics system was set on the redundancy of all system components and connections. The redundancy only is not possible in the connection from ISS to AMS-02, which requires an astronaut to swap the connection in case of failure.

### 3.5 Detector Environment on the ISS

The special challenge for the development and the construction of the AMS-02 high-precision instrument is, that the experiment will solely be operated by ground control over a period of at least three years, which does not allow any intervention to the hardware on board of the

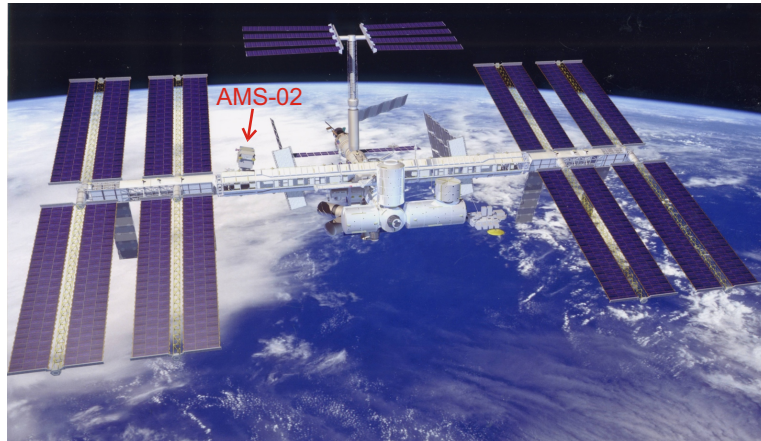


Figure 3.36: *The Alpha Magnetic Spectrometer mounted on the International Space Station. [Image by Lockheed-Martin]*

ISS. Beside the issues of the mission success under the harsh environment in space strict rules are defined by NASA, which have to be met for the transport to space with the space shuttle and during operation as a payload of the International Space Station.

A very obvious restriction applies to the experiment's mechanics construction as a payload of the Space Shuttle. Even though the AMS-02 detector will collect only critical health data in a minimal operation mode on board of the Space Shuttle, the mechanical stress on all system components is enormous at this time. The launch of the shuttle produces vibration forces of up to  $6.8g_{rms}$  onto the detector. In order to keep the precision alignment of the subdetectors and to guarantee a failure free operation after the launch, all parts have been intensively tested on shaker tables during the qualification and production phases. The transition from ground pressure inside the shuttle bay before the launch and the vacuum in space will be very fast. Trapped air inside the experiment needs to escape without damaging system components. In addition all materials need to comply with rules defined by NASA concerning the outgassing in the Space Shuttle and to the environment of the ISS.

In the end there are restriction to the volume and the weight of the experiment inside the Space Shuttle. Nevertheless the latter item is much more important for a payload of the ISS, which cannot exceed certain limits in weight in order to keep maneuverability of the station. Once in orbit on board of the space station life will still not be easy for the experiment. The ISS has an orbit of about  $400\text{ km}$  altitude. Due to a strong variation of the exposure to the sunlight and shadow of the Earth, the temperature varies strongly in short time intervals. All detector components have to survive and to keep their full functionality at each position in the orbit. This is especially for the TRD an important factor, since the gas gain strongly depends on the gas temperature in the detector and thus has to be kept stable. Furthermore it has to be ensured, that the electronics are operational in all temperature conditions. The vacuum in space does not allow to dissipate heat by convection, instead the heat from the electronics systems has to be transported by thermal conductivity of the mechanics and dissipated by radiation into the space. Depending on the position to the sun, extreme temperature variation of  $-180^{\circ}\text{C}$  to  $+50^{\circ}\text{C}$  are expected. With the means of multi-layer insulation these variation is reduced inside AMS-02. For safety all components still are tested in a thermal-vacuum test

up to a variation of  $-25^{\circ}C$  to  $+55^{\circ}C$  in the vacuum in full operation.

For the payload on board of the ISS strict limits are given for the electromagnetic emission. For that reason all electronics are tested for electromagnetic emission on the ground. Furthermore the electronics systems itself should not be influenced by electromagnetic radiation. Another big issue is the hazardous interaction with cosmic radiation. The total dose is still quite low with an expected  $1\text{ krad/a}$ , nevertheless radiation hard components were chosen. More dangerous for the experiment are single event upsets caused by heavy ions passing the detector electronics. Implication on the data acquisition are bit-flips or the latch-up of a chip. In both cases electronics and software is designed to cope with these events. The data is protected by check sums and the hardware by fast solid state fuse latch-up protection.

Finally the power consumption should not exceed  $2500\text{ W}$  for the entire experiment, which gives constraints to development of the electronics systems, but also to the heat control systems. Additionally for instance all processors can be set to a power saving mode as soon they are idle by the operating software.

In the following chapters actions are presented, which have been taken to ensure the ability to operate AMS-02 hardware, and especially the TRD readout system under responsibility of the University of Karlsruhe, under the described conditions in space. Figure 3.36 shows an artist view of AMS-02 mounted to the International Space Station in space.

Digital Electronics Crates	
J-Crate	Main DAQ Computer (JMDC) and NASA interfaces electronics
JT-Crate	Trigger and intermediate event assembly
U-Crate	TRD readout
T-Crate	Tracker readout
E-Crate	ECAL and RICH readout
S-Crate	ToF readout
UG-Crate	TRD gas control
TT-Crate	Tracker thermal control
M-Crate	Control of Star Tracker, GPS and TAS and readout of global temperature sensors
Power Distribution Boxes	
PDS	AMS-02 power distribution system with connection to ISS power
JPD	Power supply for J- and JT-Crate
UPD/UGPD	Power supply for U-Crate and UG-Crate
TSPD/TMPD	Power supply for T-Crate, S-Crate and M-Crate
ERPD	Power supply for E-Crate
SHV/EHV/RHV	High voltage supply for ToF, ECAL and RICH
CAB	Cryogenics avionics box

Table 3.2: *List of identifiers of some electronics subsystems in AMS-02. The top-level electronics is denoted by a J in the identifier.*

## Chapter 4

# The TRD Readout Electronics

For the development and test of the various AMS-02 subsystems the responsibility was distributed to small groups in the AMS-02 collaboration, which finalize the different systems to the operational readiness and space qualification. The contribution of the Institut für Experimentelle Kernphysik (IEKP) of the University of Karlsruhe is the development of the space qualified readout and slow control system for the TRD. In the following a description of the electronics elements and the effort taken to ensure the space qualification of the system is summarized.

### 4.1 Overview of the System

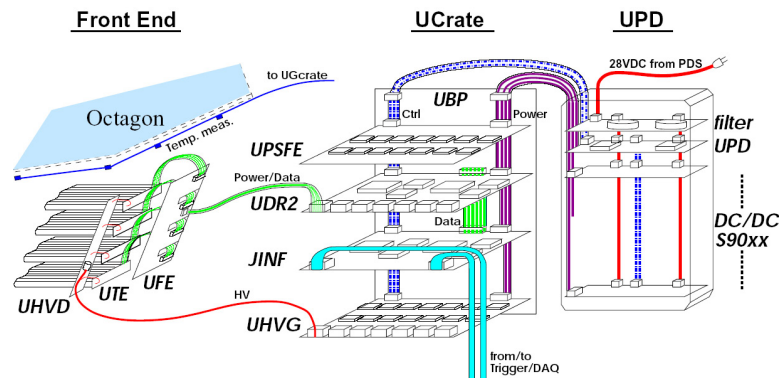


Figure 4.1: Scheme of the TRD readout and power supply electronics. The signals collected from the straw tubes of the TRD octagon are digitized by the front end electronics (UFE). The UFE board is controlled and powered by the U-Crate electronics, which is able to perform further processing of the digitized data before it is sent to the main DAQ system of AMS-02. Several redundant DC/DC converters inside the UPD box supply power to the U-Crate. The high voltage required for the operation of the TRD proportional tubes is also generated by boards inside the U-Crate.

Three main electronics parts required to operate the transition radiation detector can be distinguished, which are also physically mounted in different locations. These are the front

Front End	
UFE	Front End Board
UTE	Tube End Board
UHVD	High Voltage Distribution Board
UFS	Front End Simulator
U-Crate	
UPSFE	Power Supply for Front Ends
UDR2	Data Reduction Board electronics
JINF	AMS interface electronics
UHVG	High Voltage Generator
UBP	U-Crate Backplane
UPD Box	
S9011AU	Controller for DC/DC Converters
S9011B	28 V DC Filter

Table 4.1: *List of identifiers of the components of the TRD. The U denotes components of the TRD derived from the German word for the transition radiation *Übergangsstrahlung*.*

end electronics, directly attached to the actual detector, the U-Crate as the control unit and data concentrator and the UPD box, which provides a reliable power supply for both parts. A schematic sketch of the afore mentioned structure is shown in figure 4.1. The data reduction board (UDR2) inside the U-Crate controls and reads out the front end board (UFE), which is connected to the detector proportional tubes via the tube end board (UTE). The power for the front end board is provided by the UPSFE board, which is connected to the UFE via the U-Crate backplane (UBP) and the UDR2 board. The high voltage for the detector tubes is generated by the high voltage generator board (UHVG) and distributed to the tube end modules by the front end distributor board (UHVD). The U-Crate is connected to the AMS-02 DAQ system by a common interface board (JINF), which reads out and controls all boards on the U-Crate backplane. The UPD box houses DC/DC converters which convert the incoming 28V to the supply voltages required by the electronics inside the U-Crate. A controller board (S9011AU) allows to switch and monitor the DC/DC converters.

For simplicity abbreviations for the board descriptors are used in this chapter, which are listed in table 4.1. The **U** in most of the identifiers originates from the German word for transition radiation *Übergangsstrahlung* and describes components, which belong to the TRD. The 5248 straw tubes of the TRD or 82 front ends respectively are read out by two U-Crates, which are supplied by one UPD box each.

**Phases of Development and Production** Four phases of development and production can be distinguished for the components of the TRD electronics. The first design of the boards was produced under contract with CAEN<sup>1</sup>. The development was supported by MIT, RWTH Aachen University and the University of Karlsruhe. Only a small number of boards was produced in order to verify the basic functionality and allow a first development of firmware

---

<sup>1</sup>CAEN Aerospace, Italian company specialized on electronics development for high energy physics and aerospace application.

Board name	Description	Development Phases			Flight production		
		EM	QM1	QM2	Final version	FM	FS
UBP	U-Crate backplane		2	4	UBP_v2.1	2	2
UDR2	Data reduction electronics	2	4	10	UDR2	12	3
UPSFE	Power supply for front end	2	2	9	UPSFE_v2	6	3
UHVG	High voltage generator	4		14	UHVG	12	5
JINF	U-Crate interface board	2	2	4	JINF_v2	2	1
S9011AU	UPD controller		1	3	S9011AU_v2	2	1
S9011B	UPD input filter		1	1	S9011B	2	1
S9048	+/-2.8V DCDC converter		2	5	S9048	6	3
S9056	+120/5V DCDC converter		2	3	S9056	6	3
S9053	+3.4V DCDC converter		2	1	S9053U	2	2

Figure 4.2: Overview of the produced boards in the development and production phases. The qualification model production allows to equip two complete U-Crates and one UPD box, which are used to readout the TRD during the first test with cosmic rays as described in section 7.1. The flight production covers boards for two U-Crates and two UPD boxes. One complete flight spare UPD box and a partially equipped U-Crate are assembled as flight spare.

and software. The principal functionality of front end readout could be tested. Moreover a first test of a detector prototype could be performed in a test beam at CERN in 2002. Since no backplane was built, the boards were operated on custom made test backplanes.

From the experience gained with the EM models and the failures corrected on this level the qualification model 1 (QM1) was produced by CAEN. For the first time the boards could be tested for space qualification in a vibration test or in a thermal-vacuum chamber. The tests were performed on board level only, because of the small number of boards produced. A second test beam was conducted with a QM1 set of the electronics in 2003.

The final production was decided to be done at CSIST<sup>1</sup>, which is an institute of military defense in Taiwan. A corrected design for the qualification model 2 (QM2) of the U-Crate and UPD box electronics was passed to CSIST. From QM1 to QM2 a strict weight reduction program lead to a major modification of most of the boards, which are named with the extension v2 accordingly. This time a complete set of QM2 electronics was built for a twofold purpose. On the one hand a complete set is required in order to perform the space qualification tests and to prove the full functionality of the system, on the other hand the difficulties of a mass production at CSIST could be identified and solved before the production of the flight hardware. The qualification test was completed in October 2006 for the QM2 model of the U-Crate and the UPD Box.

The flight production finally was completed in 2007 at CSIST taking profit of the experienced gained during the QM2 production and testing. Subsequent an acceptance test only verified the production quality, since no major hardware modification was made with respect to the QM2 model. Two flight model (FM) sets of the U-Crate and the UPD box were built. A complete third UPD box was build as a flight spare (FS). An adequate number of flight spare boards is available for the U-Crate. The flight and spare boards passed all acceptance tests in summer 2007.

Figure 4.2 shows a table with the number of produced boards in the different phases of the production. In the course of the weight reduction or other design changes additional name

<sup>1</sup>Chungshan Institute of Science and Technology, Taiwan

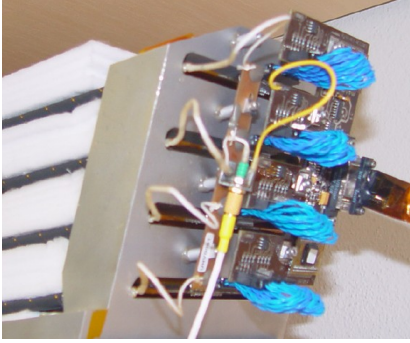


Figure 4.3: The UFE board attached to a chamber of the TRD. It reads out four layers of straw tubes. The UHVD board, which distributes the high voltage to the four modules, is visible on the left side of the UFE board.

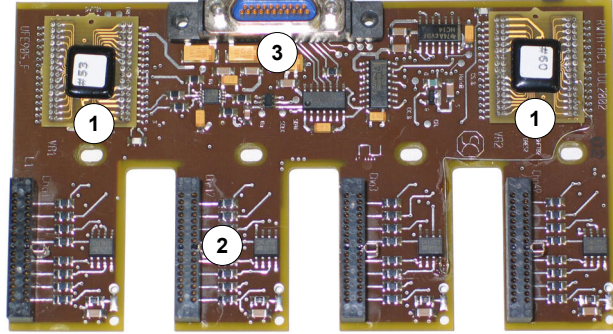


Figure 4.4: Picture of the TRD front end (UFE) board. Two VA32 chips (1) are mounted on the UFE board. Each of them is connected to 32 front end channels (2) and features preamplifiers, shapers and a multiplexer to switch the signals to the 12-bit ADC. The UFE is powered and controlled via a 21-wire cable (3) connected to the UDR2 board.

extension were introduced. The final descriptors of the flight boards are indicated on the right. This thesis deals with progress achieved during the QM2 and FM production. For information on the earlier development phases the reader is referred to [30].

## 4.2 The Front End Electronics

The front end covers the forefront part of the electronics, which is mounted directly to the proportional chambers of the detector. Three separate electronics boards were developed by RWTH Aachen. The simplest of them is the UHVD board as visible in figure 4.3, which solely provides a high voltage connector in order to distribute the voltage to the four connected UTE boards. The UTE board shown in figure 7.14 distributes the high voltage to the center wire of the connected straw tubes. The UTE board is connected to the 16 straw tubes by  $2\text{ M}\Omega$  resistors. The signal is decoupled by a  $150\text{ pF}$  high voltage suitable capacitor. A 16 wire cable connects the UTE to the UFE board, which performs two fundamental steps in the data processing. First the charge on the capacitors on UTE boards is read out and digitized by an analog to digital converter (ADC). From this point the further signal transmission and processing is possible without loss of the signal quality.

The UFE board is shown in figure 4.4. It provides a linear amplification of the collected charge up to  $1.5\text{ pC}$  with a precision of 1%. The collected charge, which can be assigned to a read out ADC unit, is about  $0.5\text{ fC}/\text{ADC}$ . The linear range of the ADC covers about 3000 ADC units at about 80 ADC units for a MIP signal with an operational gas gain. The individual channels have a varying offset in signal free state. The mean of these *pedestals* is at about 400 ADC and sweeps with a maximum of 2 ADC units. A pedestal acquisition is performed by a dedicated calibration procedure during the data taking from time to time. To conclude the UFE allows a measurement of a 0.03 up to 33-fold MIP signal [15].

The UFE board itself is controlled, read out and powered with  $\pm 2\text{ V}$  via the cable connected

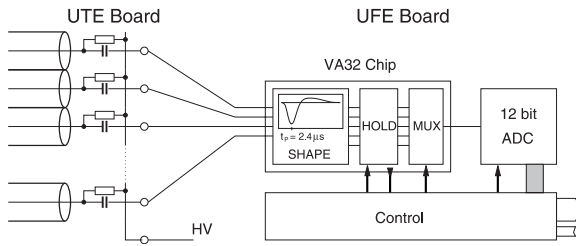


Figure 4.5: *TRD front end electronics scheme.* The VA32 chips, which switch the signals from the UTE capacitors to the ADC, and the ADC chips are controlled by a hardware control chip (HCC) on the board. The clock is given by the UDR2 board sequencer.

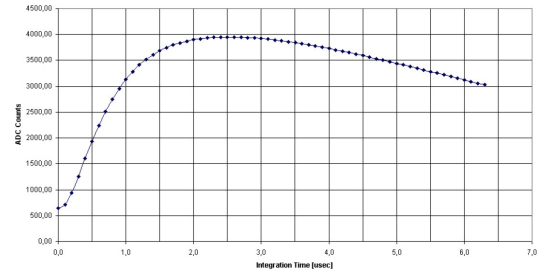


Figure 4.6: *UFE signal integration time.* The maximum charge is collected after about 2.4  $\mu$ s.

to the UDR2 board located in the U-Crate. Two power lines are provided for historical reasons. A separate digital  $\pm 2V$  supply was designed to avoid the coupling of noise of high frequency into the analogue  $\pm 2V$ . This separation still is present on the UFE boards, but was abandoned on the UPSFE and UDR2 boards in order to reduce the weight. Since a UFE board is connected to four modules of straw tubes with 16 straw tubes in each layer, each UFE board reads and digitizes 64 channels as shown in figure 4.5. The signals are forwarded to two VA32HDR12 chips. This chip houses 32 preamplifiers and shapers. An internal multiplexer switches the hold 32 signals one after the other to the outlet of the chip. Both chips are activated by the UDR2 consecutively. The read out of the signal amplitudes has to happen on the chips on the UFE board about 2.4  $\mu$ s delayed to the particle crossing. A measurement of the integration time is shown in figure 4.6. This delay with respect to the primary trigger signal has to be taken into account and can be adjusted in the JINF board inside the U-Crate. A 12-bit ADC is connected directly to the outlet of the VA32 chip and digitizes the 64 channels at the front end sequentially. The ADC of the type AD7476 is controlled by the UDR2 board via two differential lines for control and read out. In this way disturbing effects on the sensitive signal can be reduced, since firstly the analog signal is not transported over a long distance exposed to electromagnetic immission, and secondly the digital signal is protected against effects during the signal transmission.

The control of the VA32 chips is not entirely implemented on the UDR2. Instead a hybrid control circuit (HCC) located directly on the UFE board reduces the number of control signals, which have to be send by the UDR2. So the HCC chip takes over the switching of the two Viking chip one after the other. Two operating modes are implemented. The default read out mode is activated by the UDR2 as soon as a trigger signal arrives. The readout of the VA chips is started and the physics event data is retrieved by the UDR2 for further analysis and processing. A calibration mode can be set to test the functionality and linearity of the individual channels. For the latter mode advantage is taken of the digital to analog converter (DAC) of the UDR2 board. It applies a programmable voltage to the calibration input of the VA32 chip, which distributes the signal to the individual channels and reads it back.

A read out sequence of the UFE lasts 78  $\mu$ s. During this time no other operations are possible, thus a busy is set by the UDR2 board available for the higher DAQ system. After a particle

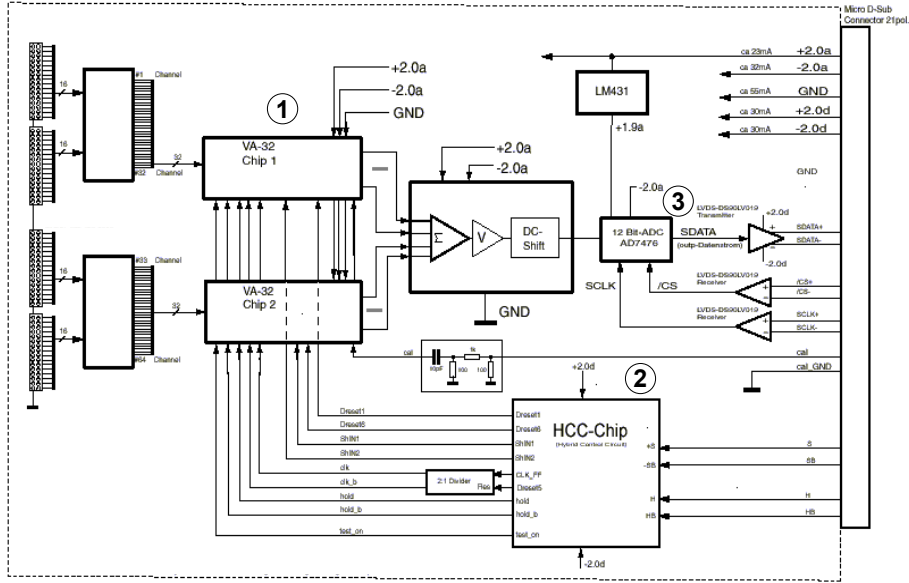


Figure 4.7: *UFE board schematics. The two VA32 chips (1) take over the pre-amplifying, shaping and multiplexing of 32 channels. The hybrid control circuit HCC (2) controls the readout sequence and the switching of the VA32 chips. The analog signals are digitized by an AD7476 ADC (3).*

has crossed the detector and triggered the event in AMS-02, the UDR2 sends a signature, which starts the transmission of the digital ADC values in synchronization with the clock of the UDR2. When all 64 values are transmitted, a reset signal is given. Schematically the three parts of the UFE board are shown in figure 4.7. The sequencer and the digital signal processing is discussed in detail in section 6.2.

### 4.3 U-Crate Readout Electronics

The entire electronics of the TRD for control of the front end readout and the data processing briefly described in the beginning of this chapter is housed in a central unit, the U-Crate. In total 16 electronics boards are fixed inside an Aluminum crate, which is specially treated on its surface. So the surface is either electrical and heat conducting, when good contact is required, or passivated on all other surfaces.

All boards are interconnected by a multi-layer backplane (UBP). Good thermal contact to the U-Crate mechanics is essential in order to transfer the dissipated power. This is ensured by metal locks, the wedge locks, which are mounted on both sides of the board and are squeezed by screws to the walls of the U-Crate during installation of the board. In addition they provide mechanical fixation of the board inside the U-Crate. There are four types of boards, which can be distinguished in their task as shown in figure 4.8. Task and operation principle of the individual boards will be explained in the following in detail.

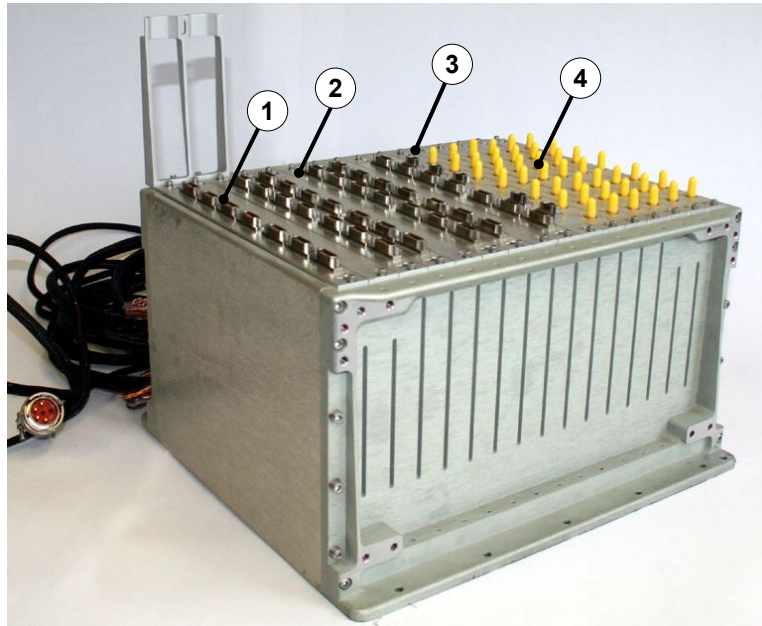


Figure 4.8: The U-Crate with installed electronics boards. The UDR2 (1), UPSFE (2), JINF (3) and UHVG (4) boards are interconnected by an electronic backplane and are mechanically fixed in machined slots of the crate walls.

#### 4.3.1 The J Interface Board JINF

The JINF board is the interface between the U-Crate and the AMS-02 higher DAQ (J-)system. One JINF is present in each crate and is equal for all subdetectors. It is the master for all

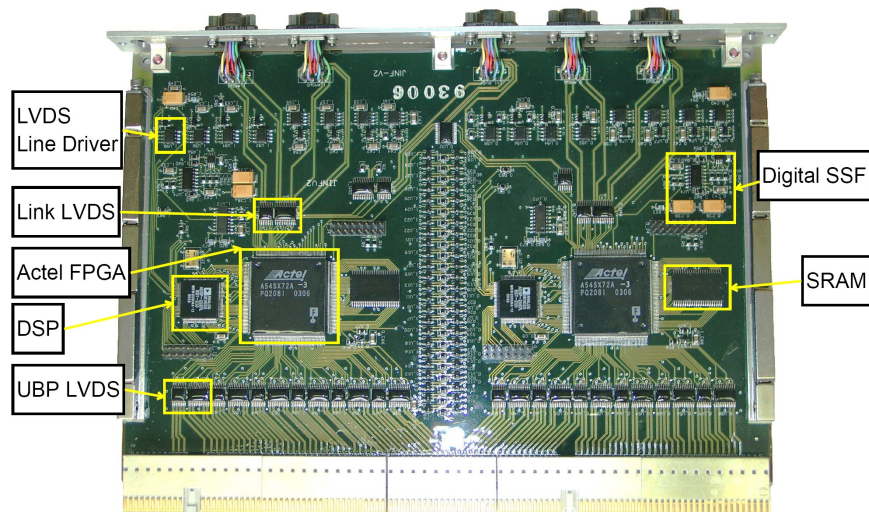


Figure 4.9: Picture of the JINF board. Four AMSWire links are present to the higher DAQ system on the front panel and one link for the trigger. The JINF connects to all nodes in the U-Crate by AMSWire links on the backplane as well as by LeCroy buses to slow control electronics.

AMSWire nodes inside the U-Crate as well as the top node in the LeCroy bus. It has four AMSWire connectors on the front panel to connect to the global AMSWire network. A fifth link is connected to the AMS-02 LV1 trigger. Figure 4.9 shows a picture of the board.

The JINF board forwards the trigger signal to the six UDR2 boards in the U-Crate. A programmable delay is provided to adjust the optimal time delay, with which the readout of the front end boards is initiated after a particle crossing. It concentrates the data retrieved from connected nodes, buffers it and sends it on request to the DAQ system via the front panel AMSWire links. Communication to the six UDR2 boards is established through the AMSWire protocol via the UBP. Before and during the data acquisition the JINF is the controller board for all boards inside the U-Crate and the UPD-Box, which are connected to the local LeCroy bus. Therefore all slow control tasks are processed by the JINF digital signal processor, which covers the initialization and monitoring of the system. The data processing and the slow control are described in detail in chapter 6. Both fully redundant halves of the JINF are active on power-up, but one side can be switched off to reduce the power consumption during normal operation.

### 4.3.2 The Data Processing and Reduction Board UDR2

The UDR2 board controls and reads out the UFE boards and performs the processing of the acquired raw data during the data acquisition. The steering command, data and power connection is established between the UDR2 and the UFE board via a 21-wire cable. For the 21-pin connectors connector sockets on the front panel of the UDR2 boards are present as visible in figure 4.10. A UDR2 board is connected to seven UFE boards in total.

The UDR2 electronic circuit can be divided into two main parts, namely the common digital part, the CDP, which is equal for all subdetector xDR2 boards, and a detector dependent part. The latter part controls the seven UFE boards connected to one UDR2. In addition the  $\pm 2V$  supply voltage, which is generated by the UPSFE regulators, is passed to the front end electronics. The CDP is powered by  $+3.4V$  supplied by the S9053U DC/DC converter

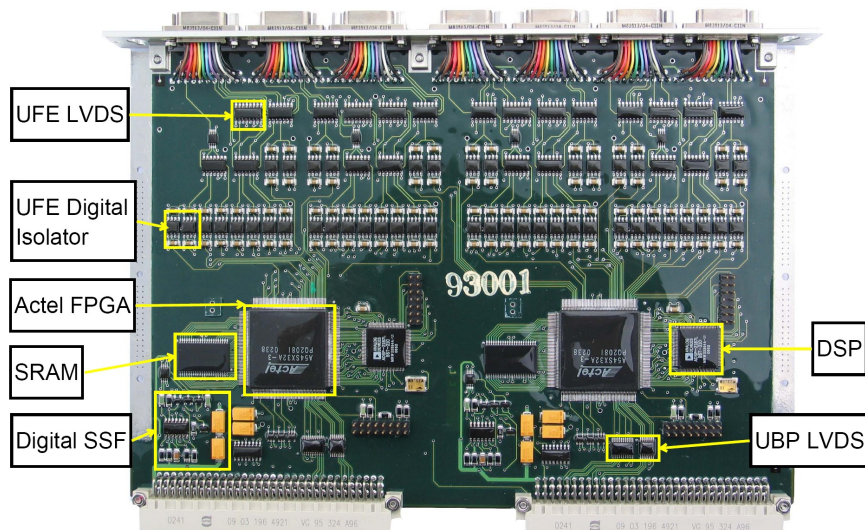


Figure 4.10: *Picture of the UDR2 board*

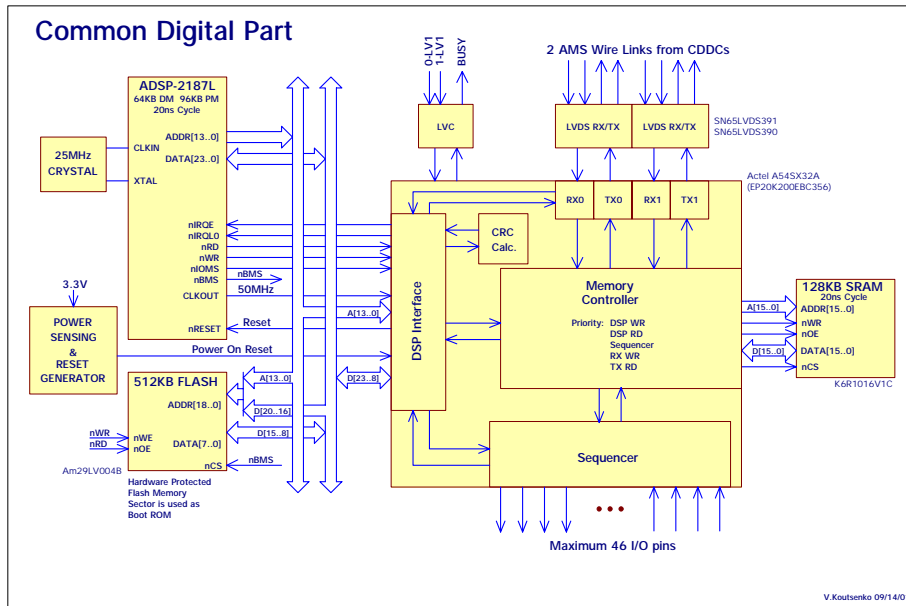


Figure 4.11: Scheme of the common digital part (CDP) of  $xDR$  nodes in AMS-02. The central part is the digital signal processor (DSP) with an internal memory of  $2 \times 64$  kByte. The operating programs are stored in a flash memory. The DSP clocks an Actel FPGA, which controls the transmissions on the AMSWire links. A sequencer part of the FPGA retrieves the digitized data from the front end electronics and stores it to a SRAM memory for the DSP's disposal.

of the UPD box. Both parts are strictly separated electrically in order to reduce the noise injection by the CDP into the analog UFE readout. Therefore high speed digital isolators are used to connect the sequencer part of the FPGA<sup>1</sup> with the detector dependent part of the UDR2 board.

The CDP shown in figure 4.11 takes over a task of central importance for the experiment, which is the processing of the raw data. It is present redundantly. Only one half can be active at a time, so a SWAP/OFF circuit controlled by the UPSFE board, allows to swap the halves or switch the currently active one off. The sequencer part of the FPGA generates the control signals to the UFE board and stores the digitized data to an SRAM<sup>2</sup>. Retrieved and stored RAW data from the front end is processed by an on board digital signal processor (DSP) of type ADSP-2187L. Amplitudes of channels without physics information are discarded in order to reduce the amount of data sent through the DAQ chain and further to the ground. A detailed description of the digital signal processing is given in section 6.2. The program running in the DSP is stored in a flash memory, which allows to store up to eight program versions, which can be rewritten via the AMSWire connection at any time. The CDP is able to buffer four unprocessed event fragments and an additional four events in the processed event buffer before the data is sent to the JINF board on request. An on board digital to

<sup>1</sup>Field Programmable Gate Array, an introduction to FPGA programming is given in [34]

<sup>2</sup>Static Random Access Memory

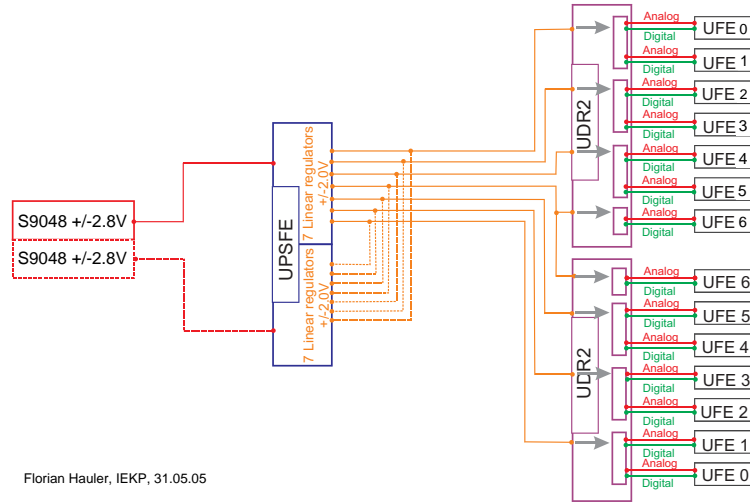


Figure 4.12: *UPSFE power distribution scheme. One UPSFE board supplies seven groups of front end boards via 14 links on two UDR2 boards.*

analog converter (DAC) allows to apply a programmable input pulse to the calibration input of the UFE readout electronics for the purpose of the test of the functionality and linearity of the signal digitization.

Next to three UPSFE boards the U-Crate houses six UDR2 boards, which are able to read out 42 UFE boards in total. In order to read out the entire TRD two U-Crates are required with twelve UDR2 boards in total accordingly.

### 4.3.3 The Linear Regulator Board for Power Supply of the Front End UPSFE

The operational voltage required by the UFE boards is provided by the UPSFE board. Linear regulators stabilize the output voltage to  $\pm 2V$ . Two Actel FPGAs [1] control and monitor the 14 linear regulators. The regulators are divided into seven primary and seven secondary regulators, which are connected to the UBP separately. So both halves can be operated in parallel in order to gain redundancy on this level.

One UPSFE board supplies 14 front end boards. The connection is made via the UDR2 boards, which are connected to seven UFE boards by 21-wire cables. This means one linear regulator supplies two front end boards. For this reason two connections to a UFE on the UDR2 links 0/1, 2/3 and 4/5 are combined to one power group each. Link 6 is combined with the link 6 of the neighboring UDR2 to one power group. Figure 4.12 shows the supply scheme of the UFE electronics. This scheme had also to be considered during the design of the front end simulator electronics, which is described in section 4.5.4.

The 14 regulator circuits of the UPSFE are supplied independently with  $\pm 2.8V$  by the UPD. Therefore the redundant half can be completely switched off by the associated DC/DC converter, which supplies the second half. This cold redundancy allows a lower power consumption of the boards. The voltage is transformed with an efficiency of 71% from 2.8V to the required 2.0V by the regulator circuit. An overcurrent protection is provided for each channel separately in order to prevent damage to the UFE circuitry due to single event latch-ups by

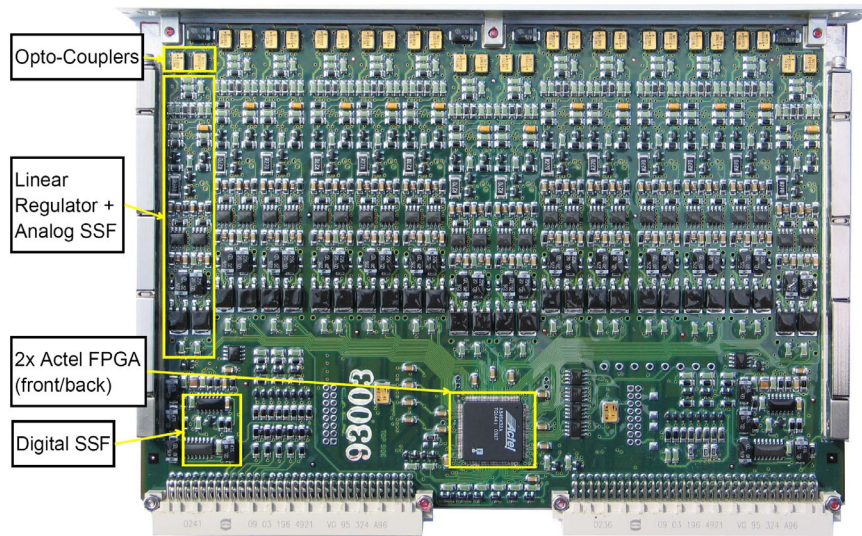


Figure 4.13: *The UPSFE board. Main task is the regulation of the front end power supply by 14 linear regulator circuits. Nevertheless the on board Actel FPGA not only monitors and controls the the linear regulators, but also the power of the UHVG and UDR2 boards inside the U-Crate.*

ions crossing the electronics. All linear regulator circuits are controlled and monitored by two redundant on-board Actel FPGAs.

Furthermore both Actel FPGAs are able to monitor the solid state fuse status on two UDR2 and two UHVG boards via the backplane. The communication between the UPSFE and the JINF board is established by the LeCroy protocol. The U-Crate houses three UPSFE boards. Figure 4.13 shows a picture of the flight model UPSFE board 95005F.

### Slow Control Features

The flight firmware of the UPSFE FPGA was programmed in September 2006. The main task is the control and the monitoring of the electronics boards inside the U-Crate and the on-board front end linear regulators. Figure 4.14 shows an overview of the UPSFE registers. The firmware provides several 2-bit control settings, which can be written, and status registers, which can be read and hold information about the status lines from the monitored hardware. A general rule is that the bit order 01 switches the connected hardware on, while bit order 10 switches it off. The registers are written and read by a corresponding LeCroy command. The LeCroy transmission protocol is described in section 6.1.3.

The control register 0 allows to switch the redundant Actel FPGA on the UPSFE board on or off. By default it is on after a power cycle. Although in normal operation it should be switched off, control lines to the hardware are ORed from both Actel FPGAs. Further bits in the register allow to switch the UDR2 boards. Each UPSFE controls two UDR2 boards with both redundant halves. One register turns off the active half, another allows to swap the active one. Register 1 controls the off signal for the UHVG boards. Each UPSFE controls two UHVG boards with both redundant halves. Registers 2 and 3 are for the control of the linear regulator halves A and B.

Writing					Reading						
Register bit	0	1	2	3	Register bit	0	1	2	3	4	5-10
15			LR A Trip Threshold	LR B Trip Threshold	15						trip counters UDR, UHVG, LR
14					14						
13			LR 6 A	LR 6 B	13	Power on		LR 6 A status	LR 6 B status	LR 6 B glob.con.	
12					12	Status Ac.		LR 5 A status	LR 5 B status	LR 5 B glob.con.	
11	Actel brother		LR 5 A	LR 5 B	11	UDR 1 B off	UHVG 1 B off	LR 4 A status	LR 4 B status	LR 4 B glob.con.	
10					10	UDR 1 A off	UHVG 1 A off	LR 3 A status	LR 3 B status	LR 3 B glob.con.	
9	UDR Trip Threshold	UHVG Trip Thr.	LR 4 A	LR 4 B	9	UDR 0 B off	UHVG 0 B off	LR 2 A status	LR 2 B status	LR 2 B glob.con.	
8					8	UDR 0 A off	UHVG 0 A off	LR 1 A status	LR 1 B status	LR 1 B glob.con.	
7	UDR 1 swap	UHVG 1 B	LR 3 A	LR 3 B	7			LR 0 A status	LR 0 B status	LR 0 B glob.con.	
6					6			Trip Thr. On	Trip Thr. On		
5	UDR 1 on/off	UHVG 1 A	LR 2 A	LR 2 B	5	Actel B off		LR 6 A control	LR 6 B control	LR 6 A glob.con.	
4					4	Trip Thr. On	Trip Thr. On	LR 5 A control	LR 5 B control	LR 5 A glob.con.	
3	UDR 0 swap	UHVG 0 B	LR 1 A	LR 1 B	3	UDR 1 swap	UHVG 1 B con.	LR 4 A control	LR 4 B control	LR 4 A glob.con.	
2					2	UDR 1 con.	UHVG 1 A con.	LR 3 A control	LR 3 B control	LR 3 A glob.con.	
1	UDR 0 on/off	UHVG 0 A	LR 0 A	LR 0 B	1	UDR 0 swap	UHVG 0 B con.	LR 2 A control	LR 2 B control	LR 2 A glob.con.	
0					0	UDR 0 con.	UHVG 0 A con.	LR 1 A control	LR 1 B control	LR 1 A glob.con.	
								LR 0 A control	LR 0 B control	LR 0 A glob.con.	

Figure 4.14: *Slow control registers of the UPSFE FPGA.*

Status register 0 shows the status of the redundant Actel FPGA. A power bit indicates a power cycle and is reset after the first readout. Further bits hold the status of the controlled UDR2 boards. Register 1, 2 and 3 hold status of the UHVG boards and the linear regulators correspondingly. Register 4 displays the global control status of the linear regulators, which is the ORed control signal of both redundant Actel FPGAs. A special feature of the UPSFE is to be able to remember on/off-trips of the monitored hardware in the trip counter registers 5 to 10. Each time a trip is detected on the status lines the counter is increased by one. Dedicated control registers allow to set a threshold of 16 for the number of trips before the hardware is switched off permanently until the trip counters are reset by the user. This feature is activated by default but can be deactivated at any time.

#### 4.3.4 The High Voltage Generator Board UHVG

The UHVG board generates the high voltage, which is required for the operation of the proportional counter tubes of the TRD. Six UHVG boards are mounted inside a U-Crate. Each of them supplies seven front end distributor boards with 64 straw tubes each. Also the UHVG boards are fully redundant on each channel. Space qualified and high voltage approved cables connect the high voltage of the UHVG to the UHVD board at the front end. The UHVG board is connected via the UBP to three different voltages. The 120V is the input voltage for the high voltage generator circuit, the 5V are needed to supply the high voltage controller MHV100 chip and 3.4V are required for the LVDS driver of the LeCroy bus. The high voltage is generated from the initially 120V by a Cockcroft-Walton high voltage chain. This high voltage generator is put together from 16 diode/capacity stages, which provide a maximum output voltage of 1750V. Figure 4.15 shows the UHVG board with the Cockcroft-Walton cascades. Basic principle is that an alternating voltage decoupled by capacities lifts charge, which enters the chain via the diodes, to a higher potential in each step. The voltage can be read out by an ADC. Each generator can be controlled by a LeCroy MHV100 chip, which is connected to the LeCroy bus and can individually be addressed.

An additional feature of the UHVG is the possibility to set overload limits, which are over-current and over-voltage protection. The high voltage is set by writing a register of the MHV100 chip, which holds the 14-bit DAC value of the comparator circuit. Figure 4.16 shows a schematic of the MHV100 control circuitry. Due to variations in electronic components

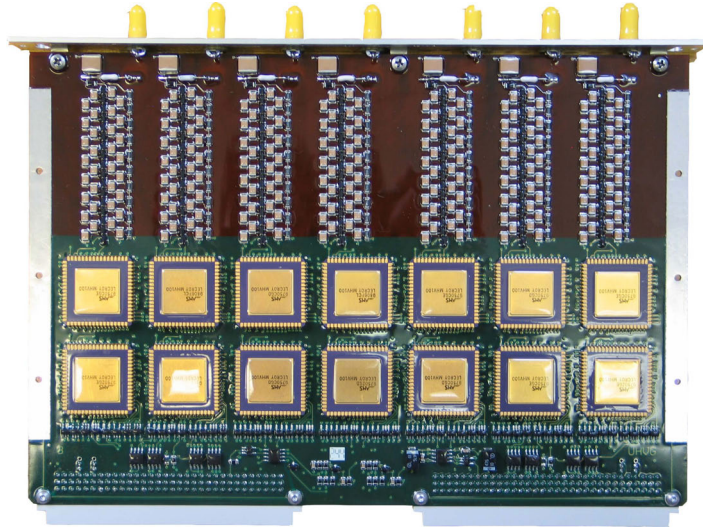


Figure 4.15: Picture of the UHVG board. Each of the seven easy to identify high voltage chains is controlled by one MHV100 chip on the bottom. The second seven MHV100 chips control the redundant chain on the backside of the board.

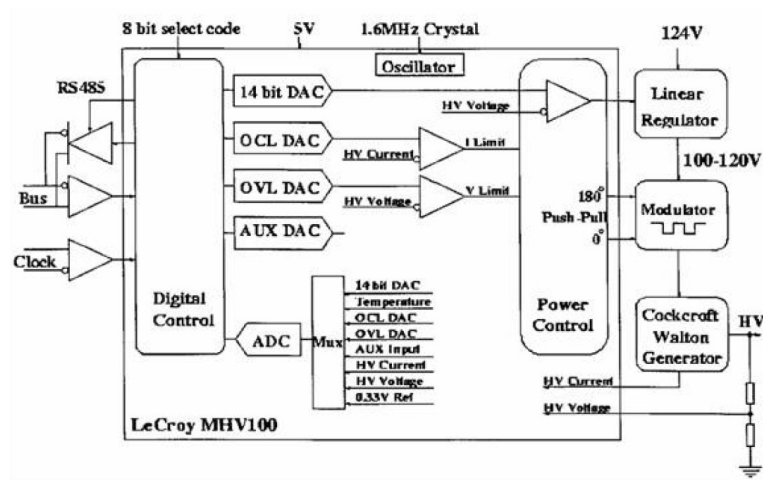


Figure 4.16: Schematic of the UHVG high voltage control circuit. The custom made MHV100 chip takes over the control and monitoring and is addressed via the LeCroy bus. The modulated peak voltage at the input of the high voltage cascade is regulated such that the feed back voltage from a divider circuit and the 14-bit DAC generated voltage match.

each channel has a slightly different output voltage for the same DAC setting. This makes it necessary to calibrate each channel, which was performed during the production of the boards as described in section 5.5.

For completeness the principle of a Cockcroft-Walton high voltage cascade will briefly be discussed. Figure 4.17 shows a simplified chain. The cascade is driven by an alternating supply voltage, which is 0 to 100V in the example. For simplicity the cascade here is reduced to two stages. In the first cycle, the capacitor C2 is charged through the diode D2. The same happens in all following stages. As soon the input voltage drops, C2 stays charged due to blocking diode D2, but through D1 the missing charge on C1 is compensated. In the next cycle, C2 can be charged even more, since it is pre-charged from the previous cycle. After a few cycles C2 stays constantly charged to 100V, which is the case for all capacitors in the chain. The only difference is that the potential is raised for each stage by the previous stage, so that with reference to ground each stage adds 100V to the initial voltage peak. From then on the alternating voltage just charges the resistors in case of current output at the end of the chain. The high voltage output is regulated by regulating the input peak voltage.

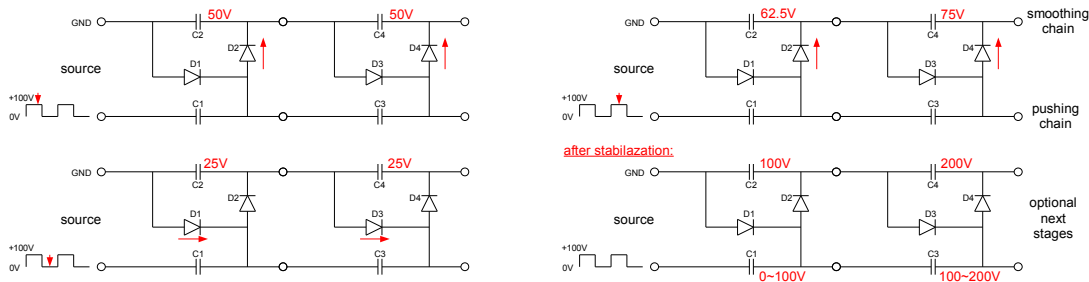


Figure 4.17: *Simplified Cockcroft-Walton high voltage chain. The working principle is explained in the text.*

## 4.4 Power Distribution Electronics

The UPD electronics box shown in figure 4.18 assures a reliable power supply for the TRD readout electronics of the U-Crate. Photo-voltaic modules mounted on the International Space Station provide an output voltage of about 126V, which will also be supplied to the AMS-02 experiment. A central AMS-02 power distribution system (PDS) converts the input voltage to the 28V supply voltage and distributes it to the subsystems. The 28V is the input voltage of the UPD-box, which converts the voltage to the required voltages by several DC/DC converters. The converters are controlled and monitored by the S9011AU electronics board inside the UPD box.

The input voltage of 28V is filtered by the S9011B board. Three S9048 converter boards supply the  $\pm 2.8V$  required by the front end power regulators inside the U-Crate. A S9053U converter board supplies all digital electronics inside the U-Crate and the S9011AU controller inside the UPD box with 3.4V. Three S9056 boards provide +120V and 5V to supply the high voltage generator boards of the U-Crate. Figure 4.19 shows the interconnection scheme. All DC/DC converters are redundantly present. Each redundant half supplies a redundant half of the U-Crate electronics, which means that under normal operation only one half of

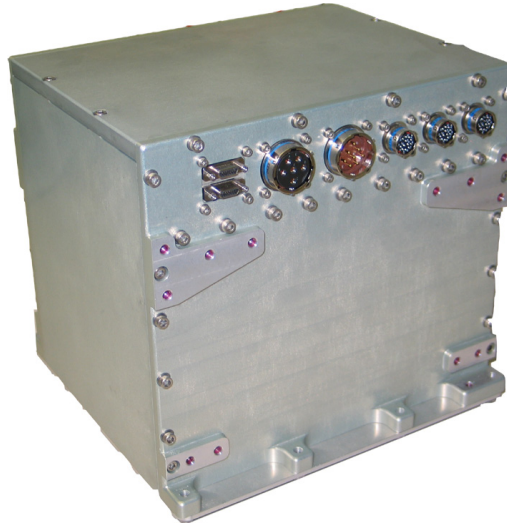


Figure 4.18: Picture of the UPD box. The DC/DC converter boards are completely covered by the aluminum housing. Receptacles attached to the walls allow to connect cables to the U-Crate to the different DC/DC converters inside the box.

the U-Crate electronics is powered and active. Only the S9053U board supplies the entire U-Crate with both halves. Therefore its output is interconnected by diodes. In order to

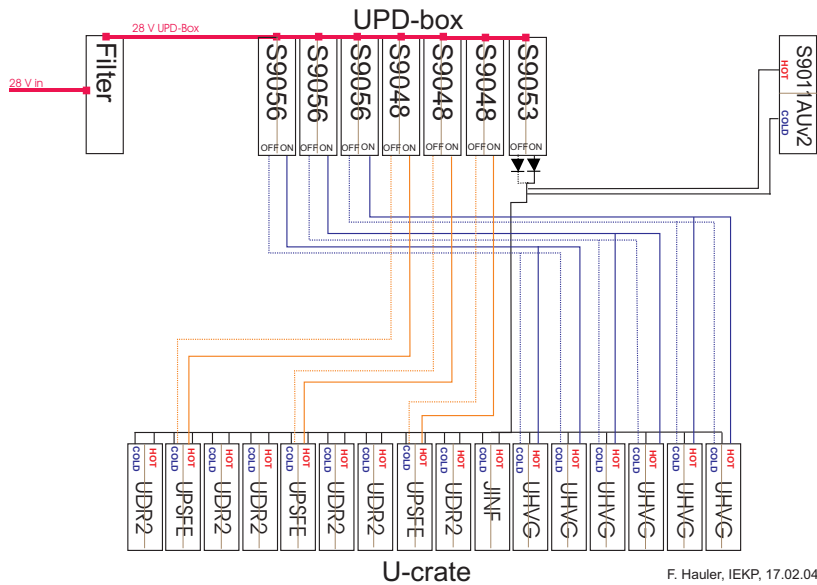


Figure 4.19: Scheme of the power distribution system. The UPD box houses three different types of DC/DC converters to supply the electronics inside the U-Crate. The input voltage from the AMS-02 PDS is filtered. All DC/DC converters can be switched by the controller board inside the UPD box.

Type	S9048	S9053U	S9056
Output Voltage [V]	$\pm 2.8$	+3.4	+5.2/+120
Maximum Load [A]	+2.4/-2.4	3	150m/35m
Nominal Load [mA]	+950/-1450	1500	54/18
Efficiency [%]	71	65	55
Weight [g]	270	340	260
Boards inside the UPD	3	1	3

Table 4.2: Overview of the DC/DC converters mounted in the UPD box. The efficiencies were measured by [30].

avoid a complete loss of the 3.4V power solid state fuses are present on all boards, which are connected to the 3.4V power lines. Besides the electronics also most cable and wire connections are designed at least redundant in order to compensate the loss of electrical contact for instance due to vibration during the shuttle launch.

The box mechanics parts are made of Aluminum, which is hardened at the surface equally to the U-Crate. In addition it is equipped with small vent holes to ensure the air can safely escape during the launch, since in contrast to the U-Crate it is a closed box.

#### 4.4.1 DC/DC Converter Boards

The DC/DC converters used in the AMS-02 xPDs are of switching type DC/DC converters designed by CAEN. Each DC/DC converter board has two identical redundant circuits, which can be separately switched on and off by the S9011AU controller board inside the UPD box.

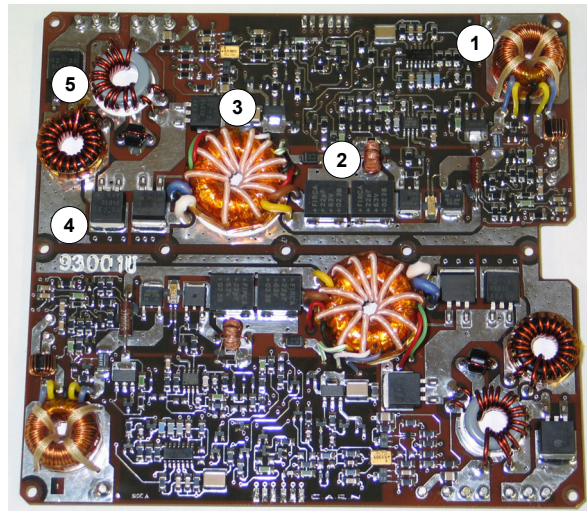


Figure 4.20: The S9053U DC/DC converter board. The board has two identical redundant halves, which are connected at the output by diodes. The converter circuit consists of a 28V input filter (1), a switcher (2) with the transformer and sense coil (3) and output rectifier diodes (4) and a filter (5). The design of the DC/DC converters is proprietary of CAEN.

The input circuit hacks the incoming  $28.4V \pm 2V$  and the output circuit generates the required voltage. Output filters are present on all DC/DC converter boards. Figure 4.20 shows a picture of a DC/DC converter board. A list of DC/DC converters used in the UPD and important features are given in table 4.2. A more detailed description of the DC/DC converters and the qualification procedure is given in [44].

#### 4.4.2 The UPD Controller S9011AU

The DC/DC converter boards of the UPD are controlled and monitored by the S9011AU controller board with two redundant Actel FPGA chips. The S9011AU board inside the UPD box is connected to the U-Crate backplane by two 9-wire cables. Two lines in each cable are present for the power supply with 3.4V from the U-Crate backplane to the S9011AU board. Four lines connect the clock and data lines of two LeCroy buses from the UBP to the controller boards. The control master in the LeCroy bus is the JINF board inside the U-Crate. The seven DC/DC converters in the UPD box are connected to the S9011AU board by seven 9-pin connectors, which are mounted on top of the S9011AU I-frame.

#### Slow Control Features

Task of the S9011AU board is the control and monitoring of the DC/DC converter boards housed by the UPD box. The flight firmware of the S9011AU board has been programmed in March 2006. Figure 4.21 shows an overview of the S9011AU FPGA registers. The firmware provides several 2-bit control settings, which can be set, and status registers, which hold information from status lines from monitored hardware. A general rule is, equally to the UPSFE slow control, that bit order 01 switches the connected hardware on, 10 switches it off. The LeCroy transmission protocol is described in section 6.1.3.

The control register 0 allows to switch the redundant Actel FPGA on this board on or off. By default it is on after a power cycle. The same register allows to switch the S9056 DC/DC converters supplying the UHVG boards inside the U-Crate. Both redundant halves

Writing			Reading				
Register bit	0	1	Register bit	0	1	2 (global control)	3 (trip indicator)
15		S9053U B on/off	15	Power on	S9053U B off	S9053U B	S9053U B
14			14	Status Ac.	S9053U A off	S9053U A	S9053U A
13	Actel brother	S9053U A on/off	13	S9056 0 B off	S9048 2 B off	S9048 2 B	S9048 2 B
12			12	S9056 0 A off	S9048 2 A off	S9048 2 A	S9048 2 A
11	S9056 0 B on/off	S9048 2 B on/off	11	S9056 1 B off	S9048 1 B off	S9048 1 B	S9048 1 B
10			10	S9056 1 A off	S9048 1 A off	S9048 1 A	S9048 1 A
9	S9056 0 A on/off	S9048 2 A on/off	9	S9056 2 B off	S9048 0 B off	S9048 0 B	S9048 0 B
8			8	S9056 2 A off	S9048 0 A off	S9048 0 A	S9048 0 A
7	S9056 1 B on/off	S9048 1 B on/off	7		S9053U B con.		
6			6	Actel control	S9053U A con.		Actel brother
5	S9056 1 A on/off	S9048 1 A on/off	5	S9056 0 B con.	S9048 2 B con.	S9056 0 B	S9056 0 B
4			4	S9056 0 A con.	S9048 2 A con.	S9056 0 A	S9056 0 A
3	S9056 2 B on/off	S9048 0 B on/off	3	S9056 1 B con.	S9048 1 B con.	S9056 1 B	S9056 1 B
2			2	S9056 1 A con.	S9048 1 A con.	S9056 1 A	S9056 1 A
1	S9056 2 A on/off	S9048 0 A on/off	1	S9056 2 B con.	S9048 0 B con.	S9056 2 B	S9056 2 B
0			0	S9056 2 A con.	S9048 0 A con.	S9056 2 A	S9056 2 A

Figure 4.21: Slow control registers of the S9011AU FPGA.

can be controlled independently. Control register 1 controls the S9048 and S9053U DC/DC converters.

The status register 0 shows the on/off status of the redundant Actel FPGA. A power bit indicates a power cycle and is reset after the readout. The same register, according to the control register, holds the status of the controlled S9056 DC/DC converter boards. Register 1 holds status of the S9048 and S9053U DC/DC converters accordingly. Register 2 shows the ORed control signal from the Actel FPGA A and B. Register 3 indicates detected power trips of the hardware after a power cycle. It is reset by the readout.

### 4.4.3 Boxes Interconnection Scheme and Cabling

The UPD box and the U-Crate are interconnected by both power and data lines. Each DC/DC converter inside the UPD box is connected to a cable receptacle on the UPD walls. The power cable is attached to the backplane inside the U-Crate to the different nets of the UBP on power bugs. Therefore the cable are crimped with ring lugs on one end, which can easily be fixed by a screw to the power bug on the backplane, and inserted into a connector on the other end, which can be connected to the corresponding receptacle on the UPD side. The connectors allow multiple connecting-disconnecting cycles, whereas the ring lugs should only be mounted once with the final torque.

The connection of the LeCroy bus and the power between the U-Crate backplane and the S9011AU controller inside the UPD is established by a 9-wire pigtail connector, which free wire ends are soldered to the corresponding network on the UBP. During the EMI test of the QM2 model it became necessary to also power the S9011AU by the 3.4V from the UBP. Two wires are used to route back the digital power to the UPD. All other wires are connector to the common ground of the digital electronics.

A complete list of the LeCroy bus connections of the U-system is given in figure 4.22. Listed are the LeCroy bus ID connected to the JINF inside the U-Crate and the connected slave or slaves. Finally the entire system consisting of the 82 front end boards, two U-Crate and two UPD boxes is schematically illustrated in figure 4.23.

bus link	slaves	Slot	board address									
			0	1	2	3	4	5	6	7	8	
0	UHVG A		14	15	16							
1	UHVG A		11	12	13							
2	UPSFE A				2			5				8
3	S9011AU A					UPD						
4	S9011AU B					UPD						
5	UHVG B		11	12	13							
6	UHVG B		14	15	16							
7	UPSFE B				2			5				8

Figure 4.22: Table of the LeCroy buses of the U-system. The board address and physical location is given for each node on the corresponding LeCroy bus link.

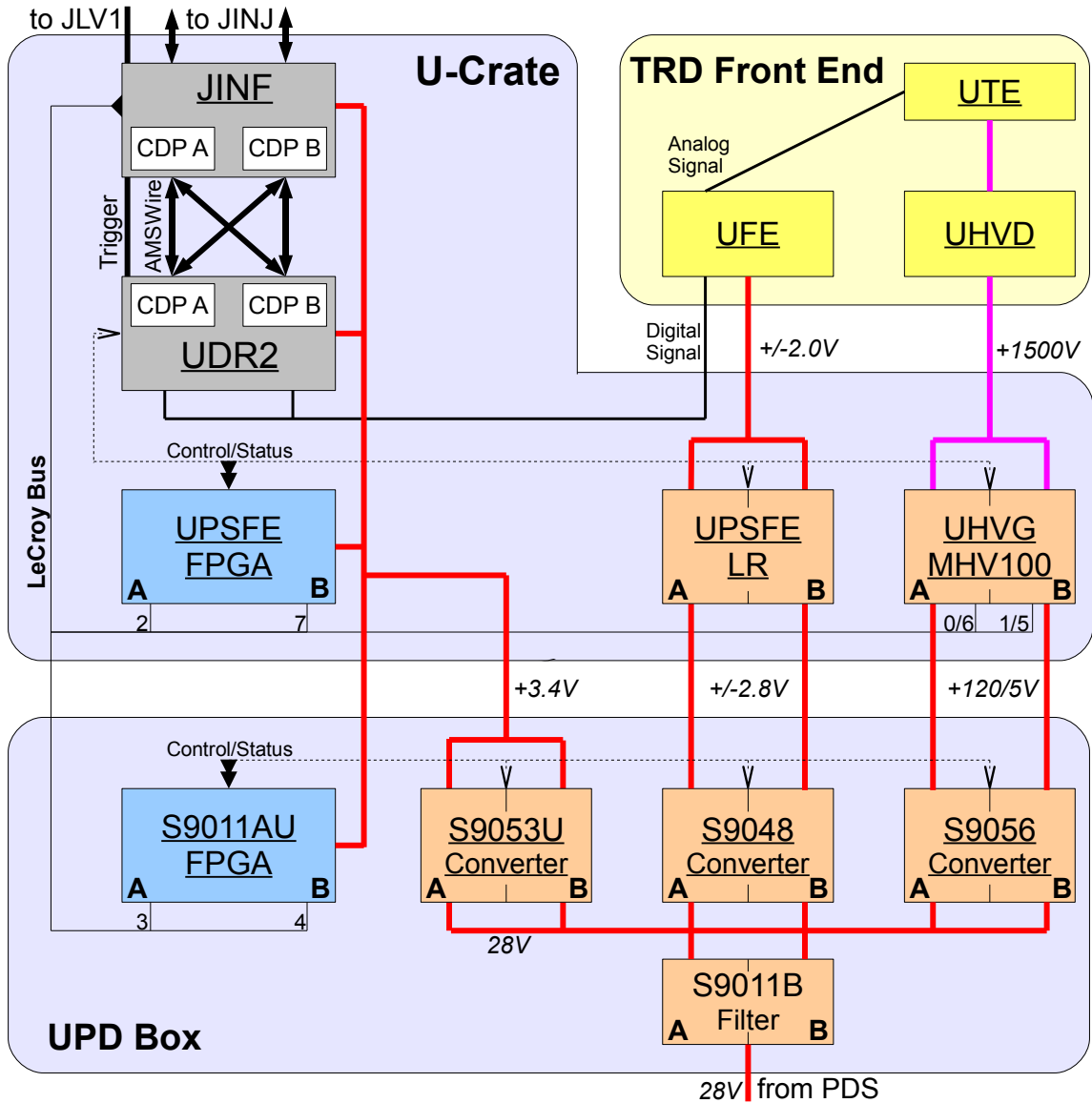


Figure 4.23: TRD readout electronics system at a glance. The system can be divided into the digital electronics on the left and the analog part on the right, which maintains a reliable power supply for operation of the system. The slow control is accomplished by FPGAs, which are addressed via the LeCroy bus. The FPGAs have access to the status and control lines of the connected hardware. The digital data retrieved from the front end is processed by common digital parts (CDP), which operate a DSP. The communication with the higher DAQ systems is established via the AMSWire protocol.

## 4.5 Space Qualification Phase

The AMS-02 experiment not only is a high precision instrument, but also is equipped with electronics of high reliability in order to survive the harsh conditions in space. Therefore intensive electrical and functional tests are carried out on the various levels of production. The parts for the printed circuit board assembly are whenever possible tested before the permanent soldering. After the electronics board production the hardware can be connected to power and the first electrical tests can be performed. Once the boards are tested, production defects are identified and repaired and the full functionality is verified, the crate is assembled. At this point the actual space qualification procedure begins. There are three stages of crate level qualification tests, which are the environmental stress screening (ESS), the electromagnetic compatibility (EMC) and susceptibility test and finally the thermal vacuum test (TVT), which consequently simulates deep space conditions. In all these tests the hardware is tested to the limits of the operational parameters. The AMS-02 qualification test specification is based on the NASA guidelines for payloads [38] and [37].

### 4.5.1 Board Level Test

The board level test mainly is conducted for the purpose to identify production defects. Therefore the boards are powered the first time directly after the production line (PCA<sup>1</sup>). A full test campaign is performed taking advantage of test backplanes designed during the development phase. On this stage a repair or replacement of defective parts still is quite easy because a conformal coating of the boards is not yet done. After the functionality is verified the boards are passed to the conformal coating processing<sup>2</sup> followed by the board level ESS.

<sup>1</sup>printed circuit assembly

<sup>2</sup>The conformal coating makes the surfaces electrically isolating.

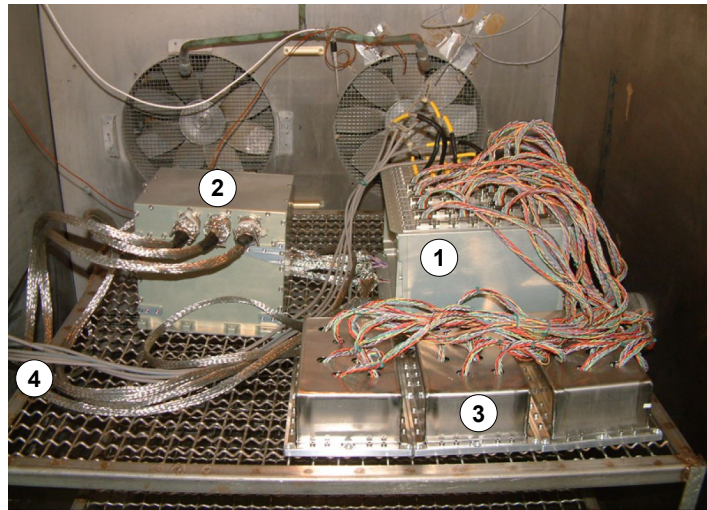


Figure 4.24: *QM2 ESS climatic chamber test setup. The U-Crate (1) and the UPD box (2) are interconnected by qualification model cables. Front end simulator (UFS) boxes (3) are connected to the UDR2 boards of the U-Crate. The chamber wall allows to connect 28V power to the UPD box and AMSWire cables (4) to the JINF board of the U-Crate.*

A climatic chamber cycles hot and cold storage temperatures to spot weak parts or soldering points on the PCB, which then can be identified in the second functional test campaign. All qualification model electronics passed the board level tests after the ESS.

#### 4.5.2 Environmental Stress Screening - Thermal and Vibration Stress

The environmental stress screening (ESS) at crate level is the key barrier, which the electronics has to pass during the qualification phase. It consists of three different phases of testing, namely the thermal cycling, the vibration test and a final thermal cycling. The qualification test was performed at CSIST facilities in Taiwan in August 2005. Although an atmospheric pressure is not what one expects for the operation in space, a strong variation of temperature is expected.

##### Temperature Cycles

The thermal cycling is performed in an air temperature controlled climatic chamber. Strong ventilators guarantee fast transitions between the different temperature levels. To avoid condensing water on the devices under test, the chamber is filled with nitrogen gas. The cold nitrogen gas from liquid nitrogen tanks is also used for the cool down of the chamber. Several feedthrough are present for power and data connections to the U-Crate. Figure 4.24 shows a picture of the ESS setup at CSIST. In order to allow a test of the actual readout front end simulator (UFS) boxes are connected to the UDR2 boards of the U-Crate. Furthermore a realistic load for the UPSFE and the DC/DC converter electronics is simulated. The working principle of the UFS boxes is described in section 4.5.4.

During the thermal cycling the focus is set on two main aspects of the test. Firstly the frequently changing temperature stresses the electronics boards to identify production defects and part failures. Secondly, the operation itself is tested at high and low temperatures, which correspond to possible conditions of operation in space on the ISS and verify the design. Storage and operational extreme temperature phases are defined by the collaboration.

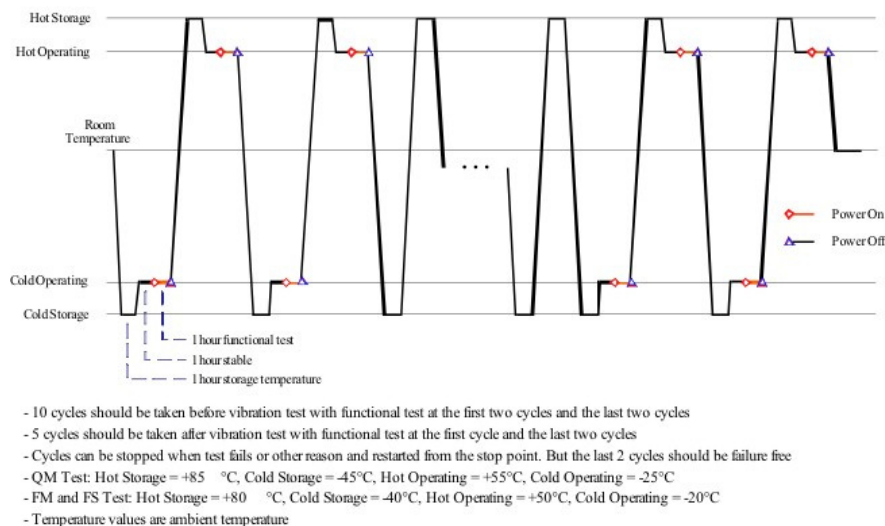


Figure 4.25: ESS thermal profile and test specifications defined by the collaboration.

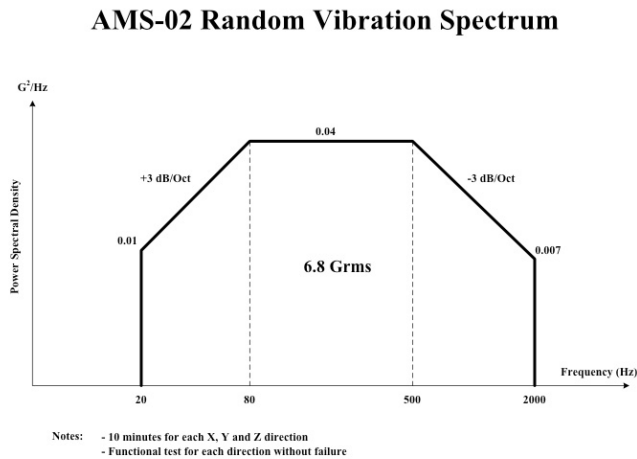


Figure 4.26: *The vibration spectrum of the ESS. Unlike the thermal stress, which will be performed again with the assembled AMS-02 instrument in a space simulator, the vibration test of the parts is the last test of mechanical stresses before the launch in the Space Shuttle.*

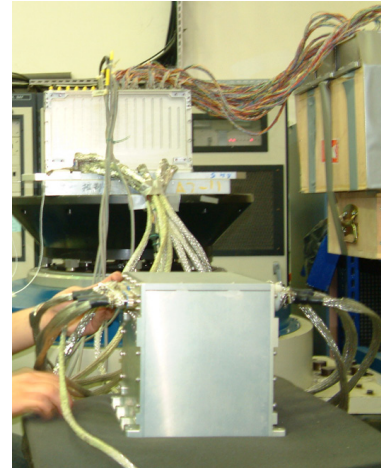


Figure 4.27: *QM2 ESS vibration table test setup. The U-crate is mounted on top of the shaker table to be vibrated in vertical direction. It is powered by the UPD and operated throughout the test.*

Each cycle starts with a cold storage phase, which is maintained for at least one hour to guarantee the temperature homogeneity. During the storage temperature phase the hardware is switched off. After the storage temperature the temperature is set to an operational level. Stabilization of one hour minimum is required followed by the actual test phase at cold operational temperature. The test sums up to about one hour of operation and testing. In the second half of the cycle the hot storage and operational temperature is tested following the same scheme. A one hour hot storage phase is followed by the operational hot temperature phase, which consist of a one hour stabilization and the one hour of operation and testing. The profile for the ESS thermal test is shown in figure 4.25, which is a common profile for all AMS-02 electronics hardware.

Two of these full cycles are performed at the beginning and the end of the first cycling phase. In between six cycles of cold and hot storage transitions are performed with at least one hour stable storage extreme temperatures. During all phases the temperature cycling may be stopped for a more detailed or failure analysis and resumed from this point.

The second cycling phase is performed after the vibration test, which will be described in the next paragraph. Like in the first phase operational tests are performed in the first and the last two cycles. In between storage transitions are conducted. In contrast to the first cycling phase the last two operational tests must be failure free to successfully pass the ESS.

### Vibration Stress

The vibration test simulates the conditions in the payload bay during the Space Shuttle launch. Figure 4.26 specifies the profile for the vibration test of AMS-02 hardware. The mean square acceleration sums up to  $6.8g_{rms}$ . This value is the root of the integral below

the power spectral density plotted in figure 4.26. During the vibration process a spectral analyzer averages and squares the acceleration for each part of the frequency spectrum in units of the earth acceleration  $g$  and divides the value by the resolution in units of  $Hz$ . The random vibration spectrum is maintained for 10 minutes during the qualification test. The test is repeated for each direction X, Y and Z by changing the vibration table or rotating the crate. Figure 4.27 shows a picture of the UPD vibration test.

The hardware is powered continuously during the vibration test. The UPD box and the U-Crate are vibrated after each other, but all time connected and in full operation. The normal operation sequence is chosen such that the redundant hardware is swapped in relatively short time intervals to allow operational testing of both redundant halves during the test. Status registers are read and verified in between the redundancy swapping and the initialization and test of the readout. Front end simulator boxes were also connected during the vibration test.

### 4.5.3 Electromagnetic Compatibility Test

A test campaign is conducted for all subsystems of AMS-02, which verifies the compliance of the system with the requirements for the operation of equipment on the ISS. The electromagnetic compatibility (EMC) test can be divided into two test objectives, which both aim to avoid electromagnetic interference (EMI) during an operation of the devices. The electromagnetic emission test covers all measurements, which evaluate the radiated power in the environment of the device as a source. Furthermore the conducted emissions through the power leads from the device are tested. The electromagnetic susceptibility test in contrast consists of a bunch of scenarios, which the device under test might be exposed to during the operation on the ISS. The immision is conducted through the power leads and radiated from antennas around the device. The correct operation under these conditions is verified. Both emission and susceptibility tests are performed according to the requirements for electronic equipment being used on the International Space Station as documented in [33].

For the conducted susceptibility test sinusoidal electromagnetic energy is injected into the power input leads of the UPD in a frequency range from 30Hz to 50MHz with a power of up to  $2.8V_{rms}$  at a low frequency (CS01 and CS02). Spikes are injected for a short duration of  $10\mu s$  and  $0.15\mu s$  with twice the nominal supply voltage of 28V (CS06). In the same frequency range the conducted emission is measured in the normal operation mode of the system (CE01 and CE03). The mode switching conducted emission should not exceed 50% of the nominal line voltage (CE07), which is especially important for AM-02 PDS hardware. The radiated field is measured in a wide frequency range from 14kHz to 15GHz, in which the limits defined by NASA must strictly be maintained (RE02). During the radiated susceptibility test a magnetic field is induced created by the same spike generator used for CS06 test to the system. Therefore a conducting wire is wrapped around the crate as closely as possible and spikes of twice the nominal voltage are generated (RS02). The correct operation has to be verified throughout the radiated susceptibility test in the frequency range from 14kHz to 15GHz, although the field strength is adjusted in frequencies of particular importance to much higher fields (RS03). These are for instance the uplink frequency band to the ISS.

The first test has been conducted with the qualification model of the U-Crate and the UPD Box at CSIST facilities in Taiwan in August 2005. Both are set up in a laboratory with a dedicated electromagnetically shielded chamber with energy absorbing walls to avoid the reflection of radiation during the test. Figure 4.28 shows an overview table of all tests per-

Test	Description	Result CSIST (Aug. 2005)	Result Terni (Sep. 2006)
<i>Conducted Emission</i>			
CE01	emission to power leads	passed	-
CE03		passed	-
CE07	emission to power leads during mode switching	passed	-
<i>Conducted Susceptibility</i>			
CS01	sinusoidal disturbances to power leads, 1.0 to 2.8 Vrms	passed	-
CS02		passed	-
CS06	spike injection of twice nominal supply voltage	passed	-
<i>Radiated Emission</i>			
RE02	field emission	passed	passed
<i>Radiated Susceptibility</i>			
RS02	spike immision	passed	-
RS03	field immision	passed with cable shielding; <i>not passed without shielding due to problems on Lecroy bus</i>	passed

Figure 4.28: Summary of the EMC verification test results. Two test campaigns were performed. The first test at CSIST in Taiwan revealed, that the system had to be modified in order to be able to pass the final test at University of Perugia in Terni.

formed and the test results. The first part of the test was passed at CSIST facilities. However the radiated susceptibility of sinusoidal radiation RS03 and the radiation emission during operation RE02 were repeated after a hardware modification at Terni facilities in Italy, which became necessary due to the problems revealed in the same test at CSIST. In the following a brief result summary is given.

### Results of the EMC test at CSIST

For the preparation of the EMC test at CSIST a metal shielding was applied to all cables between the UPD and U-Crate electronics as shown in figure 4.29. The UPD box and the U-Crate were mounted on a radiator simulation plate in order to provide a realistic grounding. The test procedure in this configuration with applied armor shielding confirmed, that the system meets all requirements for the operation on the ISS. Nevertheless without the shielding on the cables the operation of the system is strongly influenced at frequencies between 200 and 400 MHz during the RS03 susceptibility test. The LeCroy communication between the U-Crate and the S9011AU controller inside the UPD box was impossible. With unshielded cables the emission stayed below the limits, but clearly showed peaks in the few hundred MHz range. The exact reason for the non-conformance was left unspecified at this time. A further analysis was done outside the chamber. Because of the limitation on the weight a shielding as applied during these test is not applicable for the flight model. A solution had to be found to be able to pass the EMC tests without an additional shielding on the cables.

### Result of the EMC test in Terni

In the second step of the EMI/EMC test at University of Perugia in October 2006 the RS03 and RE02 tests were repeated without a shielding of the interconnecting cables. Furthermore weak points in the U-electronics hardware were identified and minor corrective hardware modifications were applied before test.

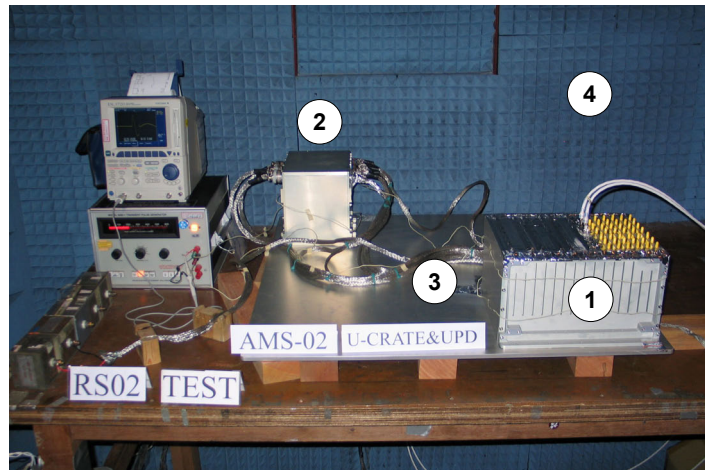


Figure 4.29: The EMC test setup at CSIST facilities. The U-Crate (1) and the UPD box (2) are interconnected by cables shielded with a metal mesh (3). An aluminum plate simulates the radiator, on which the crates will be mounted in AMS-02. The EMC test chamber is equipped with walls absorbing the electromagnetic radiation (4).

The following listed hardware modifications were done after the EMI/EMC test in Taiwan:

- New Actel FPGA firmware on UPSFE and S9011AU boards including oversampling functionality is used to be able to correct noise on the signal lines.
- The routing of the 3.4V power supply lines to the S9011AU board were changed in order to avoid grounding loops. Instead of a direct connection from the converter inside the UPD box the 3.4V power is supplied via the U-Crate backplane.
- The grounding scheme was modified to reduced the number of digital ground to shield connections. After the modification single point connection are only present on the UPSFE boards and on the UBP.
- The cable shielding on the power and signal cables was removed completely.

All listed changes became flight configuration.

The U-Crate and the UPD box again were mounted to the Aluminum radiator simulation plate of 0.9m x 0.9m to provide a realistic grounding. The plate was grounded on a single-point to the copper table of the chamber. The mounting position on the plate corresponds to the flight position relative to each other. An electrically and thermally conductive sheet of KeraTherm<sup>1</sup> was applied between the U-Crate, the UPD box and the radiator simulation plate, which replaces the Cho-Therm used for the final installation in AMS-02, but is less expensive.

Two cables for the AMSWire communication of flight-quality were available to connect the system to the outside of the chamber. For all tests the system first is set to the normal operation mode and operated in these conditions during the test. The operating procedures

<sup>1</sup>by KERAFOL company, Germany. KERATHERM heat-conducting films are characterized by their high thermal conductivity and their electrical insulation.

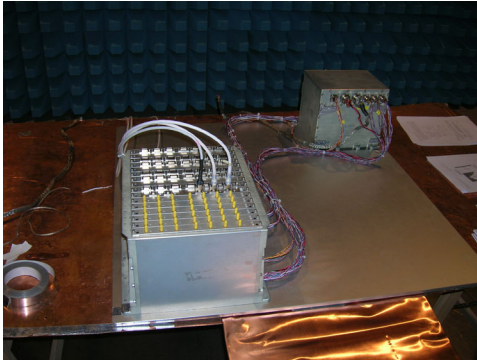


Figure 4.30: *The EMC test setup at Terni facilities. The UPD box and the U-Crate were mounted to an Aluminum plate to ensure a realistic grounding. With the applied modifications of the hardware the test was passed successfully.*

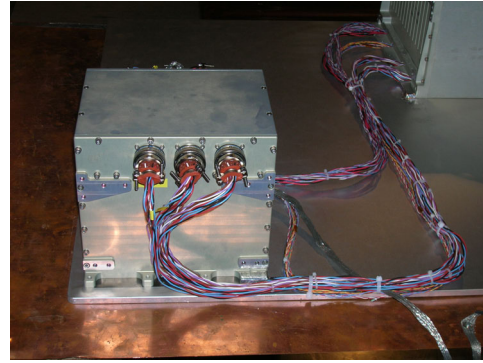


Figure 4.31: *EMC test cable preparation. The cables interconnecting the U-Crate and the UPD box are not shielded in contrast to first test in Taiwan.*

of the U-Crate include the readout of slow control registers via the LeCroy bus and the readout of science data via the AMSWire links. A special procedure was developed to focus on the test of the LeCroy bus communication accessing continuously all buses more often than in the previous tests in Taiwan. Any abnormal behavior is reported by the test software immediately.

All cables stayed unshielded during this test. Figures 4.30 and 4.31 show pictures of the U-Crate and the UPD box mounted on the radiator simulation plate. The power and LeCroy bus cables are bundled flight-like on the surface of the plate.

No errors of the communication on the LeCroy bus were observed. The slow control of the system was operational in all frequencies of radiation. However infrequent errors of the AMSWire communication were found at a frequency of 250Mhz and 300Mhz at 60V/m field strength radiated into the U-Crate during the operation. This is not a critical failure, since in the case of a failed transmission the command can be resend and the control can be recovered. Further investigation showed, that this problem is avoidable up to radiated fields of 200V/m by shielding the JINF front panels. This can be achieved by an aluminum tape. The test was passed since in any case the AMSWire communication is recoverable even in the case of failed transmission.

Figures 4.32 and 4.33 show the test setup and the recorded spectrum in the afore mentioned range of the radiated emission. Even though the limit given by the NASA specification is touched it is not exceeded. The emitted radiation test was passed in all frequency ranges. With end of this test campaign it is verified, that the operation on board of the ISS is possible within specifications.

Of course, on subsystem level only small parts of the AMS-02 instrument can be tested. An EMC test of the entire AMS-02 instrument is scheduled directly after the assembly of the detector at ESTEC<sup>1</sup> facilities in 2009.

<sup>1</sup>European Space Research and Technology Center



Figure 4.32: *Emitted electromagnetic radiation test. The antenna records the emitted radiation during the operation of the U-Crate.*

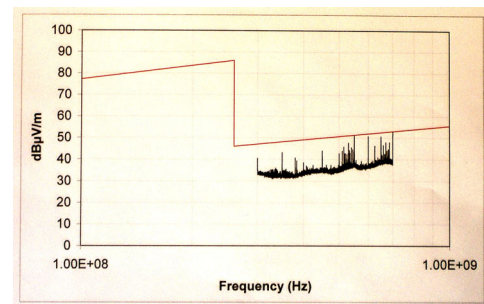


Figure 4.33: *The emitted spectrum during the operation of the U-Crate. Clearly visible are the peaks, which touch the limit of allowed radiation at a few hundred MHz.*

#### 4.5.4 Thermal-Vacuum Test

The thermal-vacuum test (TVT) is the closing test of the qualification tests with the qualification model of the electronics and represents the best simulation of deep space conditions the components of AMS-02 will face on board of the International Space Station. The temperature cycles are performed similarly to the ESS temperature profile, but unlike to the ESS conditions, the test is performed in a vacuum. The devices under test are placed in a vacuum chamber, which is air evacuated at the beginning of the test. In contrast to the ESS the temperature condition cannot be changed by control of the air temperature inside the chamber,

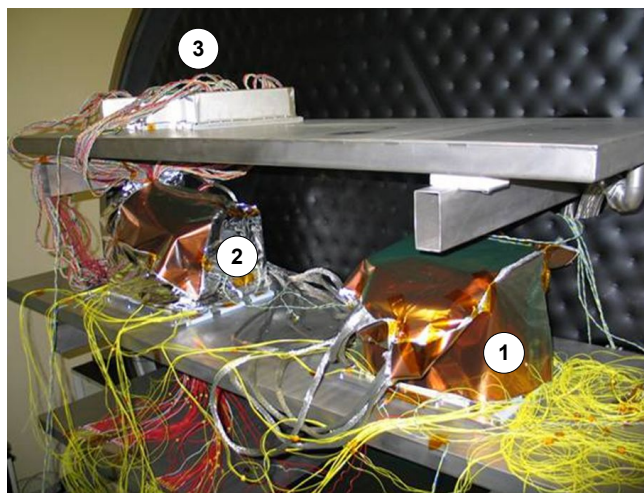


Figure 4.34: *TVT setup at the Terni vacuum chamber. The UPD box (1) and the U-Crate (2) are covered by multi-layer insulation (MLI), which will be applied to subsystems in AMS-02 during the operation on the ISS. Front end simulators (3) are connected in order to simulate a realistic load for the power supply electronics.*

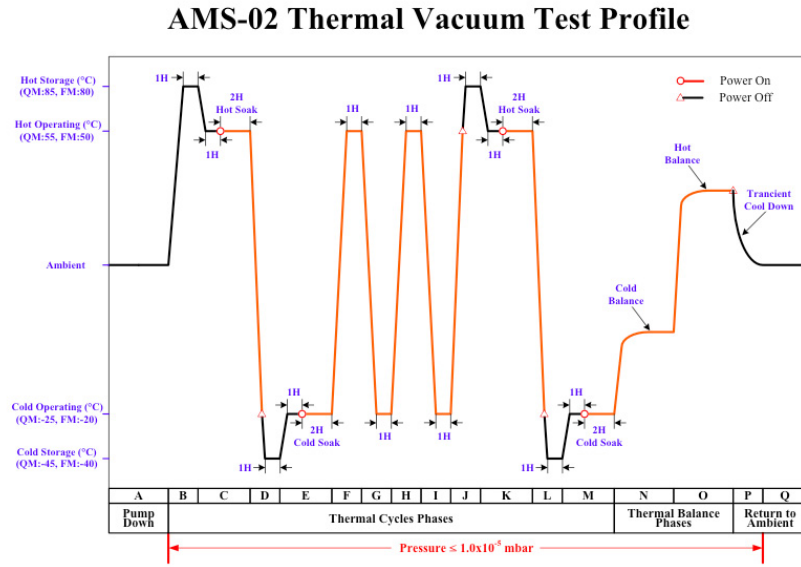


Figure 4.35: *TVT temperature cycle profile. In the beginning and the end of the test hot and cold storage temperatures are reached. During all other temperatures the electronics stays powered and is operated continuously in a test sequence.*

rather the temperature of the devices under test is varied. The crates are mounted to a cold plate, which is thermally isolated from the chamber walls. A cooling system allows to control its temperature from cold to hot extremes. To ensure a thermal contact between the crate and the cold plate a heat conductive foil is placed between them. A shroud, which is varied in temperature in parallel surrounding the chamber avoids emission of thermal radiation from the chamber walls. Figure 4.34 shows a picture of the mounted U-Crate and UPD box inside the chamber. The crate and the box are covered by multi-layer insulation (MLI) to avoid radiative dissipation of heat into the chamber. During the flight the MLI is applied to protect the AMS-02 instrument from the strong variations of the ambient temperature in space.

Figure 4.35 illustrates the common temperature profile applicable for the TVT of AMS-02 hardware defined by the collaboration. Like for the ESS four temperature levels are defined, which correspond to the conditions for hot and cold storage as well as temperatures between the hot and cold operational temperatures. In the beginning and the end functional tests are performed in hot and cold soak phases, which follow the storage temperature extremes. In these conditions it is ensured, that the adjusted temperature is found throughout the hardware under test. During all other phases the system stays in normal operation mode and the cold plate is adjusted such that the targeted temperature is measured on the crate walls. Due to the dissipated power by the electronics the temperature inside the crate might be higher during the operational phases, which consist of two cycles between hot and cold operational temperatures. The maximum and minimum levels have to be maintained for at least one hour. Another special environment condition during these cycles is the continued operation during a fast transition between hot and cold temperature, which means mechanical stress to the system. At the end again a cycle of hot and cold storage and soak phase is conducted.

Optionally a thermal balance phase may be performed in order to verify thermal models of the system, but it is not required for the U-Crate. All functional tests have to be performed without failure in order to pass the TVT.

The thermal-vacuum test has been performed with a complete set of qualification model U-Crate and UPD box accordance with the AMS-02 hardware test requirements in 2006. The test has been performed at SERMS<sup>1</sup> facilities in Terni in Italy.

The TRD front end simulator (UFS) boxes were placed inside the chamber to dissipate front end equivalent power and to simulate the functionality of the front end electronics. The U-Crate was connected to the outside of the chamber via two AMSWire cables and one additional trigger link. During the operational phases a test script, which ran on a computer outside the chamber, simulated the normal operation of the TRD electronics including slow control and data acquisition with the front end simulators. Additional scripts were available, which perform extensive functional tests for each kind of board.

Additional tests of the UDR2 boards have been performed to verify problems discovered during the ESS. Specific test with the front end simulator was done to check the timing of the serial ADC. A DAC level was set and the digitized value was read back from the front end simulator. This test had been performed during the ESS already. A problem had been found at a temperature of  $-25^{\circ}\text{C}$  with short cable lengths to the UFS boxes. For the TVT extended cables were used according to flight range of the cable length between the TRD front end boards and the U-Crate. The problem was not observed again and could be reproduced on cables, which were kept at the original short length. The thermal-vacuum test was passed without any further problems or failures of the system.

### TRD Front End Simulator UFS

The final test for the readout electronics is the thermal-vacuum test, which simulates temperature variations expected in space in an air evacuated climatic chamber. An important aspect of the test is the heat dissipation of the components, which solely has to happen through the walls of the crate, which is mounted to the chamber's cold plate. In order to ensure a realistic test environment for the test of the electronics a front end simulating device was designed and built. During the ESS and TVT it is, for obvious reasons, not possible to attach the real detector front end to the electronics under test. A cost efficient replacement has to commit two goals, which are the capability to test the power supply electronics and the digital readout electronics at the same time.

The development of the UFS took into account similar specification as the actual TRD electronics. It has to comply with the demands for an operation in a thermal-vacuum chamber, which means it has to be volume saving and to be able to conduct the dissipated power by a ground plate to the chamber. Furthermore the front end simulator has to operate reliably, since the results are used to evaluate the functionality of the U-Crate under test.

The UFS box can be divided into two main assembly groups, which are the mechanics with the mounted load resistors to dissipate power from the UPSFE boards and the UFS PCB with the IC parts and the soldered cables to the UDR2 boards. Figure 4.36 shows a picture of both parts.

Main consideration during the UFS development was to find a way to simulate the data acquisition with the UDR2 boards. It is implemented by taking profit of the on-board DAC

---

<sup>1</sup>Studio degli Effetti delle Radiazioni sui Materiali Speciali (SERMS), Terni, Italy

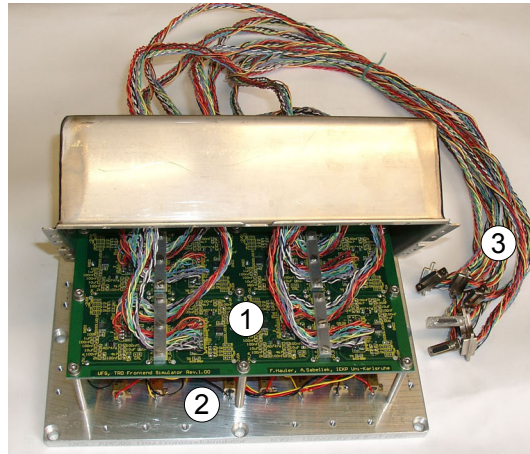


Figure 4.36: *UFS front end simulator box. The UFS box substitutes seven UFE power groups. For the readout simulation ADCs are mounted on the PCB (1), which allow to feed back the configurable DAC signal from the UDR2 board. Load resistors mounted to the ground plate (2) simulate a realistic load for the power supply electronics under test. The UDR2 boards of the U-Crate are connected by 21-wire cables (3) soldered to the UFS PCB.*

of the UDR2 boards. The voltage set by the DAC of the UDR2 is digitized again by the ADC of the UFS. This signal then is sent back to the UDR2 and can be processed as a real signal from the front end. Several test points are present on the UFS PCB allowing a measurement of currents and the feed in of an external signal to the ADC. Figure 4.37 schematically illustrates the functionality of a UFS power group.

The UFS load resistors are tuned according to the UFE board specifications. One of the

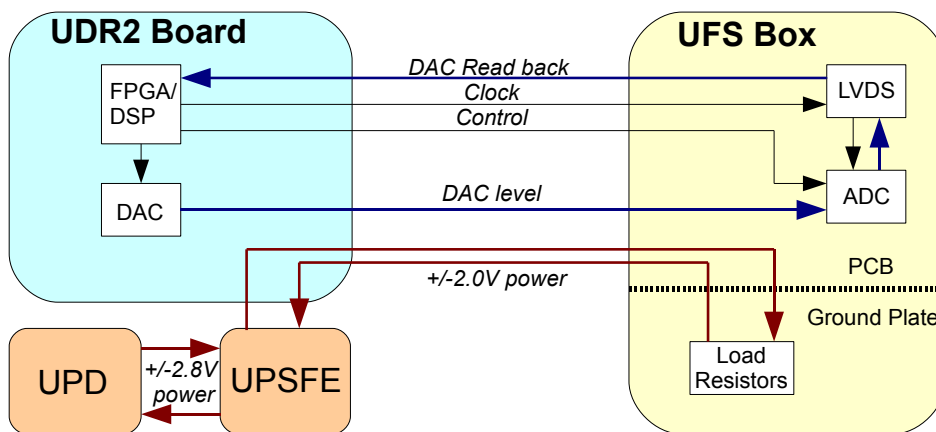


Figure 4.37: *Scheme of the Front End Simulator (UFS). The UFS box is built for twofold purpose. Load resistors mounted to a solid aluminum ground plate dissipate the UFE equivalent power supplied by the UPSFE and UPD electronics. In order to test the digital readout by the UDR2 board the DAC level set by the UDR2 is digitized by an ADC and can be read back.*

1 UFE				2 UFE			
	$I_{\text{spec}}[mA]$	$R_{\text{load}}[\Omega]$	$I_{\text{end}}[mA]$		$I_{\text{spec}}[mA]$	$R_{\text{load}}[\Omega]$	$I_{\text{end}}[mA]$
+2V	47	54 (27+27)	48.0	+2V	94	22.9 (27  150)	98.4
-2V	82.6	27	85.1	-2V	165.2	12.7 (10+2.7)	168.5

Table 4.3: Load resistors of the UFS in  $\pm 2V$  lines for 1 and 2 UFE equivalent power groups. A current of  $I_D = 11mA$  for the UFS digital part has to be added to the total current  $I_{\text{end}} = I_R + I_D$ .

two connectors of a power group are connected to one simulator group. Power lines from the UDR2 connector are distributed by the UFS PCB to the load resistors, which are mounted on the solid ground plate to allow direct dissipation of the power to the attached cold plate of the test facility. Table 4.3 shows the load resistors and the corresponding power consumption on the input lines. The total power consumption of all three UFS boxes can be calculated to

$$P_{\text{tot}} = (1888mA \cdot 3) \cdot 2V = 11.3W \quad (4.1)$$

of dissipated power. The power consumption has been chosen to be about 20% higher than specified for the UFE board in order to allow a safety margin during the tests. Although the UFS was built for use during the TVT, it has been utilized in both QM2 and FM/FS ESS and TVT.

#### 4.5.5 Summary of the Qualification Test Results

The test procedure for the qualification phase of the TRD (U) readout electronics as part of the AMS-02 electronics equipment has been performed and successfully passed in 2005 and 2006. During the ESS at CSIST facilities only minor hardware problems showed up. One UHVG board had to be repaired after a part failure of an oscillator crystal on one out of 14 channels of this board. Other noticeable observations were evaluated as not a problem.

The EMI/EMC test at CSIST revealed a failure of the system control during the radiated susceptibility test RS03 in the case no additional shielding on the cables between the U-Crate and the UPD box is applied. With the proper shielding all tests were passed. A second EMI/EMC test in Terni was performed with modifications to the grounding scheme of the system and a new firmware of the S9011AU FPGA. Main modification is a 3.4V power supply of the S9011AU controller board via the U-Crate backplane instead of a direct connection from the S9053U DC/DC converter. All tests were successfully passed without an additional shielding during the EMC test at Terni facilities.

A TVT was performed at SERMS in Terni without any problems during the operational phases of the system. All tests were passed without a problem.

## 4.6 The Prototype Cosmics Test in Karlsruhe

Space qualification of the electronics means, that a failure-free operation without restrictions under the special conditions in space is guaranteed. This is of importance not only because no maintenance or repair is possible once the detector is in space, but also because of the

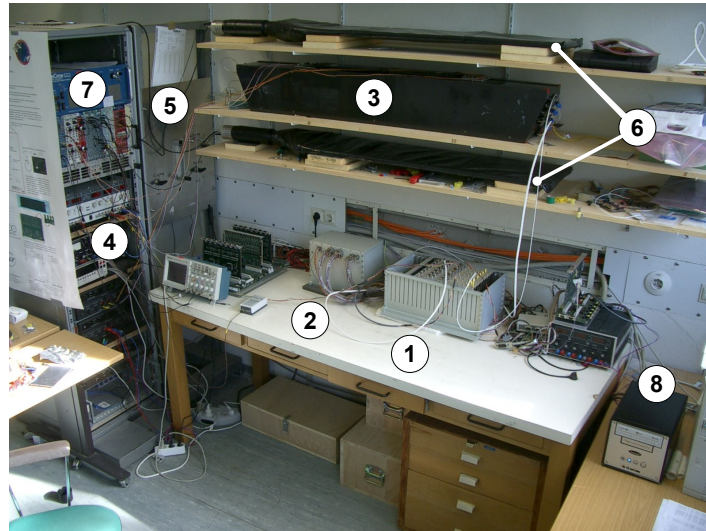


Figure 4.38: Setup of the Karlsruhe cosmics test stand. The qualification model of the U-Crate (1) and the UPD box (2) read out a TRD chamber (3), which is supplied by a ground support gas system (5). The entire DAQ system is powered by a 28V commercial power supply (4). The trigger is generated by NIM-logics modules (7) by coincidence of scintillator modules (6) placed on top and on bottom of the chamber. A DAQ computer (8) reads out and controls the U-Crate via the AMSWire protocol.

immense costs of such an experiment, which makes any kind of failure during the operation period of three years unacceptable.

A permanent source of particles, which allows a long-term functional test of the detector are cosmic muons. This is not so far off, since the TRD is designed to measure cosmic rays anyway. This chapter describes the setup of a TRD long-term test stand for a prototype chamber and the qualification model electronics at the IEKP in Karlsruhe.

### Cosmics Test Stand Setup

For testing and qualification purposes the QM2 electronics of the TRD readout consist of a fully equipped UPD box and a U-Crate including a flight-like cabling. A TRD front end board (UFE) is attached to the qualification model of a detector chamber, which was used for the qualification testing of the detector front end. The chamber is build of four layers of 16 straw tubes each. With this setup a normal data acquisition is possible as described in chapter 6. The only constraint is, that transition radiation is not produced, since muons are not sufficient energetic and a radiator fleece is not applied between the straw tube layers. Peripheral components such as the trigger system, gas supply and temperature control are replaced by ground support equipment. The cosmics test stand is shown in figure 4.38. The system is controlled by a computer with a Linux operating system.

A crossing particle triggers a signal in the test stand, which originates from the interaction with scintillator panels surrounding the detector module. This signal is analyzed by a NIM<sup>1</sup> logics module and is forwarded to the trigger input of the U-Crate in the case of a coincidence

<sup>1</sup>Nuclear Instrument Module

of the upper and lower scintillator layers. The UPD box is supplied by a 28V DC voltage as provided by the AMS-02 PDS and supplies the required voltages to the U-Crate. A custom made software controls the ground support equipment and the TRD readout system itself. The Diethorn formula allows to correct data sets taken at different environmental conditions to normal conditions and finally a common analysis of different datasets. The signal in ADC units in normal conditions is

$$ADC_{corr} = ADC \frac{G_0(V)}{G(T, p, V)} \quad , \quad (4.2)$$

with the gas gain  $G_0$  at  $T_0 = 20^\circ C$  and  $p = 1013 \text{ mbar}$  for the corresponding voltage.

### Voltage Dependence of the Gas Gain

A dependence of the signal amplitude from the high voltage, which is applied to the proportional chambers, is expected according to formula 3.25. The higher the voltage, the bigger the volume, in which electrons are accelerated to energies that allow further ionization, and with it the stronger the amplification in the avalanche near the anode wire. The ADC value read by the electronics is bigger by the same factor as the gas gain  $G(V)$ , since it is linear with the collected charge. Figure 4.39 shows the calculated dependence of the gas gain according to the Diethorn formula at normal conditions.

An actual measurement of the voltage dependence of the signal is shown, too. Therefore the most probable value (MPV) obtained from a fit of the Landau function to the recorded amplitudes is plotted. The MPVs are corrected to normal environment conditions according to equation 4.2, since the data was taken on several days with natural variation of the parameters. The error is estimated from the statistical error of the Landau fit and the error of the temperature and pressure measurements. The significantly lower variation of values after the applied correction is visible. A clear correlation according to the Diethorn formula at given gas gain can be recognized, which shows, that methods of analysis are applicable and a normal operation of the chamber and the readout electronics is possible at the cosmics test stand.

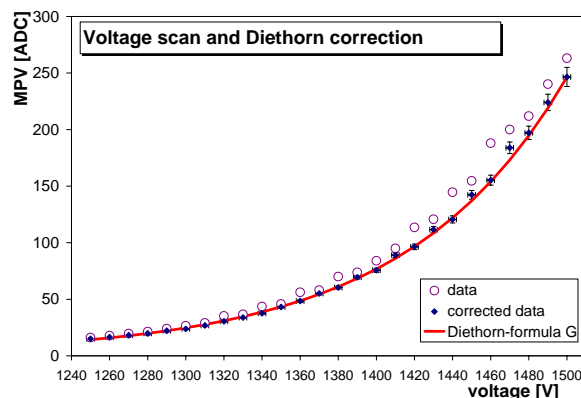


Figure 4.39: TRD signal from cosmics as a function of the voltage. The data is equalized to normal conditions according to the Diethorn formula.

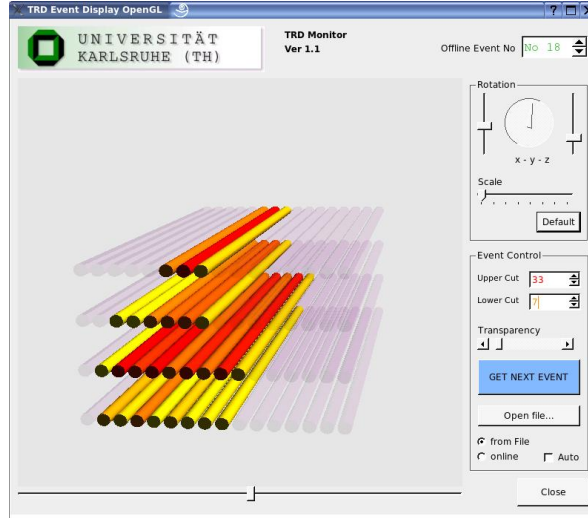
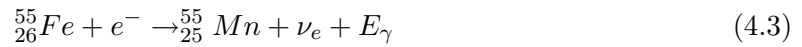


Figure 4.40: A snapshot of the event monitor with  $^{55}\text{Fe}$  radioactive source. The opening angle of the source is visible in the adapted version of the monitor averaging the amplitudes over time.

### Energy Calibration with a $^{55}\text{Fe}$ Radioactive Source

The operation of the TRD proportional counter tubes is based on the fact, that electrons are released in the detector gas by a certain amount of energy deposition, which are amplified by the factor of  $G$  according to equation 3.25. An ADC value read out by the front end electronics corresponds exactly to the amount of collected charge inside the coupling capacity of a tube. The factor between the ADC value and the ionizing energy can be determined by a calibration with a source of radiation of known energy. A convenient emitter is a  $^{55}\text{Fe}$  source. A source of this kind was also planned to be present as part of the TRD gas system allowing a continuous monitoring of the gas parameters, but was discarded during production phase. The  $^{55}\text{Fe}$  source predominantly emits x-rays of the energy  $5.9\text{ keV}$ , which are emitted when the captured electron of the K-Shell in the process



is replaced in the Manganese nucleus<sup>1</sup>. Unlike charged particles photons deposit their total energy in the point of their absorption. Hence a signal in the straw tubes is evoked by the given energy and a corresponding number of electrons. As a consequence exactly the same number of electrons is collected on the readout capacitor amplified by  $G$ . A readout in the maximum of the integration time then would give a clear peak around an ADC value, which would correspond to an energy deposition of exactly  $5.9\text{ keV}$  in the detector volume.

This approach is not applicable here, since the readout electronics would have to be self triggering in order to read in the correct moment. The U-Crate electronics is dependent on an external trigger signal, which cannot exist for x-ray photons.

<sup>1</sup>Instead of K-shell less likely electron capture may also happen from the L-shell of the nucleus. During replacement of lower shells, with 24% the emission of the  $5.899$  and  $5.88\text{ keV}$  ( $K_{\alpha 1,2}$ ) lines is more frequent than energies of equal range. Photons with  $6.49\text{ keV}$  ( $K_{\beta}$ ) are emitted with only 2.9%.

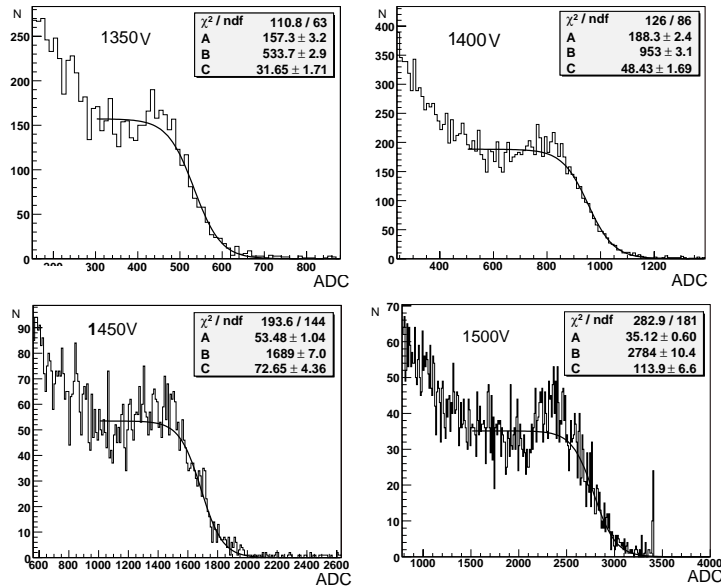


Figure 4.41: Histogram of tube hits with a  $^{55}\text{Fe}$  gamma source. Due to the uncorrelated readout the tube is read out in the maximum of the collected charge by incident only. The Gaussian becomes a Fermi-like distribution. Nevertheless the maximum value is fixed by the energy of the  $^{55}\text{Fe}$  photons at a given high voltage and can be extracted for an energy calibration.

The solution here is a periodic, but uncorrelated triggering of the readout of the channels. To reach a high data readout rate advantage is taken of the data compression routine of the UDR2 boards. Figure 4.40 shows a snapshot of the event display of the test stand with the mean energy deposition averaged over several periods of data acquisition. One can directly identify the angle of the radiation spread from the source on the top straw tube module in the four layers of the TRD module. Figure 4.6 indicates what can be expected in an early or late readout, because either not all of the collected charge is gathered on the readout capacitor, or the collected charge on this capacitor is already decreasing. So the expected distribution of ADC values in a tube underneath the source is a spectrum up to a maximum value, since a incidental readout exactly in the maximum of the capacitor charge is also possible. By approximation the Gaussian distribution spectrum of the energy deposition becomes a Fermi decline at the ADC value, which corresponds to the energy deposition of  $5.9\text{keV}$ . Figure 4.41 shows histograms with increasing position of the Fermi decline for different voltages.

The Fermi function

$$f(x) = \frac{A}{e^{(x-B)/C} + 1} \quad (4.4)$$

can be fitted to this edge. A correlation must be found between the turning point B and the width C of the Fermi function and the maximum of the Gaussian distribution centered on the actual value. A simple estimation is given by the position of the Fermi function, which corresponds to 90% of the maximum value. Actually the shape of the UFE integration time in figure 4.6 has to be taken into account, which makes the readout at the maximum charge

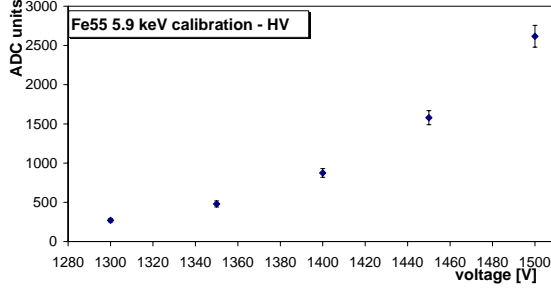


Figure 4.42: *Extracted signal amplitude for the  $^{55}\text{Fe}$  source in ADC units. The amplitude is a function of the high voltage according to the Diethorn formula.*

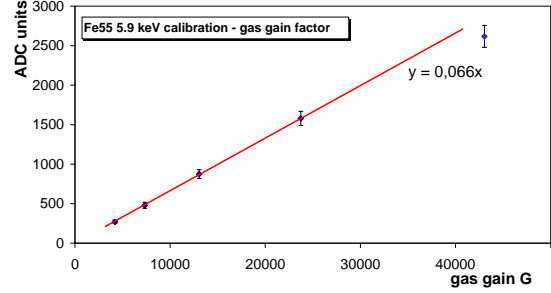


Figure 4.43: *Signal amplitude as a function of the gas gain. The gas gain is adjusted by the applied high voltage.*

more likely. The much more complex calculation of this convolution is skipped here, since only the principle of the calibration should be demonstrated. Do the maximum of the Gaussian energy deposition is

$$ADC_{Gauss} \approx B - 2.2C \quad . \quad (4.5)$$

Values obtained from this fit to the data are shown in figure 4.42 as a function of the applied voltage. An error estimate can be given from the statistical error and as an additional factor the electronic behavior of the UFE electronics. Here also the undershoot after two consecutive energy depositions in the tube has to be considered, which is unlikely with the weak source used, but not excluded. In addition to the error of the fit of the Fermi edge B a maximum error of  $\pm C$  is estimated.

Final goal of this calibration is to determine the ADC value, which is read out at a certain gas gain factor G after a defined energy deposition in the tube. Therefore the ADC values from equation 4.5 are plotted against the gas gain in figure 4.43. The linear fit gives a value of

$$ADC(E, G) = 0.066 \times G \times \frac{E}{5.9 \text{ keV}} \quad (4.6)$$

for an arbitrary energy deposition and a known gas gain in the straw tube. The data point of the highest voltage is left out because of the non-linearity of the electronic gain above 3000 ADC units.

A different plot can be seen in figure 4.44, which shows values normalized to the gas gain and energy deposition for different voltages. Extracted from the data one gets the calibration factor KF of

$$KF = 11.2 \pm 0.3 \text{ ADC/MeV} \quad , \quad (4.7)$$

which describes the signal height of a channel at an energy deposition in MeV.

As a conclusion of the previous results it is possible to correlate an energy deposition to a certain ADC value read out by the front end electronics. Figure 4.45 demonstrates the results from the conversion of the MPV in ADC to the energy deposition in the cosmic ray measurement in the cosmic test stand. The Diethorn-corrected data is taken from the voltage scan previously shown in figure 4.39. Independently of the applied voltage, which means

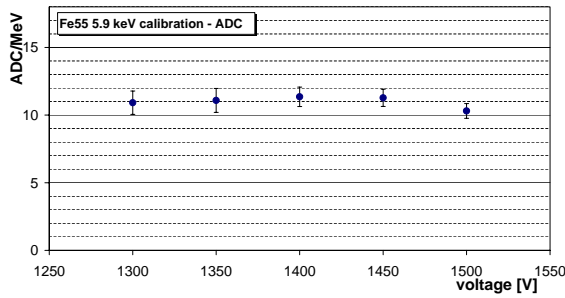


Figure 4.44: *Voltage dependence of the calibration factor. The calibration factor  $KF$  should be independent of the gas gain, which is perfectly confirmed within the errors.*

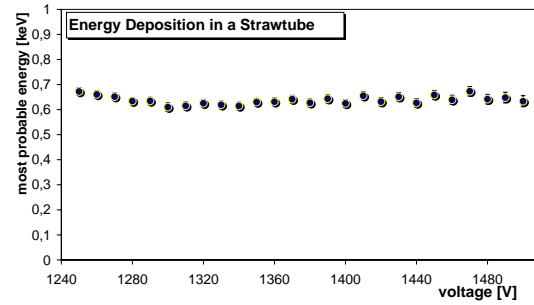


Figure 4.45: *Energy deposition of cosmic rays. The deposition is 0.63 keV in a tube averaged from measurements with different applied high voltage. The independence of the voltage is clearly visible and demonstrates, that the corrections are applied correctly.*

from the gas gain, the most probable energy deposition  $\Delta E_{MPV}$  of a Landau distribution in consideration of the calibration factor  $KF$  is calculated to

$$\Delta E_{MPV} = ADC_{MPV}/G/KF = 0.63 \pm 0.02 \text{ keV} \quad . \quad (4.8)$$

In a simple approximation of the energy deposition  $\frac{dE}{dx}$  of cosmic muons in the gas of a straw tube the volume of the tube  $\pi(3mm)^2 \cdot l$  can be approximated by a layer of the thickness  $d \approx 0.47cm$  of an equal volume. With the energy deposition of  $\Delta E^W \approx 1.2keV/cm$  for Argon gas [28] the most probable energy deposition should be  $\Delta E_{MPV} \approx 0.57keV$  for a minimal ionizing particle. The slightly higher value of the measured energy deposition can be explained by the fact, that not only MIPs hit the detector.

With this result it is shown, that the operation of the TRD module in the cosmics test stand is understood and that the readout electronics has proven full functionality on qualification level. The cosmics test stand was used for the development of the data processing routines of the data reduction board inside the U-crate and to verify its error-free operation under realistic conditions.



## Chapter 5

# Electronics Flight Assembly and Acceptance Test

*In chronological order this chapter describes the consecutive stages of assembly and quality assurance of the flight hardware of the TRD readout system. The final step, at least of what concerns the hardware development, certainly is the installation to the radiator jigs at the AMS-02 assembly site at CERN. The first detector readout started in the course of an AMS-02 cosmics test with the flight hardware in December 2007. A complete documentation of the flight assembly and test procedures is given in the acceptance data package (ADP), which is compiled for each part of AMS-02 instrument according to NASA safety directives. For details beyond the discussion in this chapter the reader is referred to [41].*

*After the production of the electronic boards tests at crate level described in the first section were performed to identify production defects at a level where repairs still are quite effortless. Nevertheless the actual acceptance test procedure presented afterwards could be performed only after the assembly of the U-Crate and the UPD box, which allowed a full operation and functional test of the system.*

### 5.1 The Board Level Acceptance Test

The acceptance testing of the readout electronics systems begins with the assembly and test of the constituent electronic boards. The go-ahead for the production was given in the beginning of 2006 after the qualification model thermal-vacuum test had been passed. So DC/DC converter boards for the UPD box were in hand in March 2006. All further boards were assembled until early 2007 and functional tests could be performed. In the following the test setups and test procedures are described. Further information can also be found in [26].

#### 5.1.1 Test Setup and Procedures

Already during the EM and QM phase of the development and production of the electronics, several test setups were designed to allow functional and electrical tests of the hardware. During the design of these test benches it was taken into account, that the test hardware has to be as compact and flexible as possible in order to be used at the different locations of production and testing. A design of the backplanes was chosen, which connects the electronics

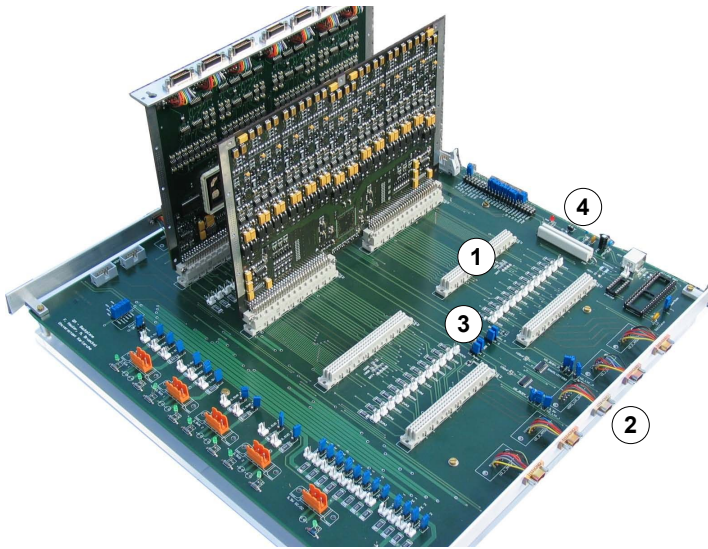


Figure 5.1: *UPSFE/UDR2 QM test backplane. The boards are powered via the backplane by VME connectors (1). AMSWire links (2) are present for the communication with the UDR2 board. Shunt resistors (3) are present in all power lines for monitoring of the current. A load resistor allows to apply a variable load by test points on the boards shown in figure 5.2.*



Figure 5.2: *UDR2 test backplane solid state fuse test. Test points on the UDR2 and UPSFE boards allow to insert a load into the digital circuit in order to test the correct switching of the solid state fuses on the boards.*

boards via the VME<sup>1</sup> connector later used for interconnection of the boards on the U-Crate backplane. The test backplanes, which will be briefly introduced, have been used in the QM2 qualification and the FM/FS acceptance tests at CSIST in Taiwan. The test setups designed and used during the EM phase are described in [30].

### The UDR2/UPSFE and Linear Regulator Test Backplane

Two different backplanes were designed and build to allow functional and electrical test of the UDR2 and UPSFE board of the U-Crate. Especially the electrical tests cannot be repeated as soon the boards are fixed inside the crate, thus it is the only way to identify defects in the control or overload protection circuits.

The UDR2/UPSFE test backplane shown in figure 5.1 allows to test two UDR2 and two UPSFE boards at the same time. The boards are interconnected and powered via VME connectors. Eight AMSWire connections are present at the backplane front panels to connect to both UDR2 boards on four links each. Either a separate or a common trigger signal can be given to both boards in order to test the readout. A Lecroy bus connects to the UPSFE interfaces.

The boards under test are powered by  $+3.4\text{ V}$  and  $\pm 2.8\text{ V}$  networks, which provide connectors on the backplane for an external power supply. A current measurement on all power lines

<sup>1</sup>VERSAmodule Eurocard, computer bus standard

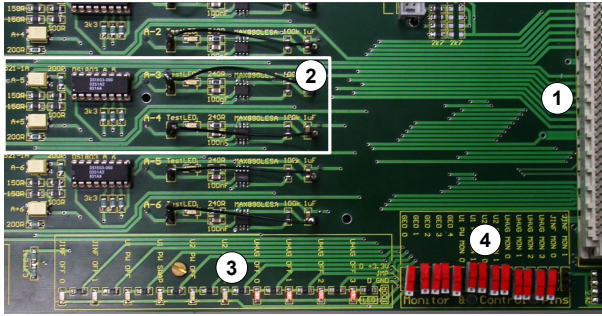


Figure 5.3: *UPSFE test backplane for linear regulator test. The UPSFE is connected to the backplane and powered via VME connectors (1). A test circuit (2) applies a variable load to the output of the linear regulator circuit of the UPSFE board in order to test the voltage stability, output power and over-load protection. The status of the control lines set by the UPSFE FPGA are monitored by LEDs (3). The state of the status lines read out by the UPSFE FPGA can be manually switched (4).*

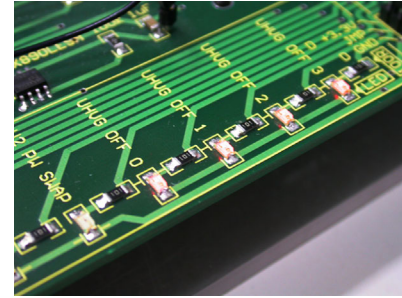


Figure 5.4: *Control line LEDs on-board of the UPSFE test backplane. Control lines are switched by the UPSFE FPGA and allow to control the UHVG and UDR2 boards inside the U-Crate.*

is performed at inserted  $0.075\ \Omega$  shunt resistors. The test sequence control is provided by a LabView<sup>1</sup> software, which is described in detail in [44]. The current is measured in all power lines by a precision multimeter and compared to the default values. In case the measurement indicates a deviation from the expected values additional measuring points are implemented on the test backplane and on the board to locate the origin of the higher current. Access to the on board I/O controller of the backplane is provided via USB from the test computer. The micro-controller controls digital potentiometers, which allow to test the over-current protection of the boards by regulating an additional current. Here advantage is taken from dedicated board test points on the UDR2 and S9011AU boards. Figure 5.2 shows the test points in the digital circuit, which are present on all boards. The status of the output voltage is fed back to the status signal registers of the micro-controller I/O ports via optocouplers and is analyzed by the control software.

A second test backplane was built to test the linear regulator circuits for the front end power supply on the UPSFE boards. Similarly to the solid state fuse test circuit on the UDR2 test backplane a variable load can be applied to all 14 linear regulator circuits of a UPSFE board via the test backplane. Status LEDs of the test circuit easily allow to identify switching of the solid state fuses of the UPSFE board. For further tests the backplanes are equipped with LEDs indicating the status of the control lines of the UPSFE FPGA. Furthermore the status of the monitor lines can be switched manually and the correct readout by the UPSFE FPGA is checked. These tests are of special importance, because the UPSFE FPGA takes over the control of almost all components inside the U-Crate and in the case of failure even is able to switch off the connected hardware permanently. Figure 5.3 shows sections of the UPSFE test backplane. A dim light on the control LEDs in figure 5.4 lead to the identification of

<sup>1</sup>graphical software developer toolkit by National Instruments



Figure 5.5: Board level test laboratory at CSIST.

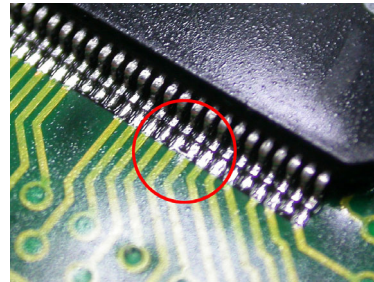


Figure 5.6: A short discovered on the S9011AU board 95001F. Remains of solder connect two status lines of the FPGA.

a design mistake, which is described in the next section. A more detailed description of the development and production of the UPSFE test backplanes is given in [19].

In addition to the electrical test for the UDR2 boards a full functional test of the digital part has been performed. Seven UFE boards were available to be connected to the front end links of the UDR2 to simulate the detector readout. Figure 5.5 shows a picture of the board level test lab with UDR2 boards under test.

### 5.1.2 Test Result Summary of the Board Level Tests

The board level test of flight hardware, unlike the test of the qualification model, is performed to identify production defects during the production. Design mistakes were already excluded by the qualification tests, which are described in [30]. Nevertheless besides some minor defects also a major problem of the UPSFE board was discovered and lead to a last-minute modification of the board. In the following the failures found on the flight hardware and the applied modifications are described.

**S9011AU FPGA Solder Failure** For the S9011AU board acceptance test a control and status line test was performed. An adapter-jig was available to connect the solder pads of the S9011AU to test wires without soldering them. During these tests a short on the Actel FPGA pin-out between two status lines was discovered. Figure 5.6 shows a picture of the shorted status lines. This was especially tricky to find, since the short connected two status lines of the same DC/DC converter and was only discovered by the separate switching of A and B side. In case only one half is switched off, the status was off for both halves due to the shorted status lines. The board 95001F has been repaired. Afterwards a visual inspection during the production process has been improved to discover such flaws.

**UPSFE Linear Regulator Failure** The UPSFE board level test has been passed by all UPSFE boards before the conformal coating process. After the ESS of the coated boards the linear regulator test revealed one defective solid state fuse circuit on the UPSFE with the serial number 95005F. The current limit was exceeded by the current drawn by the

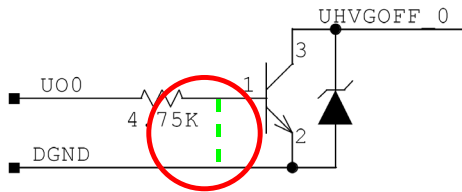


Figure 5.7: *UPSFE* schematics with the missing resistive link indicated by the circle. In case of a leakage current from *U00* the transistor may set the *OFF* level on *UHVG OFF\_0*.

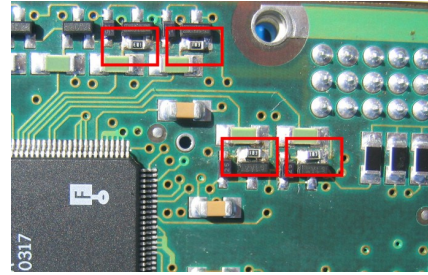


Figure 5.8: *UPSFE* with soldered pull-down resistors. The resistive link avoids switching of the transistor in the case of small currents.

linear regulator test circuit on the test backplane. A detailed investigation showed, that an operational amplifier in the circuit was defective. After exchange of the operational amplifier part the repaired board passed all functional and electrical tests.

**UPSFE Missing Pull-down Resistors** A more serious problem was revealed during the first electrical test of the flight *UPSFE* boards. Each *UPSFE* controls four halves of *UHVG* boards. Therefore four control signal lines are present on the backplane, which set the corresponding *UHVG* half to *OFF* or *ON* state. The *ON* state is set for the *UHVG*, if the current is low on the control line, whereas the *OFF* state is set, as soon as the current is high. The current on the line is controlled by a transistor to which basis the corresponding output pin of the Actel FPGA is connected.

On the *UPSFE* board with the serial number 95003F an Actel FPGA was mounted, which produced a high leakage current still within the specification on the output pins. This opened the transistor and set the *OFF* level for the *UHVG* boards permanently as a result of the Actel IO pins leakage current in the order of  $2 - 5 \mu A$ . This was observed on the test backplane control LEDs shown in picture in figure 5.4. The reason for the problem was identified by a review of the board's schematics. Resistors at the bases of the transistors were missing to keep the transistors *OFF* in the case of a small leakage current of the Actel FPGA. The pull down resistors were missing on these FPGA output pins completely already in design. The marked area in the schematics in figure 5.7 indicates the missing resistive link.

An electronics change order has been issued to correct this problem on all flight *UPSFE* boards. Small package resistors have been soldered to the transistors basis. In order to compensate the high potential caused by the small leakage currents from the Actel FPGA. Figure 5.8 shows the modified board with the soldered resistors. Each board needs eight pieces to be soldered as shown. Re-inspection of the repaired boards confirmed the full functionality after the change including the board 95003F. Undiscovered this problem could have lead to uncontrollable *UHVG* boards after aging of the Actel FPGAs in a radiation environment.

UPD Slot	Board Type	UPD0 SN	UPD1 SN
1	S9011AU	95001F	95002F
2	S9053U	94001F	94002F
3	S9048_0	94001F	94005F
4	S9048_1	94003F	94006F
5	S9011B	95001F	95002F
6	S9048_2	94004F	94007F
7	S9056_0	94001F	94004F
8	S9056_1	94002F	94005F
9	S9056_2	94003F	94006F

Table 5.1: Boards serial number record for the flight model UPD boxes.

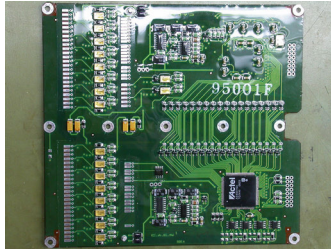
## 5.2 Assembly of the Power Distribution Boxes

The assembly of the two FM UPD boxes was carried out at CSIST facilities in Taiwan. Supervision in each work step was given by the Karlsruhe TRD group. A detailed assembly instructions document [42] had been prepared well in advance to guarantee a smooth process according to the tight schedule. In the following the main work steps are summarized and final assembly information is given.

The assembly procedure can be divided into two main steps. In a first stage of production the individual electronic boards are assembled. Figure 5.9 exemplary illustrates the main worksteps during the production of the S9011AU controller board of the UPD box. After the PCA and the functional test all boards are attached to I-Frames, which is the mechanical support and heat transfer to the walls of the UPD. Therefore a piece of Cho-Therm<sup>1</sup> is attached between the PCB and the I-Frame to avoid electrical contact, but to allow a good heat conductivity. Power and signal wires are soldered to solder pads, which are still free of conformal coating. Once the wires are soldered according to the assembly document the solder pads are sealed with conformal coating. The connectors are fixed either on the I-Frame or on the walls of the box. All screws are potted by glue as a back-off prevention. In the second stage the boards are inserted into the mechanically assembled UPD box. All boards are connected to a central terminal junction block for the power supply by 28V from the input filter. The control and monitor lines between the S9011AU controller board and the DC/DC converters are connected. Finally the boards are fixed to the walls of the box by screws. During the steps of this procedure functional tests are performed at all stages of the assembly to minimize time and effort of a potential rework in the case of a detected failure. The final torques for all screws using self locking helicoils are recorded. This requires a measurement of the running torque before fixing the screw with the total torque, which adds up the measured running and the seating torque specified for this type of helicoil. In the very end a piece of Cho-Therm is applied to the bottom of the UPD box to guarantee thermal contact for the box to any mounting surface.

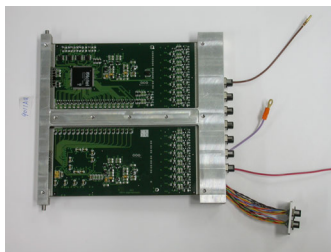
---

<sup>1</sup>by Chomerics company, a thermal insulator with maximum heat transfer and good electrical isolation



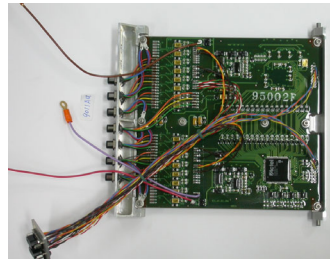
PCB with assembled parts and con-formal coating.

A "needle"-backplane allows to contact PCB pads avoiding repeated soldering of test wires to the board.



PCB with the mounted aluminum I-frame.

The board with soldered cables and the connectors mounted to the I-frame.



The S9011AU board during the insertion into the UPD box.

Crate-level thermal and vibration test of the UPD box together with the U-Crate.

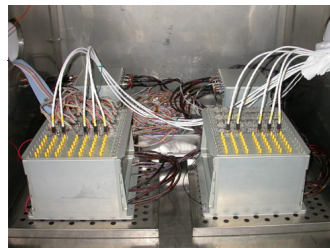


Figure 5.9: Pictures taken at different work steps during the production and acceptance test of the S9011AU board.



Figure 5.10: *U-crates during the assembly. The crates are partially equipped with electronics boards, which are slid into the corresponding slots into VME connectors on the backplane. Before the backplane has been mounted to the backside of the crate's aluminum walls.*

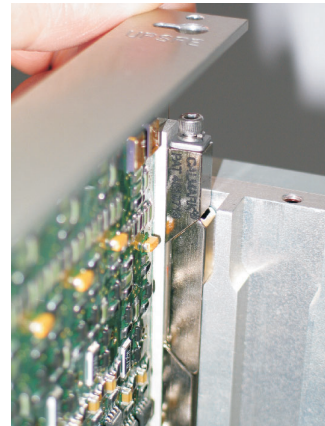


Figure 5.11: *Wedge-locks present on all boards of the U-Crate.*

### 5.3 Assembly of the U-Crates and the Power Cabling

The assembly of the U-Crates was carried out at CSIST facilities in cooperation with the Karlsruhe group in May 2007. The assembly of the U-Crate is much less complex than the assembly of the UPD box. All electronics boards were already fully functional tested on test backplanes. The instructions for the mechanics assembly are given by the designer of the crate housing CGS<sup>1</sup>. In a first stage of the assembly the U-Crate backplane was mounted to the crate walls. As for the UPD box screws all torque values are recorded for screws fixed to helicoil inserts in the torque measurement table and included in the crates' accompanying document folder and the ADP. Figure 5.10 shows the U-Crate partially equipped with the boards, which are slid one after the other into the corresponding slots. All boards have so-called wedge-locks, which are mounted to both sides of the board on metalized areas. After the insertion into the crate housing, the wedge-locks are splayed by screws in order to establish a good thermal contact to the crate walls. Figure 5.11 shows the wedge-locks on a board during insertion.

#### Assembly of Interconnecting Cables

Once all boards were inserted into the U-Crate and fixed by the front panel screws, the power connection was established to the associated UPD box. A set of cables was manufactured at CSIST facilities. Defined procedures for the cable assembly are given in the assembly instructions [40]. The length of each cable had been defined in advance according to the radiator drawings. The cable lengths had been verified with a mock-up model of AMS-02 allowing direct measurement of distances between the crates as well as by a CAD model implementation to avoid conflict with other cables. Figure 5.12 shows the power cable interconnection

<sup>1</sup>Carlo Gavazzi Space, Italian company specialized on development of space applications.

Crate Slot	Board Type	U0 SN	U1 SN
-	UBPv2.1	95003F	95001F
1	UDR2	95007F	95001F
2	UPSFEv2	95006F	95001F
3	UDR2	95008F	95002F
4	UDR2	95009F	95003F
5	UPSFEv2	95007F	95002F
6	UDR2	95010F	95004F
7	UDR2	95011F	95005F
8	UPSFEv2	95008F	95004F
9	UDR2	95012F	95006F
10	JINFv2	95002F	95001F
11	UHVG	95008F	95013F
12	UHVG	95014F	95002F
13	UHVG	95010F	95003F
14	UHVG	95009F	95004F
15	UHVG	95011F	95005F
16	UHVG	95015F	95006F

Table 5.2: Serial number record for boards of the flight model U-Crates.

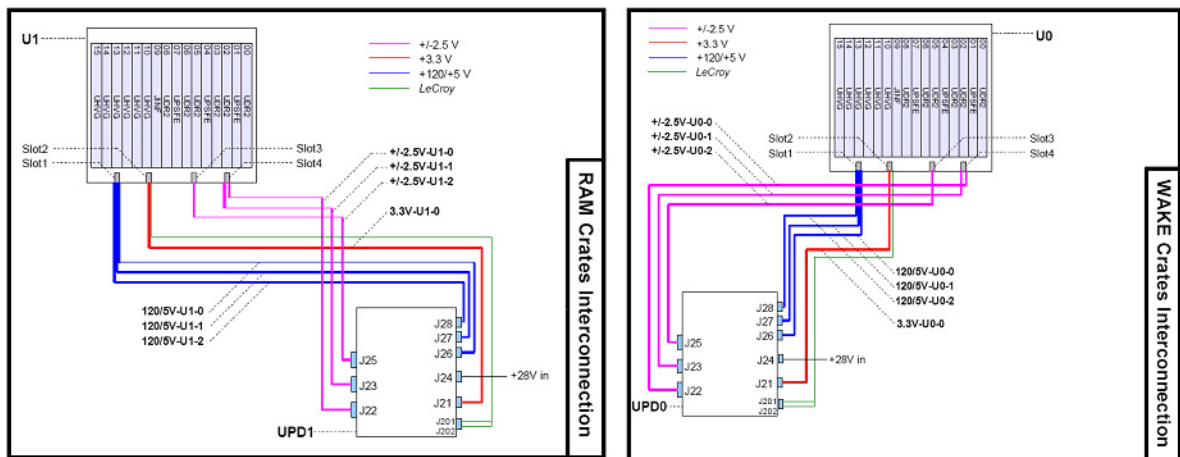


Figure 5.12: Interconnecting cables between the UPD box and the U-Crate. The 14 cables of different length were produced at CSIST.

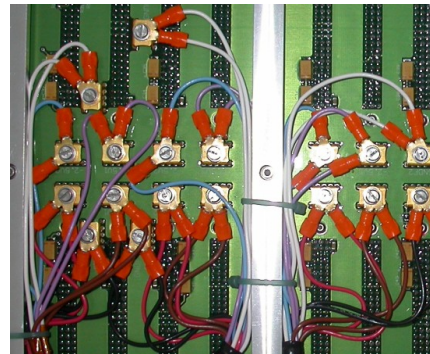
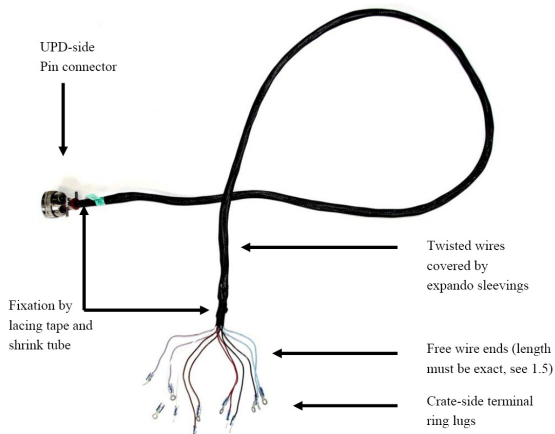


Figure 5.13: *An assembled power cable. The wires are mechanically protected by expandable sleeve. On UPD side a connector is attached, which allows easy disconnecting of the cable. On the opposite side gold plated ring lugs are crimped to the cable to be fixed to the U-Crate backplane.*

Figure 5.14: *Power bug soldered to the U-Crate backplane with attached power cables.*

scheme of the U-Crate and the UPD box. In total 14 cables were produced and tested. Figure 5.13 shows an assembled power cable with an applied expandable sleeve to avoid mechanical damage during handling and launch. Gold plated ring lugs crimped to the wire ends can be attached to the U-Crate backplane. The cables are fixed by screws to the power bugs soldered to the backplane as shown in figure 5.14. All wires in the cable bundle are present at least redundantly and are fixed to the same power bug on the backplane. The final installation with the final torque was done at CERN, since for transport the cables have to be unmounted.

## 5.4 The Flight Hardware Acceptance Test at Crate Level

The acceptance test at crate level is intended to be a full functional test of the complete system, where all operational modes of the system are passed in order to identify possible production defects. Figure 5.15 shows a picture of the flight model UPD and U-Crate after assembly ready to be acceptance tested at crate level.

### 5.4.1 Acceptance Test Parameters

The acceptance test mainly follows the procedures of the qualification test for the hardware described in section 4.5. The environmental stress screening (ESS) and the thermal-vacuum test (TVT) cover test conditions, which proof a stable operation after the launch in the Space Shuttle in deep space conditions. Nevertheless the flight hardware is exposed to less stress during the acceptance test than the qualification hardware, keeping in mind, that the flight hardware acceptance test is focused on uncovering production failures instead of identifying fundamental design mistakes. Briefly the purpose and adapted parameters for the environmental stress screening and the thermal vacuum test are summarized in the following.



Figure 5.15: *FM UPD and U-Crate after assembly.*

### Thermal Test

In the thermal chamber temperature conditions in space on board of the ISS are simulated by changing the temperature of the nitrogen gas inside the chamber.

The thermal profile during operation of the thermal chamber covers storage temperatures for both hot and cold case and operational hot and cold environment temperatures. The temperature of operation is limited to  $-20^{\circ}\text{C} \leq T_{\text{operation}} \leq +50^{\circ}\text{C}$ . Hot and cold storage temperatures reached during the ESS are between  $-40^{\circ}\text{C} \leq T_{\text{storage}} \leq +80^{\circ}\text{C}$ , which corresponds in the cold case a complete power loss of AMS-02 on the ISS and in the hot case a failure of the cooling system on the radiator. Figure 4.25 shows the thermal profile as applicable for the QM and FM tests of AMS-02 hardware.

The thermal cycle test is divided into two phases. Ten cycles between hot and cold operational temperature must be passed before the vibration test, which will be described in the next paragraph, and five additional ones have to be survived afterwards to pass the ESS. Functional test must be passed without a failure in the last two cycles. Possible causes for failures of flight model hardware are

- badly soldered parts
- internal part failure, e.g. a leakage current
- loose contact of connectors
- temperature dependent resistivity change exceeding the specifications

Figure 5.16 shows a picture of the acceptance test in the thermal chamber during the ESS at CSIST in Taiwan. In order to save time two set of FM U-Crate and UPD box were tested in parallel in the same thermal chamber. Both crates were connected to the test computers outside the chamber by two AMSWire links each and powered by separate 28V power supplies. This scheme allows extended test procedures, which read simultaneously event data on one link and slow control data on the other link of the same crate. Front end simulators were connected to one crate at a time, which were connected to a multimeter outside the chamber monitoring the output voltage of the UPSFE linear regulators.

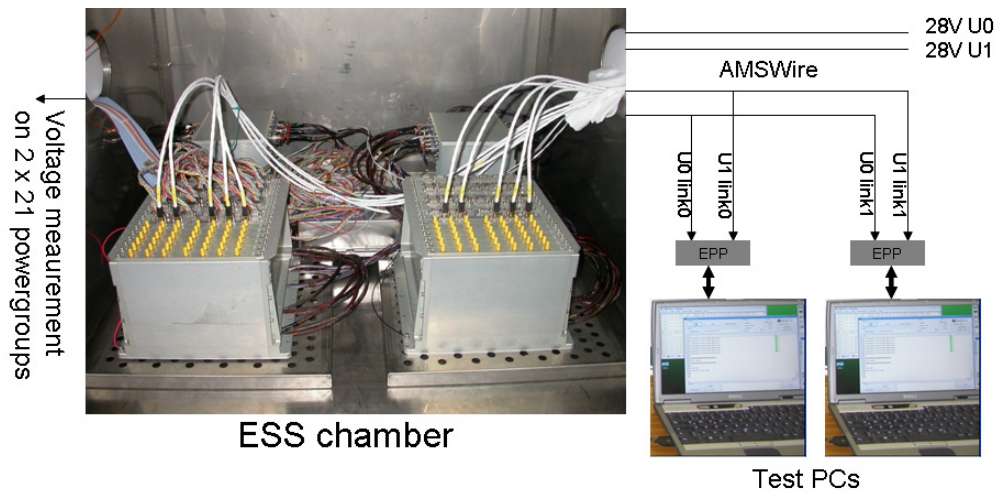


Figure 5.16: *ESS climatic chamber test setup. Both crates under test are connected to both test computers allowing a simultaneous readout of event and slow control data by separate links of the crate. A stable front end power supply by the UPSFE can be verified by monitoring the 21 power groups with an external multimeter.*

### Vibration Test

A quite essential test for all hardware, which needs to be delivered to any place in space, is the vibration test. On a vibration table vibrational frequency conditions as expected during the lift-off of a rocket or the Space Shuttle are simulated. Here and in the payload area of the shuttle a random vibration spectrum is injected to the system. The test result most time is quite obvious, since this is a survival test. Full functional tests are performed before and after the vibration test. For the duration of the vibration the system is kept in the normal operation mode checking for any abnormal behavior. Possible causes for failures are

- badly soldered parts
- weakness of the raw material
- internal part failure
- loose or broken screws or broken mechanical parts
- temporary shorts

Figure 4.26 shows the specification of the vibration spectrum for AMS-02 hardware. The vibration test is done separately for the three directions X, Y and Z. Duration is 60 seconds for the flight model hardware. In this test the purpose of the acceptance test in contrast to qualification test of the hardware is most clear. While during the qualification test the hardware has to prove to survive several times the duration of a complete shuttle launch, the hardware under acceptance test is only subject to a very short test looking for production defects.

Figure 5.17 shows a picture of the vibration test setup of the flight model UPD box at CSIST. The hardware under test mounted to the shaker-table continuously is powered for the duration



Figure 5.17: *FM ESS vibration table test setup. The UPD box is mounted on the shaker table to be vibrated in horizontal Y-direction. It is powered and connected to the U-Crate throughout the test. The test software verifies a failure free operation before, during and after the test.*

of the vibration. The UPD box and U-Crate are connected throughout the test. The modified test software swaps between the redundant halves of the hardware and verifies a failure free operation.

### Vacuum Test

The thermal vacuum test was conducted at the vacuum chamber at RWTH Aachen for the flight model. Functional tests are performed continuously in the operational temperatures for the four temperature cycles during the TVT. The TRD front end simulator (UFS) boxes were placed inside the chamber to dissipate the front end equivalent power and to simulate the front end functionality. The U-Crate and the UPD box were mounted to an adapter plate on the cooling plate of the chamber. The U-Crate is connected via two AMSWire cables and one additional trigger link to the outside of the chamber. During operational phases a test script running on a computer outside the chamber simulates a normal operation of the TRD electronics including slow control and data acquisition with the front end simulators. Additional scripts were available, which perform extensive functional test of each kind of board.

Figure 5.18 shows a picture of the thermal-vacuum test at RWTH Aachen with one set of the U-Crate and UPD box under test. In contrast to the ESS only one set of UPD and U-Crate can be tested at a time. Apart from that the setup is equal to the previously performed ESS test at CSIST. The U-Crate is connected to the outside of the chamber by two AMSWire links. The three UFS boxes are connected to the UDR2 boards of the U-Crate. The operational temperature was stabilized at the crate walls to  $-20^{\circ}\text{C} \leq T_{\text{operation}} \leq +50^{\circ}\text{C}$ . Hot and cold storage temperatures were reached between  $-40^{\circ}\text{C} \leq T_{\text{storage}} \leq +80^{\circ}\text{C}$ . Figure 4.35 shows the thermal stress profile for TVT. In addition to the acceptance testing six UHVG channels were connected to the outside of the chamber through special high voltage qualified feedthroughs. So temperature effects on the stability of the high voltage output could be tested. The results are presented in section 5.5.



Figure 5.18: *Thermal vacuum chamber at RWTH Aachen. The chamber is able to accommodate one U-Crate and one UPD box. Three UFS boxes are mounted in front of the U-Crate not yet done in the picture.*

### The Test Software

The functional test of the hardware is performed by a test software accessing the hardware's own control and monitoring capabilities. Therefore a dedicated test software has been developed to allow an automatic failure detection. The GUI the program is presented in figure 5.19. The basic principle of this software, which already was used during the qualification test in a simplified version, is to compare status output of the system with the expected values after each step in the control sequence. The main steps of the test procedure are shown in figure 5.20. As soon as any difference is found to the expected result the software tries to recover the error by repeating the last step in the control sequence. If this is successful the test continues with a recoverable error notice. In case the problem cannot be solved a user interaction is required to investigate the problem. During the failure-free operation of the hardware the test software repeats the test optionally in an infinite loop. More specific test procedures are available for each type of board, which are performed in addition to the standard test depending on the available time for testing.

#### 5.4.2 Test Result Summary

The essential result of the flight and flight spare U-Crate and UPD acceptance test is that a full functionality of the electronics system has been verified throughout the entire test procedure.

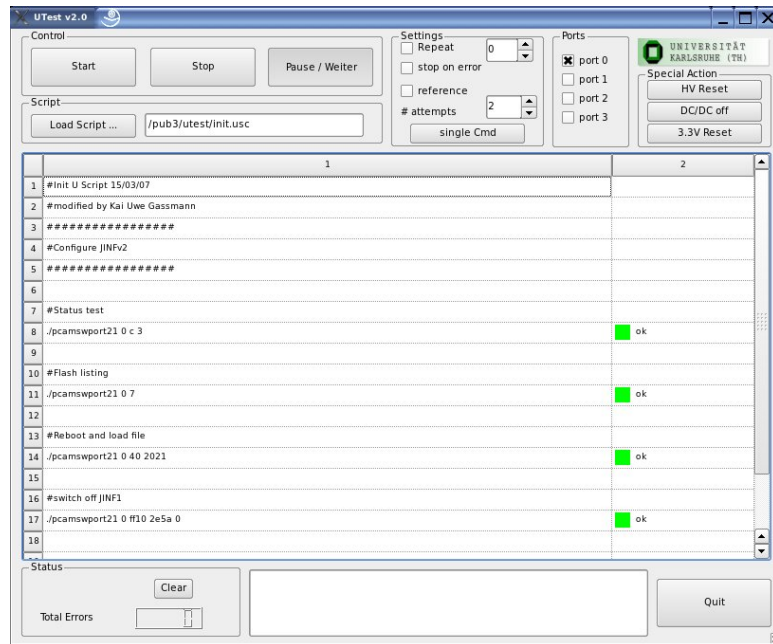


Figure 5.19: Snapshot of the U-Test software GUI. The software processes script-files, which defines a sequence of commands to be executed. As soon as the reply to a command is different from the expectation the program automatically checks for transmission errors by resending the command. Otherwise the execution of the script is stopped immediately and the problem can be investigated in detail by the operator.

At no time the system has lost the capability to operate the TRD. Nevertheless some minor problems were revealed due to the intensive tests, which are listed in the following.

**U-Crate LeCroy Bus Error** The transmission on the LeCroy bus sporadically sporadically failed to the redundant half of the UHVG board 95009F. The problem was observed in cold conditions only below  $-20^{\circ}\text{C}$ . No problems were seen on primary half of the affected board. The failure rate during the transmissions was about 80%. The investigation showed, that the problem originated from the LVDS transceiver part of side B of the UHVG board. After the replacement of the defective part further tests were passed by the repaired board without a failure.

**UHVG Oscillator Failure** The oscillator quartz crystal mounted on the UHVG boards turned out to be the reason for a bunch of problems found on this type of board. Already in the course of the board level test at room temperature a number of them had to be replaced directly after the board production. In the first cold and the first hot cycle of the ESS in total four channels on different boards could not be read controlled. The investigation showed, that the oscillators were broken, which clock the MHV100 controller chip of the UHVG board. During the TVT the same problem was found on four more channels after venting the chamber or in fast transition between the temperatures. All boards have been repaired by the replacement of the oscillator crystal and passed the functional tests afterwards. During six

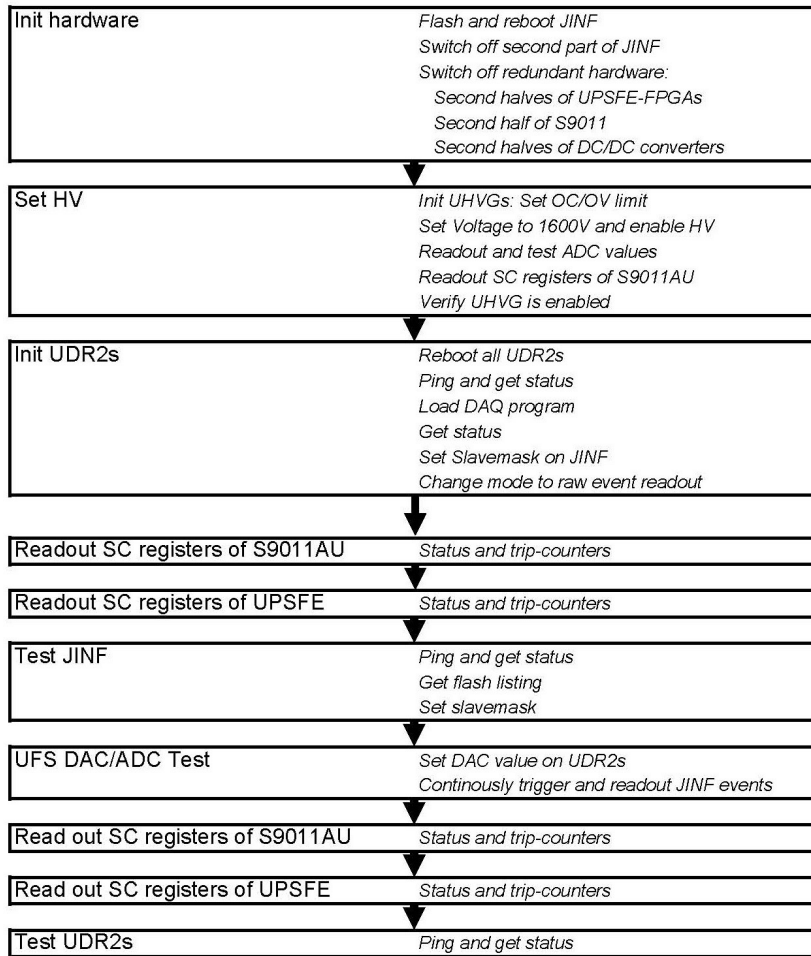


Figure 5.20: Example for a test procedure executed by the U-Test program. After the initialization of the hardware the readout of the status and a data acquisition simulation with the UFS can be executed in a loop.

months of continuous operation in the AMS-02 pre-integration phase no more oscillator failure was observed. As a conclusion the oscillator parts failed in environmental conditions only, which appeared for the first time to the part, like hot and cold, fast changing temperature or mechanical stress. After the replacement of the defective parts all boards could be operated without a failure even in extreme conditions. The assumption is, that affected parts were already defective before the mounting to the boards. However a part screening for this type of part was not possible, but may have prevented the huge number of repairs.

## 5.5 UHVG Board High Voltage Calibration

The gas gain of the detector straw tubes mainly depends on three factors, the gas temperature and pressure, whose product is kept stable by the gas system, and the high voltage applied between the anode wire and outer wall of the tube. In section 3.3.4 the gas gain as a function of applied voltage is derived. A good estimation is, that a voltage variation by 1 V results in about 1 % variation of the gas gain. This stresses the need of a stabilized high voltage source to about  $\pm 0.1$  percent of the output voltage.

The qualification model of the UHVG designed by MIT and produced by CSIST has proven a stable operation at room temperature over three years. A high voltage calibration has been performed to assign a voltage on the output to the DAC code, which is set on the MHV100 controller chip. A simple linear correlation is assumed, which is almost perfectly confirmed by the measurement up to 1700V. However during tests in the cosmic test stand in Karlsruhe an unexpectedly strong dependence on the environmental temperature was discovered. A test in a climatic chamber confirmed, that the variation in the worst case is up to 1 V per  $1^\circ\text{C}$ , which would require a stabilization of the temperature of the electronics crates to a few degree per hour. Due to the thermal variation in the sunlight, this limitation would be most time exceeded. The investigation showed, that the mounted resistors for the voltage control did not meet the manufacturer's specification. So the production of the flight model was initiated without a modification of the UHVG design. Instead a thorough preselection of resistors to

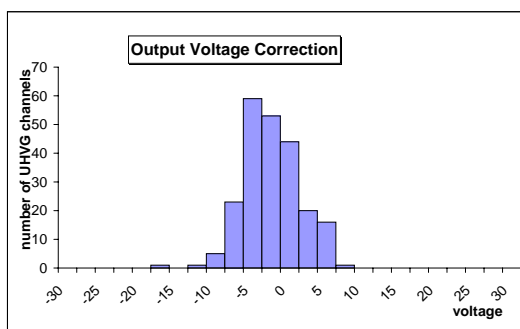


Figure 5.21: *Distribution of UHVG channel calibration correction at 1000V. The value is calculated from the difference of the output voltage to the mean DAC setting, which corresponds to 1000V.*

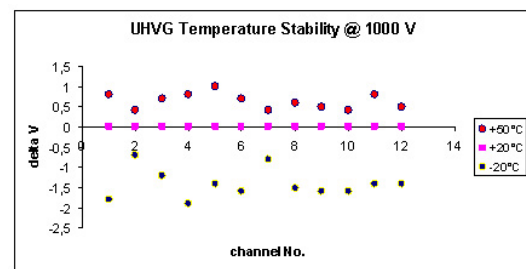


Figure 5.22: *UHVG channel temperature dependence of the output voltage. For this random sample of channels the output voltage shows a variation of about 2V at  $70^\circ\text{C}$  temperature variation, which is well within the requirement.*

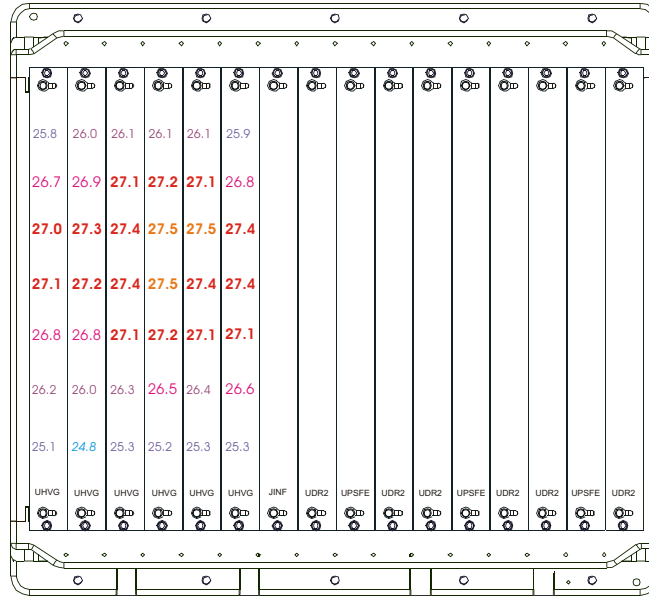


Figure 5.23: U-Crate temperature profile read out by the MHV100 sensors of the UHVG boards.

be mounted was done in order to ensure a minimum thermal dependence.

The DAC code calibration was performed in several steps. The formula accordingly for the conversion of the voltage to a DAC code is

$$code_{DAC} = \left( \frac{V(\text{in mV})}{500 \cdot corr_{div}} - offset_{DAC} \right) / mVch / gain_{DAC} \quad , \quad (5.1)$$

with different measured correction factors for the reference voltage ( $mVch$ ), the offset voltage of the DAC ( $offset_{DAC}$ ), the voltage divider correction ( $corr_{div}$ ) and the actual DAC gain ( $gain_{DAC}$ ). The calibration was performed before the conformal coating process. Afterwards the coating avoids a measurement of the output voltage. A measurement at the dioded output would lead to a voltage drop, which disturbs a precise measurement. Figure 5.21 shows the distribution of the calibration correction at 1000V output voltage.

A possible correlation to the ambient temperature was verified during the FM acceptance TVT. To allow a measurement of the voltage in a current-free state, a counter-voltage was applied to the output. In the case the output voltage and the counter-voltage is equal no current is observable. Figure 5.22 shows the temperature dependence of the measured channels. Over a wide range of temperature the voltage stays within the specification.

The on-board temperature sensors were already calibrated during the FM acceptance ESS. Directly after powering the crates after a stabilization phase the temperatures sensors were read out. Figure 5.23 shows a thermal map of the U-Crate after some time of operation based on the temperature sensor calibration correction. The shown profile of course is not of importance for the flight operation, because the conditions are quite different, but it demonstrates, that an adequate monitoring of the internal U-Crate temperature is possible.

## 5.6 The AMS-02 Pre-integration Phase

In the end of 2007 the assembly of AMS-02 was started in a cleanroom at CERN<sup>1</sup>. During this pre-integration phase the detector was assembled without the magnet, which construction was delayed. The pre-integration and the data acquired during this period is presented in section 7.2. The TRD was lifted to the top of AMS-02 in December 2007. Figure 5.24 shows pictures of the TRD lifted by the indoor crane inside the AMS-02 cleanroom. Each step has been previously documented and specified in an AMS-02 task sheet and reviewed by NASA.

The FM U-Crates and UPD boxes were installed to the radiator jig before, which hold the electronics in place until the final radiators are delivered. The reliability of the TRD and the readout electronics was already separately verified in a cosmics test at RWTH Aachen and the acceptance test. The missing element is the interconnection of the TRD and the FM U-Crates by signal and high voltage cables. Cable bridges were developed and produced at the IEKP in Karlsruhe to fix the bundles of cables between the TRD M-structure and the readout electronics in order to relieve stress from the front panel connectors of both UHVG and UDR boards. Figure 5.25 shows a closeup of the mounted U-Crate cable bridges.



Figure 5.24: *Lifting of the TRD to be mounted on top of AMS-02.*



Figure 5.25: *The U-Crate and cable support mounted to AMS-02. Cables to the detector are not yet installed.*

The final connection between the TRD and the electronics will be made in 2009. The U-Crates and the UPD boxes have already been attached to the radiator jigs and the cable bridges have been mounted with final torque. After the integration of the superconducting magnet the electronics jig will be lifted to a vertical position and attached to the AMS-02 USS and the readout electronics will be connected to the front end electronics of the detector.

---

<sup>1</sup>Site de Preveessin, Building 867



## Chapter 6

# TRD Data Processing in AMS-02

*The AMS-02 data acquisition system is designed to be able to read out and to independently analyze in parallel about 200,000 analog channels in different subdetector systems for each triggered physics event. The main DAQ Computer (JMDC) is based on a PowerPC 750 processor running at 400 MHz, which is widely used in embedded applications and spacecraft and is well known from the original iMAC by Apple. Its more than 300 connected nodes in AMS-02 operate ADSP-2187L digital signal processors. The software running in the different nodes is build up in a detector independent framework. Subdetector specific routines are only implemented as required. This chapter describes TRD specific software.*

### 6.1 The AMS-02 Data Acquisition System

The AMS-02 instrument shown partially assembled in figure 6.1 is controlled and read out by a main DAQ computer (JMDC) and a number of independently operating slave computers distributed among the various subsystems. Active slaves can be replaced by fully functional



Figure 6.1: AMS-02 at CERN in December 2007. The entire detector is read out by a flexible network of independently operating slave computers and one out of four main DAQ computers of AMS-02 as the master.

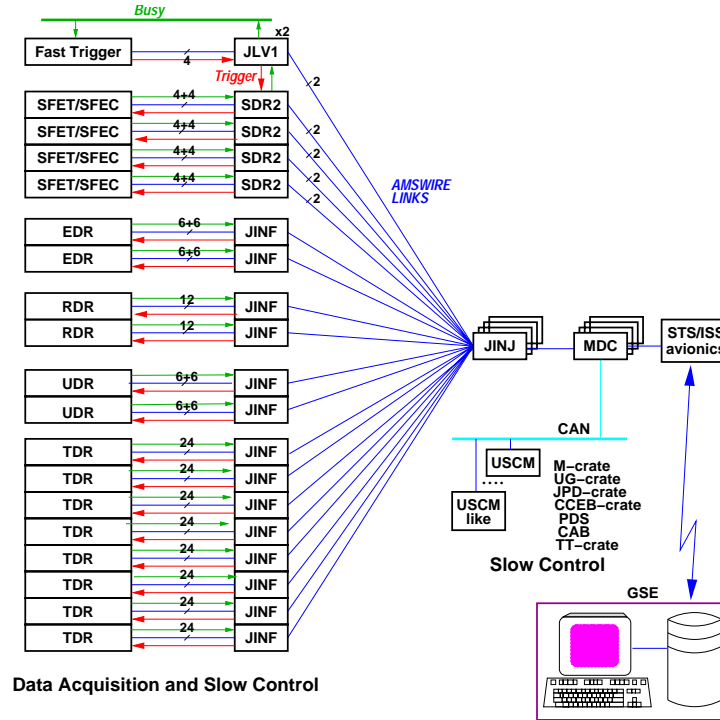


Figure 6.2: *AMS-02 data acquisition architecture.*

inactive ones at any time, so that the DAQ system is fully redundant.

The data acquisition system is based on the master-and-slave communication principle. A slave starts a transaction of data only on request from its master. The reply is given immediately to a master's request. The hierarchy in the connection scheme is shown in figure 6.2, which consists of four levels. An xDR board, which is the subdetector specific readout board in the hierarchy, has no slaves and performs the data processing of data retrieved from detector front end electronics. Each xDR has two redundant JINF masters connected by the subdetector electronics backplane. The JINF board is subdetector independent and can have up to 24 xDR slaves. A JINF has two redundant JINJ masters, which collect the data from all subsystems. Each JINJ has 24 slaves. These are 14 JINFs, eight SDRs and two JLV1 modules. A JINJ is connected to all four main DAQ computers (JMDC). In normal operation mode the redundancy on JINF and JINJ level is cold, which means one JINF is switched off by the primary half.

### 6.1.1 Physics Event Building

A particle crossing the detector triggers the readout of all 200,000 channels in AMS-02 synchronously. To ensure that all subdetectors are hit by the particle, respectively comply with the criteria of the current DAQ mode of the AMS-02 event building, the JLV1 module generates the LV1 trigger signal based on information from the ToF, ACC and ECAL subdetectors. The LV1 signal then is distributed to all JINF and SDR2 boards. After a programmable delay time, which depends on subdetector specific requirements, the trigger is forwarded to the

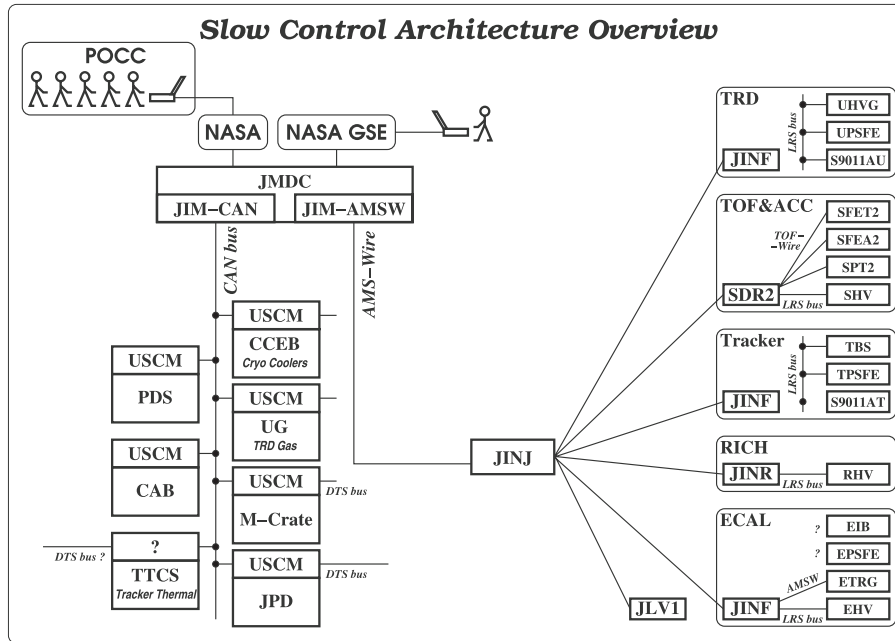


Figure 6.3: The AMS-02 slow control architecture.

connected xDR nodes. During this period the JINF board gives a busy signal to the JLV1 node. Once an xDR receives a trigger signal, the busy signal is set from its CDP and the sequencer logic starts the digitization of the analog signals and reads the digitized data from front end electronics. As soon as the data is stored in the CDP buffer memory the busy signal is removed, if the buffer of four events is not occupied by unprocessed events. Both JINF and xDR busy signals are taken into account by the JLV1 module from all active nodes and give a veto for next LV1 trigger generation.

The xDR processing runs independently from all other active nodes. The data retrieved from the front end electronics is stored in the raw event buffer. Once an unprocessed event is found in the buffer the xDR subdetector specific data processing routine is executed and the data is processed by the digital signal processor (DSP) and stored in the built event output buffer. The node masters continuously are requesting event fragments from their slaves, which is an automatic process. The JINF assembles the event fragments from all responding xDR nodes by its DSP and stores it into its own built event output buffer. The JINJ assembles the event fragment from all responding JINF, SDR2 and JLV1 nodes by its DSP and stores it into its own output buffer. The event data stored in the memory of the JINJ then can be requested by JMDC, which finalizes the AMS-02 event data block with additional information such as from GPS.

### 6.1.2 Electronics Slow Control

There are two different approaches for the slow control of the subsystems in AMS-02. Originally the design of the slow control system has foreseen, that slow control and data acquisition commanding chains are kept completely separated by the hardware. Therefore a universal

slow control board had been designed to be present in each subsystem. Based on the CAN-bus known from automobile industry, JMDC sends and receives status information on this path only. Due to the need of weight reduction the approach of the separate commanding chains was abandoned in most subsystems. Still a few dedicated slow control subsystems like the TRD gas control system use the USCM<sup>1</sup> as the interface board to JMDC. Figure 6.3 shows a schematic overview of the AMS-02 slow control chain.

Instead of the control by the USCM a subsystem's JINF board takes over slow control functionality. Commands are not send via the CAN-bus, but in an envelop command through the AMSWire links, which connect the JINF to the main DAQ computer. This modification was introduced with JINF version 2 boards, since according to the new approach the JINF needed to be modified to become connected to the LeCroy buses in the subsystem.

Slow control commands are distributed locally within a subsystem via several LeCroy buses, to which the control slaves are connected. JINF is capable to receive a list of LeCroy bus commands in one AMSWire command, but the transaction and retrieval of the reply is done sequentially. Each transaction on the LeCroy bus takes about  $150\mu s$ . To avoid conflict with the event building during the data acquisition, slow control commands are handled taking advantage of interrupt routines reducing the time the system waits for reply during monitoring requests. The approach of the QList for slow control monitoring purposes is described in section 6.4 more in detail.

### 6.1.3 Data links

Figure 6.4 illustrates the data transfer inside and outside AMS-02 as a payload of the ISS. AMS-02 internal AMSWire is used between the DAQ nodes and the LeCroy bus between the top control node and the slow control electronics. Critical health data is collected via CAN bus by JMDC bypassing AMSWire. The interface protocol of AMS-02 with NASA hardware and the format of the data sent to the ground is specified in [13].

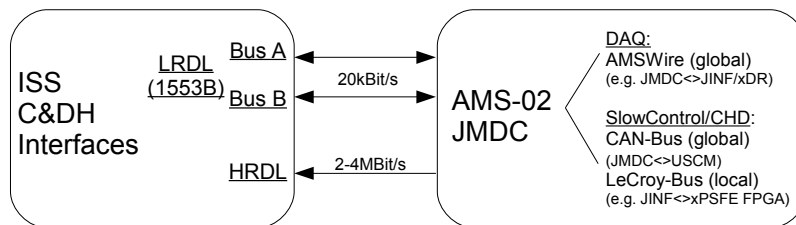


Figure 6.4: *Command and data handling interfaces between AMS-02 and the ISS. Within AMS-02 science data is transferred by AMSWire with a bandwidth of 100 MBit/s. For slow control JMDC is connected to universal slow control modules (USCM) by the CAN bus. Both USCM and JINF boards access local LeCroy buses for the communication with the associated hardware.*

### LRDL/HRDL

There are two separate data links, which connect the International Space Station with the ground control. The S-Band is the data link for critical health data and control of the ISS

<sup>1</sup>Universal Slow Control Module

and connected experiments. The Ku-band carries the big amounts of science data. So also AMS-02 has two separated data links to transmit control and science data between the ISS and the experiment. Telemetry and commanding data is send through the low rate data link (LRDL), which allows continuous monitoring of critical system parameters by the ISS crew and NASA control. The bandwidth allocated for AMS-02 data is 20 kBit/s via the downlink S-band of the station. A splitter card (JLIF) connects all four JMDC to the LRDL. Science data is transmitted through the high rate data link (HRDL) to the ISS using fiber optics technology. It is directly connected to the high rate down link of the station with between 2 and 4 MBit/s allocated bandwidth for AMS-02 science data. An internal buffer allows to hold the data as long no downlink connection is available for the experiment. Both LRDL and HRDL are bidirectional and present double redundant in the connection to the space station nevertheless requiring an astronaut operation to swap the cables to the redundant splitter on the AMS-02 patch panel to the ISS.

### AMSWire

AMSWire is the main communication protocol in AMS-02 for both science and slow control data between the subsystems and the main DAQ computer. The AMSWire protocol is used for the communication between xDR and JINx nodes. It is a bidirectional, serial point-to-point protocol based on the ESA<sup>1</sup> SpaceWire standard. The basic principle is, that the nodes only reply on request by the master. A slave does not send any data, if not requested, and it does not know, to which level of the hierarchy shown in figure 6.2 it belongs to. Only JMDC knows the entire map of AMSWire connections to the nodes.

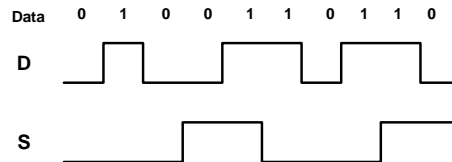


Figure 6.5: *AMSWire data strobe encoding. The strobe signal changes its state, if the data signal stays constant. In this way the clock is encoded in the data and strobe.*

AMSWire signals are transmitted through an AMSWire cable or on the PCB taking advantage of the Low Voltage Differential Signal (LVDS) technique. Transmission is based on the data-strobe encoding. One differential pair gives the strobe information, the other the data signal. An example for this principle is illustrated in figure 6.5. The strobe signal changes its state only if the data signal stays constant. In this way the clock information is encoded in the data and strobe signal and can be extracted by a XOR operation. More information about SpaceWire standard can be found in [20]. The implementation of the standard and the AMSWire protocol in AMS-02 is specified in [36].

**The AMSWire protocol** The AMSWire protocol is implemented for the communication with xDR and JINx nodes. An AMSWire command consists of a header and an optional data part. First part of the header is the addressing path to the corresponding node. The actual

<sup>1</sup>European Space Agency

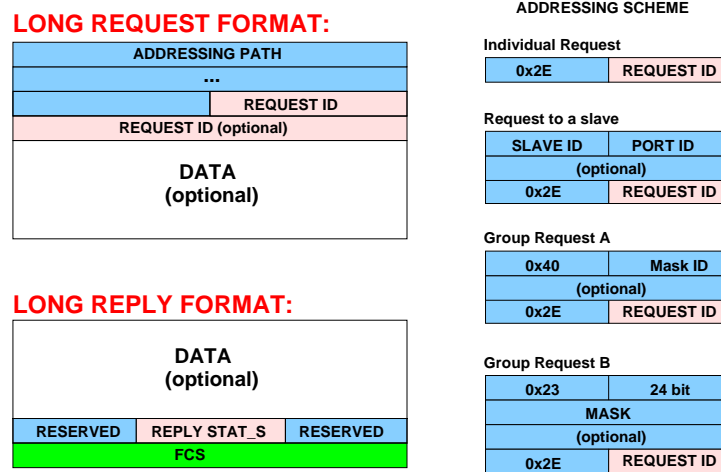


Figure 6.6: Data format of the AMSWire protocol. A command consist of the addressing path and the request ID, which optionally requires parameters in the data part. The data reply is protected by a frame check sequence.

command ID forms the second part. There are several ways to specify the addressing path. The addressing scheme is shown in figure 6.6. For direct commands to a connected node the addressing path consists of just one byte 0x2e, which means the destination is the node itself. If the destination node is a slave of the connected node, the addressing path consists of two bytes, namely the slave ID and the port. For instance 0x043f addresses slave 4 on an arbitrary port. Furthermore it is possible to address a group of slaves. In this case a slave mask can be specified after byte 0x23 in the following 24 bit or the command can be send to all connected slaves indicated by the addressing byte 0x2a.

AMSWire replies consist of the data part and a reply status word. The replying node fills the data part with the corresponding data and bits 10-5 of the status word. Other bits of the status word are used by the assembling node master to add additional information. Each assembled reply is protected by a frame check sequence, which is appended to the reply and allows the identification of corrupted data on the ground.

The list of all AMSWire commands in the framework version v8600 is given in figure 6.7. If for instance the status of a connected node should be requested, the addressing path and command ID form the complete AMSWire command 0x2e0c. Further details about AMSWire commands and its parameters can be found in [35].

## LeCroy

The LeCroy protocol is used for the communication with most peripheral hardware, which do not require high transfer rates. The data is transmitted by a clock and a data line in local and independent buses. Master in the LeCroy bus is the JINF, which generates the clock. The data lines can be accessed by both master and its slaves. A LeCroy transaction consists of 64 bits.

For big networks like the temperature sensor network, the CAN-bus is used in AMS-02. The TRD readout system is not connected to the CAN-bus. All slow control tasks were passed to

Data Type			Response time	Comments
Mnemonics	R/W	ID		
DSP Monitoring and Control Commands				
Boot	W	0x40	13ms	any node
Read Node Status	R	0x0C	10 $\mu$ s	any node
Ping	R	0x0D	10-200 $\mu$ s	any node
DSP Power Down	W	0x4E	10 $\mu$ s	any node
Program Test	W	0x55	400 $\mu$ s	any node
FLASH File Read	R	0x05	1-2ms	any node
FLASH File Write	W	0x45	70ms(4s)	any node
FLASH File Test	R	0x06	1-2ms	any node
FLASH File Load	W	0x46	1-2ms	any node
FLASH Summary Read	R	0x07	10 $\mu$ s	any node
FLASH File/Sector Erase	W	0x47	60 $\mu$ s(15s)	any node
File Attribute Set	W	0x48	20 $\mu$ s	any node
Perform I/O	R	0x0F	10-200 $\mu$ s	any node
PM Read	R	0x10	10-200 $\mu$ s	any node
PM Write	W	0x50	10-200 $\mu$ s	any node
DM Read	R	0x11	10-200 $\mu$ s	any node
DM Write	W	0x51	10-200 $\mu$ s	any node
DAQ Monitoring and Control Commands				
Physics Event Read	R	0x01	10-200 $\mu$ s	not ROM
Read Last Evevnt No	R	0x02	10 $\mu$ s	not ROM
Reset Event FIFO	W	0x42	10 $\mu$ s	not ROM
Read HK Info	R	0x03	10-200 $\mu$ s	not ROM
Configuration Read	R	0x09	10-100 $\mu$ s	not ROM
Configuration Write	W	0x49	10 $\mu$ s-500ms	not ROM
Processing Mode Read	R	0x12	10 $\mu$ s	not ROM
Processing Mode Set	W	0x52	10 $\mu$ s	not ROM
Calibration Status	R	0x13	10-400 $\mu$ s	not ROM, CDP only
Calibration Control	W	0x53	10 $\mu$ s	not ROM, CDP only
SD Procedure Status	R	0x14	10-400 $\mu$ s	not ROM, CDP only
SD Prosedure Control	W	0x54	10 $\mu$ s	not ROM, CDP only
Slave Test Status	R	0x16	10 $\mu$ s	not ROM, not CDP
Slave Test Control	W	0x56	10 $\mu$ s	not ROM, not CDP
Slave Mask Read	R	0x17	10 $\mu$ s	not ROM, not CDP
Slave Mask Write	W	0x57	10 $\mu$ s	not ROM, not CDP
BUSY Mask Read	R	0x18	10 $\mu$ s	JINF
BUSY Mask Write	W	0x58	10 $\mu$ s	JINF
DELAY value Read	R	0x19	10 $\mu$ s	JINF
DELAY Value Write	W	0x59	10 $\mu$ s	JINF
BUSY Status Read	R	0x0A	10 $\mu$ s	JINF
BUSY Errors Read	R	0x0A	10 $\mu$ s	JINF
SSF Status	R	0x1A	10 $\mu$ s	JINF
SSF Control	W	0x5A	10 $\mu$ s	JINF
Slow Control and Monitoring Commands				
QLIST Entry Delete	W	0x5B	10 $\mu$ s	not ROM
QLIST Read	R	0x1C	10 $\mu$ s	not ROM
QLIST Write	W	0x5C	10-50 $\mu$ s	not ROM
LeCroy Bus Read	R	0x1D	(150-N) $\mu$ s	not ROM
LeCroy Bus Write	W	0x5D	300 $\mu$ s	not ROM

Figure 6.7: List of AMSWire commands. [35]

Header Frame [16 bit]							DATA Frame [16 bit]	Echo Header Frame [16 bit]							Reply Data Frame [16 bit]
1	Parity	Power	Broadcast	ADR[8]	Write/Read	Register[3]	DATA[16]	0	Echo Parity	Echo Power	Echo Broadcast	Echo ADR[8]	Echo Write/Read	Echo Register[3]	DATA[16]
1	0	1	0	00110000	0	010	0000 0000 0000 0000	0	0	1	0	00110000	0	010	0000 0000 0000 0001

Figure 6.8: *Format of a LeCroy command.*

JINF electronics in the course of the weight reduction. Information about the CAN bus and the prior integration in the U-Crate electronics can be found in [12] and [30].

**The LeCroy protocol** A LeCroy request consists of a command header and a data part as exemplary shown in figure 6.8. The header and the data part are of 16 bit length each. Bit 0-2 of the header specify the register to be written, bits 4-11 give the address on the corresponding bus. In case the broadcast bit 12 is set, all slaves on the bus are addressed. The header and the data part are protected by a parity check, which is written to bit 13. In a request bit 15 of the header it set. The header of the reply echoes the request header, but bit 15 is not set. The actual reply data is written to the data part of the reply.

The LeCroy command to be written is specified in an envelop AMSWire command. The AMSWire command consists of six words excluding the addressing path. The command ID as described in the previous section is 0x1d for the LeCroy bus access followed by the number of requested transactions and the time delay to the previous command. The next word specifies the bus number in bits 6-4. The last two words contain the actual LeCroy command like discussed previously. A valid AMSWire to Lecroy bus command for example is

```
2e1d 0001 0000 0030 e180 0000 ,
```

which addresses the UPD controller board on bus 3 register 0 for reading of the DC/DC converter status.

## 6.2 Digital Signal Processing of the TRD

Due to the limitation of the downlink bandwidth from ISS it is essential to reduce the amount of collected data without losing physics information. This is accomplished by independently operating xDR nodes, which retrieve the raw data from the front end electronics of the detector. The digital data from the TRD front end electronics is processed by twelve UDR2 boards located in the two U-Crates in parallel. Each of the boards is running a DSP processing the data from seven front end links. The processing software is based on a common framework developed for use in all subdetector nodes. Detector specific parts need not be developed independently. In contrast on JINF level all subsystems use the same event building software. Figure 6.9 shows the complete hierarchy of the TRD readout electronics.

### 6.2.1 DSP Programming

In order to demonstrate functionality and the capability of the DSP a short introduction to the principle of the operation of a DSP will be given. Digital signal processing directly on each node in AMS-02 is a main principle to cope with the huge amount of data collected

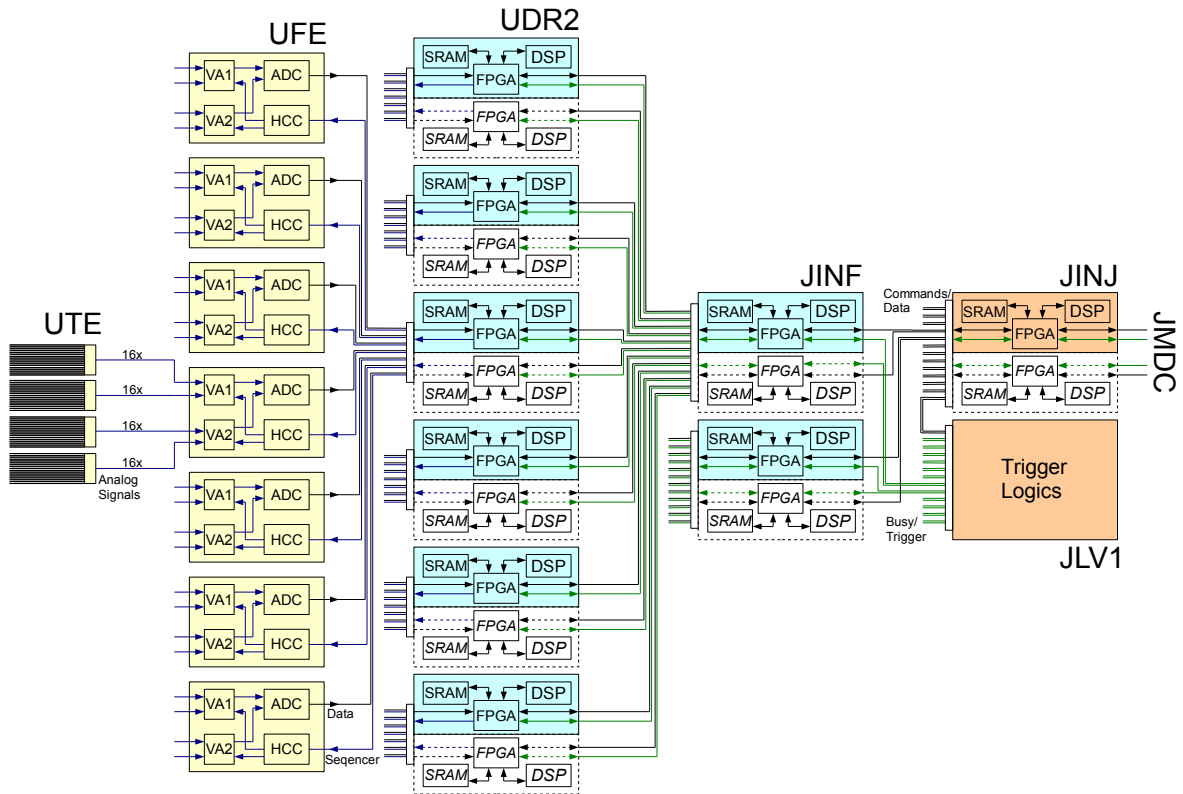


Figure 6.9: *Scheme of the TRD DAQ electronics. The analog signals are digitized on the front end already by the UFE board. The VA chips on the UFE board are controlled by the UDR2 sequencer implemented on the FPGA. After the data processing by the DSP the built event is stored in the memory of the UDR2 and can be retrieved by the JINF board. The entire TRD event is assembled by the JINJ. The event data block together with all other subdetectors can be requested from the JINJ by JMDC for transmission to the ground. A busy signal is generated on all levels by the FPGA and is analyzed by JLV1 electronics, which generates the trigger to the system.*

in the detector. This technology is already known from many applications on Earth, even when we do not notice it most of the time. In AMS-02 more than 300 processors of the type ADSP-2187L are running in parallel to process the data coming from the front end electronics of the detector.

### The ADSP-2187L Digital Signal Processor

The ADSP-21xx is the first processor family from Analog Devices. The ADSP-2187L architecture can be divided into the following functional units illustrated in figure 6.10. A complete description of the ADSP-2187L features is given in the hardware reference [6].

**Computational Units** All arithmetic operations are performed by three independent computational units. The ALU is responsible for the basic arithmetical and logical operations. These are addition and subtraction of 16-bit input values as well as bitwise logics like AND,

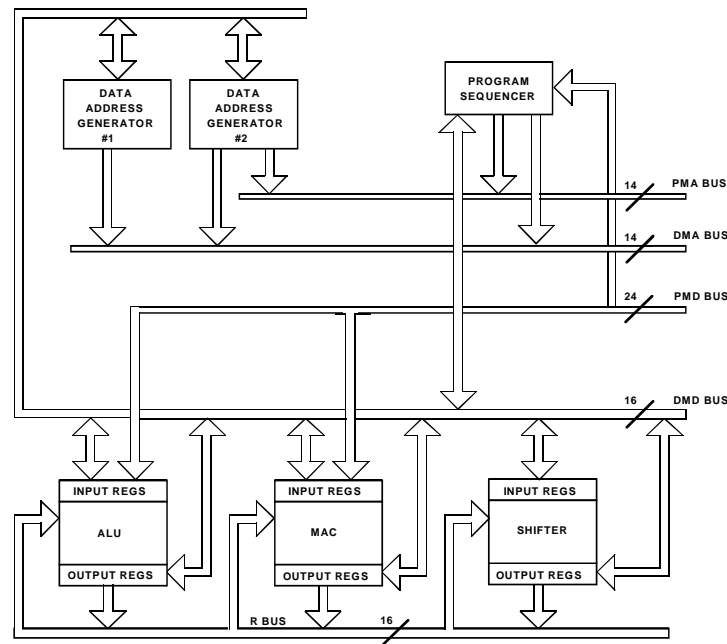


Figure 6.10: Core architecture of the ADSP-2187L. The function of each unit is briefly summarized in this section. [6]

OR and NOT. Furthermore the bitwise manipulation allows to set, clear or swap specific bits of an input value. The MAC is a multiplier and accumulator unit, which allows to multiply two registers. In the same step results can be added or subtracted from the result register with a 40-bit result data. The third unit, the barrel shifter, performs bit-shifts of the input register according to a given number of bits. This function is widely used to perform fast divisions, if the divisor is an exponent of 2. A result bus connects all three computational units, so that the result is directly available for the input in any other arithmetic operation in the next cycle.

**Data address generators** The ADSP-2187L chip-set possesses 32kByte of 24-bit program memory and 32kByte of a separate 16-bit data memory. The data address generators are responsible for the flow of the data from and to the computational units. They provide memory addresses during the transfer of the data to or from the input or output registers. Two DAGs are present, which can handle requests for two addresses at a time in parallel. The first DAG can access the data memory only, whereas the second DAG is able to access both data and program memory. This feature is utilized to make the code as fast as possible. In the same cycle, two registers can be written or read reducing the processing time by factor of two.

**Program Sequencer** The program sequencer controls the entire program and data flow. The actual program is stored in the program memory. The program sequencer reads all instruction one by one to the program data bus and executes them. A dedicated register holds the current position in program memory. The instruction in this position is copied to

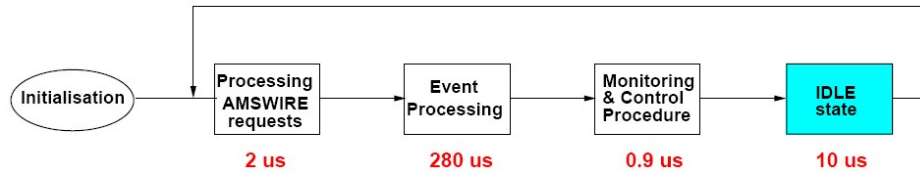


Figure 6.11: *Infinite loop of DAQ program. In between servicing AMSWire request and slow control procedures, control is passed to the event building routine, which is subdetector specific.*

the instructions register. In addition it can read the status registers of the ALU, registers for the loop counter and timer interrupts. In a stack the information about function calls, loops and breaks is stored. The program operation is controlled by processing this information by the logical unit.

There are a few main instructions to control the program sequence in a program. The JUMP instruction allows to jump to a given code marker in the program. Subroutines can be executed with the CALL instruction. After the execution the program pointer jumps back to calling point as soon as the RTS instruction is found in the subroutine. The DO..UNTIL instruction allows to implement loops with an arbitrary number of executions. The conditional instruction IF evaluates a given condition and correspondingly execute the specified command. Only result and status registers are allowed for the conditional input.

### 6.2.2 AMS-02 Flight Software Framework

The AMS-02 data acquisition and control network operates more than 600 independent computational nodes for the control and data acquisition tasks. In order to reduce the amount of design expenses all these nodes operate an ADSP-2187L digital signal processor, which also allows the development of a common software framework. A detector dependent part then is implemented to take into account detector specifics. This is the case on xDR level for the actual data processing, but also on JINF level, which is the top node in the subdetector electronics. Subdetector specific routines for initialization and housekeeping information are required.

Main part of the framework is the handling and processing of the AMSWire protocol between the nodes. A complete definition of AMSWire commands can be found in [35]. A main routine as shown in figure 6.11 continuously checks for any request from the nodes master. If a request interrupt is detected, the main routine passes control to the appropriate subroutine in the framework. Already on this level format errors are detected and corresponding reply is given. Data-blocks are protected by frame check sequence algorithms before the transaction to allow an identification of corrupted data.

The on-board flash memory can be accessed by a flash update utility included in the framework. It allows to store DAQ programs as well as calibration data or sets of configuration parameters. Several test routines are available to verify the functionality of the node.

On JINF and JINJ level the framework provides event building routines, which are common for all subdetectors on this level. Likewise error detection and event assembly information is processed in the same way on all the nodes.

The framework also takes care of the front end readout of raw data in xDRs. This data is

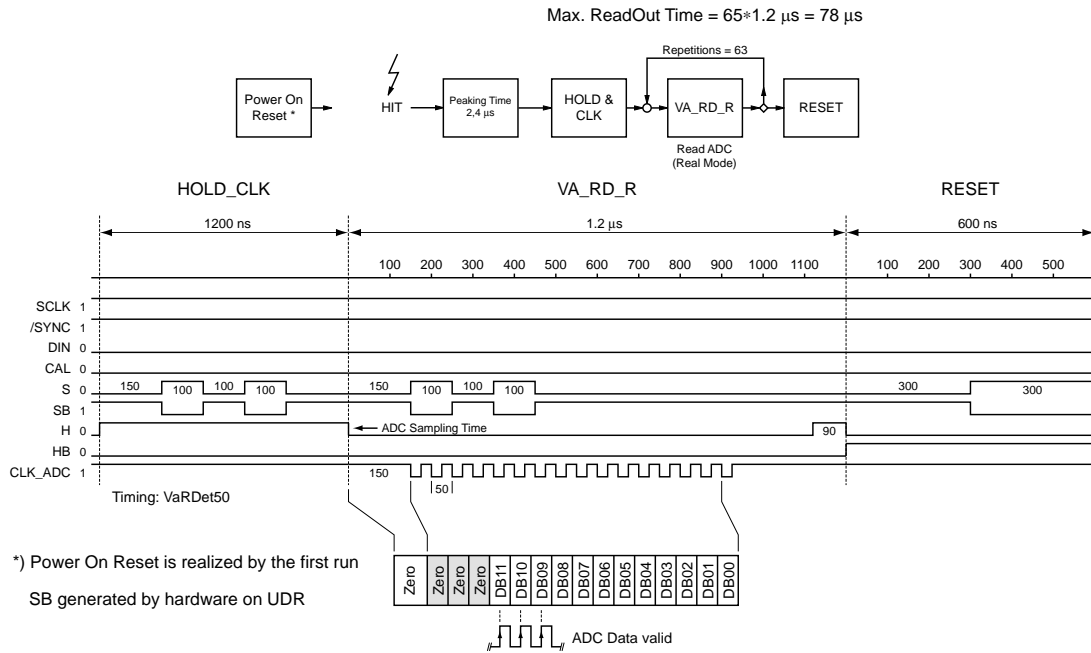


Figure 6.12: *Readout Sequence Definition for UFE Boards.*

stored in the raw event buffer of the xDR and is processed by the data reduction routine, which is described in the next section. If the processing mode is set to raw data, the routine is not called and the raw event fragment is assembled by the corresponding framework routine. A very basic version of the software framework, called ROM monitor, is stored with threefold redundancy in the flash memory and is booted automatically after a power cycle.

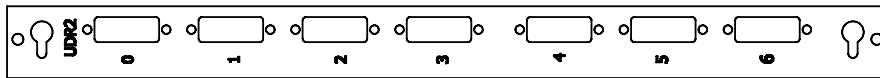
## 6.3 The Data Processing in the UDR2

This section describes the science data processing and data format as implemented on the on-board DSP of the UDR2 board. The software is based on the common framework as documented in [35]. There are two main UDR2 specific data processing routines. The data calibration routine is executed from time to time to determine the channel quality and pedestals. The data reduction routine processes the RAW data of each triggered readout preserving physics information. This description corresponds to version **v861E** of the UDR2 software.

### 6.3.1 The UDR2 Sequencer

The UDR2 sequencer collects the data from the seven front end links of the board independently from the DSP. The readout is triggered by the LV1\_OUT set by the JINF top node in the U-Crate. The delay between the LV1\_OUT signal and the HOLD to the UFE is about 180ns. The sequencer writes the data to the RAW buffer memory requiring guaranteed access to the memory at minimum every 60ns, which is taken into account by the DSP program. Figure 6.12 illustrates the readout sequence for the UFE board.

	15	14	13	12	11	10	9	8	7	6	5	4	3	2	1	0
0	SEQUENCER EVENT NUMBER															
	<i>UFE ADC Amplitude</i>															
1	0	0	0	0	UFE 0 CHANNEL 0											
...	...															
7	0	0	0	0	UFE 6 CHANNEL 0											
...	...															
442	0	0	0	0	UFE 0 CHANNEL 63											
...	...															
447	0	0	0	0	UFE 5 CHANNEL 63											
448	P3	P2	P1	P0	UFE 6 CHANNEL 63											

Figure 6.13: *Format of sequencer data in the RAW buffer.*Figure 6.14: *Front panel of the UDR2 board.*

### Sequencer Data Format

The length of the raw data fragment stored to the RAW buffer memory is fixed to 449 words. The first word is the event number assigned by the sequencer. The following 448 words contain the amplitudes of the 12-bit ADC as shown in figure 6.13. The data values follow the order, in which the same channel from all UFE links is read before proceeding with the next channel. The UFE identification is reversed with respect to front panel inscription, which means link 6 is read out first, link 0 last. Figure 6.14 shows a sketch of the UDR2 front panel with the seven connectors for cables to UFE boards. In the final vertical mounting position on the AMS-02 radiator link 0 is on bottom and link 6 on top of the U-Crate.

The four most significant bits (15-12) are set to 0 for the first 447 amplitudes. The last word contains four power bits (P0-P3) for the four UFE power groups of a UDR2 in bits 15-12. The corresponding bit is set to 1, if the front end power is on, and to 0 in case of a power loss during or in between the last and the current reading. P0 is set for link 0,1, P1 for link 2,3, P2 for link 4,5 and P3 for link 6.

### 6.3.2 The Data Calibration Routine

The pedestal calibration procedure as part of the data acquisition is executed from time to time to calculate and possibly adjust the pedestal position for each channel. The noise behavior of each channel before and after a common noise subtraction for each VA is determined. Furthermore the channel quality is tested and corresponding flags are set for the channel in the memory. All parameters are updated for use during the event processing when the data reduction routine is called.

### Description of the Calibration Routines

In each call of the calibration routine exactly one event is processed and the calibration routine is left afterwards. The calibration process word (shown in figure 6.16) allows to identify in the next call, in which step of processing the next event is expected. As soon as the calibration

procedure is completed or aborted either by a user interaction or an error, a calibration status word is updated. Additional precision is gained by a bit shift of the values retrieved from the UFE by 3-bit in all calculations.

**Pre-pedestal Calculation** In a first step preliminary pedestals are defined from a relatively small number of readings. This is necessary to allow the identification and elimination of incidentally hits during the pedestal calculation. Pre-pedestals are defined by determination of the minimum value out of eight readings for each channel

$$pPED_{ch} = \min(RAW_i) \quad , \quad i=1..8. \quad (6.1)$$

Once the detector will be kept in stable hardware conditions these pedestals will be loaded from flash or from the previous calibration. Only a small variation of pedestals is expected over time with a calibration interval of about one hour.

**Pedestal Calculation** During the pedestal calculation 1024 ( $2^{10}$ ) samples of each channel are read from the front end electronics. Since data is commonly uncorrelated with any particle crossing the detector, but triggered by a generator, one expects only very few physics signals in the data. A decision is taken for each sample, if a signal is likely in the data sample taking advantage of the pre-pedestal values according to

$$RAW_i - pPED_i > 60 \text{ ADC} \quad . \quad (6.2)$$

If a RAW data value is found above the cut, the entire sample is rejected for all channels of the UDR2. A maximum of 128 readings is repeated during the pedestal calculation before channels are used regardless of the above condition. In this case the channels are flagged with a likely signal in the pedestal calculation in figure 6.15.

Once 1024 samples are collected the average of each channel is calculated by

$$PED_{ch} = \frac{1}{1024} \sum_{i=1}^{1024} RAW_i^{ch}. \quad (6.3)$$

The calculated pedestals are stored to the memory to be available during the data reduction routine during the data processing.

**Raw noise calculation** The raw noise calculation is performed to test the channel quality and to identify dead or noisy channels for the final noise calculation. The raw noise, which means the common noise of each VA chip is not taken into account, is calculated from 1024 data samples. The raw data values are pedestal subtracted and averaged. A maximum value of 14 ADC is added. The raw noise of a channel is calculated by

$$\sigma_{\text{raw}_i} = \sqrt{X_i^2 - \bar{X}_i^2} \quad . \quad (6.4)$$

In a next step the channel quality is tested. The median noise of each VA chip  $\tilde{\sigma}_{VA}$  is determined and is taken into account in following conditions for dead or noisy channels:

$$\sigma_{\text{dead}} < \frac{1}{2} \tilde{\sigma}_{VA} \quad (6.5)$$

channel flag word	
bit	if set
0	user flag, ignore channel in DR
1	user flag, reserved (e.g. force output)
2	pedestal used with likely hit (PED>PED_p+60 ADC)
3	low/high pedestal (<60 or >2000 ADC)
4	raw noise dead (<0.5*VAmedian)
5	raw noise noisy (>3*VAmedian)
6	final noise dead (<0.5*VAmedian)
7	final noise noisy (>3*VAmedian)
8-15	reserved

Figure 6.15: Calibration channel flags.

and

$$\sigma_{noisy} > 3\tilde{\sigma}_{VA} \quad . \quad (6.6)$$

Dead and noisy flags are set according to table 6.15 and written to the memory available for the further processing steps. The raw noise values are written to the memory to be available for the data processing routine.

**Noise calculation** On the basis of the final calculated noise of a channel the data reduction routine identifies channels containing a hit, which means physics information. In the data of 1024 samples the pedestals are subtracted. In addition a common mode noise correction for each VA chip is performed. To exclude channels with an incidental hit in the detector the median of 32 channels is determined for each VA chip. It is  $CM_{VA} = \tilde{A}_{VA}$ . The common mode value is subtracted from each channel of the corresponding VA chip in order to correct for the common mode noise of the chip:

$$A_i^{VA} = A_i^{VA} - CM_{VA} \quad . \quad (6.7)$$

The final noise value is calculated from the corrected sample of 1024 values by

$$\sigma_{raw} = \sqrt{A_i^2 - \bar{A}_i^2} \quad . \quad (6.8)$$

The final noise values are written to the memory available for the data reduction hit identification. The calibration status word is modified indicating that the calibration calculation is completed. The calibration-completed-bit is set. A detailed description of the median determination and the square root calculation as implemented in the UDR2 DSP code is given in [43].

**Calibration Status** The calibration status word shown in figure 6.16 is updated either on calibration success or any unexpected abort of the calculation procedure. On an abort the corresponding abort bit is set. An abort can be triggered by a user interaction with the stop calibration command or by an error in the calculation process. A possible cause is an error in the sequencer or in development versions of the code an error in calculation algorithms. In case of an error the corresponding error bits are set in the status word. After power on of

Calibration progress word		Calibration status word		
bit	if set	bit	if set	
0	pedestal calculation completed	0	calibration running	
1	raw noise calculation completed	1	internal trigger used	
2	final noise calculation completed	2	calibration completed, wait for stop	
3	remaining events in current calibration routine	3	error in pedestal routine	
4		4	error in raw noise routine	
5		5	error in final noise routine	
6		6	<i>impossible</i>	
7		7	eventnumber error	
8		8	calibration aborted with error	
9	<i>impossible</i>	9	calibration aborted	
10		10	no calibration done after power-on	
11		<i>impossible</i>	11	<i>impossible</i>
12			12	
13			13	
14			14	
15	15			

Figure 6.16: Status words format of the calibration routine.

the UDR2 board the calibration is not performed automatically, thus a status word bit is set until a calibration has been performed.

The calibration status is stored to the memory available for the read calibration request and the processing routine. Figure 6.17 illustrates the calibration procedure.

### Calibration Commands

The calibration routine is controlled by the *calibration control command* (0x53) of the xDR framework, which starts or stops the calibration according to following parameters.

**parameter 0x0 - start calibration** In the first call the calibration routine in any case clears all channel flags excluding the user flags and resets the progress and status words in figure 6.16. The calibration-running-bit is set in the status word. A second parameter specifies whether an external (0x8000) or an internal trigger is used with the specified frequency.

**parameter 0x1 - stop calibration** The calibration stop command is required by the calculation routine to finalize the calibration. The calibration stop command may be received during a running or an aborted calibration (status bit 2 not set) or after the successful calibration (status bit 2 set). In the latter case the status word bit 2 is just reset and the status word will be 0x0000, otherwise the abort bit 9 is set and possible error bits are preserved.

**parameter 0x2 - create flash file** Available calibration results can be stored to flash by the create-flash-file command. A second parameter specifies the file name.

The results of the calibration procedure are read out by the *calibration status command* (0x13) of the xDR framework.

**parameter 0x0 - read calibration status** The read status command reads the calibration status words of the framework software.

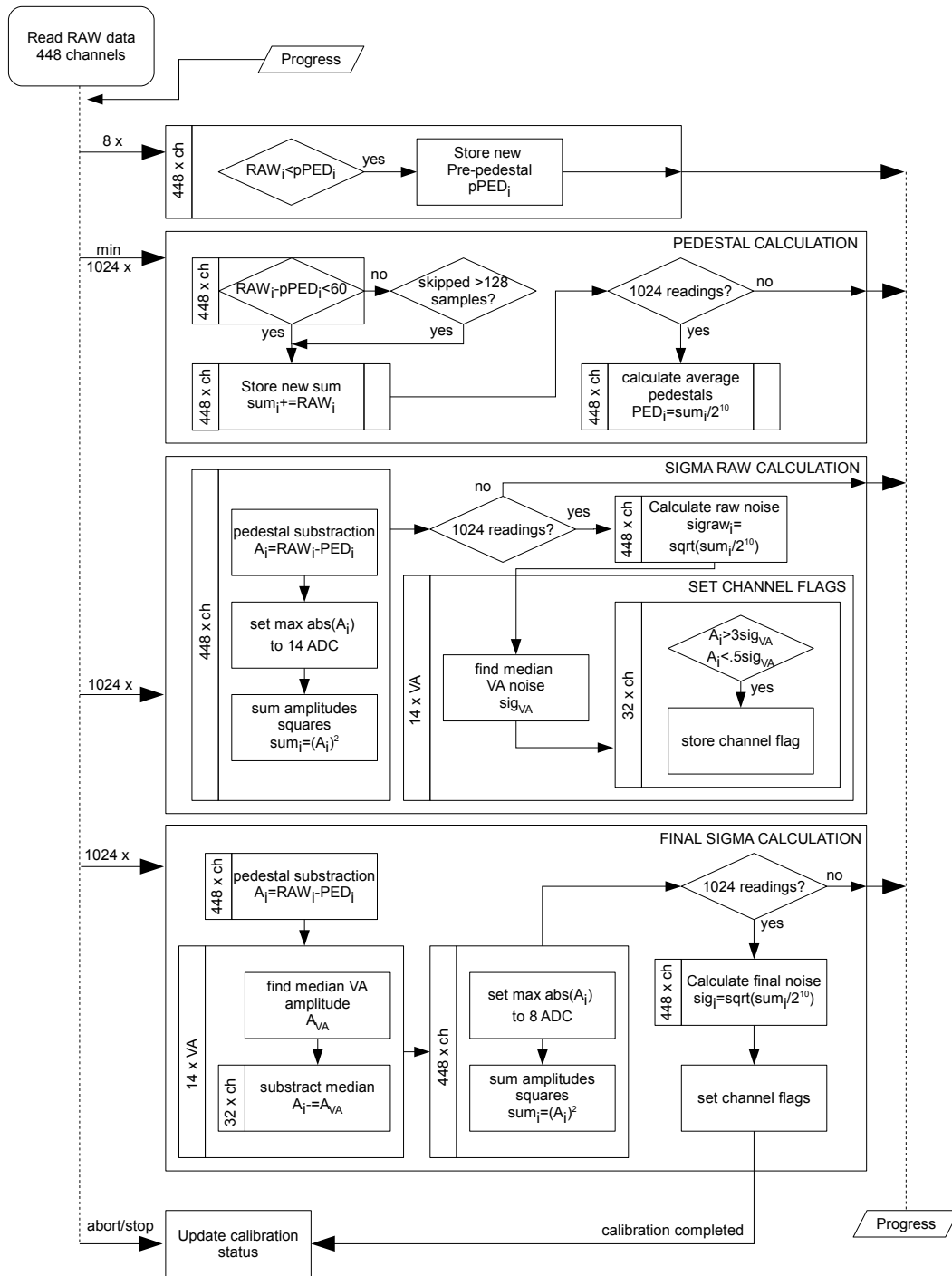


Figure 6.17: Simplified flowchart of the UDR2 data calibration routine. The routine consists of three main parts. During the pedestal calculation the electronic pedestals of all channels are determined. The two noise calculation routines determine the noise with and without a common mode correction. Each routine requires 1024 data samples. A process word stores the information about the progress of the calculation after each call of the routine. In each call exactly one reading is processed.

word (calibration running/failed)	word (calibration successful)	byte 1	byte 0
	0	pedestal (3-bit precision)	
	...		
	447		
	448	final noise (3-bit precision)	
	...		
	895		
	896	raw noise (3-bit precision * 10)	
	...		
	1343		
	1344	channel flags	
	...		
	1791		
0	1792	time of completion (16 LSBits)	
1	1793	time of completion (16 MSBits)	
2	1794	reserved	calibration id
3	1795	calibration progress	
4	1796	calibration status	

Figure 6.18: *Output format of the calibration results.*

**parameter 0x1 - read calibration results** The read calibration results command can be executed anytime after or before a calibration stop command is given. In the latter case the output consist of five words according to figure 6.16 indicating the progress and status. The same output is read after the calibration stop command, if the calibration was aborted by an error or by the stop command itself. If the calibration is successfully completed, the output consists of five blocks containing the values of pedestal, final and raw noise, the flags of each channel and the status output indicating the time of the calibration completion. The order of the values corresponds to the order of the sequencer readout shown in figure 6.13.

A full overview of the status output of the UDR2 calibration routine is shown in figure 6.18. In total a minimum of 3080 and a maximum of 3208 external triggers are required.

### 6.3.3 The Data Processing and Reduction Routine

The data processing routine is called each time a raw event data is found in the raw event buffer and the readout mode is not set to OFF (0x0). Depending on the readout mode one of the following routines is called. The general format of the data is shown in figure 6.19 composed of the processed data block, a build status word and the frame check sequence.

#### RAW Mode

The RAW mode data processing is part of the xDR framework. The unmodified sequencer data block as described in figure 6.13 is appended by the UDR2 build status word and a frame check sequence and stored to the processed event buffer. The total event length retrieved by the top node of the UDR2 board is 451 (0x1c3) words.

Processing Mode	Reply to read event request					
	ID	1w	448words	Nhits * 2words	1w	1w
OFF	0	x	x	x	STAT	FCS
RAW	1	EVNO	SEQUENCER DATA	x	STAT	FCS
COMPRESSED	2	EVNO	x	CHANNEL/AMP	STAT	FCS
MIXED	3	EVNO	SEQUENCER DATA	CHANNEL/AMP	STAT	FCS

Figure 6.19: *Format of the TRD event data. Four processing modes are implemented in the UDR2 event processing routine.*

### COMPRESSED Mode

The data reduction routine is called each time raw event data is found in the raw event buffer and the data processing mode is not set OFF or to RAW mode. The processed event is stored into the built event buffer and can be retrieved by the JINF together with event fragments from the other UDR2 boards. The data processing by the DSP of the UDR2 consists of three main parts, which are the pedestal subtractions of the ADC value of each channel, the common mode correction, which applies for each VA chip and the hit identification. Though the DSP needs to take into account some further actions to decrease the average and peak event size for TRD event data, which is affected by UFE specific problems described in section 7.1.2. A simplified overview of the UDR2 data reduction routine is presented in figure 6.20. The average processing time for an event is about 280 microseconds in the code version v821E.

In the case invalid calibration data is found in the program memory the data reduction routine is aborted and a corresponding error bit is set in the build status word. The validity is checked with the calibration status word described in figure 6.16.

**Pedestal Subtraction** If valid calibration results are available in the program memory, the pedestals are subtracted from the raw data loaded from the raw event buffer. Additional precision is gained by a bit shift of the read sequencer values by 3-bit in all following calculations. The pedestal subtraction is done for all 448 channels in a loop according to

$$A_i = RAW_i - PED_i \quad . \quad (6.9)$$

The pedestal subtracted amplitudes are stored to the data memory for further processing.

**Common Mode Correction** An initial event data characterization is necessary due to a problem of the UFE board with fast consecutive triggers. Firstly M-type UFE boards with channels showing downwards shifted pedestals are identified and excluded from the correction, and secondly commonly up shifted pedestals on the S-type UFE boards are identified to allow an extended correction. Since in both cases only the first VA chip of a UFE board is affected, a characterization is done for the first 32 channels of each UFE only. The number of channels below and above 12 ADC units is counted separately for each first VA chip of a UFE board:

$$N_{pos} = \sum_i (A_i > 12ADC) \quad N_{neg} = \sum_i (A_i < -12ADC) \quad . \quad (6.10)$$

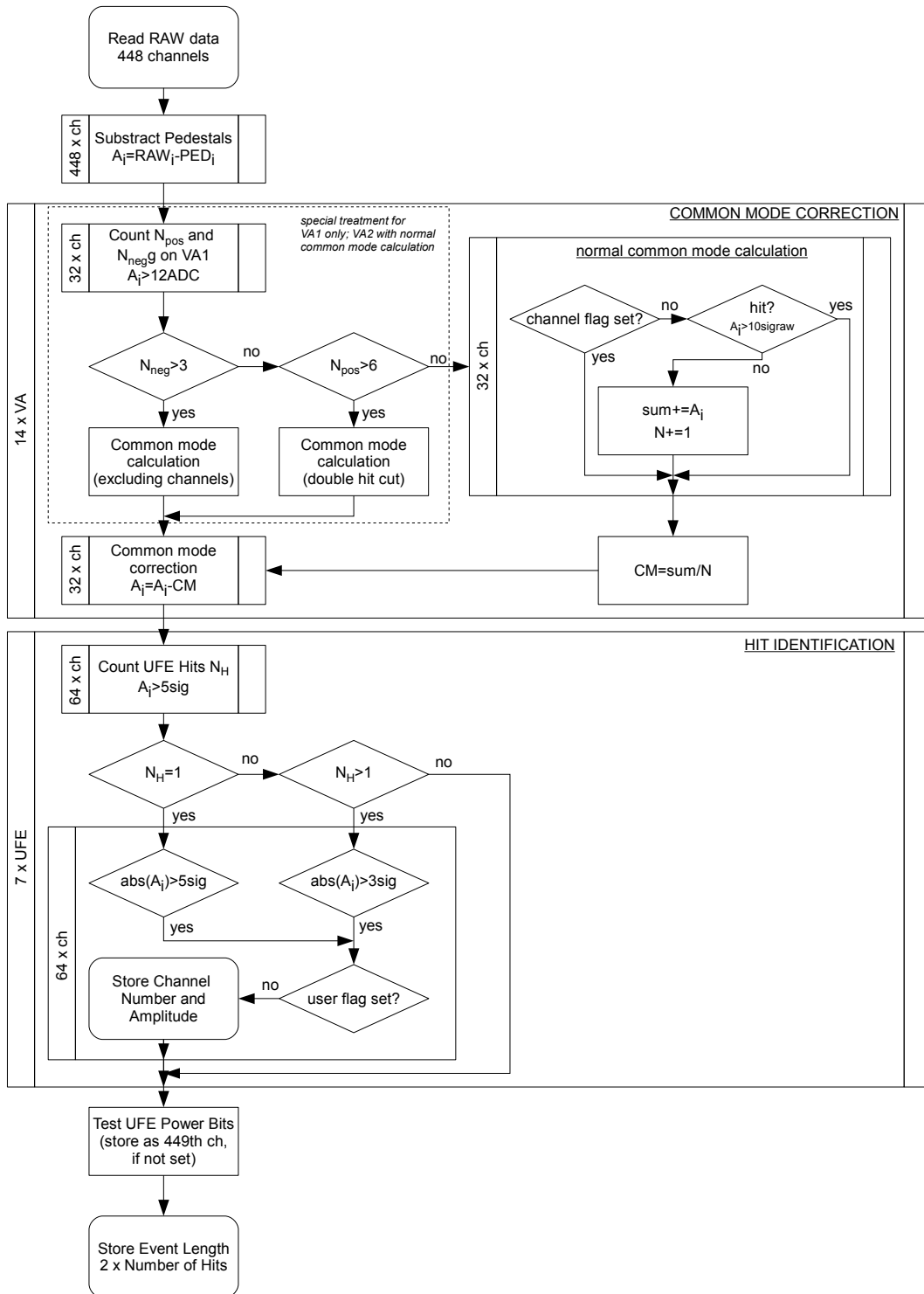


Figure 6.20: Simplified flowchart of the data reduction routine of the UDR2. Before the hit identification routine the raw data values retrieved from the front end electronics are pedestal subtracted and a common noise correction for each VA chip is applied.

The results are stored for each of the seven UFE boards to the memory available for the common mode correction routine.

The common mode correction is calculated individually for each VA chip. Hit channels are excluded from the calculation, if they do not meet the condition

$$|A| < 10\sigma_{raw} \quad . \quad (6.11)$$

Furthermore channels are excluded from common mode calculation, if a channel flag is set by the calibration procedure. The common mode is calculated from the remaining data values  $A^{nc}$  by

$$CM = \frac{1}{n} \sum_{i=1}^n A_i^{nc} \quad . \quad (6.12)$$

A modified calculation applies for  $N_{pos} > 6$ , when an extended hitcut with the condition  $A < 20\sigma_{raw}$  is used, and for  $N_{neg} > 3$ , when channels according to a predefined pattern are excluded by default (these are channels 18, 23, 28, 29, 30 and 31).

The amplitudes then are corrected for each VA chip according to the results

$$A_i^{corr} = A_i - CM \quad . \quad (6.13)$$

The corrected amplitudes are stored to the data memory for further processing.

**Event Data Characterization** In order to decrease the event size caused by a non-Gaussian noise of the UFE without compromising the information for the physics data a variable cut during the hit identification is applied. Channels with a low signal can be considered as noise, if no other hit channel is found in the UFE, whereas valuable information would be lost, if this information is discarded near to a track. For this reason a tentative counting of hit channels is performed to identify UFEs with possible track data by

$$N_{UFEHits_{5\sigma}} = \sum_i (A_i^{corr} > 5\sigma_i) \quad . \quad (6.14)$$

This information is calculated for each UFE and stored to the memory available for the hit identification routine.

**Hit Identification** The hit identification is done separately for each UFE board. The number of identified hits in the previous event characterization is checked. In the case more than one hit was identified the following more strict condition applies for the hit identification

$$|A_i^{corr}| \geq 3\sigma_i \quad , \text{ for } N_{UFEHits_{5\sigma}} \geq 2 \quad , \quad (6.15)$$

otherwise

$$|A_i^{corr}| \geq 5\sigma_i \quad , \text{ for } N_{UFEHits_{5\sigma}} \leq 1 \quad (6.16)$$

applies. Amplitudes identified as a hit are written to the built event buffer. Therefore the channel number (9-bit) word assigned by the UDR2 is preceding its amplitude according to a consecutive counting of channels from 0 for channel 0 on the front panel link 0 to 447 for channel 63 on the front panel link 6 in the order of the sequencer readout shown in figure 6.21.

UDR2 Link 6	Channel 0 to 63 (0x0 to 0x3F)
UDR2 Link 5	Channel 64 to 127 (0x40 to 0x7F)
UDR2 Link 4	Channel 128 to 191 (0x80 to 0xBF)
UDR2 Link 3	Channel 192 to 255 (0xC0 to 0xFF)
UDR2 Link 2	Channel 256 to 319 (0x100 to 0x13F)
UDR2 Link 1	Channel 320 to 383 (0x140 to 0x17F)
UDR2 Link 0	Channel 384 to 447 (0x180 to 0x1BF)

Remark: due to reverse sequencing, UFE on Link 6 is referred to as UFE0 and so forth

Figure 6.21: Channel identification in the compressed mode data.

	(bit 8-0)	(bit 14-0)	
<b>word 0</b>	1st Hit Channel No.	1st Hit Amplitude	<b>word 1</b>
<b>word 2</b>	2nd Hit Channel No.	2nd Hit Amplitude	<b>word 3</b>
...	...	...	...
<b>word 2*N-2</b>	Nth Hit Channel No.	Nth Hit Amplitude	<b>word 2*N-1</b>
<b>word 2*N</b>	Channel No. = 449 (0x1c1)*	power bits P3-P0 (bit 3-0)*	<b>word 2*N+1</b>

\* output only in case any power bit P3-P0 is not set

Figure 6.22: Format of the UDR2 event data fragment in the compressed mode.

**UFE Power Bit Check** The UFE power bits P3-P0 read by the sequencer with the last data value are checked at the end of the data reduction procedure. In the case one of the bits is not set indicating a power cut all four power bits are written to the output in bits 3-0 as the amplitude word of the 449th channel. Figure 6.22 shows the format of the event data output in the compressed mode.

### MIXED Mode

If the processing mode is set to MIXED mode, the COMPRESSED data event fragment described in the previous paragraph is appended to the unmodified sequencer RAW data. The length of the MIXED mode event fragment consists of variable number of words, but is of minimum size of 451 words in the case no hit has been identified by the reduction routine.

### 6.3.4 The DAC Calibration Routine

The DAC<sup>1</sup> calibration routine is executed on request only, which main purpose is to analyze the detector state. The procedure is part of the diagnostics tools, which are used in the case of problems seen in the data. The DAC calibration routine is called by the SubD-procedure AMSWire command.

The DAC calibration takes advantage of a UDR2 board feature. A DAC mounted on the UDR2 boards allows to apply a configurable pulse to the input of the VA chips on the UFE boards. The DAC pulse then is injected into all 64 channels of the UFE and read back by the calibration sequence. Figure 6.23 shows the calibration sequence definition of the UFE board. A complete calibration sequence takes about 1.2 ms for a VA chip. With these means

<sup>1</sup>digital to analog converter chip

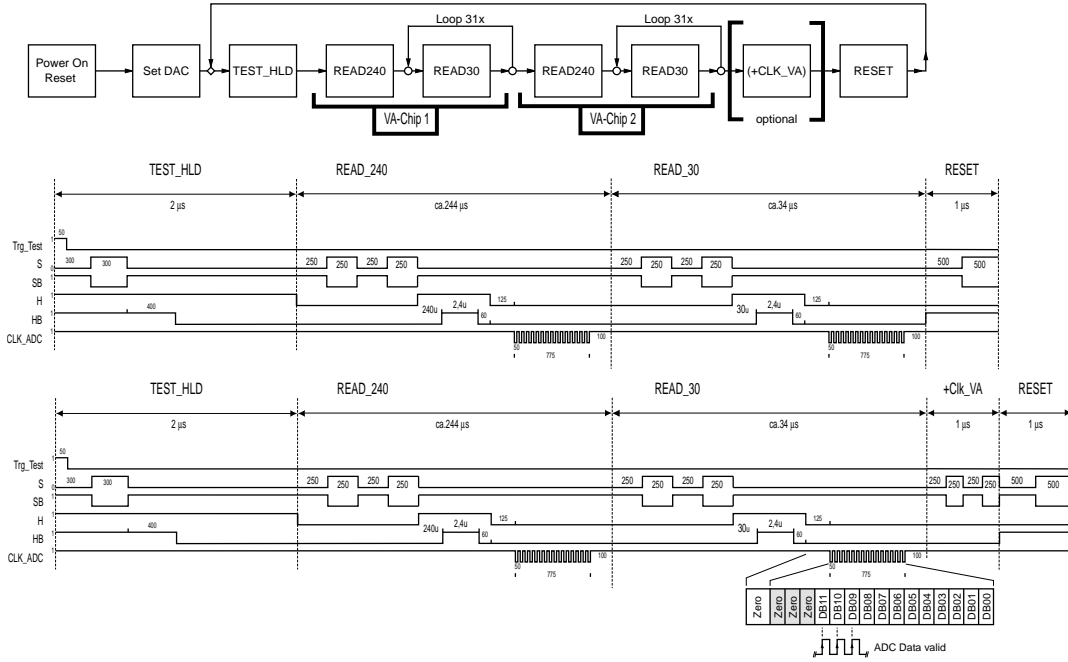


Figure 6.23: UFE DAC calibration sequence

the DSP calibration procedure is able to perform a test of the channel functionality and the gain. Two modes are implemented to call the routine.

The first mode allows the offline analysis of the channel behavior analyzing the output of the calibration routine. A certain DAC value can be specified on the call of the routine as a parameter, which is set by the DSP on the UDR2 DAC. Similarly to the pedestal calibration routine the mean value of the channel output with the applied DAC level in repeated readings is calculated. The pedestal subtraction is done for all 448 channels in a loop

$$A_{ch} = RAW_{ch} - PED_{ch} \quad . \quad (6.17)$$

Once 128 data samples are collected the average of each channel is calculated by

$$A_{ch}^{DAC} = \frac{1}{128} \sum_{i=1}^{128} A_i^{ch} \quad . \quad (6.18)$$

The number of readings from which the DAC amplitude is averaged is limited due to the long duration of the UFE calibration sequence of about 2.6 ms for both VA chips. The results are written to the memory and can be read out by the corresponding Subd-procedure read request AMSWire command.

In a second mode the DSP already tests the linearity of the ADC autonomously. Therefore the correlation between the input pulse set by the DAC and the output ADC value is calculated. This preferably reduces the amount of commands, which have to be send to the UDR2 via the AMSWire links, since the calculation is just initiated. The slope of the ADC readout as a function of the DAC setting is evaluated from three readings with different DAC setting.

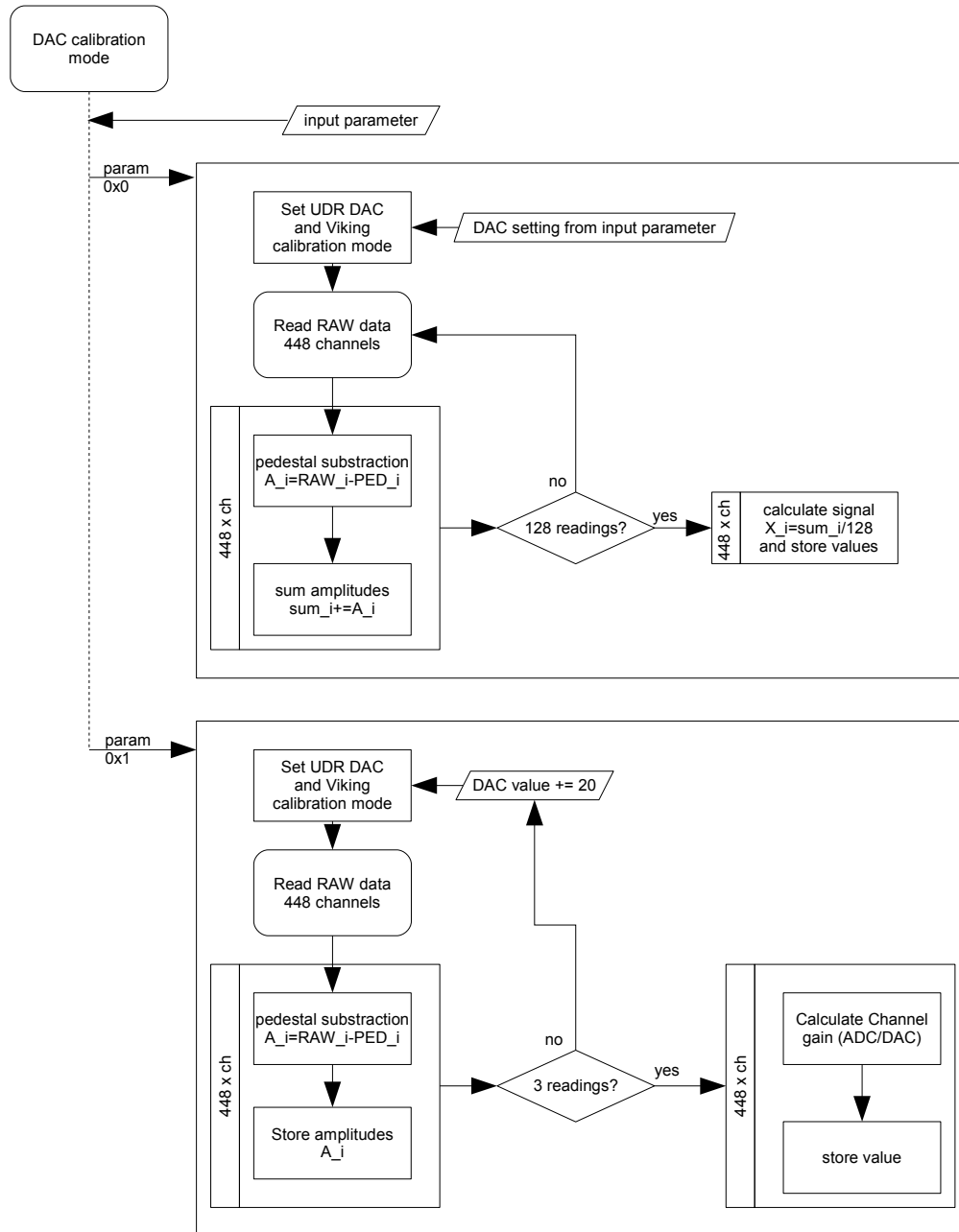


Figure 6.24: Flowchart of the DAC calibration routine of the UDR2. Two modes of the DAC calibration are implemented, which can be executed with the corresponding command parameter. In a first mode the DAC amplitude of a specified setting is calculated from a sample of 128 readings for offline analysis. In the second mode the ADC gain is calculated by the DSP from different DAC settings in order to test the linearity of the ADC.

In a first step the DSP verifies, that the DAC setting of 0x0 corresponds to an ADC response of 0x0. The pedestal subtractions 6.17 is performed for acquired ADC values of all channels. The DSP tests, if the amplitudes of all channels are within  $5\sigma_{ch}$  noise interval, otherwise an error is reported.

Starting at a DAC setting of 0x0, the value is increased in two more cycles by 0x20 in each step and the slope is simply calculated by

$$m_1 = \frac{RAW_{0x40} - RAW_{0x20}}{0x20}, \quad (6.19)$$

where the division can simply be implemented as a bit-shift. The value is written to the memory for the readout by the corresponding SubD-procedure read request. In the case a single channel does not show linearity or has any other unexpected behavior, it can easily be identified in between the other values.

A simplified overview of the UDR2 DAC calibration routine is presented in figure 6.24.

## 6.4 Subsystem Status Monitoring by the QList

During the data acquisition the system has to be kept in stable conditions, which makes it necessary to monitor variable system parameters. The QList is a list of commands, which are executed from time to time independently from JMDC or the ground control by the JINF nodes autonomously. The purpose is to collect system status information, thus the commands in the list are mainly of read type. The necessity of such an approach becomes clear considering the special location of the AMS-02 instrument. Due to the operation in space the bandwidth for telemetry data to the experiment is very limited. The data about the system status must be send continuously without request from the ground. In principle

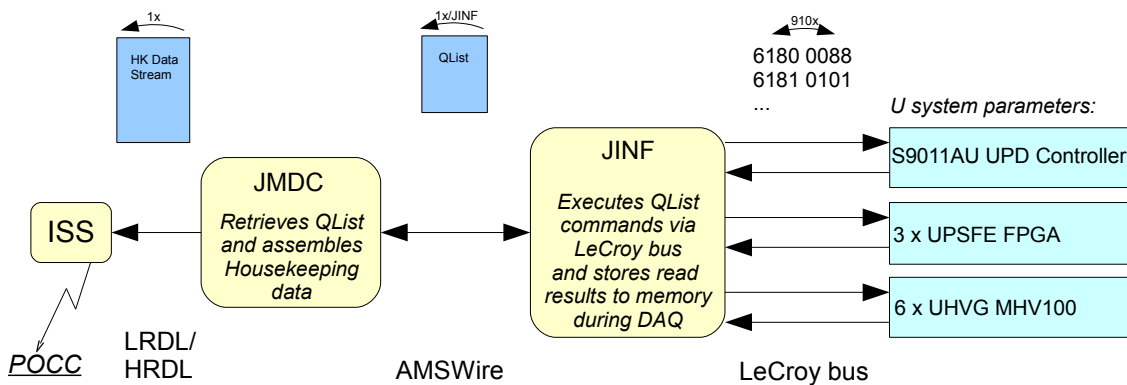


Figure 6.25: *Housekeeping data acquisition. The system parameters are collected independently and synchronized with the data acquisition by the JINF executing LeCroy commands summarized in a QList. Only a single request is necessary by the top node to read all results in the QList minimizing the interference with the science data collection. JMDC analyzes the retrieved QLists fragments from the subsystems, strips off default data and assembles the housekeeping data for the entire system. The housekeeping data is sent via the LRDL/HRDL links to payload operations control center (POCC) for further analysis and recording.*

	f	e	d	c	b	a	9	8	7	6	5	4	3	2	1	0			
0	0	1	ATT			FILE NAME										0	0	0	1
1	0	1	Segment length (N-2 words)																
2	0	0	1	0	0	0	0	0	0	0	0	0	0	0	0	0			
3	Number of QList Commands																		
...																			
i	Execution frequency, 8MSbits							0	Attribute			Location		Type					
i+1	F	Number of repetitions / Time offset																	
i+2	Execution frequency, 16LSbits																		
i+3	First parameter value																		
i+4	Second parameter value																		
...																			
N	FCS																		

Figure 6.26: *Format of a QList entry of the JINF.*

also JMDC is able to collect this data, since it is the top node for all subsystems in AMS-02, but a further aspect is, that due to a weight reduction, both slow control commands and the event building is processed by the same DSP on the JINF boards. Furthermore the same AMSWire links are used to transmit slow control commands. For this reason the JINF software is designed to handle the coordination of slow control reading by the QList and the data processing by its own convenience. In the end JMDC will use the same AMSWire links to read both the event fragments and the available slow control data fragments from JINF nodes. Figure 6.25 shows a scheme of the approach of the housekeeping data acquisition by the QList.

The QList procedure is designed to consume only a minimum processor time of the JINF's DSP in order to minimize the interference with the physics data acquisition. Only one command from the QList is processed in the main loop shown in figure 6.11 at a time. Main source for slow control data are nodes on the LeCroy buses connected to the JINF board. The format of a QList command allows to specify a command frequency and the number of repetitions. Once the command has been executed the next execution time is stored on each call corresponding to the execution frequency. On each pass the next execution time is compared with the node base time and the command is accordingly executed again. For execution frequencies in the order of  $100\text{ s}$  the average time spend by the DSP is about  $0.9\mu\text{s}$ . This is accomplished by initiating the transaction on the LeCroy bus only, when a command is processed. An interrupt routine sets a completion flag when the transaction is completed and the QList can be updated by the slow control procedure. This saves time, since a transaction on the LeCroy bus typically takes about  $150\mu\text{s}$ , while the DSP is free for event building or servicing AMSWire requests. The detailed format of the QList is specified in figure 6.26. A maximum of 910 fixed-format commands can be included in QList, which might also be combined in groups with the same execution parameters. An example of the data collected by the QList during the data acquisition of the pre-integration phase is shown in section 7.2.

Though QList is designed for slow control data collection, in current operation of AMS-02 it is also utilized to initialize system hardware, since it is not constrained to read-only commands. In future releases system initialization will be moved to a configuration procedure, which reads and sets a configurable set of parameters by detector dependent subroutines.

15	14	13	12	11	10	9	8	7	6	5	4	3	2	1	0	Area
L	SIZE															Primary Header
SIZE_EXT (if L=1)																
RR	RW	NODE										TYPE				
TYPE_EXT (if TYPE=0x1F)																
FBI/STATUS					TAG											Secondary Header
TIME (MSB)																
TIME (LSB)																
DATA ...																Data

Figure 6.27: *Format of an AMS data block. [11]*

## 6.5 Data of the TRD in the AMS-02 Data Format

The final question a user of AMS-02 certainly might have is, how to get the data he is interested in. As discussed the front end electronics of each subdetector digitizes the analog signal, which is digitally processed by the xDR nodes. The CDDC nodes, which are subdetector JINFs and the JINJ assemble the event data to event fragments. These fragments or directly the xDR data, which is format compatible since all nodes are running the same framework software, is received on request by the AMS-02 main DAQ computer JMDC.

JMDC is responsible for the final event building of an AMS-02 physics event data block. Additional level-3 trigger processing might be active to achieve an additional data reduction. The processed event is packed into a standard AMS block format, which will be discussed in the following more in detail down to the node data. The basic structure is shown in figure 6.27.

The standard AMS block data is a data block of variable length and of arbitrary data type. It consists of a primary and a secondary header and the data part. In the primary header the length of the entire block is specified as well as the replying node ID and the type of data. The secondary header gives information about data block time and allows to identify the reply by a tag information. The data part contains the data specified by the type, which can be housekeeping data, a command reply or science data.

Only and at least one physics event will be packed into an AMS block of the event data type. Depending on the mode of operation the data part may contain several data groups organized in sub-blocks. The normal operation mode should only deliver only one detector data sub group, the one from the active JINJ, which collects and assembles the data from all connected JINFs and xDR nodes. In this case the data part of a science data AMS block consists of the JMDC data sub block, the detector data group sub-block of the JINJ and a level-3 trigger sub-block.

The JMDC sub-block contains the event information and is created for each event by the active JMDC. Among other information the run number and the event number is specified for the event fragment. The run number is assigned on the start of a run by JMDC and a user specified run tag can be added. The run number starts with 1 for each run. Optional GPS data can be appended. A primary AMS block header is prepended.

15	14	13	12	11	10	9	8	7	6	5	4	3	2	1	0
L	SIZE														
RR=1	RW=0	NODE=Top node of the group										TYPE=1			
Event Number															
Data from DSP (xDR or CDDC) node 1															
...															
Data from DSP node N															
Node Status Word (from top node of the group)															
CRC 16 (from event number up to status word)															

Figure 6.28: AMS sub-block format. During normal operation the only sub-block is the JINJ sub-block containing the JINF and SDR board data.

The detector data group sub-block may contain data from any node specified as a data taking group. Most commonly the data is received from a JINJ node, which sends a buffered event fragment. The data is previously collected from its slaves and assembled by the DSP. The JINJ and JINF data format contains the event number assigned by the DSP, which can be crosschecked with the event number assigned by JMDC. In the data body the data from the replying nodes are combined. A status word from the top node of the group and a frame check sequence is appended. A primary AMS block header is prepended as shown in figure 6.28.

The format of the slave DSP data body is detector dependent on the xDR level. In the following the UDR2 format is focused. In common is the information about the fragment size and the appended node status word. Actually also the xDR node data includes the event number assigned by the DSP and a frame check sequence, but this information is stripped off by the master node and combined in its event fragment. In the case of inconsistency the corresponding error bits are set in the master node status word.

For future analysis of the event data the AMS block bit-stream will be converted into ROOT file databases, which allow an easy access to the data by analysis tools. A preliminary version is available, but still is subject to the current development of software. A documentation can be found in [14].

### TRD Channel Table

In order to read out the 5248 straw tube channels the TRD front end consists of 82 UFE boards connected to twelve UDR2 boards. Installed to RAM and WAKE main radiator two U-Crates house six UDR2 boards each. Table 6.30 defines the flight configuration for the physical interconnection of UDR2 and UFE boards, which allows to uniquely identify a hit channel detected by the UDR2 data reduction routine with a tube position in the detector. The labeling of the UFE boards is based on figure 6.29, which shows the position of the 82 UFE boards attached to the 82 straw tube modules. The TRD can be divided into five layers of four sub-layer straw tube modules. The modules in layer 1 and 5 are rotated by 90° with respect to the layers 2, 3 and 4.

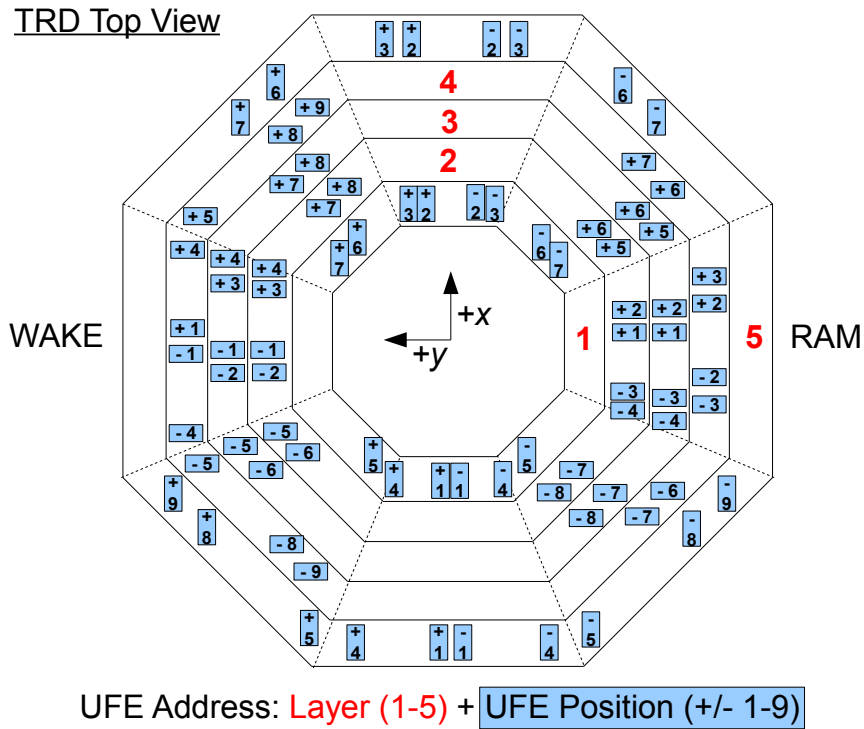


Figure 6.29: Map of the mounting position of the UFE boards on the TRD. The UFE address is used to identify the chamber, which is connected to a UDR2 front end link in table 6.30. [49]

RAM (U1-Crate)						
UDR2 Slot #	9	7	6	4	3	1
Top	5-7	5-6	4+2	4+3	3-8	3-7
	5-3	2+6	3+2	4-7	2-8	5-9
	5-2	2+5	3+1	4-6	2-7	5-8
	4+7	1-7	2+2	4-3	1-5	5-5
	4+6	1-6	2+1	4-2	1-4	5-4
	3+6	1-3	2-4	3-4	1-1	5+1
Bottom	3+5	1-2	2-3	3-3	NC	5-1
WAKE (U0-Crate)						
UDR2 Slot #	9	7	6	4	3	1
Top	3-6	3-5	4-4	4-5	2+7	2+8
	5+9	2-6	4+1	4+5	1+7	5+7
	5+8	2-5	4-1	4+4	1+6	5+6
	5+5	1+5	3-2	3+4	1+3	5+3
	5+4	1+4	3-1	3+3	1+2	5+2
	4-9	1+1	2-2	2+4	3+8	4+9
Bottom	4-8	NC	2-1	2+3	3+7	4+8

Figure 6.30: Table of the UDR2 link to UFE assignment. The UFE boards are labeled according to figure 6.29. [49]



## Chapter 7

# Cosmic Ray Test and Data Analysis with the TRD

*The transition radiation detector and the associated readout electronics have been developed and built under responsibility of RWTH Aachen and the University of Karlsruhe. A close cooperation was substantial during all phases of the process in order to guarantee the compatibility of the components. Therefore a test of the completed detector had been set up at facilities of the RWTH Aachen before the flight model of the readout system and the detector itself were delivered to the AMS-02 assembly area at CERN. For this purpose the qualification model of the readout electronics was attached to the detector and run control software was prepared. In the following details of the setup and the results of this four-week detector run are given. Detector distinctive features identified during the operation and solutions to handle them are described in the next section.*

*In the second part of the chapter the data acquisition during the AMS-02 pre-integration phase is presented. In contrast to the Aachen standalone test the TRD was operated through the final DAQ chain of the AMS-02 readout system. The TRD was the only subdetector, which was operational throughout the pre-integration phase of AMS-02. The main intention of this phase was to solve problems showing up during the mechanical integration and to develop procedures and software of the AMS-02 DAQ system. Nevertheless also production runs could be performed allowing a more detailed analysis of the detector characteristics.*

### 7.1 The TRD Cosmic Ray Test at RWTH Aachen

The standalone test of the transition radiation detector was performed subsequent to the final assembly of the TRD at RWTH Aachen in October 2007. A dedicated environment was set up to provide a trigger for crossing cosmic ray particles. For the detector control and the readout of the TRD two QM2 U-Crates were available allowing the read out of all 82 front end boards of the detector. The data acquisition phase roughly covered four weeks. During this time debugging of the full system and a detailed analysis of failures could be carried out.

#### 7.1.1 TRD Standalone Test Setup

The TRD was assembled mounted inside an aluminum transport frame in a cleanroom environment. It is kept mounted to it during all following standalone phases. For the detector

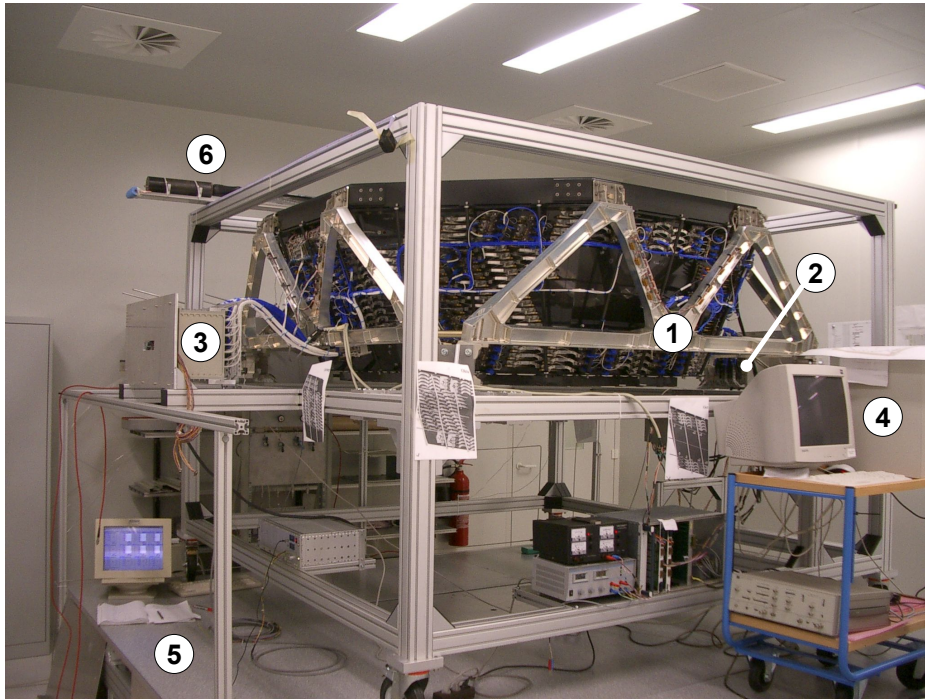


Figure 7.1: *The TRD standalone readout test at RWTH Aachen in 2007. The picture shows the detector and the TRD M-structure (1) mounted inside an aluminum transport frame. The readout is accomplished by the qualification model of the U-Crate powered by a UPD box (2) and an independently powered U-Crate equipped with QM1 and FS electronics boards (3), which are read out via the AMSWire links by the DAQ computer (4). Trigger to the system is provided by scintillator panels deployed below the floor (5) and a small movable one on top of the transport frame (6).*

control and readout two qualification model U-Crates are available mounted on both WAKE and RAM side of the TRD to the transport frame. The mounting position corresponds to the relative position on the flight radiators of AMS-02. This allows a final routing of the DAQ and high voltage cables already during the TRD assembly. The QM2 U0-Crate is powered by a fully functional QM2 UPD box, whereas the U1-Crate is power by a commercial power supply.

The trigger for cosmic rays is provided by scintillator modules underneath the TRD. The entire floor below the TRD had been equipped with scintillator panels. A veto detector was not available, which could reject horizontal particles triggering the scintillators, but do not hit the TRD at all. However it was possible to deploy a second scintillator layer with the dimension of 220 times 40 cm on top of the TRD frame. In coincidence with the bottom layer only vertical tracks can be selected, but with a much lower rate due to the reduced sensitive area. The position of the top layer panel could be varied to allow to scan certain areas or chambers of the TRD. Figure 7.1 shows a picture of the TRD operated standalone in the cleanroom at RWTH Aachen in October 2007.

## DAQ System

The readout of the TRD was accomplished by two qualification model U-Crates. A test with the flight model hardware of course would have been desirable, but could not be provided since the integration work on AMS-02 had already started and should not be delayed by the subdetector tests. The second option was to use the qualification model of the U-Crate. A second qualification-like U-Crate consisted of QM1 crate mechanics equipped with a mix of QM 1 and 2 and flight spare boards powered by a custom made power supply with the appropriate commercial DC/DC converters.

Each of the crates is connected to one link of the AMSWire-EPP<sup>1</sup> converter box, which connects both U-Crates to the main DAQ computer. The ground support DAQ computer has to assemble the event fragments retrieved from both crates to a single event data block. This functionality is implemented into a run control software. Figure 7.2 shows the scheme of the event building procedure in the TRD run control. Apart from some minor simplification this is very similar to the event building procedure in the AMS main DAQ computer.

The run control software package for the TRD standalone test provides both a graphical user interface and a set of command line tools used for a remote control. It provides an easy access to the main configuration parameters of the TRD DAQ, which are the readout mode, calibration execution, setting of trigger delay and the logging of all actions. In addition it takes over slow control tasks such as the initialization of UHVG boards and the ramping of the high voltage to given values. The data is stored to disk in a simplified AMS block format consisting of a header with the block time, node and event size information and the two JINF sub-blocks. A routine continuously checks for new data on the nodes connected to the AMSWire-EPP interface box. As soon as data is found in one JINF it tries to retrieve the data from the missing JINF node. The command line tools were developed to allow a remote control of the TRD with equal features, which becomes necessary during the operation at CERN in the integration cleanroom. The command line tool `uhv` initializes and controls the TRD high voltage on UHVG boards. Optionally it uses calibration parameters for the individual channels of the QM2 or FM UHVG boards. The command line tool `trdrun` reads a configuration file to initialize the main DAQ parameters of the TRD readout system. The output data format is the standard AMS block format, which brings some advantages. Already existing programs can be used without modification. Figure 6.28 shows the standard sub-block science data format. The two TRD JINF sub-blocks are packed into a standard science data block with one sub-block for each JINF. The JLV1 sub-block is removed.

### 7.1.2 Data Analysis and Results

Between September and October 2007 the TRD delivered an almost continuous stream of data with about 50 million tracks of cosmic ray particles, although the data acquisition from time to time had to be interrupted to investigate and fix problems discovered in the DAQ chain or the hardware. A first view to the data was directly possible in an event display developed for the cosmics test. This graphical presentation allows to quickly evaluate data coming from the detector. Furthermore it is helpful for the investigation of recognized problems of the data acquisition or the recorded data itself.

The event display is based on the ROOT software package and takes advantage of the

---

<sup>1</sup>Enhanced Parallel Port, computer standard interface

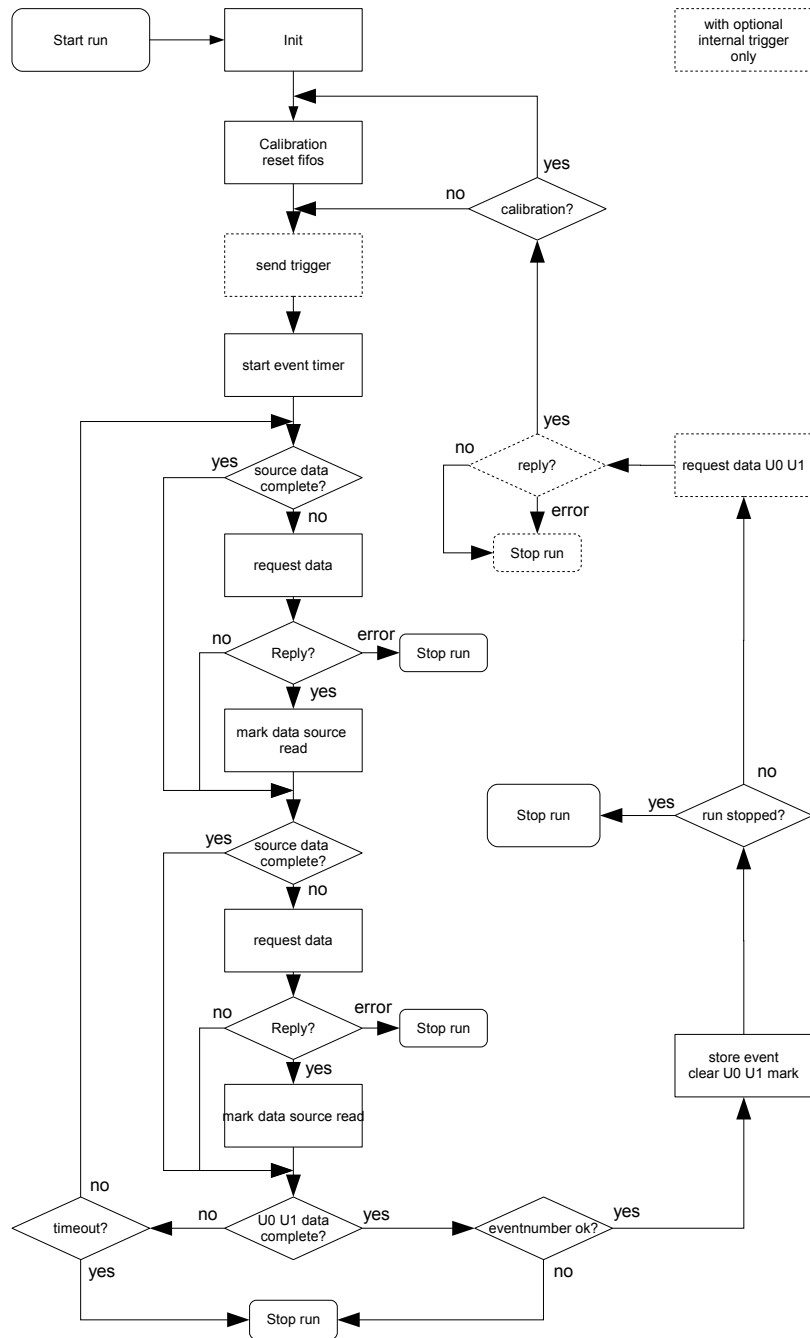


Figure 7.2: Flowchart of the DAQ loop of the run control program during the standalone operation. After the initialization and data calibration, the routine enters an infinite loop requesting data from the connected crates. As soon as one crate answers with event data, data with an equal event number is expected from the missing crate. If the event numbers do not match or a timeout is detected for one of the crates the run is stopped. Optionally the routine can generate triggers, which allows to read out the detector without external trigger for the purpose of testing.

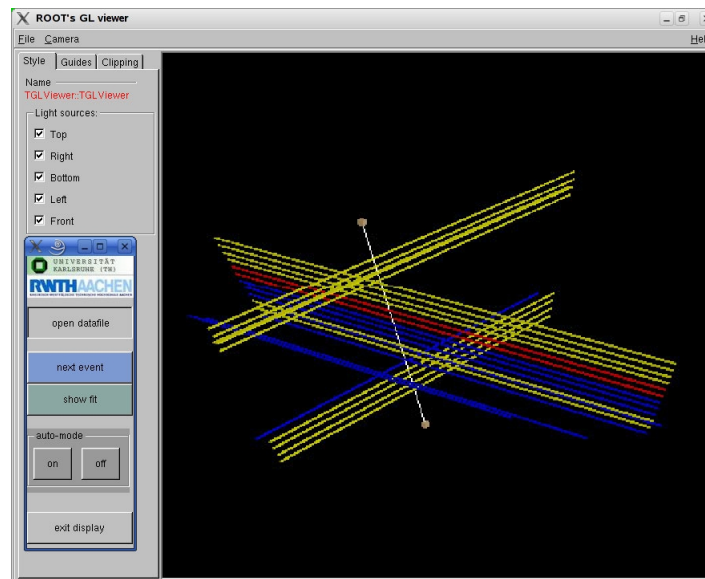


Figure 7.3: *The TRD event display in the three-dimensional view.*

OpenGL<sup>1</sup> environment. It is possible to display a three dimension model of the 5248 straw tubes corresponding to the position in the TRD. The OpenGL environment allows to rotate, zoom and move the displayed straw tubes by computer mouse control. In addition it is possible to display the projection of the detector in each plane. A GUI<sup>2</sup> supports the user to select the data and to control the 3D event display. Hit tubes are displayed in color. To distinguish signal amplitudes the color is given according to the signal height. A tube of low amplitude is shown in blue, values at about the most probable value in light yellow and very high signals in red. Negative amplitudes are shown in purple. Tubes without an entry in the compressed data are displayed transparent for the purpose of clarity. Optionally the display can be set to an automatic mode, which shows the next event data set as soon it is available on disk storage. Figure 7.3 shows a snapshot of the 3D event display and the GUI.

In addition to the three dimensional event display also a more simple two dimensional display was developed, which turned out to be even more helpful. It equals the 3D-projection in the x-z and y-z plane. The amplitude is shown as a bar above the hit tube with a height according to the signal amplitude. Both types of the display can also be displayed in parallel to allow more flexibility for debugging purposes.

The display described so far shows all hit tubes, which is helpful to get a complete picture of the processes, which can be found in the TRD. Especially focusing on the noise behavior and problems of the TRD readout, this is a strong tool to discover irregularities. Nevertheless for a further analysis it is unavoidable to exclude tube hits, which do not contribute to the on track energy deposition of particles. The on track energy deposition can be considered as a MIP<sup>3</sup> signal, since the detector has been crossed without a strong energy loss. For this reason

<sup>1</sup>Open Graphics Library for platform independent development of three dimensional real-time computer graphics.

<sup>2</sup>Graphical User Interface

<sup>3</sup>Minimal Ionizing Particle

a track-finder algorithm was implemented. It identifies single track events in the data, which allows to select only hits with a MIP signal.

For a first calculation of the regression line only tubes with amplitudes in the range of the MPV of energy deposition are taken into account. In a next step the distance of hit channels to this line is calculated. If this value does not exceed a certain value, the hit can be found in a corridor around the line and is included in the next step of regression. All other tubes are rejected. The regression line is calculated again from these tubes and the distance of the channels is tested considering a more narrow corridor. If enough tubes meet the restriction and not too many tubes are rejected, the event is regarded as a single track event. The calculated regression line defines the reconstructed track of the particle. The tubes on track can be considered to show the energy deposition of a MIP. A more detailed description of the applied track-finder algorithm can be found in [44].

The fitted track can optionally also be shown in the 3D and 2D event displays. Figure 7.4 illustrates the 2D display with a fitted track. Figures 7.5 and 7.6 show two more cosmic ray event in the TRD recorded during the standalone test at RWTH Aachen. Some more details about the development and application of the event display can be found in [3].

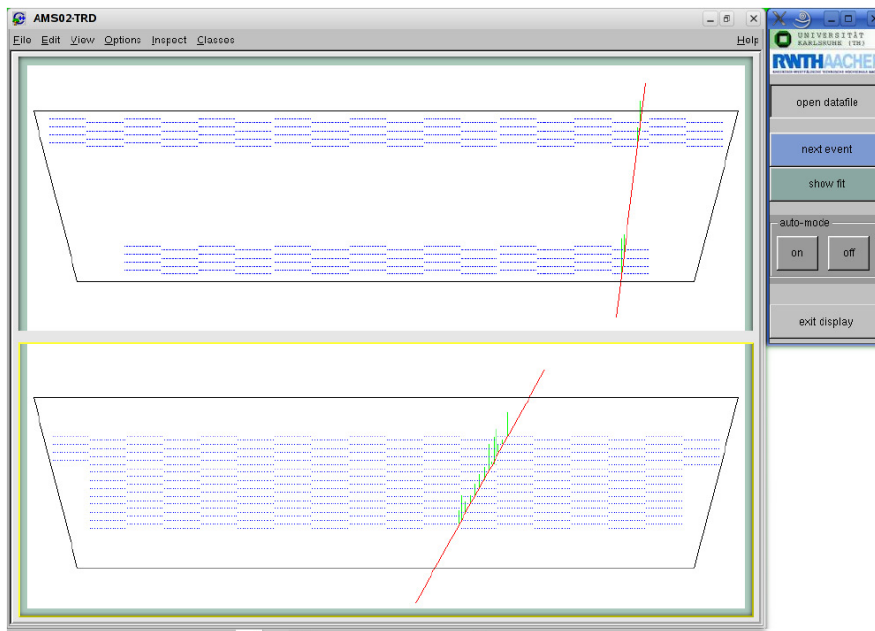


Figure 7.4: *The TRD event display in the two dimensional projection. The reconstructed particle track is indicated by a drawn-through line. The Amplitude is visualized by a bar on top of the hit tube.*

Another simple tool to analyze the data is the occupancy mapping, which also was available for the online analysis of the data. The occupancy of the TRD straw tubes of course is dependent on the length of the straw tube. The shorter the tube is, the less particles will cross it. For the TRD geometry this means, that with increasing distance to the detector center the occupancy decreases, since the chambers and with them the straw tubes are shorter in the outer positions. Of special interest are tubes, which show a lower or higher occupancy and could indicate a problem. Figure 7.7 shows an occupancy mapping of the detector with

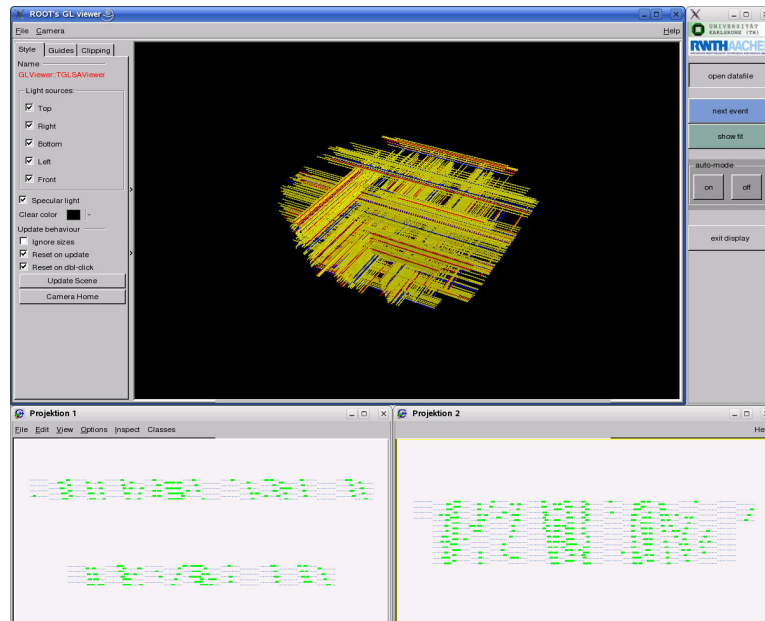


Figure 7.5: A shower event in the TRD event display. The silhouette of the TRD octagon is nicely visible.

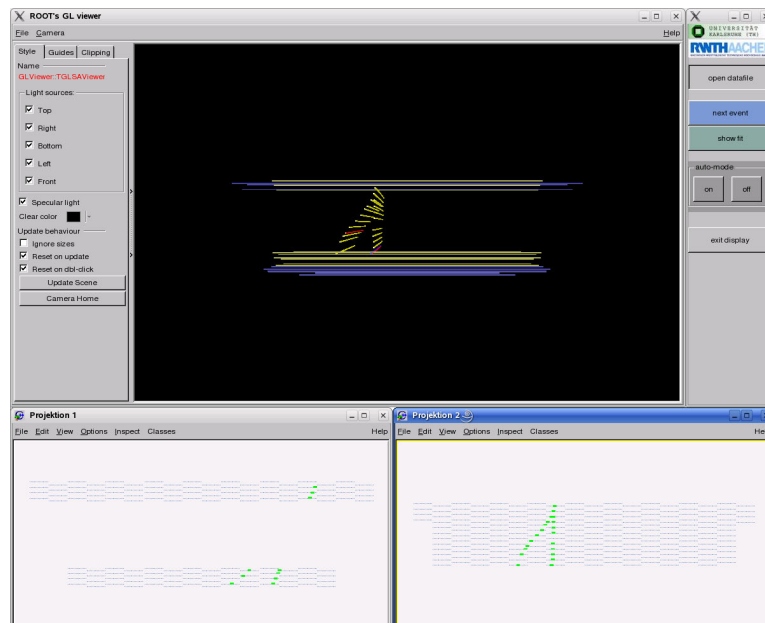


Figure 7.6: An event in the TRD event display. The incoming particle creates a secondary  $\delta$ -electron on top of the detector. Due to its low energy the trajectory is not a straight line and is rejected by the track finder algorithm.

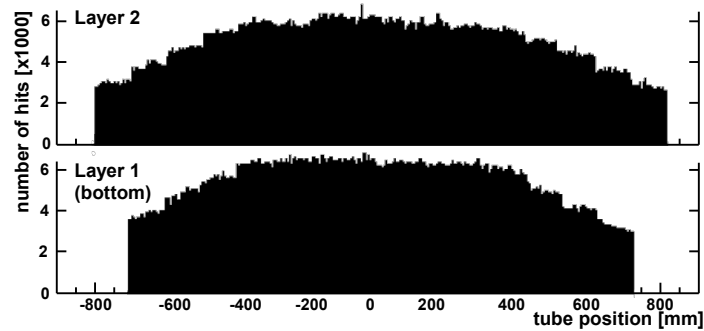


Figure 7.7: Occupancy plot of the bottom two TRD layers. The number of hits is decreasing with shorter tubes towards the edges.

decreasing number of hits to the edges. None of the layers indicates a problem of a channel.

In order to obtain the pedestals and noise values required by the data reduction routine before each run the data calibration routine is executed and the results are stored to disk. Figure 7.8 shows the electronic pedestals of all flight model UFE boards as acquired during the data acquisition. The flight UFE boards were chosen such that a mean pedestal of about 400 ADC units is achieved. The UFE boards with too many channels of high or low pedestal are kept as flight spare parts. The noise as calculated by the DSP of all 5248 TRD channels is shown in figure 7.9. The noise per channel is below 1.5 ADC units with an applied common mode correction.

Although the TRD stand alone test gives already a good picture of the detector properties, the main effort was focused on the development of analysis and control software. A more detailed picture of the TRD performance will be given in the AMS-02 cosmic ray test section 7.2.

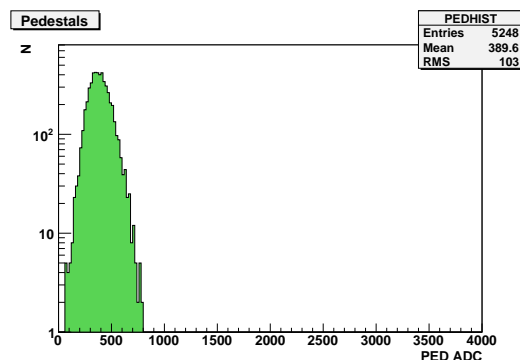


Figure 7.8: Distribution of the TRD channel pedestals. The mean for the 5248 channel pedestals is about 390 ADC units.

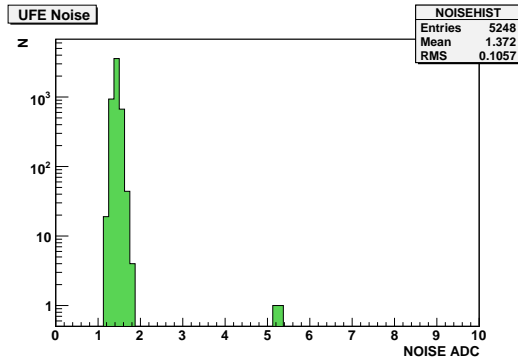


Figure 7.9: *The distribution of the TRD channel noise with UHVG half B active. The output has 3-bit precision as in the calculation by the DSP resulting in a decimal precision of 0.125 ADC units. Only two out of 5248 channels show a high noise.*

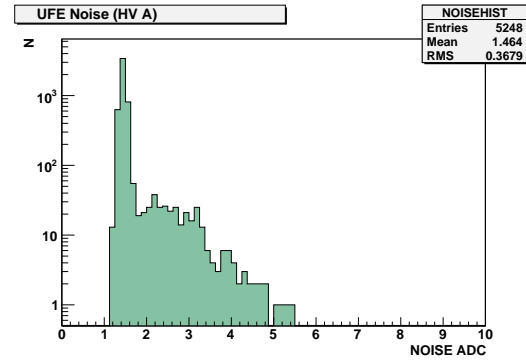


Figure 7.10: *The distribution of the TRD channel noise with UHVG half A active. About one sixteenth of the channels shows a higher noise, which cannot be observed with UHVG half B active.*

### Identified Problems

The TRD cosmic ray test was the opportunity, that the entire detector could be operated with a realistic acquisition of data. As presented in previous section the operation and data acquisition went quite smoothly, nevertheless a few problems showed up, which cannot be neglected in future data acquisition. So two out of 5248 channels show an anti-correlated noise discussed in the next section. As well presented is the noise behavior using UHVG half A for the high voltage supply of the proportional chambers as shown in figure 7.10. About one sixteenth of the detector tubes show a noise up to three times higher than with a high voltage supplied by UHVG half B. In the following the identified problems are described, the influence on the TRD overall data quality is estimated and solutions to handle them in the future data acquisition are given.

**UFE 3-5 Channel Pair with Crosstalk** During the data calibration of all channels performed by the DSP two neighboring channels showed noise values, which are about five times higher than the average noise. A strong anti-correlation between the amplitudes of both channels can be found in the raw data. A likely reason for this observation is a crosstalk on the UFE board or the jumper-cable to the UFE board. Figure 7.11 shows the amplitudes of both channels with the strong anti-correlation. Figure 7.12 shows the noise calculated by the DSP for the 64 channels of the UFE board.

Nevertheless this problem cannot be repaired because of the limited accessibility of the detector tube end on the assembled detector. Both affected channels still show a signal, if they are hit by a particle, even though the noise is higher. A modification of the hardware is not foreseen.

**UFE 5+7 with sporadic Pedestal Shift** Another localized problem also was detected early during the cosmic ray test phase from results of the data calibration by the DSP. All 32 channels read out by the first VA chip of UFE board 5+7 showed a sporadic shift of the

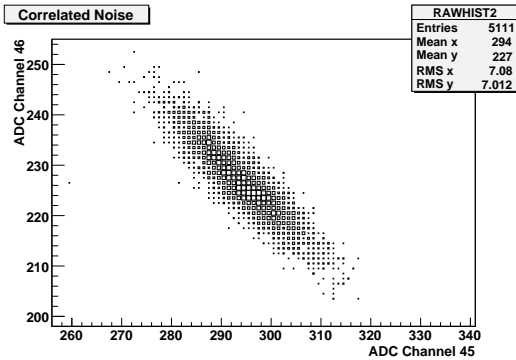


Figure 7.11: Amplitudes of two defective channels on UFE board 3-5. The plot shows the strong anti-correlation of the read ADC values.

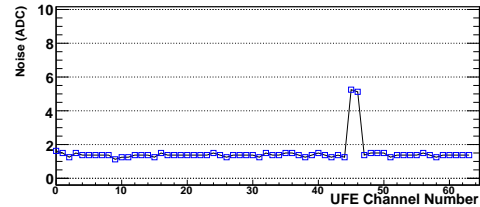


Figure 7.12: UFE noise with UHVG half B on. As an example the UFE board is picked, which shows two crosstalk channels discussed in the first paragraph of this section.

electronic pedestals. Since this shift can incidentally happen during the data calibration, a high noise on this 32 channels could be seen from time to time. The problem was identified to be localized on the UFE electronics by disconnecting the jumper-cable to the associated chamber. Fortunately in this case a repair was easy to apply and was arranged during the AMS-02 pre-integration phase at CERN. The affected UFE board was replaced in June 2008 and a failure-free operation was verified afterwards.

**HV Induced Noise from UHVG Half A** The noise analysis revealed a further effect, which only appears with applied high voltage to the detector chambers. The first tube of almost all straw tube modules shows a noise up to three times higher than without high voltage applied. The noise is clearly correlated within a chamber of four modules as shown in figure 7.13. The investigation shows, that the tubes are located on the position of the tube end board, which the high voltage wire connecting the UTE to the UHVD board is soldered to. A glob of glue seals the solder point as shown in the picture in figure 7.14, but might amplify a capacitive coupling to the first tube making the effect vary from module to module due to the different sizes of the glue. All other 15 tubes of the modules are not affected. Source of the noise is the UHVG board. Further tests revealed, that only the UHVG half A circuit produces the sinusoidal noise most likely due to the close location of the control circuit to the high voltage generator circuit. Half B of all boards is not affected as shown exemplary for the channels read out by one UFE board in figure 7.12. Figure 7.15 shows the noise behavior of the very same UFE board with a high voltage supplied by UHVG half A with the four peaks, one for each first tube in a module. For completeness the corresponding pedestals are shown in figure 7.16.

Several options were considered to solve the problem. There are two possible approaches for improvement. Either the front end could be modified to reduce the higher noise or the noise itself originating from the UHVG board half A circuitry could be eliminated.

Investigation showed, that considering the first option an additional capacitor on the UHVD board is able to eliminate the noise. Nevertheless a few difficulties appear for the hardware

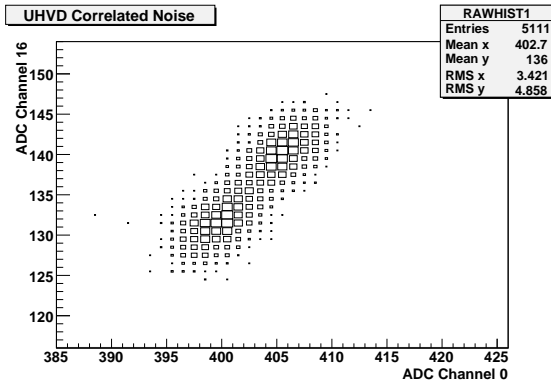


Figure 7.13: Amplitude correlation caused by UHVG noise. The plot shows the correlated noise on the first channels (0,16,32,48) of the modules of a chamber with a high voltage supplied by UHVG half A.

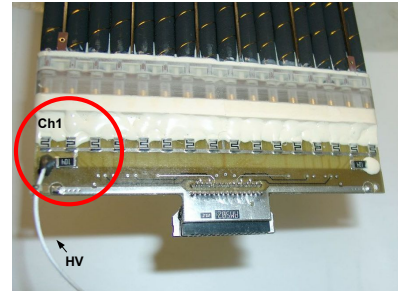


Figure 7.14: The UTE board with the high voltage wire from the UHVD board soldered near to the first tube of the module.

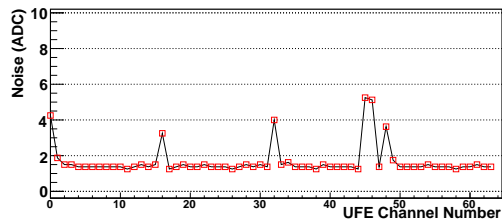


Figure 7.15: UFE noise with UHVG half A high voltage supply. A high noise is observed on the first channels of the four modules of a chamber.

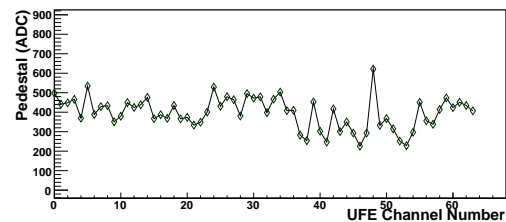


Figure 7.16: The pedestal distribution of the chosen UFE board 3-5.

modification. In account for safety of the experiment all wires under high voltage are sealed with resistant glue. Since there are no spare solder pads on the UHVD PCB, the mounting of a capacitor would require to free solder pads with a significant amount of effort. To comply with the requirement for vibration resistance special measures would have to be taken to fix the additional capacitor on the UHVD PCB or nearby. In addition most of the UHVD boards are installed in a position on the detector with a difficult accessibility. The risk of damage of already installed parts is imminent. Taking all this together, the amount and risk if such kind of repair was considered as to be too high. A modification of the UHVD board therefore was rejected.

The second approach to find a solution on the UHVG board itself suffers from similar problems and risk. Tests have shown doubling the output capacity of the half A circuitry is able to reduce the noise from the UHVG. Since on the PCB no additional solder pads are present, a considerable solution could be to solder a second capacitor on top of the existing one. But again the concerns of vibration resistance and a reduced distance to the neighboring boards inside the U-Crate do not allow to follow this modification.

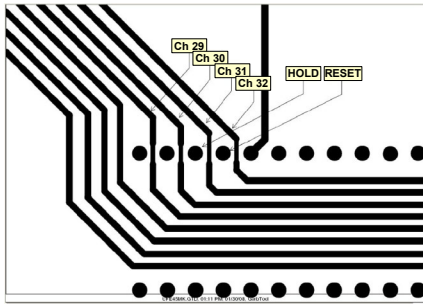


Figure 7.17: Extract of the M-Type UFE PCB layout. The track transmitting the RESET signal to the VA chips are close to the signal tracks of channels 29 to 32 on the UFE PCB.

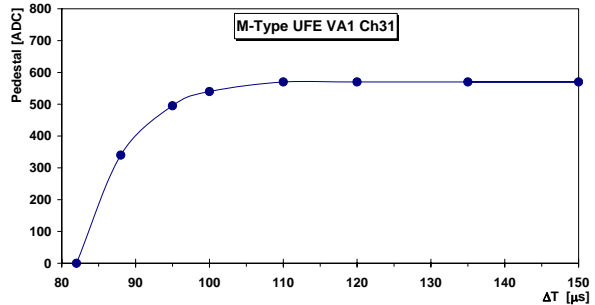


Figure 7.18: M-Type UFE pedestal drop at fast consecutive readout. Due to crosstalk the channels near PCB tracks with the reset signal indicated in figure 7.17 show a strong drop of the pedestal.

In conclusion none of the discussed changes is applicable for the flight hardware considering the risk during the repair and operation. Still there is the option to treat affected channels by the DSP in a next release of the software. A common mode correction for the channel amplitudes is possible to apply, because four channels of a chamber are exposed to the same noise from the same UHVG output channel. But even without a correction the maximum noise of 5 ADC units is still below the expected most probable value of about 40 ADC. About one third of the first tubes of the modules of the detector is affected in this extend. During the pre-integration phase half B of all UHVG boards was operated by default and half A as cold redundancy.

**Problem of the UFE Reset Signal at High Rate Readout** After an extended time of data acquisition a problem with the UFE board electronics became obvious. Large negative amplitudes can be found in the data from time to time in a defined pattern of channels throughout the detector. Observed channels can be identified to belong to M-type UFE boards, which make up about one half of the UFE boards. The problem occurs, if very close consecutive triggers are given to the system in a time interval from  $80\mu s$  to  $110\mu s$  after the first trigger. The investigation revealed, that affected channels are very close to tracks on the PCB, which transmit the reset signal to the VA chip directly after a readout. Figure 7.17 shows the M-type UFE layout, which is mirrored with respect to the standard (S-type) UFE boards and the reset line. Six out of the 64 channels show a strong effect. Figure 7.18 shows the pedestal of a channel as a function of the time difference between two consecutive readings. The pedestal even drops to zero with a decreasing time difference. The minimum time difference, which can occur during the operation is  $90\mu s$  according to the dead time of AMS-02 defined by the tracker subdetector.

A modification of UFE PCB layout would imply a new design and production of the boards, which was the reason to abandon this as a solution. On the other hand about 5% of 5248 TRD channels are affected, since two triggers within  $90 - 110\mu s$  are expected for about 4% of the events at  $2kHz$  trigger rate<sup>1</sup>, a special handling needs to apply on only  $< 0.2\%$  of

<sup>1</sup>Estimation by the exponential distribution  $p(\Delta t) = e^{-\nu\Delta t}$ , with  $\nu = 1 / \langle \Delta t \rangle$ : The fraction of events in

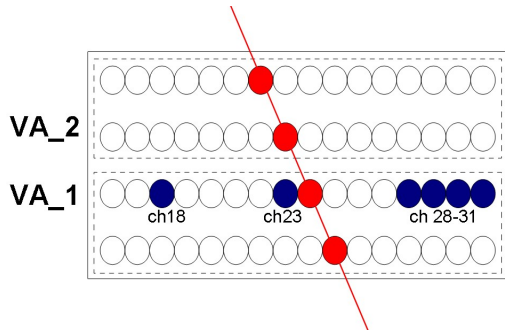


Figure 7.19: *Affected channels of the M-type UFE board. Only channels of one out of four modules of a chamber show the pedestal shift at fast consecutive readings, which allows a track reconstruction even in the case a particle hits such a tube losing the amplitude information.*

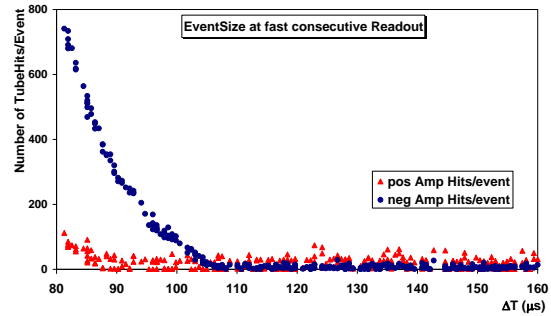


Figure 7.20: *TRD event size at fast consecutive triggers. Below time differences of about  $110 \mu\text{s}$  the number of channels with a negative amplitude due to the reset signal crosstalk increases strongly.*

the TRD hits. In the DSP special routines are implemented to identify a readout at close consecutive triggers. In the case such a condition is found the affected channels are excluded from the common mode correction in order to avoid any disturbing effects. Although a signal in these channels is lost, still most of the tubes hit on the track of a particle are not affected allowing still excellent TRD performance at consecutive readouts. Figure 7.19 illustrates the effect of the downwards shifted channels during the readout. Only one module per chamber is affected, which fortunately means that a particle hits at maximum one of the channels in a chamber. For an offline analysis of the data the trigger time is known, which makes it easy to take this problem into account to gain a higher precision.

Figure 7.20 shows the event size as a function of the time difference between the triggers from cosmic ray test data. One can easily recognize the strong increase of the number negative amplitudes per event below  $110 \mu\text{s}$  trigger difference. Values below  $90 \mu\text{s}$  are only shown for completeness, but are without interest for the performance in AMS-02. The dead time of the system is defined by the tracker subdetector, which is above  $90 \mu\text{s}$ . Events below this value are blocked by the system busy and are never read out. The number of positive hits stays constant down to the dead time of the TRD, which proves that physics data is affected in a minimum extend only. A readout of negative values is not foreseen for normal operation on the ISS, hence a problem of increasing event size is not expected for the AMS-02 data flow caused by the TRD subsystem.

**Asynchronous Readout Induced Noise** The data calibration can be performed in two different ways as implemented in the xDR2 boards. One option a readout trigger generated by the DSP software. Since in this case each UDR2 in a crate starts its own software pulse generator for the calibration, soon they are not synchronous in their readout anymore due to different latencies during the calculations. This certainly does not correspond to the mode

$$\text{the first } 20 \mu\text{s is } 1 - \frac{\int_{20\mu\text{s}}^{\infty} e^{-2000Hz \cdot x} dx}{\int_0^{\infty} e^{-2000Hz \cdot x} dx} = 1 - e^{-2000Hz \cdot 20\mu\text{s}} \approx 0.04 .$$

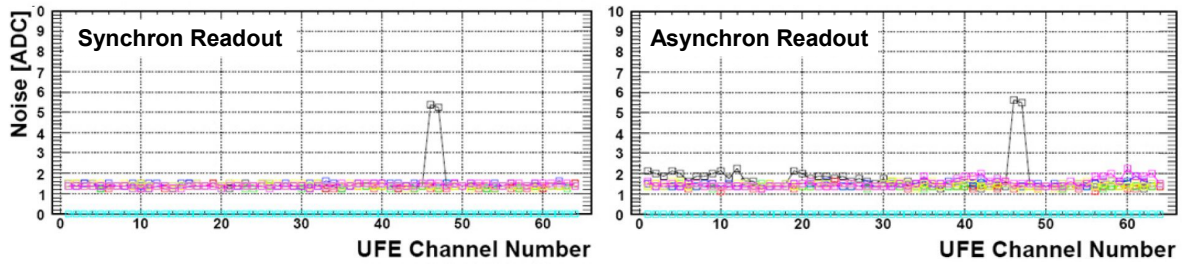


Figure 7.21: Comparison of the channel noise with synchronous and asynchronous readout in the different UFE boards.

of data acquisition, when all ADC chips digitize the signal at exactly the same time avoiding noise amongst each other when switching modes.

Figure 7.21 shows the noise of the channels of several UFE boards. The noise is significantly more uniform and lower, if the readout is started in all UFE boards at the very same moment by an external trigger. The second option therefore is to use a crate external trigger for the calibration. The appropriate way to perform the calibration is a common trigger for the readout, which is distributed by the JINF board and allows to trigger the readout in all UDR2s in the crate at the very same moment. With this approach the calibration mode is not much different to the readout mode, but instead the data is used by the calibration routine and not processed by the event building routine. Therefore a modification of the DSP code had to be made. A calibration mode was introduced, which reads externally triggered data for the calculation of data calibration results. This led to the common AMS-02 approach for the calibration, in which the JLV1 board of AMS-02 distributes the trigger to all slaves for data calibration procedure.

## 7.2 The AMS-02 Cosmic Ray Test at CERN

For a long time the various subdetectors and subsystems of AMS-02 were developed by the collaborators mainly at the home institutes in responsibility of relatively small groups. Finally in the beginning of 2008 the assembly of AMS-02 begun in a dedicated cleanroom at CERN. This is a phase known as the pre-integration phase of AMS-02, which simply means AMS-02 was assembled without the magnet. The following section will describe the pre-integration phase and the collected data of cosmic rays. Valuable experience was gained for the assembly procedures. Issues of conflicting mechanics were solved. Moreover the pre-integration phase gave the possibility to operate the entire detector and to collect a huge amount of data of cosmic rays. The data acquisition and interesting results showing the good performance focusing the AMS-02 TRD will be presented. Figure 7.22 shows an event in the AMS-02 event display, which is part of a reconstruction and analysis software package under development [14].

### 7.2.1 AMS-02 Pre-Integration Phase

In 2007 it became apparent, that the AMS-02 subdetectors would be ready for the flight integration well in advance of the completion of construction of the AMS-02 superconducting

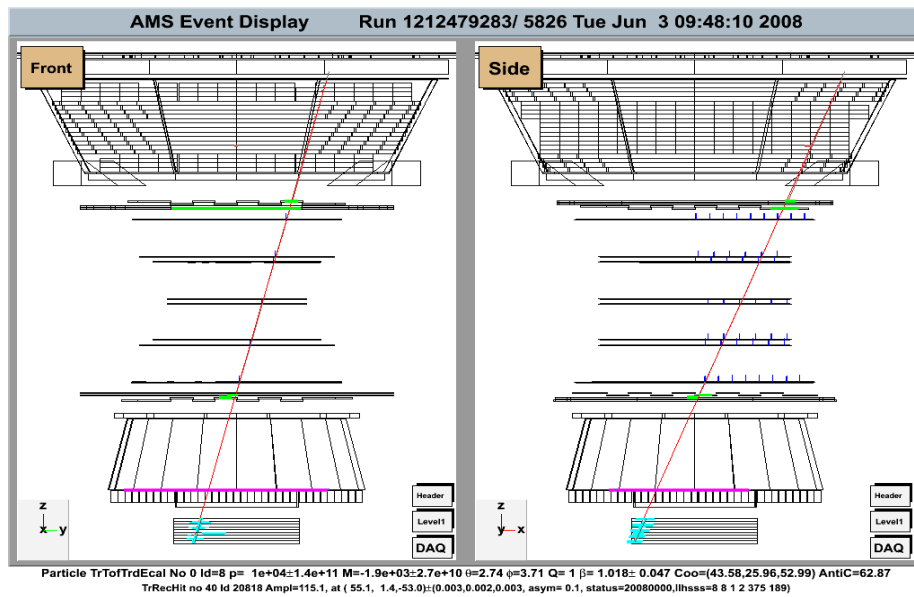


Figure 7.22: AMS-02 event display side view. A fitted track is indicated crossing all subdetectors of the AMS-02 instrument. Nicely visible is the linked readout of the tracker sensors on a module as described in section 3.2. Without the information from other subdetectors the track is ambiguous.

magnet. For obvious reasons it was not advisable to put the subdetectors and subsystems to storage during this standby time. So it was decided to exercise the assembly of the completed flight hardware in a pre-integration phase. The pre-integration phase was scheduled to be conducted for four months until February 2008, but was finally extended up to the end of June. During this period not only hardware related problems were discovered, discussed and solved, but also the chance was seized to develop and test the ground support and flight software on all levels of control and data processing. Gradually more and more subsystems were included

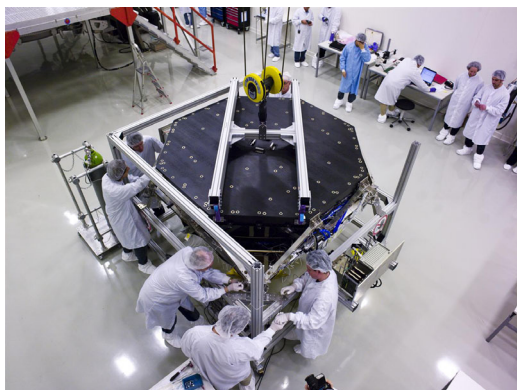


Figure 7.23: Lifting operation of the TRD during the pre-integration phase.



Figure 7.24: The TRD mounted on top of AMS-02.

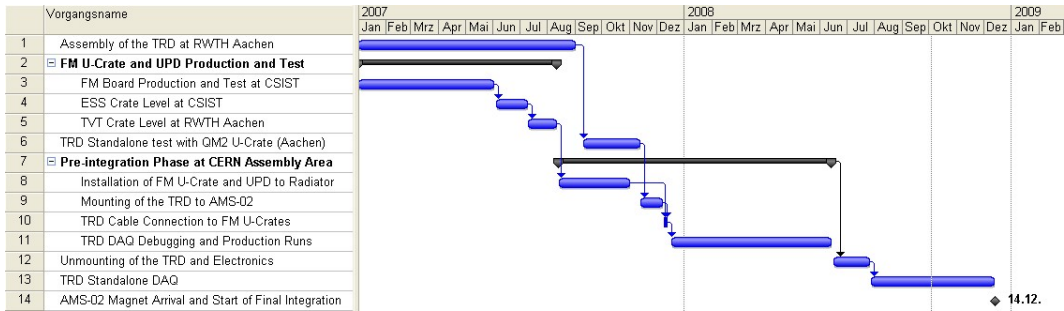


Figure 7.25: Schedule of the FM TRD readout electronics production and the TRD pre-integration phase. A complete readout of the TRD was possible with QM2 electronics in September 2007 and finally with FM electronics, which in parallel were integrated into the DAQ system, in December 2007. The final assembly of AMS-02 is scheduled to take place in early 2009 after the arrival and test of the superconducting magnet.

into the readout and control procedures. In the end all major systems and detectors of AMS-02 were running, although without a magnetic field, nearly in normal operation mode recording the first time in combination and redundantly data of tracks of cosmic rays.

The TRD was shipped from RWTH Aachen to CERN in November 2007 still with the QM2 readout electronics attached to the system. A functional test on arrival confirmed that there was no destructive impact of the transport to the detector. In a first assembly step the upper ToF planes were attached to the TRD M-structure before the TRD and ToF were lifted together to the AMS-02 USS in December 2007 as shown in figures 7.23 and 7.24. The ACC and tracker subdetectors were already integrated at this time. In March 2008 finally the



Figure 7.26: AMS-02 rotation test at the end of the pre-integration phase. The main aspect was the test of the mechanical stability mainly of the tracker. The position of the ladders was monitored throughout the test by the tracker alignment system (TAS).

lower USS had been equipped with the lower ToF, RICH and ECAL subdetectors, and was mounted to the AMS-02 USS. Data together with all subdetectors was collected until June 2008. Figure 7.25 shows an overview of the pre-integration schedule for the TRD. In June the subdetectors were dismantled in turn and stored to their transport structures awaiting the arrival of the superconducting magnet.

The TRD data acquisition started in December 2007 already, which is described in the following. During the normal operation phase, the detector was switched off over night. There are two running periods with 24-hour operation in May and June. Just before the end of the DAQ phase in June AMS-02 has been rotated in order to test the tracker alignment under stress. Figure 7.26 shows the AMS-02 instrument in different rotations. This was the last action with the pre-assembled AMS-02 detector before the preparation of the magnet installation.

### 7.2.2 Run Control Development for the Ground Support Computer

Most of the AMS-02 subsystems were delivered to CERN in early 2008. Before only a few subsystems were present to develop a robust run control software for AMS-02. Nevertheless the development started with two systems in place, which were the J- and JT-Crate and the two U-Crates. A run control program has to satisfy three main tasks, namely the power on initialization, the calibration control and the control of the actual run. Calibration and run control tasks can be implemented in a common approach, since all nodes are based on the AMSWire protocol at a similar level of the event building framework version.

The run control software is based on the idea to operate the AMS-02 instrument in the same way as later on board of the ISS. The complete commanding chain is used to operate the system. The ground support computers (GSC) are connected to the HRDL and LRDL links of the J-Crate. In order to reduce the amount of commands sent through these links<sup>1</sup>, the run control software only sends the initialization parameters for a requested action and JMDC takes all actions to execute the request. The best example might be the high voltage ramping of the UHVG boards. The run control software only transmits the data type to initialize the ramping and JMDC then sends initializing commands to JINF boards on its own. All Lecroy commands required to set the high voltage on the UHVG boards are generated or read from the QList by the JINF board on its own. With this approach described in section 6.4 the number of commands between the nodes is reduced to a minimum.

The calibration request from the run control software likewise initializes the calibration procedure in JMDC only. All nodes are set to calibration mode by JMDC. The JLV1 electronics is initialized to send a predefined number of triggers to all nodes in the system. As soon as the requested number of triggers is sent the calibration stop command is sent to the system. The calibration results are read from the nodes and transmitted to the ground support computer to be stored on disk.

The start of the data acquisition follows a similar procedure. All data taking nodes, which are included in the run by a configurable slave mask are set to the data acquisition mode specified in the individual configuration windows of the software. The default mode is the compressed mode for all slaves. In order to ensure a synchronous data acquisition all event buffers are cleared in the system by group commands before the run. Finally the trigger is enabled in the JLV1 logics, which generates the trigger from the coincidence of ToF layer

---

<sup>1</sup>Each uplink to the ISS needs to be requested from NASA during the normal operation.

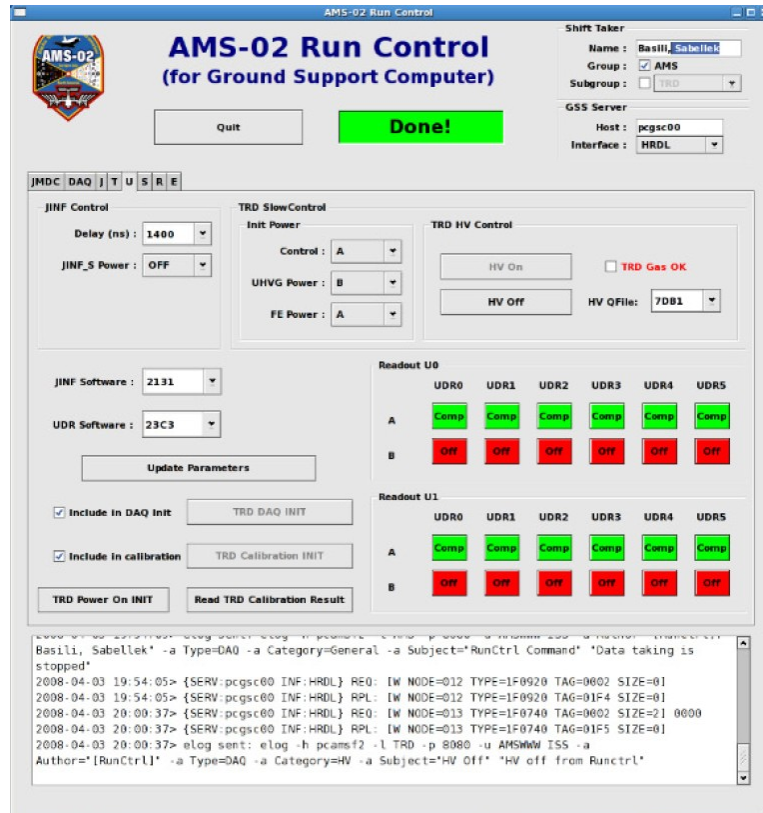


Figure 7.27: The AMS-02 run control configuration GUI for the TRD readout electronics. The implementation allows easy switching of the redundancy of all system parts and control of the high voltage supply of the TRD.

signals and the veto signal of the ACC subdetector. The event data is collected by JMDC according to an infinite loop of the on-board DAQ software and is sent to the GSC for disk storage. The event information is added to complete the AMS science data block as described in section 6.5.

The TRD readout system initialization is performed together with other subdetector initialization procedures at the power-up of the system to a default status.

Figure 7.27 shows a snapshot of the U initialization tab for the TRD readout electronics of the run control GUI. A goal of the cosmic ray test is to allow test of the complete system and its redundancy. Since at the end of the pre-integration phase the access to all parts is easy the discovery of a hardware failure still means only a minimum effort during repair unlike in a later phase of the detector assembly. Therefore the configuration implemented in the GUI and JMDC is designed to easily allow to switch between the various redundant parts of the system by the shift-taker. In the power control section the DC/DC converters of both UPD boxes can be swapped to supply redundant halves of the UPSFE and UHVG inside the U-Crate. In the same step the control part of the slow control electronics is swapped between the Actel FPGA redundancy. Also the digital part of the UDR2 boards can individually be swapped between hot and cold redundancy. Moreover single UDR2s can be set to OFF or to different readout modes for debugging purposes.

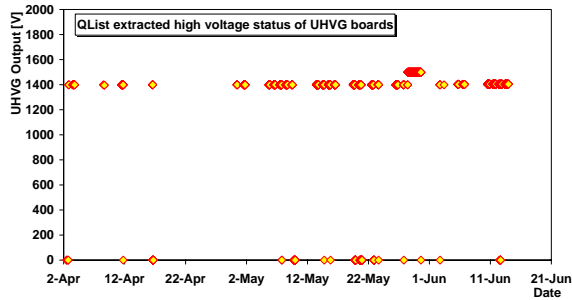


Figure 7.28: *Housekeeping data steadily collected by JMDC from the U-Crate QList during the second half of the pre-integration phase. The high voltage for the TRD was kept stable at 1400 volts except for a short running period in order to compensate a lower gas gain with high gas pressure during a TRD gas system test.*

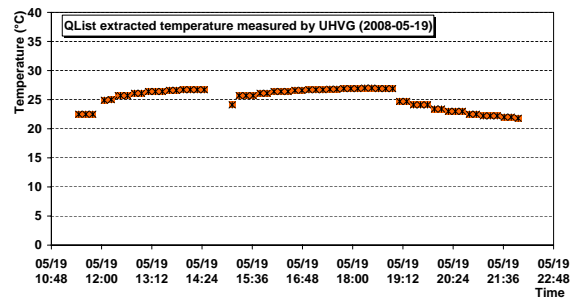


Figure 7.29: *UHVG board temperature measurement extracted from the QList. In the same way temperature and pressure information from the gas (UG) system will be acquired as soon the electronics is finalized.*

The JINF is initialized according to a common procedure. The trigger delay time is set and optionally the redundant half is switched off. A major TRD specific part is the high voltage initialization. Even though the high voltage generator electronics is equipped with overload protection it is advisable to check the gas status before applying the high voltage to the detector tube end. However the gas system was not yet available during pre-integration phase to be read out by JMDC. Therefore a ground support gas system has been set up allowing to the check gas parameters such as pressure and gas flux. These are checked by an external program. Only in the case the parameters are within the specification the run control software allows to activate the control panel of the high voltage. An automatic electronic logbook entry is created for each high voltage control action.

It is worthwhile to stress, that the run control GUI only collects the parameters for the system initialization, which are sent to JMDC. On request JMDC interprets the list of parameters and assembles the commands sent to the nodes. The experience gained during the cosmic ray test lead to a new approach of control and monitoring, which is subject of current slow control development. The list of parameters created by any software or the run control GUI is sent to JMDC. Instead of JMDC command building the list is sent to the corresponding subdetector nodes and stored to the flash memory permanently. In this case the initialization will be performed by the corresponding JINF or xDR nodes itself reducing the amount of commands sent through the entire commanding chain within AMS-02. Furthermore the initialization will be more strictly stay under the control of the subdetector responsible persons. A single command from JMDC will then trigger the initialization procedures defined by the subdetector groups.

The acquisition of system status information during the run was accomplished by the QList implementation described in section 6.4. Figure 7.28 shows the pre-integration running periods of the TRD as extracted from the housekeeping data, which was steadily recorded from both U-Crates since April 2008. Each data point represents the value of the high voltage

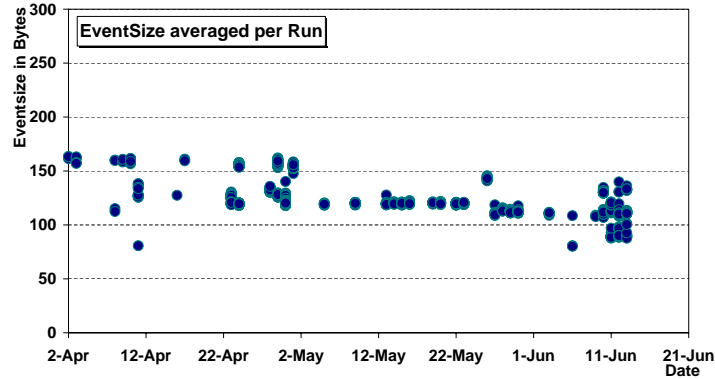


Figure 7.30: *The TRD event size during the pre-integration data acquisition. The event size is averaged for a run. The size of about 120 bytes of the TRD event corresponds to about 17 hits of 4 bytes each and additional 60 bytes of event building status information.*

setting in the corresponding run. Figure 7.29 exemplary shows the read out temperature of the UHVG board sensors of a day with operational and non operation phases. Although a few systems were already read out by JMDC, some essential status information was not read out due to missing final electronics. So the TRD gas temperature and pressure information is not available, which makes a correction of the acquired data for gas gain complicated.

### 7.2.3 Results from Cosmic Ray Data for the TRD

The data acquired during the AMS-02 pre-integration phase from April to June 2008 contains about  $10^8$  particle tracks in the TRD. Primarily the data acquisition phases were used to test in detail the performance of the entire AMS-02 DAQ chain and to perform failure analysis of the data acquisition system. Furthermore the development of slow control and run control procedures and software continuously was done in parallel as presented in the previous section. Therefore the configuration of the system as well as the parameters of the data acquisition changed several times, moreover hardware has been included or excluded in the DAQ system as required by the flight production processes. Especially the trigger configuration has a big influence also on the TRD data, depending on the number of ToF panels, which were included for the LV1 trigger generation. Stable run condition were maintained in dedicated runs at the end of the pre-integration phase only. Nevertheless a number interesting results can be presented in the following focusing on production runs in stable conditions.

In the TRD data reduction routine used from April to June as described in section 6.2 the readout of channels of a negative amplitude was active for the data acquisition. Figure 7.30 shows the dates of data acquisition and the average event size of the TRD event. A few features can be recognized. There are two levels of average event size depending on the ToF trigger configuration. For the data acquisition phases with two out of four ToF layers coincidence condition the average size can be found at 17 hit channels per event corresponding to a data size of about 120 bytes. A more strict coincidence level of four out of four layers in the ToF clearly leads to a higher average event size in the early runs, since a complete particle track inside the TRD is more likely. A drop of the event size at the end of the data taking phase in June originates from the rotation of the AMS-02 detector, when more particles are

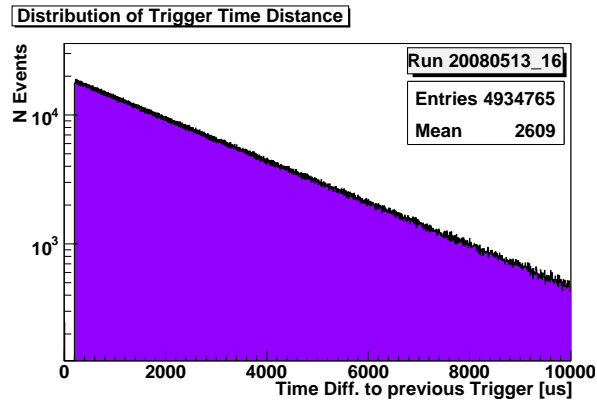


Figure 7.31: *Distribution of the trigger time difference. The exponential increase of the number of events with a decreasing time difference is visible on logarithmic scale. This means the bulk of the events are triggered in quick succession. So the readout of about 50% of the events are triggered within 0.5 ms, which stresses the necessity of unprocessed event data buffering with a processing time of about 500  $\mu$ s per event. Also the dead time has to be as short as possible. The design value of AMS-02 is 90  $\mu$ s fixed by the tracker readout sequence.*

triggered, which do not pass the TRD at all.

A more clear picture about the event size can be made on the basis of the data of a single run. The chosen run for further analysis is from 13th of May with a sample of about 5 million cosmic ray events. The ToF coincidence configuration was set to default values meaning a coincidence of two out of four layers. An artificial dead time of 200  $\mu$ s was set as requested by the tracker group, which can be extracted from figure 7.31, which shows the number of events for a given time difference of two consecutive triggers. The distribution also stresses

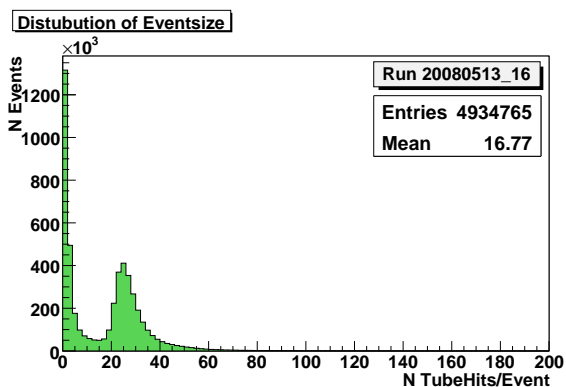


Figure 7.32: *Distribution of the event size of all recorded events. A big amount of events has no or only a few hits in the TRD.*

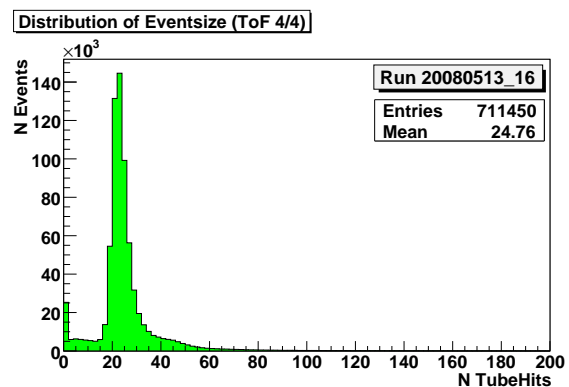


Figure 7.33: *Distribution of the event size of selected events, which caused a signal in all four ToF layers. A clear peak is visible at about 25 hits in the TRD.*

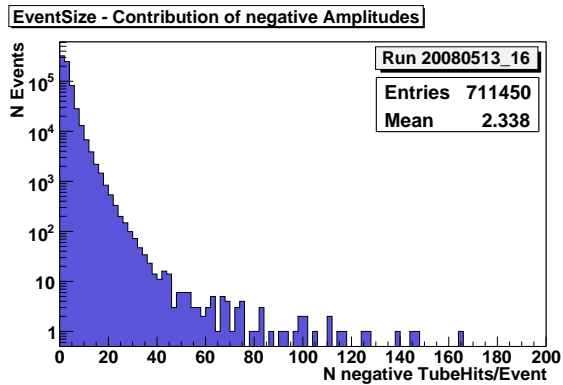


Figure 7.34: Contribution of the number of negative amplitude hits. Most events can be found with less than five negative amplitudes in the detector. The mean contribution is about two negative channels in the TRD.

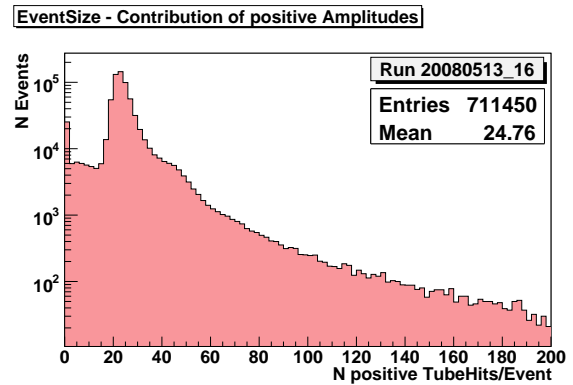


Figure 7.35: Contribution of the number of positive amplitude hits. As expected about 25 positive channels according to 20 layers in the TRD are read out for a particle crossing the detector.

the importance of minimizing the dead time of the entire experiment. Its maximum is at the lowest time difference between impacting particles. A huge effort was made to achieve a dead time of the system of  $90 \mu\text{s}$ , which is five times smaller than the dead time of AMS-01. About 50% of the hits are collected at a trigger difference below  $500 \mu\text{s}$ .

Figure 7.32 shows the distribution of the number of hit tubes per event. The expected number of hits per event can easily be estimated. The TRD has 20 layers of straw tube modules, thus a particle, which crosses the detector from top to bottom leaves a signal in 20 tubes. Of course, due to the overlap of modules some tracks might also produce more than 20 hits. The analysis of the data shows a clear peak at about 25 hits per event, which corresponds to the expectation.

The huge number of events without or with only a few hit tubes can be explained by the trigger coincidence setting of ToF. A lot of particles do not cross the TRD. Figure 7.33 shows a selected sample of events, which are triggered by four out of four ToF layer coincidence. As expected the number of events without any hit is suppressed. The average event size is about 25 hits per event for the data sample, which corresponds to an average event data size of the TRD of 150 bytes per event fragment in flight-like conditions. In order to suppress empty events in the TRD, events are selected with four out of four ToF hits for further analysis.

Figures 7.34 and 7.35 show a differentiation between hits of negative and positive amplitude. The histogram for the positive amplitude hits shows the peak at 23 hits per event from single track events. The histogram for the number of negative hits does not show a feature at all. Rather a constant number of negative hits can be found in every event with two negative amplitudes hits in average. This proves the number of negative hits is independent from the number of positive hits, otherwise a peak like structure would be visible. The origin of the negative amplitudes is well known and described in section 4.2. Due to undershoot in the front end electronics a constant number of *ghost hits* is visible from previous particle crossings.

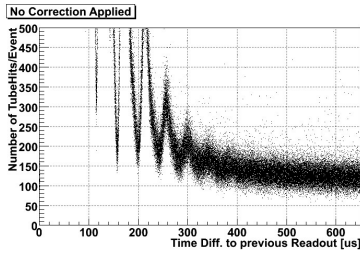


Figure 7.36: *TRD event size without any data correction by the DSP.*

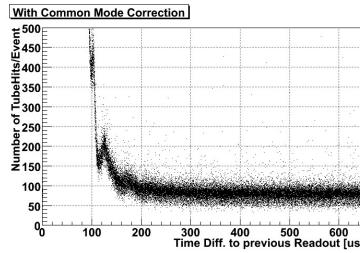


Figure 7.37: *TRD event size with a common mode correction by the DSP.*

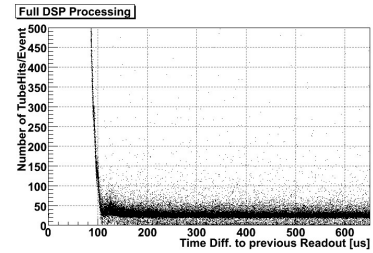


Figure 7.38: *TRD event size with the full processing by the DSP.*

### Event Size at High Rates

Special attention has to be paid for events, which consecutively are triggered within a short time interval to a previous one. Problems of the front end electronics at fast consecutive triggers are discussed in section 7.1.2. The reset signal induces a common mode noise to S-type UFE boards and strong downwards shifted pedestals on M-type UFE boards. Dedicated runs were performed with events down to a time difference  $dt = 80\mu s$ . Therefore the tracker was excluded from the data acquisition for two reasons. Firstly similar problems of the tracker front end boards prevent to take data with an artificial dead time below  $200\mu s$  in the current reduction software. Large event data blocks of the tracker would prevent the readout of any other subdetector, since the JINJ board, which assembles the data from all JINF boards, has a limited buffer size of 21 kByte. Secondly the hardware dead time of the tracker is  $90\mu s$  compared to the dead time of the TRD of  $80\mu s$ .

Figure 7.36 shows the event size of the TRD at low trigger time difference without any correction by the DSP. In this mode only the pedestals are subtracted and all amplitudes are written to the output buffer outside a  $3\sigma$ -range. Visible oscillations up to  $400\mu s$  are traced back to the reset signal of the VA chips leading to unacceptable event sizes below  $150\mu s$ . Of course, this is not a standard mode at all, but it stresses the necessity of the corrections applied by the DSP as described in section 6.2.

However a common mode correction for each VA chip is done by the DSP, which suppresses most of the induced noise as shown in figure 7.37. Still the data reduction is not sufficient below  $150\mu s$  with a strongly increasing event size. This can be explained by the S-type UFE problem and the downwards shifted channels of M-type UFE, which finally drop to a pedestal of 0 ADC. But why is it so inevitable to care about fast consecutive events? The effort to recover these events becomes obvious by figure 7.31. The number of events triggered with a given distance to the previous event describes an exponential law. More than 10% of the events are expected at a time difference of less than  $150\mu s$ . A loss of the events would have a non negligible influence on the detector performance.

Furthermore figure 7.37 shows an offset of the event size over the complete range. Since also events with no particle track in the TRD are expected, event sizes at zero should be visible. Against this expectation one can clearly find an offset of about 30 hits, which originates from the contribution of a non-Gaussian noise of the channels. A simple solution, namely setting the cut for the channel rejection in the UDR2 hit identification routine to  $5\sigma$ , would reject also valuable information of hits on a track with low energy deposition, which is essential

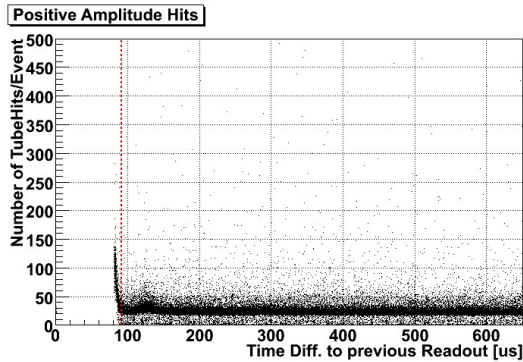


Figure 7.39: Contribution to the event size at fast consecutive triggers by positive amplitude channels.

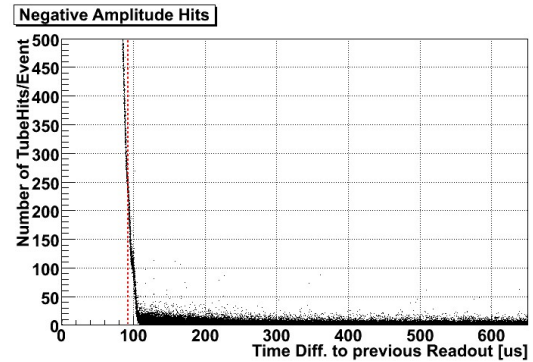


Figure 7.40: Contribution to the event size at fast consecutive triggers by negative amplitude channels.

for the separation of electrons and protons. Therefore a variable hit cut has been introduced setting the cut to  $3\sigma$  in the case a track is identified as likely by a previous analysis and to  $5\sigma$  in else case.

Finally figure 7.38 shows the event size with a full processing by the DSP as described in section 6.2. At the minimum event size no hits are written to the output, which corresponds to the expectation, if no track is found in the TRD. A more detailed picture is given by figures 7.39 and 7.40 showing the event size separated for negative and positive amplitudes. The number of hits of positive amplitude has a clear accumulation at about 23 hits in the TRD, which corresponds to tracks through all 20 detector layers. Down to a trigger difference

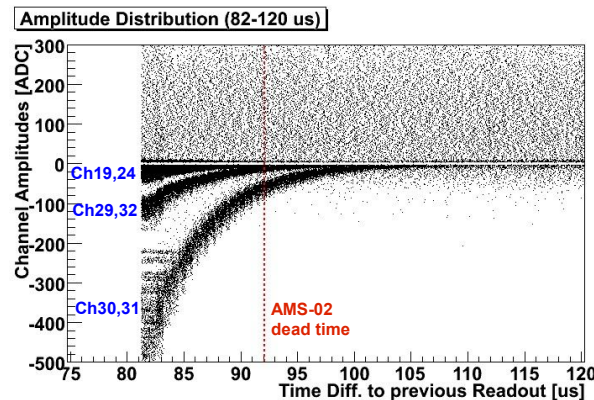


Figure 7.41: The amplitude as a function of the trigger time difference. The positive amplitude distribution independently of the readout time corresponds to a certain particle energy deposition. Negative amplitudes are caused by the undershoot in electronics from a previous particle hit and in addition below about  $100\ \mu\text{s}$  by the crosstalk problem on M-type UFE boards. The pedestals strongly decrease to zero resulting in deeply negative amplitudes. Nevertheless at a minimum trigger time difference for AMS-02 of  $90\ \mu\text{s}$  as indicated the effect can be assigned to a known pattern of channels of the M-type UFE board as indicated in the plot.

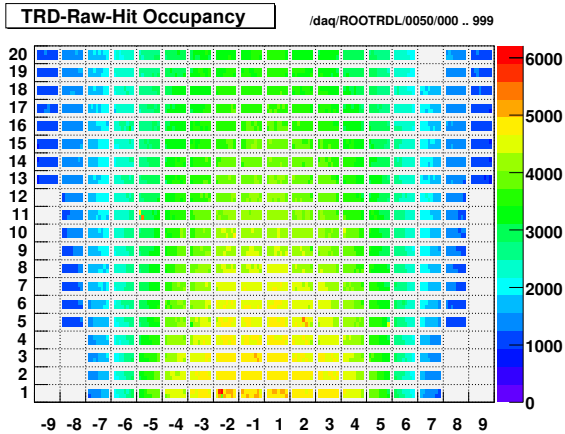


Figure 7.42: *Occupancy mapping of the TRD for a run. The plot shows the number of hits for each tube arranged in 20 layers and the 18 towers of the TRD. The image in the comic rays of the ToF detector below the TRD, which provides the trigger, is visible.*

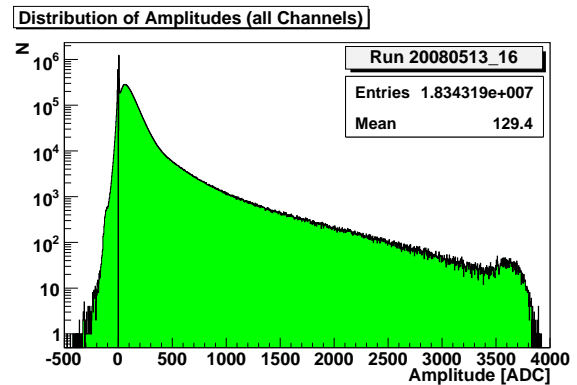


Figure 7.43: *Histogram of the amplitudes from all TRD channels hits. The distribution describes a Landau function with a tail up to the ADC range of about 4000 ADC units. Negative amplitudes are caused by undershoot of UFE electronics from previous positive signal.*

of  $80\mu\text{s}$  almost no influence by the UFE problems is visible after the processing by the DSP. For negative amplitudes an average of two hits per event can be found originating mainly from the discussed undershoot by a previous particle crossing. At about  $100\mu\text{s}$  trigger time difference about 5% of the channels show the decreasing pedestal and with it an increasing event size, which can be extracted from figure 7.41 showing read out amplitudes with respect to the time difference. There are two types of downwards shifted channels affected to a different extend. In contrast the diffuse positive amplitude region is almost not affected representing the Landau distribution of the particles' energy deposition.

### Uniformity of the Cosmic Ray Signal in the UFE Boards of the TRD

The distribution of cosmic ray hits in the TRD is shown in the map in figure 7.42. Only a few channels show a higher occupancy, but also a anomalous amplitude distribution as shown at the end of the section. The lower number of hits towards the edges on the one hand originates from the shorter proportional tubes in the octagon, on the other hand from the trigger configuration of the upper and lower ToF, which favors vertical particle crossings. The overall amplitude distribution from cosmic rays is shown in figure 7.43. The most probable value (MPV) of the distribution can be found at about 70 ADC units. A narrow noise peak at about 5 ADC units can be identified. Again the ten percent of negative amplitudes are visible caused by the UFE electronics undershoot. A tube by tube analysis is given in the following part of this section.

In order to get rid of the noise and undershoot channels read out in an event a track finding algorithm is applied for each event. As soon as a track is found amplitudes off the track are excluded from the analysis. Figure 7.44 shows the amplitude histogram of a single channel. The negative hit amplitudes are almost completely suppressed, but of course incidentally a

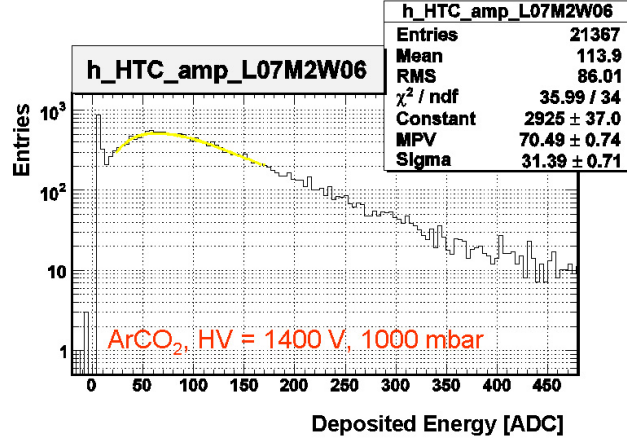


Figure 7.44: Histogram of on track amplitudes of a single tube. As expected negative amplitudes cannot be found on track of a particle.

track still can go through a previous particles track, which leaves negative amplitudes. The most probable energy deposition  $\frac{dE}{dx}$  is determined as the maximum of the Landau distribution

$$L(\lambda) = \frac{1}{2\pi i} \int_{c-i\infty}^{c+i\infty} \exp(\lambda s + s \ln s) ds \quad (7.1)$$

fitted to the histogram, which describes the energy loss of charged particles in matter. Due to the statistical character of the ionization inside the gas, the most probable energy loss is found at the maximum of the distribution. With a small probability also big amounts of energy can be lost by a particle in the gas. The mean energy loss of an impacting particle is described by the Bethe-Bloch formula. The most probable energy deposition is about 70 ADC units for the selected tube, whereas the mean is about 110 ADC units.

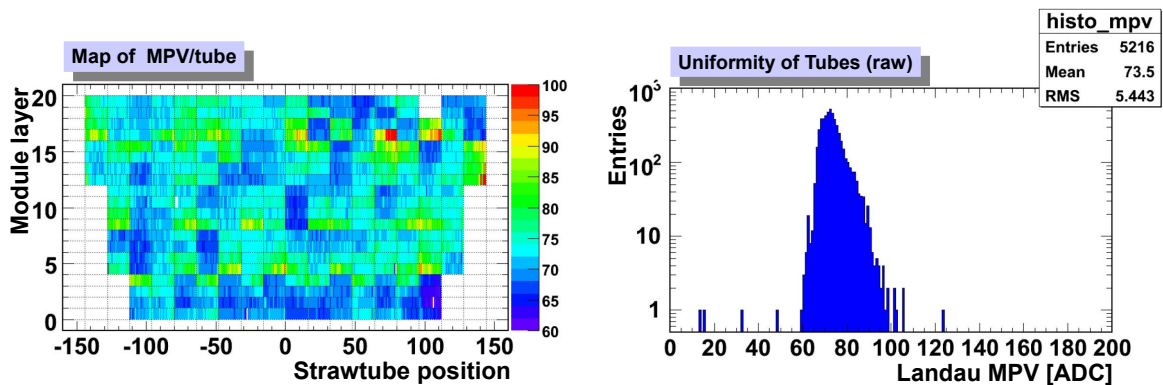


Figure 7.45: Mapping of the MPV obtained by a fit of the Landau function to the amplitude distribution of the on-track energy deposition in a tube.

Figure 7.46: MPV distribution of all TRD straw tubes. The overall spread is about 5% without applied module inter-calibration factors.

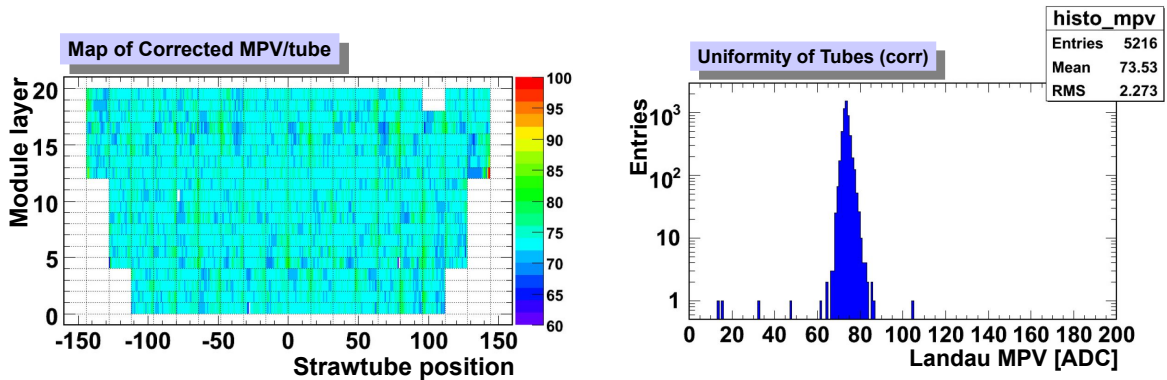


Figure 7.47: Mapping of the MPV obtained by a fit of the Landau function to the amplitude distribution of the on track energy deposition of a tube after inter-calibration of the modules.

Figure 7.48: MPV distribution of all TRD straw tubes after the correction. The overall spread is about 2%. Four channels show an anomalous low MPV, which is a problem is still under investigation.

A good picture of the TRD performance is given by the map of the most probable energy loss inside the tubes of the detector as shown in figure 7.45. On the horizontal axis the position of each straw tube is given with respect to the center of the detector. The vertical axis gives information about the layer assignment. Each tube is represented by a vertical bar for a better visibility. What first catches ones eyes is the empty position in layer 19 and 20. This is the mounting position of the defective UFE 5+7 which has been exchanged after the pre-integration phase. It was excluded form the data acquisition during the data taking phases. The UFE gain correction is already applied. The gain correction is based on the measurements with a radioactive source before the integration of the modules to the TRD octagon. The UFE gain correction applies to two module read out by the same VA chip. Figure 7.46 shows the distribution of the MPV in logarithmic scale. The gain correction in described in detail in [15].

In a second correction the specific gain in each module has to be taken into account. Therefore the mean of the MPV in each module is calculated. A correction relatively to each other has to be done for two reasons. Firstly the mechanical parameters might be different for the modules and secondly and more significant is the fact, that the TRD was operated with flowing gas during the pre-integration phase. A pressure difference is not avoidable at the inlet and outlet of the modules with an influence on the gas gain as described in section 3.3.2. The correction to each tube amplitude is applied according to

$$A_{MPV,tube_{corr}} = A_{MPV,tube} \cdot (A_{MPV,overall}/A_{MPV,module}) \quad . \quad (7.2)$$

Figure 7.47 shows the corrected tube amplitude map for the entire TRD. The uniformity of the straw tube most probable energy deposition is about 2% extracted from figure 7.48.

The uniformity of the straw tubes is within expectations. Figure 7.49 shows the deviation from the mean value after the correction for the different tube positions in the module. Tubes at the edge of the modules clearly show a bigger spread than the inner ones. This can be explained by the gas flux, which results in a higher pressure in the first tubes in a module.

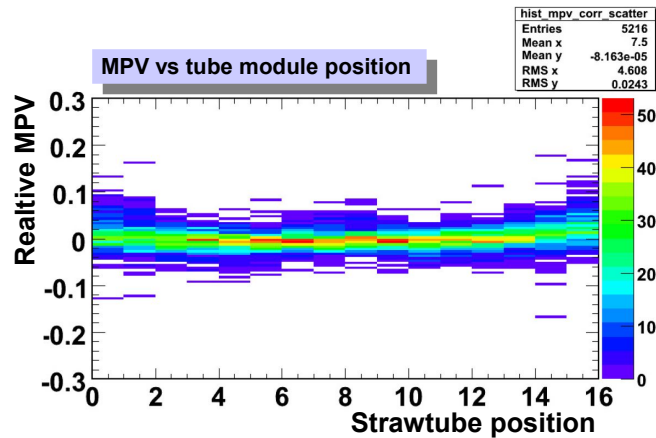


Figure 7.49: Spread of the MPV after the correction depending on the tube position in the module. The MPV is slightly higher at outer tubes at the gas outlet of the module.

Nevertheless four tubes show completely unexpected behavior. The MPV is far below the average for four tubes, which therefore are drawn in white in the map in figure 7.47. The problem is still under investigation.

The TRD has proven an excellent particle detection performance during the data acquisition phases with cosmic rays. A further improvement can be expected from the flight calibration of the tube gas gain, which will allow to correct for small gain variations within a few percent for each tube, and the operation with the final TRD gas system. Nevertheless keeping in mind, that the pre-integration phase has been conducted in order to solve issues of the mechanical integration and to develop procedures to ensure stable running condition for AMS-02, the results are very promising and show the excellent properties of the AMS-02 TRD.

# Chapter 8

## Summary

The AMS-02 instrument is a high precision spectrometer for charged particles and energetic photons in space. Its many subdetectors, ranging from a silicon tracker in the field of a large superconducting magnet, to a transition radiation detector, a ring imaging Cherenkov counter and an electromagnetic calorimeter allow for superb particle identification for all leptons and nuclei below  $Z \approx 26$ . The excellent particle identification is needed to also separate particles from antiparticles and identify leptons in the cosmic rays. Especially the rare components of the cosmic rays in this way can be measured with unprecedented precision and may reveal astonishing results for astroparticle physics.

Within the scope of this thesis the operation of the AMS-02 transition radiation subdetector on board of the International Space Station by remote ground control has been prepared. Space qualification and the production of the maintenance free readout electronics was finalized. Control procedures and software were developed taking into account all aspects of data acquisition with AMS-02. The readout system has been integrated in the AMS-02 detector together with the TRD itself and successfully tested during the first data acquisition with cosmic rays of the entire AMS-02 instrument in 2008.

The flight model of the TRD readout system consists of two U-Crates housing electronics boards for the front end power supply and digital data acquisition and two UPD-Boxes with DC/DC converters to supply the U-Crates. The slow control of the system is accomplished via the JINF board, which is the interface of the crate to the higher DAQ system. Redundancy in all stages of the system allows to compensate any failure of a part including the processors as well as single wire connections.

Thorough testing has been conducted during the space qualification phase carried out subsequent to the production of the first qualification model of the readout electronics. In order to withstand the harsh conditions in space and to guarantee a maintenance free operation three stages of tests were performed. During the environmental stress screening, extreme temperature conditions in a climatic chamber as well as mechanical stress on a vibration table are applied. The latter test ensures, that the system will survive the shuttle launch without a damage. The electromagnetic compatibility test not only targets the mission success, since an influence on the performance by conducted or radiated electromagnetic radiation has to be excluded, but also the radiated emission needs to comply with limits for operation on the International Space Station defined by NASA. The thermal vacuum test finally simulates the expected temperature and pressure conditions in space, where heat cannot be dissipated by convection.

All tests were carried out successfully for the TRD readout electronics qualification model in 2005 and 2006. Modifications of the system, necessary to fulfill the criteria, were applied and verified in the final tests. At the end of these tests in October 2006 the design was approved to be qualified for space operation. From 2006 on the qualification model of the readout electronics has been continuously operated either with a prototype chamber in Karlsruhe or with the final detector at RWTH Aachen or CERN analyzing the recorded tracks of cosmic rays. No failure of the system readout or power supply nor a degrading of the signal quality has been observed.

Immediately following the qualification tests the production of the flight model of the system was initiated. The production was coordinated according to a strict schedule in order to complete the detector in time. A full documentation has been compiled to support a smooth assembly on the site of production at CSIST, a Taiwanese military-industrial institute. During the assembly each step has been supervised during several periods in Taiwan.

So acceptance tests have been conducted on the various levels of production. Board level tests before and after the finalization of the assembly of boards revealed first production defects as well as a mistake in the design, which could be corrected. Also on crate level an acceptance test campaign was performed for the flight as well as the spare electronics. The acceptance test covers the same tests as carried out during the qualification phase, but the mechanical stress is reduced to a minimum, since the main objective is to identify production defects and assembly mistakes. All failures found were repaired directly on the spot by CSIST technicians in Taiwan. A final acceptance thermal-vacuum test was passed at a vacuum chamber at RWTH Aachen in July 2007. The amount of problems identified and repaired during the testing period shows, a painstaking testing of the system is essential. Nevertheless due to the early readiness of flight readout electronics, the TRD was the first subdetector, which was fully operational with the flight model hardware in December 2007.

In parallel to the flight model production the assembly of the TRD and the front end electronics was finalized by RWTH Aachen in 2007. In order to prepare the data acquisition with the entire TRD slow control and DAQ software have been developed on two levels of data acquisition. Firstly a set of programs allows to operate the TRD. The main part is the run control program storing the event data in the AMS data format to disk. Control and monitoring of the high voltage applied to the straw tubes is done by a separate program. Secondly the development of the DAQ software for data reduction and calibration routines running in the on-board digital signal processors of the readout electronics (UDR2) boards of the U-Crate was continued and a final release was made to be used for the first test in AMS-02. Conceptual changes not only related to the TRD, but also affecting the AMS-02 framework, were discussed in the collaboration and introduced for all subdetectors. A implementation of the system configuration procedure to the JINF nodes for instance is based on the concept used for the TRD electronics initialization.

In addition intensive testing of the new code was performed. For that purpose a cosmic ray test stand operating a detector chamber of 64 straw tubes was set up in Karlsruhe. Software was developed to analyze the output of the data reduction routine in order to verify an error-free calculation.

End of 2007 a first readout of tracks of cosmic rays with the completed transition radiation detector was set up at RWTH Aachen. For this test two qualification model U-Crates were prepared. In a four-week data acquisition period millions of particle tracks were recorded and analyzed. Besides the intensive test of the readout electronics reading out and processing for

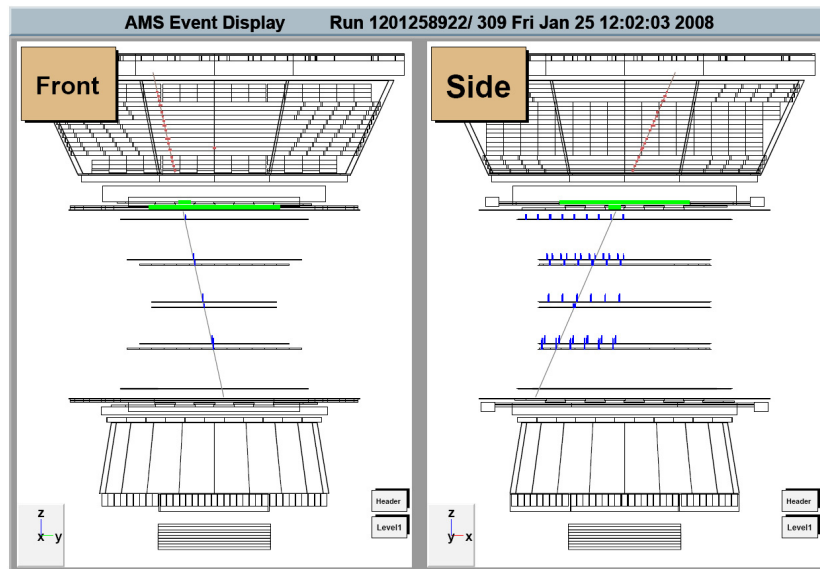


Figure 8.1: *Cosmic ray track recorded with AMS-02 during the pre-integration phase in January 2008.*

the first time the 5248 channels of the TRD special attention was paid to the performance of the detector. Recording and analyzing the data with the entire detector, minor problems of the detector were identified and appropriate handling was implemented in the software. So a special treatment of a few percent of the channels was implemented in the data reduction code of the on-board processors.

In early 2008 a pre-integration of all subdetectors at CERN was decided for the AMS-02 detector due to a delay of the magnet construction. The integration of the TRD flight model readout system was coordinated and documented according to the NASA procedure. Finally the TRD was operational and read out by the flight electronics from December 2007 until the end of the pre-integration phase in June 2008. The readout procedure was implemented in the main DAQ computer of AMS-02 and TRD related parts were developed for the ground support run control software framework. Although a lot of technical issues had to be solved, the focus of the test was set on the stability of the data acquisition system and the detector performance. During the six month of the operation of the flight model electronics and analysis of the recorded cosmic ray data, no major problem was observed. Modifications of the data processing code of the readout electronics were made to fine-tune the data acquisition with the TRD according to the observed characteristics with cosmic rays. The operation of the TRD continuously was controlled and monitored by the developed software utilities either on-site at CERN or remotely from Karlsruhe. Figure 8.1 shows a particle track in AMS-02 recorded during the cosmic ray test.

In both data acquisition phases with the TRD the analysis of the data retrieved from the detector showed an excellent noise behavior with less than 2 ADC units at a dynamic range up to 3,500 ADC units. Only a minimal variation of the gain factors for the charge amplification between single tubes can be observed. The stability of the electronic pedestals could be confirmed. A variation of the signal amplitude clearly can be correlated with parameters

dependent on the ground support gas system. With the successful operation during the pre-integration phase the TRD has proven to be ready for the operation as an important part of the AMS-02 precision instrument.

With the final assembly and test of AMS-02 scheduled for early 2009, the collaboration will successfully have completed the detector. Figure 8.2 shows a picture of the AMS-02 instrument with all integrated subdetectors assembled and operational at CERN. The AMS-02 experiment will be flown to the International Space Station on an additional flight of the Space Shuttle in 2010. Once in the orbit the history has proven, that it is impossible to predict what will be discovered in the end. But AMS-02 as the most precise tool of particle physics in space so far is the key to explore the unknown and to find the unexpected.



Figure 8.2: *The Alpha Magnetic Spectrometer 02 in the assembly area at CERN.*

## 8.1 AMS-02 Flight Status and Outlook

In the frame of this thesis the TRD and the readout electronics have been finalized and operated during the pre-integration phase of AMS-02. The integration and operation were performed in flight configuration. With the successful operation during the pre-integration phase the subdetectors are prepared and ready for the final integration scheduled for the first quarter of 2009.

For the AMS-02 collaboration the final integration phase is of particular importance, because the superconducting magnet will be integrated into the experiment for the first time. A magnetic field map will be recorded before the tracker installation to the inner core of the magnet. A cryogenic ground support equipment is available to fill the liquid Helium tank

already at the CERN site.

A major milestone is the concluding thermal vacuum test in the large space simulator chamber at ESTEC facilities in Noordwijk in the Netherlands shown in figure 8.3. This test is scheduled to take place directly after the integration period in the second half of 2009. Infrared lamps are present to simulate sunlight periods expected for operation on the ISS. For this test of 40 days duration the AMS-02 instrument has to be finally assembled and fully operational. An electromagnetic compatibility test will show if additional shielding is required for the operation on the ISS in compliance with the specifications. Back at CERN facilities a beam test is scheduled in order to allow the calibration of all subdetectors in the strong magnetic field of the AMS-02 magnet.



Figure 8.3: *The Large Space Simulator at ESTEC, NL.*



Figure 8.4: *The Kennedy Space Center in Florida.*

A cargo flight will carry the AMS-02 detector from Geneva airport to the Kennedy Space Center (KSC) in Florida in early 2010. Figure 8.4 shows a picture of the starting and landing site of the NASA Space Shuttle. Once installed into the Space Shuttle's payload bay a continuous operation ensures full functionality until the mounting to the International Space Station. During the transport to the ISS only a minimum part of the system is powered to monitor the critical health data retrieved from AMS-02.

On October 15th, 2008 the president of the United States has signed the NASA bill H.R. 6063, which allows NASA to add to its baseline flight manifest two Space Shuttle

missions to the International Space Station after 2009. One of these flights will be used to carry AMS-02.

Once in space the Space Shuttle's robotic arm will attach the experiment to the S3-truss of the space station. A single astronaut operation is foreseen to connect the AMS-02 instrument to power and data links of the ISS. Immediately afterwards AMS-02 can be switched to the normal operation mode.

Another particle spectrometer known as PAMELA flying on a satellite is already collecting data and delivering results, which are quite promising for the AMS-02 experiment. Amongst other observation the positron excess at high energies measured by the HEAT balloon experiment can be confirmed [2]. Nevertheless the acceptance of the detector and with it the statistics are well below the capabilities of the AMS-02 instrument. For this reason AMS-02 is often regarded as the big brother of PAMELA. Figure 8.5 shows a picture of the International Space Station as of today with the empty slot on the S3-truss mounting position of AMS-02.



Figure 8.5: *The International Space Station today.*



# Bibliography

- [1] ACTEL COOPERATION. SX-A Family FPGAs v5.3, February 2007. [http://www.actel.com/documents/SXA\\_DS.pdf](http://www.actel.com/documents/SXA_DS.pdf).
- [2] ADRIANI, O., ET AL. Observation of an anomalous positron abundance in the cosmic radiation. The PAMELA Collaboration.
- [3] AGHDIRI, A. Entwicklungen für Bestrahlungen am Karlsruher Kompaktzyklotron und erste Tests des Weltraumdetektors AMS-02 mit kosmischer Strahlung, 2008. IEKP, University of Karlsruhe, Diploma Thesis (German).
- [4] AGUILAR, M., ET AL. Physics reports, 2002. vol.366/6 pp.331-404.
- [5] AMS COLLABORATION. AMS on ISS - Construction of a Particle Physics Detector on the International Space Station, 2009. to be published, preprint available at <http://ams.cern.ch/AMS/AMS.pdf>.
- [6] ANALOG DEVICES. *ADSP-218x DSP Hardware Reference*, 2001. Part Number 82-002010-01.
- [7] BARWICK, S. W., ET AL. Measurements of the cosmic-ray positron fraction from 1-GeV to 50-GeV. *Astrophys. J.* 482 (1997), L191–L194.
- [8] BERNABEI, R., ET AL. Dark matter search. *Riv. Nuovo Cim.* 26N1 (2003), 1–73.
- [9] BETHGE, K., WALTER, G., AND WIEDEMANN, B. *Kernphysik*. Springer Verlag, 2001. ISBN 3-540-41444-4.
- [10] BLUM, W., AND ROLANDI, L. *Particle Detection with Drift Chambers*. Springer Verlag, 1994. ISBN 3-540-58322-X.
- [11] CAI, X. AMS-02 Science Data Format, 2007. Preliminary Internal Note.
- [12] CAN IN AUTOMATION. CAN in Automation (CiA) Website, 2008. <http://www.can-cia.org>.
- [13] CAPELL, M., LEBEDEV, A., AND DENNETT, P. AMS-02 Command and Data Handling Interface Control Document, December 10 2004. Revision 05m.
- [14] CHOUTKO, V., AND CHOUMILOV, E. AMS-02 Offline Software Website, 2008. <http://ams.cern.ch/AMS/Analysis/hpl3itp1/ams02.html>.

- [15] CHUNG, C. H. *Space Qualification of the Transition Radiation Detector of the AMS-02 Experiment and Indirect Search for Dark Matter*. PhD thesis, Fakultät für Physik, RWTH Aachen, 2007.
- [16] DE BOER, W. Indirect Dark Matter Signals, 2008. 0810.1472 arXiv astro-ph.
- [17] DE BOER, W., HEROLD, M., SANDER, C., AND ZHUKOV, V. Indirect evidence for neutralinos as dark matter. *Eur. Phys. J. C33* (2004), s981–s983. hep-ph/0312037.
- [18] DE BOER, W., SANDER, C., ZHUKOV, V., GLADYSHEV, A. V., AND KAZAKOV, D. I. EGRET excess of diffuse galactic gamma rays as tracer of dark matter, August 2005. *Astronomy & Astrophysics* 444, 51-67.
- [19] EGGERT, R. Development of a Fuse-Test Backplane for a Multi-Channel Power Supply (UPSFE) within the AMS Project. Master's thesis, Institut für Experimentelle Kernphysik, Universität Karlsruhe, 2004. IEKP-KA/2003-9.
- [20] EUROPEAN COOPERATION FOR SPACE STANDARDIZATION. ECSS-E-50-12A Spacewire - Links, nodes, routers and networks, 24 January 2003. <http://spacewire.esa.int>.
- [21] EVERETT, J. E., ET AL. The milky way's kiloparsec-scale wind: A hybrid cosmic-ray and thermally driven outflow. *The Astrophysical Journal* 674, 1 (2008), 258–270.
- [22] FERMI, E. On the Origin of the Cosmic Radiation. *Phys. Rev.* 75 (1949), 1169–1174.
- [23] FINKBEINER, D., ET AL. Microwave ISM Emission Observed by WMAP, October 2004. 614, 186 and astro-ph/0311547.
- [24] FOPP, S. *Entwicklung und Bau eines auf Proportionalkammern basierenden Übergangsstrahlungsdetektors für das AMS-02-Weltraumexperiment*. PhD thesis, I.Physikalischen Institut der RWTH Aachen, 2004.
- [25] GARIBYAN, G. M. Transition radiation effects in particle energy losses. *Soviet Physics JETP* 37(10), 2 (1960), 372–376.
- [26] GASSMANN, K. Entwicklung und Test der raumfahrtqualifizierten Datenakquisition für den Übergangsstrahlungsdetektor des AMS-02 Experiments, 2007. IEKP, University of Karlsruhe, Diploma Thesis (German).
- [27] GINSBURG, V. L., AND FRANK, I. M. . *J. Exptl. Theoret. Phys. (U.S.S.R.)* 16, 15 (1946).
- [28] GRUPEN, C. *Teilchendetektoren*. BI Wissenschaftsverlag, 1993. ISBN 3-411-16571-5.
- [29] HATTENBACH, J. *Gasverstärkungsmessung mit Proportionalkammern des Übergangsstrahlungsdetektors für das AMS02-Weltraumexperiment*. 2004. I.Physikalischen Institut der RWTH Aachen.
- [30] HAULER, F. P. *Entwicklung der raumfahrtqualifizierten Datenakquisition für den Übergangsstrahlungsdetektor des AMS-02-Experiments auf der Internationalen Raumstation*. PhD thesis, Fakultät für Physik, Universität Karlsruhe, 2005. IEKP-KA/2005-24.

- [31] HINSHAW, G., ET AL. Five-Year Wilkinson Microwave Anisotropy Probe (WMAP) Observations: Data Processing, Sky Maps and Basic Results, 2008.
- [32] HUNTER, S., ET AL. EGRET Observations of the Diffuse Gamma-Ray Emission from the Galactic Plane, June 1997. 481, 205-240.
- [33] INTERNATIONAL SPACE STATION. Space Station Electromagnetic Emission and Susceptibility Requirements, 17 May 2001. Revision F, Space Standard SSP30237.
- [34] JUNGERMANN, L. *Elektronik für das Weltraum-Experiment AMS-02 und Bildgebung in der Strahlenmedizin*. PhD thesis, Fakultät für Physik, Universität Karlsruhe, 2005. IEKP-KA/2005-6.
- [35] KOUNINE, A., AND KOUTSENKO, V. *Flight Software for xDR and JINx nodes in AMS-02*, 2008.
- [36] LIN, C. AMSWire, AMS-2 DAQ Link Protocol, June 4 2003. v3.1.
- [37] MULVILLE, D. Payload Test Requirements, NASA-STD-7002, July 1996. [http://klabs.org/DEI/References/design\\_guidelines/content/nasa\\_specs/7002.pdf](http://klabs.org/DEI/References/design_guidelines/content/nasa_specs/7002.pdf).
- [38] MULVILLE, D. Payload Vibroacoustic Test Criteria, NASA-STD-7001, June 1996. [http://klabs.org/DEI/References/design\\_guidelines/content/nasa\\_specs/7001.pdf](http://klabs.org/DEI/References/design_guidelines/content/nasa_specs/7001.pdf).
- [39] ORBOECK, J. *The final 20-Layer-Prototype for the AMS Transition Radiation Detector: Beamtest, Data-Analysis, MC-Studies*. PhD thesis, RWTH Aachen, 2003.
- [40] SABELLEK, A. AMS-02 UPD to U-Crate Cabling Assembly Procedure, 2007. Internal Report, available at [http://www-ekp.physik.uni-karlsruhe.de/~amswww/downloads/cable\\_docs/UCabling\\_Assembly\\_v.2.1.pdf](http://www-ekp.physik.uni-karlsruhe.de/~amswww/downloads/cable_docs/UCabling_Assembly_v.2.1.pdf).
- [41] SABELLEK, A. TRD Readout Electronics Acceptance Data Package, 2008. Internal Report, available at [http://www-ekp.physik.uni-karlsruhe.de/~amswww/downloads/adp/TRDElec\\_ADP\\_v1.pdf](http://www-ekp.physik.uni-karlsruhe.de/~amswww/downloads/adp/TRDElec_ADP_v1.pdf).
- [42] SABELLEK, A., AND SCHMANAU, M. AMS-02 TRD Power Distribution Box Assembly Procedure, 2007. Internal Report, available at [http://www-ekp.physik.uni-karlsruhe.de/~amswww/downloads/assembly\\_docs/UPD\\_Assemblyv01.9.pdf](http://www-ekp.physik.uni-karlsruhe.de/~amswww/downloads/assembly_docs/UPD_Assemblyv01.9.pdf).
- [43] SCHEULEN, M. DSP Software Development for TRD electronics of the AMS-02 Detector, 2007. IEKP, University of Karlsruhe, Diploma Thesis (German).
- [44] SCHMANAU, M. *Data Acquisition Development and Background Studies for the spaceborn Detector AMS-02 and the CMOS Detector Mimoso-V*. PhD thesis, Fakultät für Physik, Universität Karlsruhe, 2008. IEKP-KA/2008-25.
- [45] STRUCZINSKI, W. *Identifizierung Hochenergetischer Teilchen durch "Übergangsstrahlung"*. 1986. III. Physikalisches Institut der RWTH Aachen.
- [46] THE AUGER COLLABORATION. Official website, 2008. <http://www.auger.org>.
- [47] THE GLAST COLLABORATION. Official website, 2008. <http://fermi.gsfc.nasa.gov/>.

- [48] THE PAMELA COLLABORATION. Official website, 2008. <http://pamela.roma2.infn.it/index.php>.
- [49] VON DOETINCHEM, P. Documentation of the AMS-02 TRD Mock-Up MLI Tailoring and Cabling, May 4, 2006. Internal Note.
- [50] WAKELY, S., PLEWNIA, S., MÜLLER, D., HÖRANDEL, J., AND GAHBAUER, F. Transition radiation detectors for energy measurement at high Lorentz factors. *Nuclear Instruments and Methods in Physics Research A* 531 (2004), 435–444.
- [51] WWW.ASTROTEILCHENPHYSIK.DE/SERVICE/IMPRESSUM.HTM. Astroteilchenphysik in Deutschland. Website: <http://www.astroteilchenphysik.de/>, November 2008.
- [52] ZWICKY, F. Spectral displacement of extra galactic nebulae. *Helv. Phys. Acta* 6 (1933), 110–127.

# Danksagung

Die Mitwirkung im Rahmen dieser Arbeit im AMS Projekt war stets eine Herausforderung, welche aber auch mit viel Spaß erledigt werden konnte. Dies ist sowohl dem großen Zusammenhalt in der AMS Kollaboration, aber auch dem guten Arbeitsklima am Institut für Experimentelle Kernphysik (IEKP) der Universität Karlsruhe zuzuschreiben.

An erster Stelle möchte ich daher Prof. Dr. Wim de Boer für die Möglichkeit der Arbeit in diesem Projekt an diesem Institut danken. Durch die einzigartige Betreuung während dieser Zeit wurden mir immer wieder neue Perspektiven aufgezeigt, welche in die Aufgaben eines Experimentalphysikers einführten. Das hervorragende Arbeitsklima am Institut ist natürlich im gleichen Maße meinem Korreferenten Prof. Dr. Thomas Müller zu verdanken, welcher als Institutsleiter immer mit Interesse meine Arbeit am AMS Projekt verfolgte.

Meinen Kollegen danke ich für die zahlreichen Gespräche und Einblicke in vielfältige Projekte, welche am Institut verfolgt werden. Die ehemaligen Mitglieder meiner Arbeitsgruppe Dr. Levin Jungermann und Dr. Florian Hauler konnte ich bei Problemen jederzeit um Hilfe bitten. Besonders möchte ich meinen Kollegen im Büro Dipl.-Phys. Mike Schmanau erwähnen, welcher für eine abwechslungsreiche Zeit am Arbeitsplatz sorgte.

Während der zeitweisen Mitarbeit an den Produktionstests der CMS Trackermodule gemeinsam mit Dr. Peter Blüm, Dr. Hans-Jürgen Simonis und Dr. Bernhard Ledermann habe ich viele hilfreiche Erfahrungen sammeln können.

Sicher wäre die Arbeit nicht so erfolgreich verlaufen, hätte ich mich nicht auf den vorbildlichen Einsatz unserer Diplomanden Dipl.-Phys. Kai Uwe Gassmann, Dipl.-Phys. Max Scheulen und Jochen Ebert verlassen können. In der Natur der Qualifikationstests in Taiwan lag erschwerend neben den durchgehenden Arbeitszeiten auch ein ungewohntes Klima und während der Datenaufzeichnung mit dem Detektor die Unvorhersehbarkeit der Ereignisse zu jeder Tageszeit. Hierbei möchte ich besonders Dipl.-Phys. Asim Aghdiri danken, der durch seinen Spaß an der Arbeit auch ein Freundschaftsverhältnis über die Diplomarbeitszeit hinaus geschaffen hat.

Wie einleitend erwähnt habe ich mich in der AMS Kollaboration immer sehr gut aufgehoben gefühlt. Hierzu trug die gute Unterstützung durch die AMS-Gruppe an der RWTH Aachen mit Dr. Thorsten Siedenburg, Dr. Thomas Kirn und Dr. Chanhon Chung unter der Leitung von Prof. Dr. Stefan Schael und Prof. Dr. Klaus Lübelmeyer bei.

Die sicher wertvollsten Erfahrungen als Doktorand habe ich durch die Zusammenarbeit mit den Mitgliedern der MIT-Gruppe am CERN erlangt. Hierbei möchte ich vor allem Dr. Mike Capell, Dr. Vladimir Koutsenko, Dr. Alexei Lebedev, Dr. Andrei Kounine und Dr. Xudong Cai erwähnen. Ihre Erfahrung ist die Basis des gesamten AMS Projekts. Speziell danke ich dem Leiter der AMS Elektronikgruppe Dr. Giovanni Ambrosi.

Mein Dank gilt auch den Mitarbeitern der Elektronik- und Feinmechanikwerkstatt des IEKP, als auch Pia Steck und Tobias Barvich, der in allen mechanischen Fragen sofort zur Stelle war, und Brigitte Schulz, die alle Verwaltungsangelegenheiten effizient regelte.

In der Zeit meines Studiums fand ich immer Unterstützung bei meiner Familie. Ich danke auch meiner langjährigen Lebensgefährtin Anja, welche mir immer sehr viel Kraft und Motivation gab und mich erst kurz vor Abschluss dieser Arbeit verlassen hat.

Für die einzigartige Zusammenarbeit während meines gesamten Studiums der Physik möchte ich Dipl.-Phys. Martin Niegel danken. Ohne diese Freundschaft wäre vieles anders verlaufen.

Das Foto in Abbildung 8.6 zeigt einen Teil der TRD-Gruppe während der Datennahme mit kosmischer Strahlung an der RWTH Aachen.

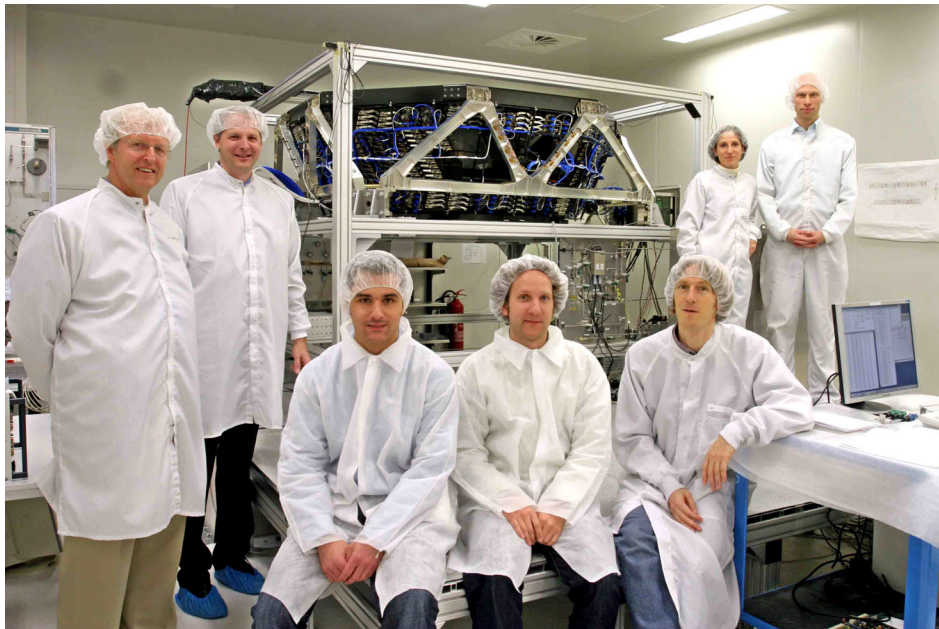


Figure 8.6: *Picture of TRD group members taken during the cosmic ray test at RWTH Aachen. From left to right: Prof. Dr. Wim de Boer, Prof. Dr. Stefan Schael, Asim Aghdiri, Andreas Sabellek, Dr. Thorsten Siedenburg, Dr. Francesca Giovacchini and Michael Kosbow. For an exciting time I want to thank all collaborators of the AMS-02 project.*



